Part I

Textile structure and moisture transport

1

Characterizing the structure and geometry of fibrous materials

N. PAN and Z. SUN, University of California, USA

The textile manufacturing process is remarkably flexible, allowing the manufacture of fibrous materials with widely diverse physical properties. All textiles are discontinuous materials in that they are produced from macroscopic sub-elements (finite length fibers or continuous filaments). The discrete nature of textile materials means that they have void spaces or pores that contribute directly to some of the key properties of the textiles, for example, thermal insulating characteristics, liquid absorption properties, and softness and other tactile characteristics.

Fibrous materials can be defined as bulk materials made of large numbers of individual fibers, so to understand the behaviors of fibrous materials, we have to discuss issues related to single fibers. However, it should be noted that the behavior of fibrous materials is remarkably different from that of their constituent individual fibers. For instance, the same wool fiber can be used to make a summer T-shirt or a winter coat; structural factors have to be included to explain the differences.

1.1 Geometrical characterization of single fibers

1.1.1 The fiber aspect ratio

A fiber is, in essence, merely a concept associated with the shape or geometry of an object, i.e. a slender form characterized by a high aspect ratio of fiber length l_f to diameter D_f

$$s = \frac{l_f}{D_f} \tag{1.1}$$

with a small transverse dimension (or diameter) at usually 10^{-6} m scale.

1.1.2 The specific surface

For a given volume (or material mass) V_o, different geometric shapes generate different amounts of surface area by which to interact with the environment.

For heat and moisture transport, a shape with higher specific surface S_v value is more efficient.

For a sphere

$$s_v^s = \frac{3\left(\frac{4}{3}\pi\right)^{\frac{1}{3}}}{V_o^{\frac{1}{3}}} \approx \frac{4.836}{V_o^{\frac{1}{3}}} \tag{1.2}$$

For a cube

$$s_v^c = \frac{6}{V_o^{\frac{1}{3}}} \tag{1.3}$$

For a fiber (cylinder)

$$s_v^f = \frac{2\pi r^2}{V_o} + \frac{2}{r} \tag{1.4}$$

That is, for a given volume V_o, a cubic shape will generate more surface area than a spherical shape. However, since the fiber radius r can be an independent variable as long as

$$l\pi r^2 = V_o$$

remains constant, so

$$r = \sqrt{\frac{V_o}{\pi l}} \tag{1.5}$$

reduces as the fiber length increases. In other words, theoretically, the specific surface area for fiber s_v^f could approach infinite if $r \to 0$ so $l \to \infty$. This is one of the advantages of nano fibers; also why the capillary effect is most significant in fibrous materials.

It may be argued that a cuboid with sides a, b and c such that the volume $V_o = abc$ remains constant would have the same advantage, i.e.

$$s_v^e = \frac{2(ab + bc + ca)}{V_o} = 2\left(\frac{1}{a} + \frac{1}{b} + \frac{1}{c}\right) \tag{1.6}$$

where we have used $c = \frac{V_o}{ab}$ so that c and ab cannot change independently; if we choose $c \to \infty$ then $ab \to 0$, in other words, the cuboid becomes a fiber with non-circular (rectangular) cross sectional shape.

1.2 Basic parameters for porous media

1.2.1 Total fiber amount – the fiber volume fraction V_f

For any mixture, the relative proportion of each constituent is obviously the most desirable parameter to know. There are several ways to specify the proportions, including fractions or percentages by weight or by volume.

For practical purpose, weight fraction is most straightforward. For a mixture of n components, the weight fraction W_i for component i (= 1, 2, …, n) is defined as

$$W_i = \frac{M_i}{M_t} \qquad [1.7]$$

where M_i is the net weight of the component i, and M_t is the total weight of the mixture.

However, it is the volume fraction that is most often used in analysis; this can be readily calculated once the corresponding weight fractions M_i and M_t and the densities ρ_i and ρ_t are known:

$$V_i = \frac{(M_i/\rho_i)}{(M_t/\rho_t)} = \frac{M_i}{M_t}\frac{\rho_t}{\rho_i} = W_i\frac{\rho_t}{\rho_i} \qquad [1.8]$$

For a fibrous material formed of fibers and air, it should be noted that, although the weight fraction of the air is small, its volume fraction is not due to its low density.

1.2.2 Porosity ε

The porosity of a material is defined as the ratio of the total void spaces volume V_v to the total body volume V:

$$\varepsilon = \frac{V_v}{V} \qquad [1.9]$$

Obviously, the porosity ε is dependent on the definition of the pore sizes, for at the molecular level everything is porous. So, in the case of circular pore shape, the porosity is a function of the range of the pore size distribution from $r_{\max}$ to $r_{\min}$

$$\varepsilon = \int_{r_{\min}}^{r_{\max}} \frac{d\varepsilon}{dr} = \int_{r_{\min}}^{r_{\max}} f(r)\,dr \qquad [1.10]$$

where

$$f(r) = \frac{d\varepsilon}{dr} \qquad [1.11]$$

is the so-called pore size probability density function (*pdf*) and satisfies the normalization function.

$$\int_0^{\infty} f(r)\,dr = 1$$

1.2.3 Tortuosity ξ

The tortuosity is the ratio of the body dimension l in a given direction to the length of the path l_t traversed by the fluid in the transport process,

$$\xi = \frac{l_t}{l} \qquad [1.12]$$

1.2.4 Pore shape factor δ

The pore shape factor reflects the deviation of the pore shape from an ideal circle. In the case of an oval shape with longer axis a and shorter axis b;

$$\delta = \frac{b}{a} \qquad [1.13]$$

Apparently, $\delta < 1$.

1.3 Characterization of fibrous materials

Even for a fibrous material made of identical fibers, i.e. the same geometrical shapes and dimensions and physical properties, the pores formed inside the material will exhibit huge complexities in terms of sizes and shapes so as to form the capillary geometry for transporting functions. The pores will even change as the material interacts with fluids or heat during the transport process; fibers swell and the material deforms due to the weight of the liquid absorbed.

Such a tremendous complexity inevitably calls for statistical or probabilistic approaches in describing internal structural characteristics such as the pore size distribution as a prerequisite for studying the transport phenomenon of the material.

1.3.1 Description of the internal structures of fibrous materials

Fibrous materials are essentially collections of individual fibers assembled via frictions into more or less integrated structures (Fig. 1.1). Any external stimulus on such a system has to be transmitted between fibers through either the fiber contacts and/or the medium filling the pores formed by the fibers. As a result, a thorough understanding and description of the internal structure becomes indispensable in attempts to study any behavior of the system. In other words, the issue of structure and property remains just as critical as in other materials such as polymers: with similar internal structures, except for the difference in scales.

1.3.2 Fiber arrangement – the orientation probability density function

Various analytic attempts have already been made to characterize the internal structures of the fibrous materials. There are three groups of slightly different approaches owing to the specific materials dealt with. The first group aimed at paper sheets. The generally acknowledged pioneer in this area is Cox. In his report (Cox, 1952), he tried to predict the elastic behavior of paper (a bonded planar fiber network) based on the distribution and mechanical properties of the constituent fibers. Kallmes (Kallmes and Corte, 1960; Corte and Kallmes, 1962; Kallmes and Bernier, 1963; Kallmes *et al.*, 1963; Kallmes 1972) and Page (Seth and Page, 1975, 1996; Page *et al.*, 1979; Page and Seth, 1980 a, b, c, 1988 Michell, Seth *et al.*, 1983; Schulgasser and Page, 1988; Page and Howard, 1992; Gurnagul, Howard *et al.*, 1993; Page, 1993, 2002) have contributed a great deal to this field through their research work on properties of paper. They extended Cox's analysis by using probability theory to study fiber bonding points, the free fiber lengths between the contacts, and their distributions. Perkins (Perkins and Mark, 1976, 1983a, b; Castagnede, Ramasubramanian *et al.*, 1988; Ramasubramanian and Perkins, 1988; Perkins and Ramasubramanian, 1989) applied micromechanics to paper sheet analysis. Dodson (Dodson and Fekih, 1991; Dodson, 1992, 1996; Dodson and Schaffnit, 1992; Deng and Dodson, 1994a, b; Schaffnit and Dodson 1994; Scharcanski and Dodson, 1997, 2000; Dodson and Sampson, 1999; Dodson, Oba *et al.*, 2001; Scharcanski, Dodson *et al.*, 2002) tackled the problems along a more theoretical statistics route.

Another group focused on general fiber assemblies, mainly textiles and other fibrous products. Van Wyk (van Wyk, 1946) was among the first who studied the mechanical properties of a textile fiber mass by looking into the microstructural units in the system, and established the widely applied compression formula. A more complete work in this aspect, however, was carried out by Komori and his colleagues (Komori and Makishima, 1977, 1978; Komori and Itoh, 1991, 1994, 1997; Komori, Itoh *et al.*, 1992). Through a series of papers, they predicted the mean number of fiber contact points and the mean fiber lengths between contacts (Komori and Makishima, 1977, 1978; Komori and Itoh, 1994), the fiber orientations (Komori and Itoh, 1997) and the pore size distributions (Komori and Makishima, 1978) of the fiber assemblies. Their results have broadened our understanding of the fibrous system and provided new means for further research work on the properties of fibrous assemblies. Several papers have since followed, more or less based on their results, to deal with the mechanics of fiber assemblies. Lee and Lee (Lee and Lee, 1985), Duckett and Chen (Duckett and Cheng, 1978; Chen and Duckett, 1979) further developed the theories on the compressional properties (Duckett and Cheng, 1978; Beil and Roberts, 2002). Carnaby and

Pan studied fiber slippage and compressional hysteresis (Carnaby and Pan, 1989), and shear properties (Pan and Carnaby, 1989). Pan also discussed the effects of the so called ‘steric hinge’ (Pan, 1993b), the fiber blend (Pan *et al.*, 1997) and co-authored a review monograph on the theoretical characterization of internal structures of fibrous materials (Pan and Zhong, 2006).

The third group is mainly concerned with fiber-reinforced composite materials. Depending on the specific cases, they chose either of the two approaches listed above with modification to better fit the problems (Pan, 1993c, 1994; Parkhouse and Kelly, 1995; Gates and Westcott, 1999 Narter and Batra *et al.*, 1999).

Although Komori and Makishima’s results are adopted hereafter, we have to caution that their results valid only for very loose structures, for if the fiber contact density increases, the effects of the steric hinge have to be accounted to reflect the fact that the contact probability changes with the number of fibers involved (Pan, 1993b, 1995).

1.3.3 Characterization of the internal structure of a fibrous material (Pan,1994)

A general fibrous structure is illustrated in Fig. 1.1. As mentioned earlier, we assume that all the properties of such a system are determined collectively by the bonded areas and the free fiber segments between the contact points as well as by the volume ratios of fibers and voids in the structure. Therefore, attention has to be focused first on the characterization of this microstructure, or more specifically, on the investigation of the density and distribution of the contact points, the relative proportions of bonded portions and the free fiber segment between two contact points on a fiber in the system of given volume V.

According to the approach explored by Komori and Makishima (1977, 1978), let us first set a Cartesian coordinate system X_1, X_2, X_3 in a fibrous

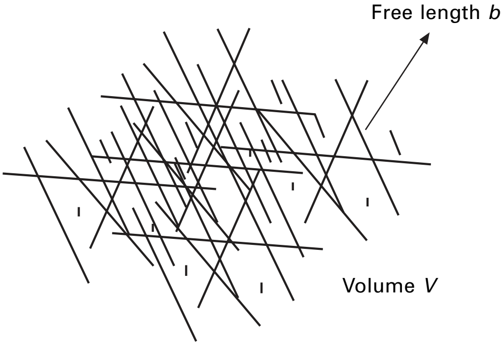

1.1 A general fibrous structure.

structure, and let the angle between the X_3-axis and the axis of an arbitrary fiber be θ, and that between the X_1-axis and the normal projection of the fiber axis onto the X_1X_2 plane be ϕ. Then the orientation of any fiber can be defined uniquely by a pair (θ, ϕ), provided that $0 \le \theta \le \pi$ and $0 \le \phi \le \pi$ as shown in Fig. 1.2.

Suppose the probability of finding the orientation of a fiber in the infinitesimal range of angles $\theta \sim \theta + d\theta$ and $\phi \sim \phi + d\phi$ is $\Omega(\theta, \phi) \sin \theta d\theta d\phi$ where $\Omega(\theta, \phi)$ is the still unknown density function of fiber orientation and θ is the Jacobian of the vector of the direction cosines corresponding to θ and ϕ. The following normalization condition must be satisfied:

$$\int_0^\pi d\theta \int_0^\pi d\phi \Omega(\theta, \phi) \sin \theta = 1 \qquad [1.14]$$

Assume there are N fibers of straight cylinders of diameter $D = 2r_f$ and length l_f in the fibrous system of volume V. According to the analysis by Komori and Makishima (1977), the average number of contacts on an arbitrary fiber, $\bar{n}$, can be expressed as

$$\bar{n} = \frac{2DNl_f^2}{V} l \qquad [1.15]$$

where l is a factor reflecting the fiber orientation and is defined as

$$I = \int_0^\pi d\theta \int_0^\pi d\phi J(\theta,\phi)\Omega(\theta, \phi) \sin \theta \qquad [1.16]$$

where

$$J(\theta, \phi) = \int_0^\pi d\theta' \int_0^\pi d\phi' \Omega(\theta', \phi') \sin \chi(\theta,\phi,\theta',\phi') \sin \theta' \qquad [1.17]$$

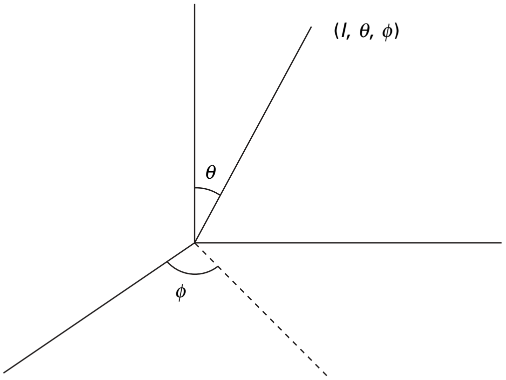

1.2 The coordinates of a fiber in the system.

and $$\sin \chi = [1 - (\cos \theta \cos \theta' + \sin \theta \sin \theta' \cos (\phi - \phi'))^2]^{\frac{1}{2}} \quad [1.18]$$

χ is the angle between two arbitrary fibers. The mean number of fiber contact points per unit fiber length has been derived by them as

$$n_l = \frac{\bar{n}}{l_f} = \frac{2DNl_f}{V} I = \frac{2DL}{V} I \quad [1.19]$$

where $L = Nl_f$ is the total fiber length within the volume V. This equation can be further reduced to

$$n_l = \frac{2DL}{V} I = \frac{\pi D^2 L}{4V} \frac{8l}{\pi D} = 8l \frac{V_f}{\pi D} \quad [1.20]$$

where $V_f = \dfrac{\pi D^2 L}{4V}$ is the fiber volume fraction and is usually a given parameter. It is seen from the result that the parameter I can be considered as an indicator of the density of contact points. The reciprocal of n_l is the mean length, $\bar{b}$, between the centers of two neighboring contact points on the fiber, as illustrated in Fig. 1.3, i.e.

$$\bar{b} = \frac{\pi D}{8IV_f} \quad [1.21]$$

The total number of contacts in a fiber assembly containing N fibers is then given by

$$n = \frac{N}{2} \bar{n} = \frac{DL^2}{V} I \quad [1.22]$$

The factor $\frac{1}{2}$ was introduced to avoid the double counting of one contact. Clearly these predicted results are the basic microstructural parameters and the indispensable variables for studies of any macrostructural properties of a fibrous system.

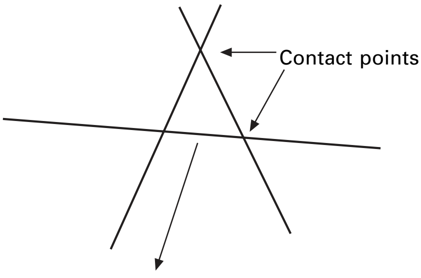

1.3 A representative micro-structural unit.

1.4 Mathematical descriptions of the anisotropy of a fibrous material

As demonstrated previously, the fiber contacts and pores in a fibrous material are entirely dependent on the way that the fibers are put together.

Let us take a representative element of unit volume from a general fibrous material in such a way that a simple repetitive packing of such elements will restore the original whole material.

Consider on the representative element a cross-section, as shown in Fig. 1.4, of unit area whose normal is defined by direction (Θ, Φ), just as we defined a fiber orientation previously. Here we assume all fibers are identical, with length l_f and radius r_f. If we ignore the contribution of air in the pores, the properties of the system in any given direction are determined completely by the amount of fiber involved in that particular direction. Since, for an isotropic system, the number of fibers at any direction should be the same, the anisotropy of the system structure is reflected by the fact that, at different directions of the system, the number of fibers involved is a function of the direction and possesses different values.

Let us designate the number of fibers traveling through a cross-section of direction (Θ, Φ) as $\Psi(\Theta, \Phi)$. This variable, by definition, has to be proportionally related to the fiber orientation *pdf* in the same direction (Pan, 1994), i.e.

$$\Psi(\Theta, \Phi) = N\Omega(\Theta, \Phi) \qquad [1.23]$$

where N is a coefficient. This equation, in fact, establishes the connection between the properties and the fiber orientation for a given cross-section. The total number of fibers contained in the unit volume can be obtained by integrating the above equation over the possible directions of all the cross-sections of the volume to give

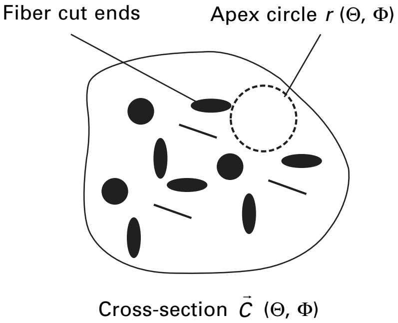

1.4 The concept of the 'aperture circle' of various radii on a cross-section. Adapted from Komori, T. and K. Makishima (1979). 'Geometrical Expressions of Spaces in Anisotropic Fiber Assemblies.' *Textile Res. J.*, 49: 550–555.

$$\int_{\Psi} \Psi(\Theta,\Phi)\, d\Psi(\Theta,\Phi) = \int_0^{\pi} d\Theta \int_0^{\pi} d\Phi N \Omega(\Theta, \Phi) \sin\Theta = N \qquad [1.24]$$

That is, the constant N actually represents the total number of fibers contained in the unit volume, and is related to the system fiber volume fraction V_f by the expression

$$N = \frac{V_f}{\pi r_f^2 l_f} \qquad [1.25]$$

Then, on the given cross-section (Θ, Φ) of unit area, the average number of cut ends of the fibers having their orientations in the range of $\theta \sim \theta + d\theta$ and $\phi \sim \phi + d\phi$ is given, following Komori and Makishima (1978), as

$$d\Psi = \Psi(\Theta, \Phi) l_f \,|\cos\chi|\, \Omega(\theta, \phi) \sin\theta d\theta d\phi \qquad [1.26]$$

where, according to analytic geometry,

$$\cos\chi = \cos\Theta \cos\theta + \sin\Theta \sin\theta \cos(\phi - \Phi) \qquad [1.27]$$

with χ being the angle between the directions (Θ, Φ) and θ, ϕ). Since the area of a cut-fiber end at the cross-section (Θ, Φ), ∇S, can be derived as

$$\nabla S = \frac{\pi r_f^2}{|\cos\chi|}, \qquad [1.28]$$

the total area S of the cut-fiber ends of all possible orientations on the cross-section can be calculated as

$$S(\Theta,\Phi) = \int_0^{\pi} d\theta \int_0^{\pi} d\phi \times \nabla S \times d\Psi \times \Omega(\theta, \phi) \sin\theta$$
$$= \Psi(\Theta,\Phi) \int_0^{\pi} d\theta \int_0^{\pi} d\phi \pi r_f^2 l_f\, \Omega(\theta, \phi) \sin\theta = \Omega(\Theta,\Phi) N\pi r_f^2 l_f \qquad [1.29]$$

As $S(\Theta, \Phi)$ is in fact equal to the fiber area fraction on this cross-section of unit area, i.e.

$$S(\Theta, \Phi) = A_f(\Theta, \Phi), \qquad [1.30]$$

we can therefore find the relationship in a given direction (Θ, Φ) between the fiber area fraction and the fiber orientation *pdf* from Equations [1.29] and [1.30]

$$A_f(\Theta, \Phi) = \Omega(\Theta, \Phi) N\pi r_f^2 l_f = \Omega(\Theta, \Phi) V_f \qquad [1.31]$$

This relationship has two practical yet important implications. First, it can provide a means to derive the fiber orientation *pdf*; at each system cross-section (Θ, Φ), once we obtain through experimental measurement the fiber area fraction $A_f(\alpha, \Phi)$, we can calculate the corresponding fiber orientation *pdf* $\Omega(\Theta, \Phi)$ for a given constant V_f. So a complete relationship of $\Omega(\Theta, \Phi)$ versus (Θ, Φ) can be established from which the overall fiber orientation *pdf* can be deduced. Note that a fiber orientation *pdf* is by definition the function of direction only. Secondly, it shows in Equation [1.31] that the only case where $A_f = V_f$ is when the density function $\Omega(\Theta, \Phi) = 1$; this happens only in the systems made of fibers unidirectionally oriented at direction (Θ, Φ). In other words, the difference between the fiber area and volume fractions is caused by fiber misorientation.

The pore area fraction $A_a(\Theta, \Phi)$, on the other hand, can be calculated as

$$A_a(\Theta, \Phi) = 1 - A_f(\Theta, \Phi) = 1 - \Omega(\Theta, \Phi)V_f \qquad [1.32]$$

In addition, the average number of fiber cut-ends on the plane, $\nu(\Theta, \Phi)$, is given as

$$\begin{aligned}\nu(\Theta,\Phi) &= \int_0^{\pi} d\theta \int_0^{\pi} d\phi \times d\Psi \times \Omega(\theta, \phi)\sin\theta \\ &= N\Omega(\Theta,\Phi)l_f \int_0^{\pi} d\theta \int_0^{\pi} d\phi|\cos\chi|\,\Omega(\theta, \phi)\sin\theta \\ &= \frac{V_f}{\pi r_f^2}\,\Omega(\Theta, \Phi)\Upsilon(\Theta, \Phi) \qquad [1.33]\end{aligned}$$

where

$$\Upsilon(\Theta,\Phi) = \int_0^{\pi} d\theta \int_0^{\pi} d\phi|\cos\chi|\,\Omega(\theta, \phi)\sin\theta \qquad [1.34]$$

is the statistical mean value of $|\cos\chi|$.

Hence, the average radius of the fiber cut-ends, $\rho(\Theta, \Phi)$, can be defined as

$$\rho(\Theta,\Phi) = \sqrt{\frac{S\Theta,\Phi)}{\pi\nu\Theta,\Phi)}} = r_f\sqrt{\frac{1}{\Upsilon(\Theta,\Phi)}} \qquad [1.35]$$

Since $\Upsilon(\Theta, \Phi) \leq 1$ there is always $\rho(\Theta, \Phi) \geq r_f$.

All these variables (S, ν and ρ) are important indicators of the anisotropic nature of the short-fiber system structure, and can be calculated once the fiber orientation *pdf* is given. Of course, the fiber area fraction can also be calculated using the mean number of the fiber cut-ends and the mean radius from Equations [1.30] and [1.35], i.e.

$$A_f(\Theta, \Phi) = \nu(\Theta,\Phi)\pi\rho^2(\Theta, \Phi) \qquad [1.36]$$

It should be pointed out that all the parameters derived here are the statistical mean values at a given cross-section. These parameters are useful, therefore, in calculating some system properties, such as the system elastic modulus in the direction whose values are based on averaging rules of the elastic moduli of the constituents at this cross-section. As to the study of the local heterogeneity and prediction of other system properties such as the strength and fracture behavior, which are determined by the local extreme values of the properties of the constituents, more detailed information on the local distributions of the properties of the constituents, as deduced below, is indispensable.

1.5 Pore distribution in a fibrous material

In all the previous studies on fibrous system behavior, the system is assumed, explicitly or implicitly, to be quasi-homogeneous such that the relative proportion of the fiber and air (the volume fractions) is constant throughout the system. This is to assume that fibers are uniformly spaced at every location in the system, and the distance between fibers, and hence the space occupied by air between fibers, is treated as identical. Obviously, this is a highly unrealistic situation. In practice, because of the limit of processing techniques, the fibers even at the same orientation are rarely uniformly spaced. Consequently, the local fiber/air concentration will vary from point to point in the system, even though the total fiber and air volume fractions remain constant.

As mentioned above, if we need only to calculate the elastic properties such as the modulus at various directions, a knowledge of $A_f(\Theta, \Phi)$ alone will be adequate, as the system modulus is a statistical average quantity. However, in order to investigate the local heterogeneity and to realistically predict other system properties such as strength, fracture behavior, and impact resistance, we have to look into the local variation of the fiber fraction or the distribution of the air between fibers.

In general, the distribution of air in a fibrous system is not uniform, nor is it continuous, due to the interference of fibers. If we cut a cross-section of the system, the areas occupied by the air may vary from location to location. According to Ogston (1958) and Komori and Makishima (1979), we can use the concept of the 'aperture circle' of various radius r, the maximum circle enclosed by fibers or the area occupied by the air in between fibers, to describe the distribution of the air in a cross-section, as seen in Fig. 1.4.

In order to derive the distribution of the variable r, let us examine Fig. 1.5 where an aperture circle of radius r is placed on the cross-section (Θ, Φ) of unit area along with a fiber cut-end of radius $\rho(\Theta, \Phi)$. According to Komori and Makishima (1979), these two circles will contact each other when the center of the latter is brought into the inside of the circle of radius $r + \rho$, concentric with the former. The probability $f(r)dr$, that the aperture circle

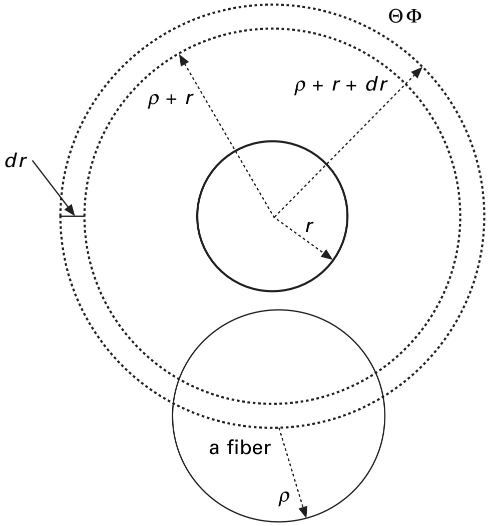

1.5 An aperture circle of radius *r* is placed on the cross-section (Θ, Φ) of unit area along with a fiber cut end of radius *ρ* (Θ, Φ). Adapted from Komori, T. and K. Makishima (1979). 'Geometrical Expressions of Spaces in Anisotropic Fiber Assemblies.' *Textile Res. J.*, 49: 550–555.

and the fiber do not touch each other, but that the slightly larger circle of radius $r + dr$, does touch the fiber, is approximately equal to the probability when $v(\Theta, \Phi)$ points (the fiber cut-ends) are scattered on the plane, no point enters the circle of radius $r + \rho$, and at least one point enters the annular region, two radii of which are $r + \rho$ and $r + \rho + dr$.

When x fiber cut-ends are randomly distributed in a unit area, taking into account the area occupied by the fiber, the probability that at least one point enters the annular region $2\pi(r + \rho)dr$ is

$$\frac{2x\pi(r+\rho)dr}{1-[\pi(r+\rho)^2-\pi\rho^2]} \quad (x = 0, 1, 2, \ldots) \tag{1.37}$$

and the probability of no point existing in the area $\pi(r + \rho)^2 - \pi\rho^2$ is

$$\{1-[\pi(r+\rho)^2-\pi\rho^2]\}^x \tag{1.38}$$

Then the joint probability, $f_x(r)dr$, that no point is contained in the circle of radius $r + \rho$ but at least one point is contained in the circle of radius $r + \rho + dr$, is given by the product of the two expressions as

$$f_x(r)dr = 2x\pi(r+\rho)dr\{1-[\pi(r+\rho)^2-\pi\rho^2]\}^{x-1} \tag{1.39}$$

Because the number of fiber cut-ends is large and they are distributed randomly, their distribution can be approximated by the Poisson's function

$$\frac{\nu^x}{x!}\,e^{-\nu} \qquad [1.40]$$

Therefore, the distribution function of the radii of the aperture circles $f(r)$ is given by

$$\begin{aligned} f(r)\,dr &= \sum_{x=0}^{\infty} \frac{\nu^x}{x!}\,e^{-\nu} f_x(r)\,dr \\ &= 2\pi\nu(r+\rho)e^{-\nu}dr \sum_{x=0}^{\infty} \frac{[\nu+\pi\nu\rho^2-\pi\nu(r+\rho)^2]^{x-1}}{(x-1)!} \\ &= 2\pi\nu(r+\rho)e^{-\nu}e^{\nu+\pi\nu\rho^2-\pi\nu(r+\rho)^2}\,dr \\ &= 2\pi\nu(r+\rho)e^{\pi\nu\rho^2}\,e^{-\pi\nu(r+\rho)^2}\,dr \end{aligned} \qquad [1.41]$$

It can be readily proved that

$$\int_0^{\infty} f(r)\,dr = \int_0^{\infty} 2\pi\nu(r+\rho)e^{\pi\nu\rho^2}\,e^{-\pi\nu(r+\rho)^2}\,dr = e^{\pi\nu\rho^2}\,e^{-\pi\nu\rho^2} = 1$$

So this function is valid as the *pdf* of distribution of the aperture circles filled with air, or it provides the distribution of the air at the given cross-section. The result in Equation [1.41] is different from that of Komori and Makishima (1979), which ignores the area of fiber cut-ends and hence does not satisfy the normalization condition.

The average value of the radius, $\bar{r}(\Theta,\Phi)$, can then be calculated as

$$\begin{aligned} \bar{r}(\Theta,\Phi) &= \int_0^{\infty} rf(r)\,dr = \int_0^{\infty} 2r\pi\nu(r+\rho)e^{\pi\nu\rho^2}\,e^{-\pi\nu(r+\rho)^2}\,dr \\ &= e^{\pi\nu\rho^2}\int_0^{\infty} 2\pi\nu t(t-\rho)e^{-\pi\nu t^2}\,dt \approx e^{\pi\nu\rho^2} \\ &= \int_0^{\infty} 2\pi\nu t^2 e^{-\pi\nu t^2}\,dt = \frac{e^{\pi\nu\rho^2}}{2\sqrt{\nu}} \end{aligned} \qquad [1.42]$$

where $t = (r + \rho)$ has been used in the integration. Similarly, the variance $\Xi_r(\Theta, \Phi)$ of the radius can be calculated as

$$\begin{aligned} \Xi_r(\Theta,\Phi) &= \int_0^{\infty} r^2 f(r)\,dr \\ &= \int_0^{\infty} 2r^2\pi\nu\,(r+\rho)e^{\pi\nu\rho^2}\,e^{-\pi\nu(r+\rho)^2}\,dr = \frac{e^{\pi\nu\rho^2}}{\pi\nu} = \frac{2}{\pi\sqrt{\nu}}\bar{r}(\Theta,\Phi) \end{aligned} \qquad [1.43]$$

Note that for a given structure, the solution of the equation

$$\frac{d\,\Xi_r(\Theta, \Phi)}{d\,(\Theta, \Phi)} = 0 \qquad [1.44]$$

gives us the cross-sections in which the pore distribution variation reaches the extreme values, or the cross-sections with the extreme distribution non-uniformity of the air material.

1.6 Tortuosity distributions in a fibrous material

The variable r specifies only the areas of the spaces occupied by the air material. The actual volumes of the spaces are also related to the depth or length of the pores. The tortuosity is thus defined as the ratio of the length of a true flow path for a fluid and the straight-line distance between inflow and outflow in Fig. 1.6. This is, in effect, a kinematical quantity as the flow itself may alter the path.

In a fibrous system, the space occupied by air material is often interrupted because of the existence or interference of fibers. If we examine a line of unit length in the direction (Θ, Φ), the average number of fiber intersections on this line is provided by Komori and Makishima (1979) and Pan (1994) as

$$n(\Theta, \Phi) = 2 r_f N l_f J(\Theta, \Phi) = 2\frac{V_f}{\pi r_j} J(\Theta, \Phi) \qquad [1.45]$$

where $J(\Theta, \Phi)$ is the mean value of $|\sin\chi|$,

$$J(\Theta, \Phi) = \int_0^{\pi} d\theta \int_0^{\pi} d\phi \, |\sin\chi| \, \Omega(\theta, \phi) \sin\theta \qquad [1.46]$$

a parameter reflecting the fiber misorientation.

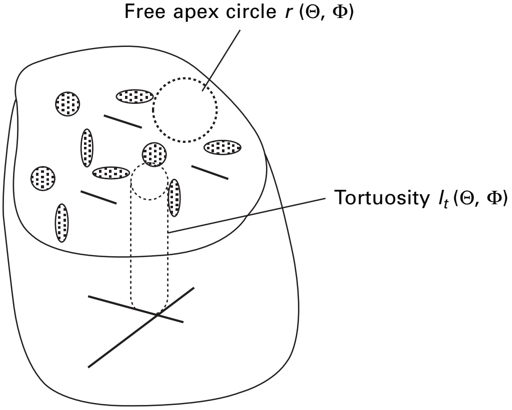

1.6 Tortuosity in a fibrous material.

Following Komori and Makishima (1979) at a given direction, we define the free distance as the distance along which the air travels without interruption by the constituent fibers, or the distance occupied by the air between two interruptions by the fibers. Here we assume the interruptions occur independently.

Suppose that $n(\Theta, \Phi)$ segments of the free distance are randomly scattered along this line of unit length. The average length of the free distance, l_m, is given as

$$l_m(\Theta, \Phi) = \frac{1 - \pi r_f^2 N l_f}{n(\Theta, \Phi)} = \frac{1 - V_f}{n(\Theta, \Phi)} \qquad [1.47]$$

According to Kendall and Moran's analysis (1963) on non-overlapping intervals on a line, the distribution of the free distance l is given as

$$f(l)\,dl = \frac{1}{l_m} e^{-\frac{l}{l_m}}\,dl \qquad [1.48]$$

It is easy, as well, to prove that

$$\int_0^\infty f(l)\,dl = \int_0^\infty \frac{1}{l_m} e^{-\frac{1}{l_m}}\,dl = 1 \qquad [1.49]$$

This is also a better result than the one given by Komori and Makishima (1979), for their result again does not satisfy the normalization condition. We already have l_m in Equation [1.47] as the mean of l, and the variance of l is given by

$$\Xi_l(\Theta, \Phi) = \int_0^\infty l^2 f(l)\,dl = \int_0^\infty l^2 \frac{1}{l_m} e^{-\frac{1}{l_m}}\,dl = 2l_m^2 \qquad [1.50]$$

These statistical variables can be used to specify the local variations of the fiber and air distributions or the local heterogeneity of a system. Also, because of the association of the local concentration of the constituents and system properties, these variables can be utilized to identify the irregular or abnormal features caused by the local heterogeneity in a system.

However, when dealing with a system with local heterogeneity, the system properties are location dependent. Consequently, using the system or overall volume fractions will not be valid, and the concept of local fiber volume fraction is more relevant. Locations where the radius of the aperture circles and the free distance possess the highest or lowest values will likely be the most irregular spots in the system.

1.7 Structural analysis of fibrous materials with special fiber orientations

Since we have all the results of the parameters defining the distributions of constituents in a fibrous system, it becomes possible to predict the irregularities of the system properties. To demonstrate the application of the theoretical results obtained, we will employ the two simple and hypothetical cases below.

1.7.1 A random distribution case

For simplicity, let us first consider an ideal case where all fibers in a system are oriented in a totally random manner with no preferential direction; the randomness of fiber orientation implies that the density function is independent of both coordinates θ and ϕ. Therefore, this density function would have the form of

$$\Omega(\theta, \phi) = \Omega_0 \qquad [1.51]$$

where Ω_0 is a constant whose value is determined from the normalization condition as

$$\Omega_0 = \frac{1}{2\pi} \qquad [1.52]$$

Using this fiber orientation *pdf*, we can calculate the system parameters by replacing (Θ, Φ) with $(0, 0)$. The results are provided below to reveal the internal structure of the material:

- $\cos\chi = \cos(\Theta, \theta, \Phi, \phi) = \cos(0, \theta, 0, \phi) = \cos\theta$;
- $\sin\chi = \sin\theta$;
- $\Upsilon(\Theta, \Phi) = \frac{1}{2}$;
- $J(\Theta, \Phi) = \frac{\pi}{4}$;
- $A(\Theta, \Phi) = \frac{1}{2\pi} V_f$
- $v(\Theta, \Phi) = \frac{V_f}{4\pi\pi r_f^2}$;
- $\rho(\Theta, \Phi) = \sqrt{2} r_f$
- $n(\Theta, \Phi) = \frac{V_f}{2r_f}$;
- $\bar{r}(\Theta, \Phi) = \frac{\pi r_f}{\sqrt{V_f}} e^{\frac{V_f}{2\pi}}$;

- $\Xi_r\,(\Theta, \Phi) = \dfrac{4\pi r_f^2}{V_f} e^{\frac{V_f}{2\pi^2}}$;
- $l_m\,(\Theta, \Phi) = 2r_f\left(\dfrac{1}{V_f} - 1\right)$
- $\Xi_r\,(\Theta, \Phi) = 8r_j^2\left(\dfrac{1}{V_f} - 1\right)^2$;

The following discussion of several other system parameters provides detailed information on the distributions of both the fibers and air in this isotropic fibrous system. As seen from the above calculated results, for this given fiber orientation *pdf*, all of the distribution parameters are dependent on the system fiber volume fraction V_f and fiber radius r_f, regardless of the fiber length l_f. Therefore, we will examine the relationships between the distribution parameters and these two factors.

Figure 1.7 depicts the effects of these two factors on the number of fiber cut-ends v per unit area on an arbitrary cross-section using the calculated results. As expected, for a given system fiber volume fraction V_f, the thinner the fiber, the more fiber cut-ends per unit area, whereas for a given fiber

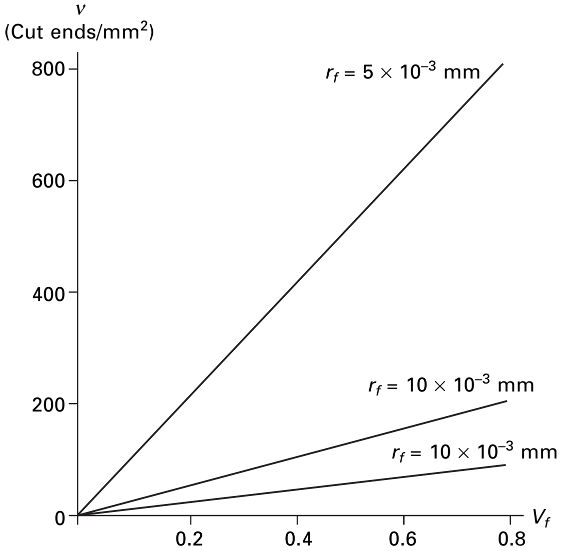

1.7 Effects of fiber volume fraction V_f and fiber radius r_f on the number of fiber cut ends v per unit area. Adapted from Pan, N. (1994). 'Analytical Characterization of the Anisotropy and Local Heterogeneity of Short-fiber Composites – Fiber Fraction as a Variable.' *Journal of Composite Materials* 28(16): 1500–1531.

radius r_f, increasing the system fiber volume fraction will lead to more fiber cut-ends.

The distribution density function $f(r)$ of the radius r of the aperture circles is constructed based on Equation [1.41], and the illustrated results are produced accordingly. Figure 1.8(a) shows the distribution of $f(r)$ at three fiber radius

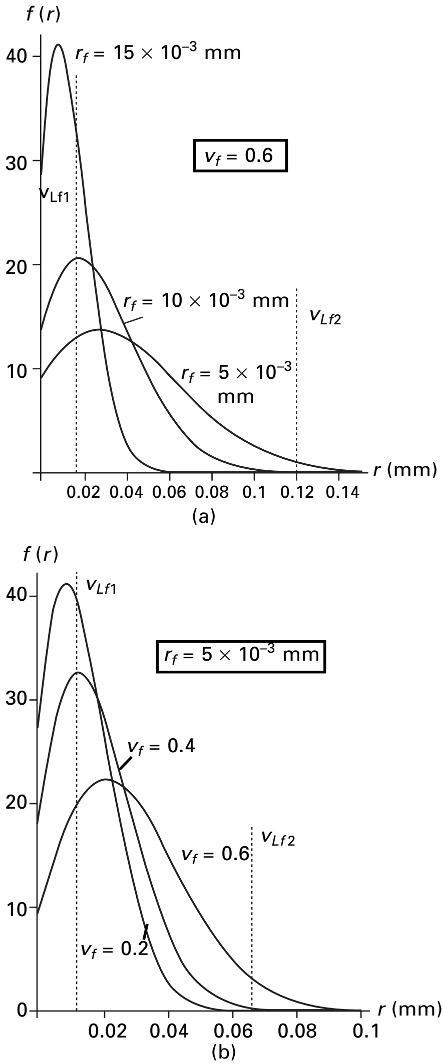

1.8 Distribution of the aperture circles radius r in random case. Adapted from Pan, N. (1994). 'Analytical Characterization of the Anisotropy and Local Heterogeneity of Short-fiber Composites – Fiber Fraction as a Variable.' *Journal of Composite Materials* 28(16): 1500–1531. (a) at three fiber radius r_f levels while $V_f = 0.6$. (b) at three V_f levels while $r_f = 5.0 \times 10^{-3}$ mm (c) variance Ξ_r of r against V_f (d) the mean radius $\bar{r}$ against V_f.

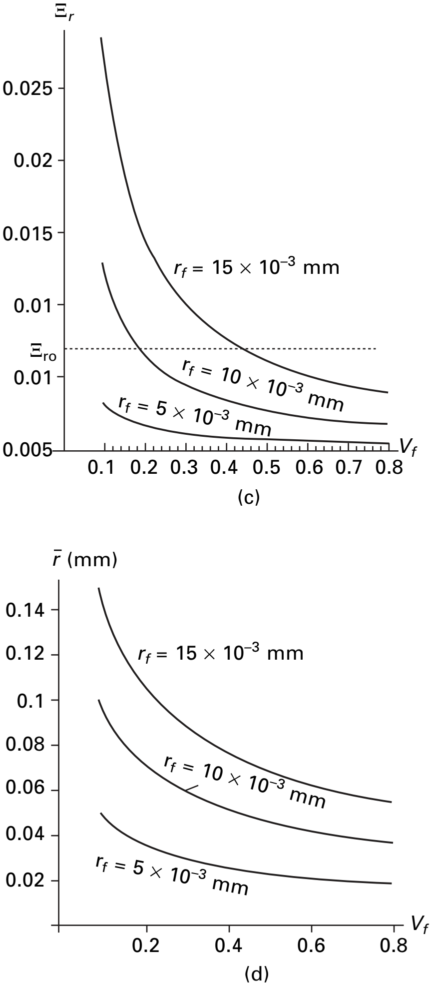

(c)

(d)

1.8 Continued

r_f levels when the overall fiber volume fraction $V_f = 0.6$, whereas Fig. 1.8(b) is the result at three V_f levels when the fiber radius is fixed at $r_f = 5.0 \times 10^{-3}$ mm.

It is seen in Fig. 1.8(a) when the fiber becomes thicker, there are more aperture circles with smaller radius values. The pore sizes become less spread out. Decreasing the overall fiber volume fraction V_f has a similar effect, as seen in Fig. 1.8(b).

To verify the conclusions, the variance Ξ_r of the aperture circle radius distribution is calculated using Equation 1.43 as shown in Fig. 1.8(c). Again, a finer fiber or a greater V_f will lower the variation of the aperture circle radius r. Moreover, since the extreme fiber volume fractions are related to high variation of r values, we can define the allowable local fiber volume fraction v_{Lf1} and $v_{L/2}$ to bound the allowable variance level Ξ_{ro} represented by the dotted line in the figure, and the condition $\Xi_r \leq \Xi_{ro}$ will in turn determine the corresponding allowable fiber size r_f and the system fiber volume fraction V_f to avoid a massive number of large aperture circles.

Finally, Fig. 1.8(d) is plotted based on Equation [1.42], showing the average radius $\bar{r}$ of the aperture circles as a function of the system fiber volume fraction at three fiber size levels. The average radius of the aperture circles will decrease when either the fiber radius reduces (meaning more fibers for the given fiber volume fraction V_f), or the system fiber volume fraction increases.

The distribution function $f(l)$ of the free distance l is formed from Equation 1.48, and the results are illustrated in Fig. 1.9(a) and (b). When increasing either the fiber size r_f or the system fiber volume fraction V_f, the number of free distances with shorter length will increase and those with longer length

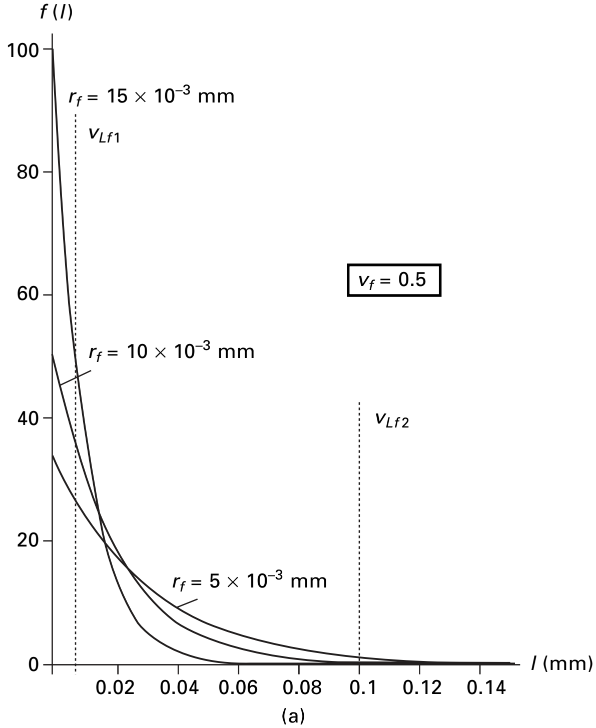

1.9 Distribution of the tortuosity length *l* in a random case. Adapted from Pan, N. (1994). 'Analytical Characterization of the Anisotropy and Local Heterogeneity of Short-fiber Composites – Fiber Fraction as a Variable.' *Journal of Composite Materials* 28(16): 1500–1531. (a) at three fiber radius r_f levels; (b) at three V_f levels; (c) variance Ξ_r of the tortuosity length *l*; (d) the mean value *lm* against V_f.

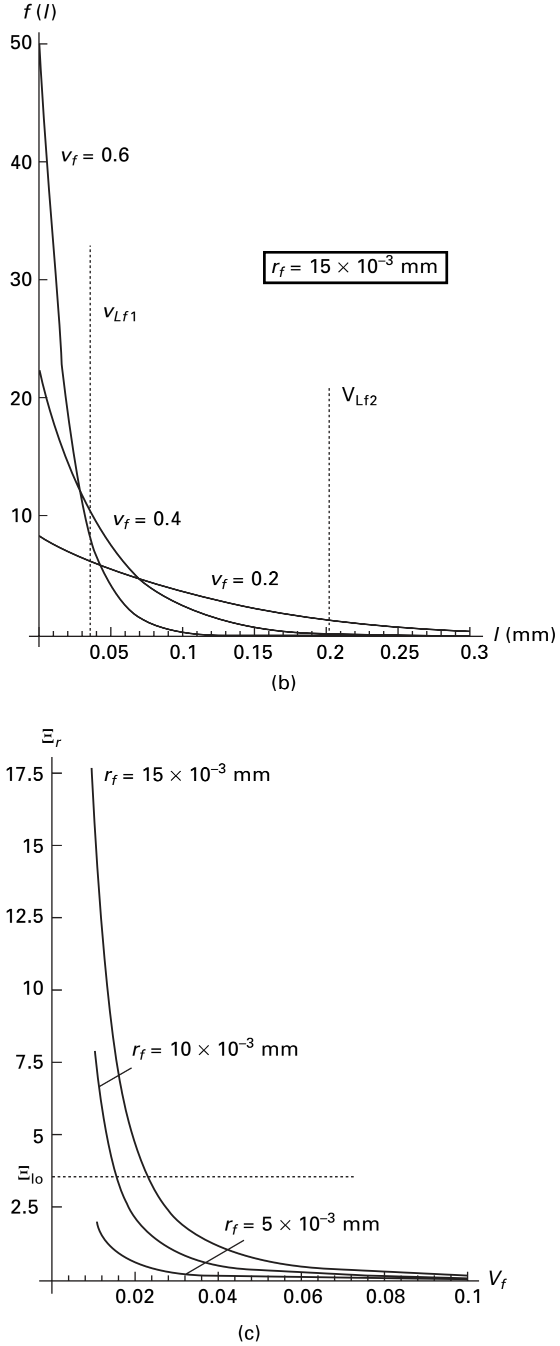

(b)

(c)

1.9 Continued

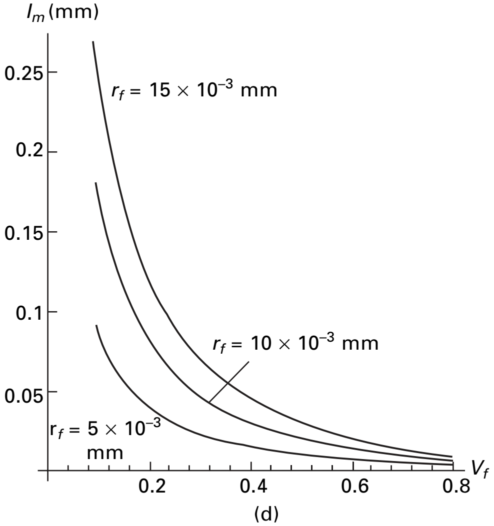

1.9 Continued

will decrease. Again, the allowable range of the free distances is defined by the two local fiber volume fractions v_{Lf1} and v_{Lf2}.

The variance Ξ_i of the free distance distribution as well as the critical value Ξ_{lo} is provided in Fig. 1.9(c), and the effects of r_f and V_f on Ξ_l are similar but less significant compared to the case in Fig. 1.8(c). Furthermore, it is interesting to see that, although the system dealt with here is an isotropic one in which all fibers are oriented in a totally random manner with no preferential direction, there still exist variations or irregularities in both r and l, leading to a variable local fiber volume fraction v_{Lf} value from location to location. In other words, the system is still a quasi-heterogeneous one.

Figure 1.9(d) shows the effects of the two factors on the average free distance l_m of the air material using Equation 1.49. It follows the same trend as the average radius of the aperture circles, i.e. for a given fiber volume fraction V_f, thinner fibers (more fibers contained) will lead to a shorter l_m value. A reduction of l_m value can also be achieved when we increase the system fiber volume fraction, while keeping the same fiber radius.

1.7.2 A planar and harmonic distribution

The planar 2-D random fiber orientation is of practical significance since planar cases are independent of the polar angle. We can hence set in the following analysis $\theta = \Theta = \frac{\pi}{2}$. To illustrate the effect of the structural anisotropy, let us assume a harmonic *pdf* as the function of the base angle ϕ, i.e.

$$\Omega(\phi) = \Omega_0 \sin \phi \qquad [1.53]$$

where Ω_0 again is a constant whose value is determined using the normalization condition as

$$\Omega_0 = \frac{1}{2} \qquad [1.54]$$

Using this fiber orientation *pdf*, we can calculate the system parameters to illustrate the internal structure of the material. Because of the randomness of fiber orientation, all the related parameters are calculated below:

- $\cos \chi = \cos(\phi - \Phi)$;
- $\sin \chi = \sqrt{1 - \cos^2(\Theta, \phi)} = \sin(\phi - \Theta)$;
- $\Upsilon(\Phi) = \frac{1}{2} \cos \Phi + \frac{\pi}{4} \sin \Phi$;
- $J(\Phi) = \left| \frac{\pi}{4} \cos \Phi - \frac{1}{2} \sin \Phi \right|$;
- $A(\Phi) = \frac{1}{2} V_f \sin \Phi$;
- $v(\Phi) = \dfrac{V_f}{4\pi r_j^2} \sin \Phi \left(\cos \Phi + \frac{\pi}{2} \sin \Phi \right)$
- $\rho(\Phi) = r_f \sqrt{\dfrac{1}{\frac{1}{2} \cos \Phi + \frac{\pi}{4} \sin \Phi}}$;
- $n(\Phi) = \dfrac{2V_f}{\pi r_f} J(\Phi)$;
- $\bar{r}(\Phi) = \dfrac{1}{2\sqrt{v(\Phi)}} e^{\frac{V_f}{2\pi} \sin \Phi}$;
- $\Xi_r(\Phi) = \dfrac{1}{\pi v(\Phi)} e^{\frac{V_f}{2\pi} \sin \Phi}$;
- $l_m(\Phi) = \dfrac{(1 - V_f)\pi r_f}{2V_f J(\Phi)}$;
- $\Xi_l(\Phi) = \dfrac{(1 - V_f)^2 \pi^2 r_f^2}{2V_f^2 J(\Phi)^2}$;

The system parameters as the functions of direction Φ are illustrated in Fig. 1.10(a) through Fig. 1.13. The fiber orientation *pdf* in Equation [1.53] indicates a non-uniform fiber concentration at different directions, with lowest value at Φ = 0° and the highest at Φ = 90°. This is clearly reflected in the characteristics of the aperture circle radius r shown in Fig. 1.7.

Figure 1.10(a) illustrates the distribution of r at three selected directions, and Fig. 1.10(b) provides the corresponding variance of r. In Fig. 1.10(a), r value ranges with the widest span from 0 to infinity at direction Φ = 0°, but covers narrowest range at direction Φ = 90°. Consequently, the mean radius $\bar{r}$ of the aperture circles shown in Fig. 1.10(c) reaches its maximum value (approaching infinity) at direction Φ = 0° and descends to the minimum at Φ = 90°, whereas the variance in Fig. 1.10(b) is the highest at Φ = 0° and lowest at direction Φ = 90° correspondingly. (For easy comparison, the variance value at Φ = 18° direction is used in Fig. 1.10(b) to replace the infinity value at Φ = 0°.

Moreover, the average number of fiber cut-ends $v(\Phi)$ in Fig. 1.11 possesses the minimum values at Φ = 0° but the maximum values at around 70° to 80°, and becomes slightly lower at the direction Φ = 90° due to the more severe fiber-obliquity effect at high Φ levels.

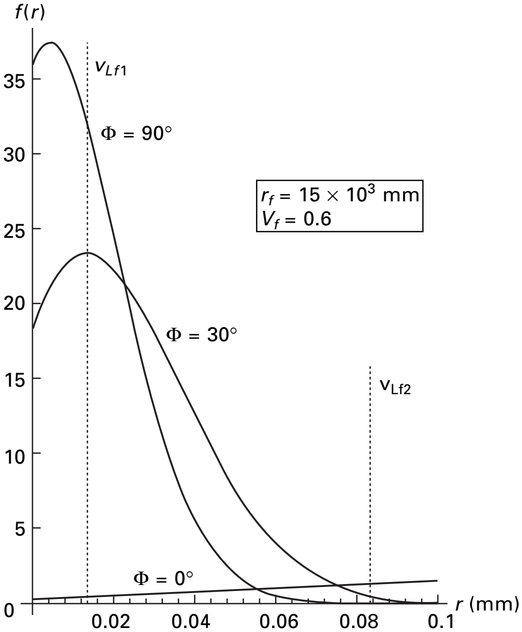

(a)

1.10 Distribution of the aperture circles radius r in an anisotropic case. Adapted from Pan, N. (1994). 'Analytical Characterization of the Anisotropy and Local Heterogeneity of Short-fiber Composites – Fiber Fraction as a Variable.' *Journal of Composite Materials* 28(16): 1500–1531. (a) r at three cross-sections; (b) variance Ξ_r of r at three cross-sections; (c) the mean value $\bar{r}$ versus the direction Φ.

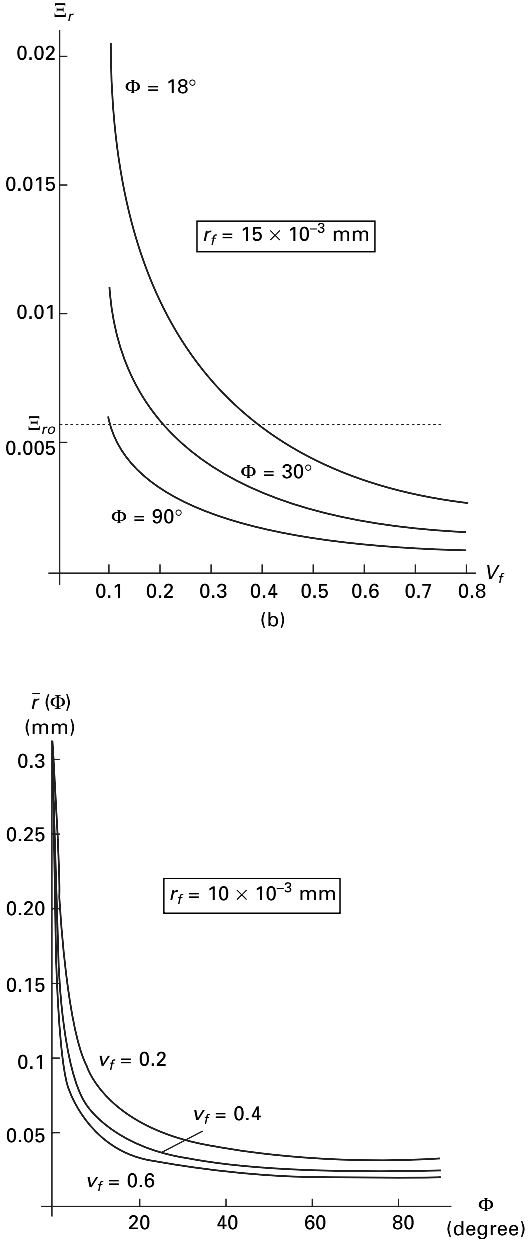

(b)

(c)

1.10 Continued

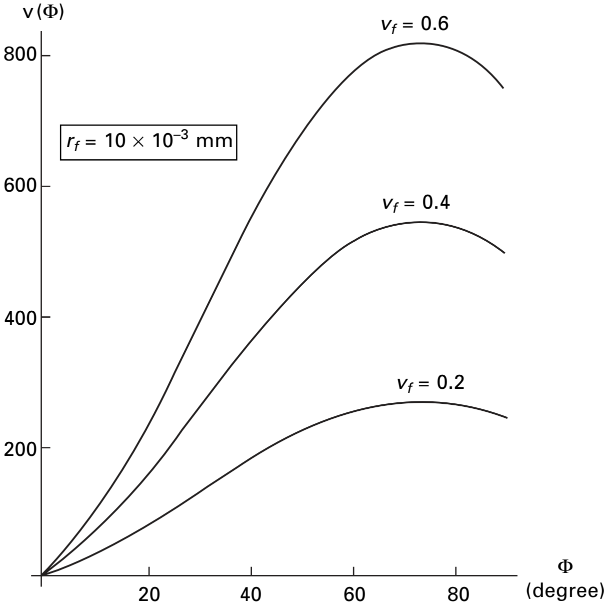

1.11 Mean fiber cut ends *v*(Φ) versus the direction Φ. Adapted from Pan, N. (1994). 'Analytical Characterization of the Anisotropy and Local Heterogeneity of Short-fiber Composites – Fiber Fraction as a Variable.' *Journal of Composite Materials* 28(16): 1500–1531.

The effect of the system fiber volume fraction V_f on r distribution is depicted in Figs 1.10(b) and (c). It is easy to understand that increasing V_f value will reduce the number of the aperture circles with larger r values, causing lower variance of the r values in Fig. 1.10(b), and resulting in a smaller value of the mean radius $\bar{r}$ of the aperture circles in Fig. 1.10(c).

Furthermore, as specified above, either extreme of the r value will lead to violation of the boundaries defined by the allowable local fiber volume fractions v_{Lf1} and v_{Lf2}. It can hence be concluded from Fig. 1.10(a) that direction $\Phi = 0°$ with most extreme r values is the weakest direction in the system, while direction $\Phi = 90°$ with least extreme r values is the strongest direction; a reflection of the anisotropic nature of this system. Additionally, the v_{Lf1} and v_{Lf2} restraints can be translated into the allowable variance value Ξ_{ro} in Fig. 1.10(b) which in turn determines the minimum allowable system fiber volume fraction V_f so as to eliminate the excessive number of large r aperture circles.

There is one more direction, $\Phi = 30°$, provided in Figs 1.10(a) and (b) for comparison. It is deduced from the results that when Φ value decrease from $\Phi = 90°$ to $\Phi = 30°$, the r distribution will shift towards the region of greater values, leading to more larger aperture circles and fewer smaller ones. Overall, reduction of Φ value in the present case results in greater variance or more diverse r distribution as seen in Fig. 1.10(b). On the other hand, there are two other parameters related to the fiber cut-ends and the air free length in the list of calculated results:

$$\Upsilon(\Phi) = \frac{1}{2}\cos\Phi + \frac{\pi}{4}\sin\Phi \quad \text{and} \quad J(\Phi) = \left|\frac{\pi}{4}\cos\Phi - \frac{1}{2}\sin\Phi\right|$$

Both expressions reach their extremes at the direction $\Phi = 57.518°$. Correspondingly, our predictions indicate that the average radius of the fiber cut-ends, $\rho(\Phi)$, becomes the minimum in Fig. 1.12, while the average free length $l_m(\Phi)$ of the air material in Fig. 1.10(c) approaches its maximum at this direction, because of the fact of too few fibers oriented in this direction.

Further evidence is provided in Figs 1.13(a) and (b). Figure 1.13(a) shows the distribution of the free distance l at three directions at given fiber size r_f and total fiber quantity V_f. It is seen that l value is distributed over the full spectrum from 0 to the infinity at the cross-section $\Phi = 57.518°$, again because of the extremely small number of fibers associated with this direction, leading to an excessively great range of l, and high variance value at this direction as seen in Fig. 1.13(b). (For the same reason as above, the variance at $\Phi = 72°$ instead of the infinity value at $\Phi = 57.518°$ is shown here.)

Likewise, the allowable range of the l value is indicated by the v_{Lf1} and v_{Lf2} boundary in Fig. 1.13(a), and the minimum system fiber volume fraction V_f is given in Fig. 1.13(b) according to the condition $\Xi_l \leq \Xi_{lo}$. It can be

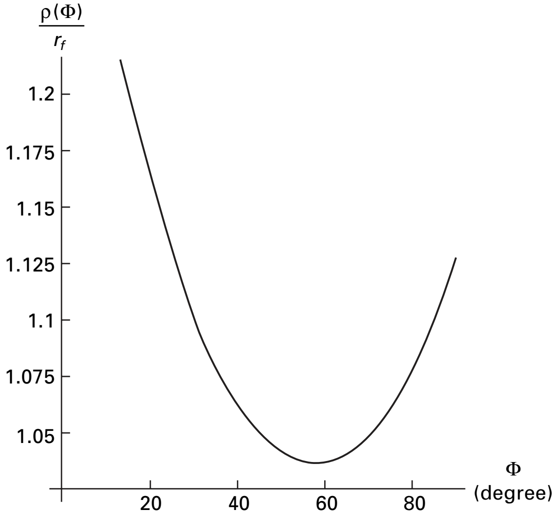

1.12 Relative cut fiber ends $\rho(\Phi)$ versus the direction Φ. Adapted from Pan, N. (1994). 'Analytical Characterization of the Anisotropy and Local Heterogeneity of Short-fiber Composites – Fiber Fraction as a Variable.' *Journal of Composite Materials*, 28(16): 1500–1531.

speculated, based overall on Fig. 1.13, that when $\Phi < 57.518°$, contrary to the case of r distribution in Fig 1.10, increasing Φ value will shift the l distribution in the direction of greater value, and at the same time result in greater variance. The trend will reverse once $\Phi > 57.518°$.

In addition, it can be concluded from Figures 1.10 to 1.13 that even at a given cross-section Φ in the system, the parameters such as r and l are still variables at different locations on the cross-section. In other words, this system is both anisotropic and quasi-heterogeneous. It may suggest, based on the above two general distribution cases, the spatial random and planar harmonic, that quasi-heterogeneity is an inherent feature of fiber systems, and it exists in all fiber systems regardless of the fiber distributions. Even for a unidirectional fiber orientation, although it is possible to achieve a quasi-homogenity at individual cross-sections, irregularities of local fiber volume fraction between cross-sections still exist.

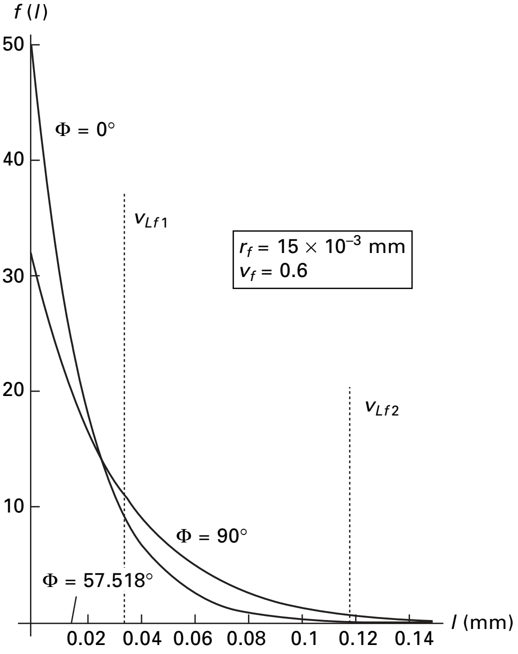

(a)

1.13 Distribution of the tortuosity length l in an anisotropic case. Adopted from Pan, N. (1994). 'Analytical Characterization of the Anisotropy and Local Heterogeneity of Short-fiber Composites - Fiber Fraction as a Variable.' *Journal of Composite Materials* 28(16): 1500–1531. (a) l at three cross-sections; (b) the variance of l at three cross-sections; (c) the mean value lm versus the direction Φ.

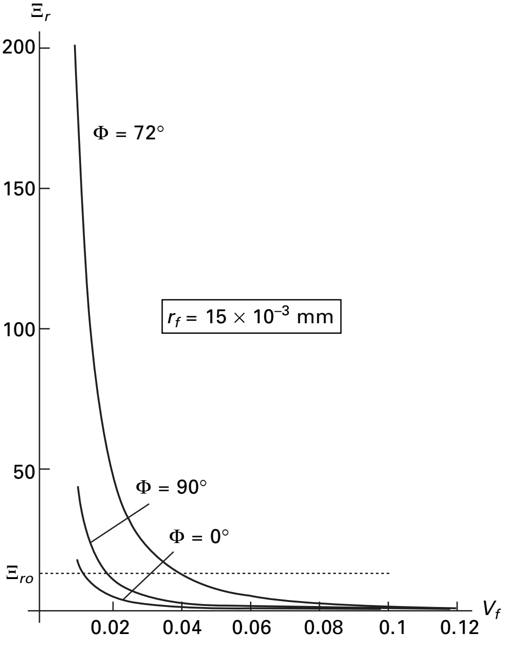

(b)

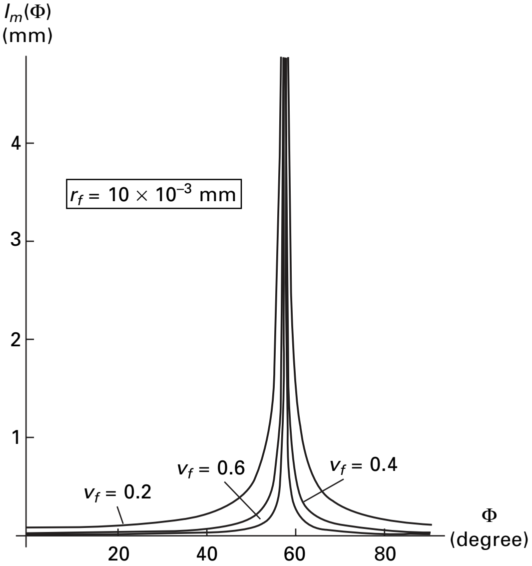

(c)

1.13 Continued

1.8 Determination of the fiber orientation

It has to be admitted that, although the statistical treatment using the fiber orientation *pdf* is a powerful tool in dealing with the structural variations, the major difficulty comes from the determination of the probability density function for a specific case. Cox (1952) proposed for a fiber network that such a density function can be assumed to be in the form of Fourier series. The constants in the series are dependent on specific structures. For simple and symmetrical orientations, the coefficients are either eliminated or determined without much difficulty. However, it becomes more problematic for complex cases where asymmetrical terms exist. Pourdeyhimi *et al.* have published a series of papers on determination of fiber orientation *pdf* for nonwovens (Pourdeyhimi and Ramanathan, 1995; Pourdeyhimi, Ramanathan *et al.*, 1996; Pourdeyhimi and Kim, 2002). Because of the central limit theorem, the present author has proposed (Pan, 1993a) to apply the Gaussian function, or its equivalence in periodic case, the von Mises function (Mardia, 1972) to approximate the distribution in question, provided that the coefficients in the functions can be determined through, most probably, experimental approaches. Sayers (1992) suggested that the coefficients of the fiber orientation function of any form be determined by expanding the orientation function into the generalized Legendre functions. Recent work by Tournier, Calamante *et al.* (2004) proposed a method to directly determine the fiber orientation density function from diffusion-weighted MRI data using a spherical deconvolution technique.

1.8.1 BET–Kelvin method for pore distribution

Litvinova (1982) proposed a method of determining some of these parameters on the basis of the BET equation for a given sorption isotherm. In the beginning, the sorption isotherm curve is almost linear (usually for $0.01 < M < 0.35$). When the capillary walls are covered by a monomolecular layer of liquid, the BET equation can be written as follows:

$$\frac{a_w}{M(1 - a_w)} = \frac{1}{cV_A} - \frac{c - 1}{cV_A} \qquad [1.55]$$

where M is the moisture content at sorbed air humidity a_w, V_A is the volume of monomolecular layer and c is the constant resulting from thermal effect of sorption. By plotting M vs. a_w using given data, the above equation gives a straight line on the graph with slope $(c - 1)/cV_A$ and intercept $1/cV_A$. It thus allows calculation of the 'volume' of a monomolecular layer of water and then the specific surface of porous body a (m^2/g)

$$a = sV_AN \qquad [1.56]$$

where s is the surface occupied by molecules and N is the Avogadro's number.

Strumillo and Kudra proposed another method by which we can calculate the corresponding pore radius r and pore volume V (Strumillo and Kudra 1986). From the Kelvin–Thomson equation,

$$r = \frac{2\sigma V_m \cos\gamma}{RT \ln(1/RH)} \qquad [1.57]$$

where V_m is the molar volume. For a given relative humidity RH and the corresponding value of the moisture content M on the desorption isotherm, the radius of the pore can be calculated from above equation. Hence the volume of pores of radius r filled with water can be expressed as (m^3/kg of dry material)

$$V = M\frac{1}{\rho} \qquad [1.58]$$

Repeating these calculations for a range of RH, the function $V = f(r)$ can be obtained. By means of graphical differentiation, the pore size distribution can be easily acquired.

For example, the sorption isotherm of a fiber mass is given in Fig. 1.14(a), and the data is also listed in Table 1.1. We can then determine the integral and differential curves of the pore size distribution for the fiber mass, given the parameters in Equation [1.57] as $\sigma = 71.97 \times 10^{-3}$ N/M, $V_m = 0.018$ m^3/mole $P = 0.101$ MPa, $T = 293$ K, $\cos\gamma = 0.928$, $R = 8314$ J/mol. K), $\rho = 998.2$ $\mathrm{kg/m^3}$.

For each RH value we can find the corresponding moisture content M from Fig. 1.14(a) Table 1.1. Then by using Equations [1.57] and [1.58], we can calculate the pore radius r and the corresponding pore volume V as in Table 1.1.

Table1.1 Results of calculations

RH	$r * 10^{-10}$ m	*M*	$V * 10^5$ m^3
0.04	3.07	0.0390	3.91
0.06	3.51	0.0445	4.46
0.08	3.91	0.0505	5.06
0.10	4.29	0.0565	5.66
0.20	6.13	0.0750	7.51
0.30	8.20	0.0925	9.27
0.40	10.77	0.108	10.82
0.50	14.24	0.122	12.22
0.60	19.32	0.135	13.52
0.70	27.67	0.149	14.93
0.80	44.23	0.165	16.52
0.90	93.68	0.185	18.53

Adapted from Strumillo, C. and T. Kudra (1986)

By plotting the data, we obtain the pore volume distribution $V = f(r)$ curve shown in Fig. 1.14(b) and differentiating the figure yields the differential pore volume distribution curve in Fig. 1.14(c).

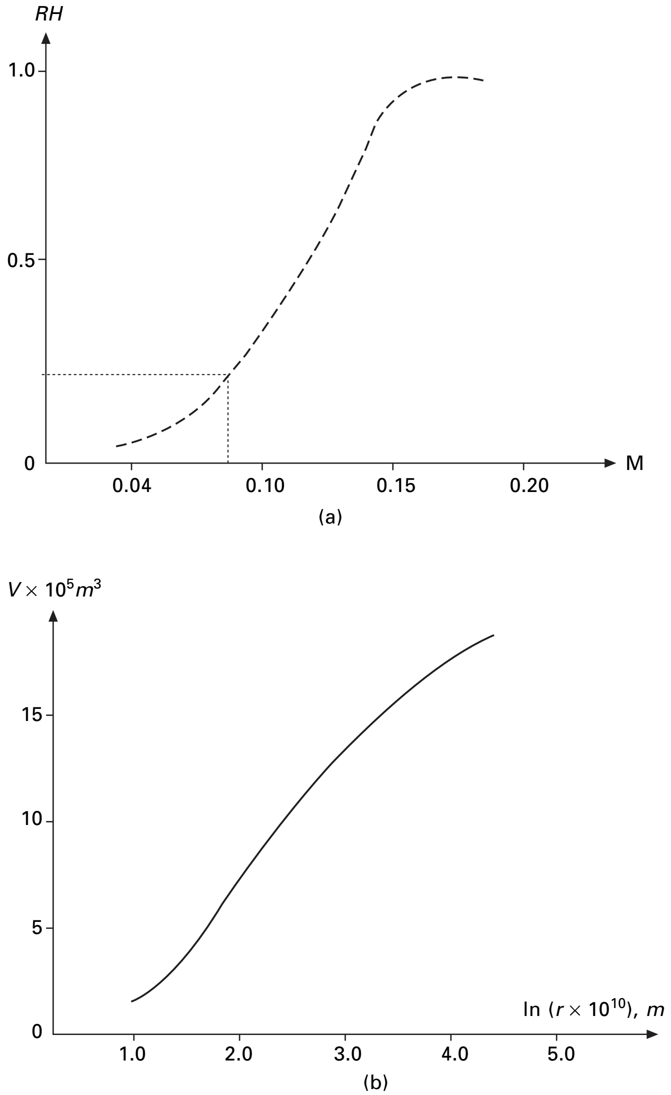

1.14 BET–Kelvin method for pore distribution. Adapted from Strumillo, C. and T. Kudra (1986). *Drying: Principles, Applications and Design*. New York, Gordon and Breach Publishers. (a) the sorption isotherm curve *RH*/*M* of a fiber mass; (b) the pore volume *V*/pore radius *r*; (c) the differential pore volume distribution curve $\frac{dV}{dr}/r$.

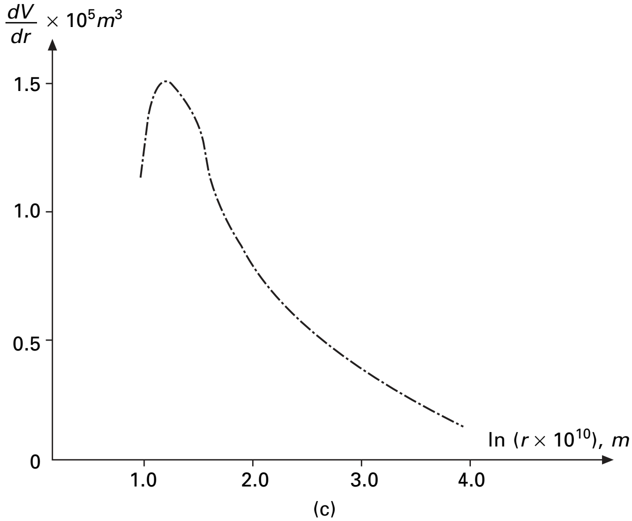

1.14 Continued

1.8.2 The Fourier transformation method for fiber orientation

The fiber orientation function (ODF) can also be determined using the Fourier transformation method. An image of a fibrous structure shows the special arrangement of fibers in the form of brightness transitions from light to dark and vice versa. Thus, if the fibers are predominantly oriented in a given direction, the change in frequencies in that direction will be low, whereas the change in frequencies in the perpendicular direction will be high. We use this characteristic of the Fourier transformation to obtain information on the fiber orientation distribution in the fibrous structure. Fourier transformation decomposes an image of the spatial distribution of fibers into the frequency domain with appropriate magnitude and phase values. The frequency form of the image is also depicted using another image in which the gray scale intensities represent the magnitude of the various frequency components.

In two dimensions, the direct Fourier transformation is given as

$$F(u, v) = \int_{-\infty}^{+\infty} \int_{-\infty}^{+\infty} f(x, y) \exp[-j2\pi(ux + vy)]dxdy \qquad [1.59]$$

where $f(x, y)$ is the image and $F(u, v)$ is its transformation, u refers to the frequency along x-direction and v represents the frequency along the y-axis.

Since the Fourier transformation has its reference in the center, orientations may be directly computed from the transformed image by scanning the image radially. An average value of the transform intensity is found for each of the angular cells. Subsequently, the fiber orientation distribution function (ODF) is determined by normalizing the average values with the total transform intensity at a given annulus. A full description of this Fourier transformation method can be found in Kim (2004).

1.9 The packing problem

Research on the internal structure and geometry of fibrous materials is still very primitive. In order to understand the behavior of fibrous structures, we have to better examine the micro-structure or the discrete nature of the structure. Yet a thorough study of a structure formed by individual fibers is an extremely challenging problem. It is worth mentioning that the problem of the micro-geometry in a fiber assembly can be categorized into a branch of complex problems in mathematics called 'packing problems'.

Taking, for example, the sphere packing problem, also known as the Kepler problem, based on the conjecture put forth in 1611 by the astronomer Johannes Kepler (Peterson, 1998; Chang, 2004), who speculated that the densest way to pack spheres is to place them in a pyramid arrangement known as *face centred cubic* packing (Fig. 1.15). This statement has become known as 'Kepler's conjecture' or simply the sphere packing problem. To mathematically solve the sphere packing problem has been an active area of research for mathematicians ever since, and its solution remains disputable (Stewart, 1992; Li and Ng, 2003; Weitz, 2004). Yet, it seems that sphere packing would be the simplest packing case, for one only needs to consider one characteristic size, i.e. the diameter of perfect spheres, and ignore the deformation due to packing. Therefore it does not seem to be the case that

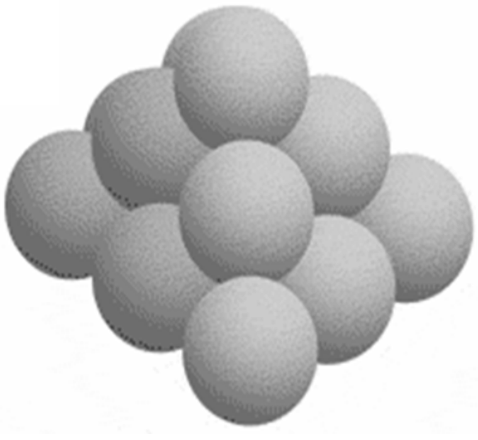

1.15 The Kepler conjecture – The sphere packing problem. Adapted from Kenneth Chang, 'In Math, Computers Don't Lie. Or Do They?', *The New York Times*, April 6, 2004.

the fiber packing problem, which obviously is much more of a complex topic, can be solved completely anytime soon.

1.10 References

Beil, N. B. and W. W. Roberts (2002). 'Modeling and Computer Simulation of the Compressional Behavior of Fiber Assemblies - I: Comparison to Van Wyk's Theory.' *Textile Research Journal* **72**(4): 341–351.

Carnaby, G. A. and N. Pan (1989). 'Theory of the Compression Hysteresis of Fibrous Assemblies.' *Textile Research Journal* **59**(5): 275–284.

Castagnede, B., M. K. Ramasubramanian, *et al.* (1988). 'Measurement of Lateral Contraction Ratios for a Machine-made Paper and Their Computation Using a Numerical Simulation.' *Comptes Rendus De L'Academie Des Sciences Serie Ii* **306**(2): 105–108.

Chang, K. (2004). 'In Math, Computers don't Lie. Or do They?' *The New York Times*. New York: April 6.

Chen, C. C. and K. E. Duckett (1979). 'The direction Distribution on Cross-contacts Points in Anisotropic Fiber Assemblies.' *Textile Res. J.*, **49**: 379.

Corte, H. and O. Kallmes (1962). *Statistical Geometry of a Fibrous Network,Formation and Structure of Paper*. London, Tech. Sect. Brit. Papers and Board Makers Assn.

Cox. H.L. (1952). 'The Elasticity and Strength of Paper and Other Fibrous Materials.' *Br. J. Appl. Phys.*, **3**: 72.

Deng, M. and C. T. J. Dodson (1994a). *Paper: An Engineered Stochastic Structure*. Atlanta, TAPPI Press.

Deng, M. and C. T. J. Dodson (1994b). 'Random Star Patterns and Paper Formation.' *Tappi Journal* **77**(3): 195–199.

Dodson, C. T. J. (1992). 'The Effect of Fiber Length Distribution on Formation.' *Journal of Pulp and Paper Science* **18**(2): J74–J76.

Dodson, C. T. J. (1996). 'Fiber Crowding, Fiber Contacts, and Fiber Flocculation.' *Tappi Journal* **79**(9): 211–216.

Dodson, C. T. J. and K. Fekih (1991). 'The Effect of Fiber Orientation on Paper Formation.' *Journal of Pulp and Paper Science* **17**(6): J203–J206.

Dodson, C. T. J., Y. Oba, *et al.* (2001). 'Bivariate Normal Thickness-density Structure in Real Near-planar Stochastic Fiber Networks.' *Journal of Statistical Physics* **102**(1–2): 345–353.

Dodson, C. T. J. and W. W. Sampson (1999). 'Spatial Statistics of Stochastic Fiber Networks.' *Journal of Statistical Physics* **96**(1–2): 447–458.

Dodson, C. T. J. and C. Schaffnit (1992). 'Flocculation and Orientation Effects on Paper-formation Statistics.' *Tappi Journal* **75**(1): 167–171.

Duckett, K. E. and C. C. Cheng (1978). 'Discussion of Cross-point Theories of Van Wyk.' *Journal of the Textile Institute* **69**(2–3): 55–59.

Gates, D. J. and M. Westcott (1999). 'Predicting Fiber Contact in a Three-Dimensional Model of Paper.' *Journal of Statistical Physics* **94**(1–2): 31–52.

Gurnagul, N., R. C. Howard, *et al.* (1993). 'The Mechanical Permanence of Paper – a Literature-review.' *Journal of Pulp and Paper Science* **19**(4): J160–J166.

Kallmes, O. (1972). *A Comprehensive View of the Structure of Paper*. Syracuse, Syracuse University Press.

Kallmes, O. and G. Bernier (1963). 'The Structure of Paper: IV. The Bonding States of Fibers in Randomly Formed Papers.' *Tappi* **46**: 493.

Kallmes, O. and H. Corte (1960). 'The Structure of Paper: I. The Statistical Geometry of an Ideal Two-dimensional Fiber Network.' *Tappi* **43**: 737.

Kallmes, O., H. Corte, and G. Bernier (1963). 'The Structure of Paper: V. The Free Fiber Length of a Multiplanar Sheet.' *Tappi* **46**: 108.

Kendall, M. G. and P. A. P. Moran (1963). *Geometrical Probability*. London, Charles Griffin and Co. Ltd.

Kim, H. S. (2004). 'Relationship Between Fiber Orientation Distribution Function and Mechanical Anisotropy of Thermally Point-Bonded Nonwovens.' *Fibers And Polymers* **5**(3): 177–181.

Komori, T. and M. Itoh (1991). 'Theory of the General Deformation of Fiber Assemblies.' *Textile Research Journal* **61**(10): 588–594.

Komori, T. and M. Itoh (1994). 'A Modified Theory of Fiber Contact in General Fiber Assemblies.' *Textile Research Journal* **64**(9): 519–528.

Komori, T. and M. Itoh (1997). 'Analyzing the Compressibility of a Random Fiber Mass Based on the Modified Theory of Fiber Contact.' *Textile Research Journal* **67**(3): 204–210.

Komori, T., M. Itoh, *et al.* (1992). 'A Model Analysis of the Compressibility of Fiber Assemblies.' *Textile Research Journal* **62**(10): 567–574.

Komori, T. and K. Makishima (1977). 'Numbers of Fiber to Fiber Contacts in General Fiber Assemblies.' *Textile Research Journal* **47**(1): 13–17.

Komori, T. and K. Makishima (1978). 'Estimation of Fiber Orientation and Length in Fiber Assemblies.' *Textile Research Journal* **48**(6): 309–314.

Komori, T. and K. Makishima (1979). 'Geometrical Expressions of Spaces in Anisotropic Fiber Assemblies.' *Textile Res. J.*, **49**: 550–555.

Lee, D. H. and J. K. Lee (1985). *Initial Compressional Behavior of Fiber Assembly. Objective Measurement: Applications to Product Design and Process Control*. S. Kawabata, R Postle, and M. Niwa, Osaka, The Textile Machinery Society of Japan: 613.

Li, S. P. and K. L. Ng (2003). 'Monte Carlo study of the sphere packing problem.' *Physica a-Statistical Mechanics and Its Applications* **321**(1–2): 359–363.

Litvinova, T. A. (1982). *Calculation of Sorption-structural Characteristics of Textile Materials*. Moscow, Moscow Textile Institute.

Mardia, K. V. (1972). *Statistics of Directional Data*. New York, Academic Press.

Michell, A. J., R. S. Seth, and D. H. Page (1983). 'The Effect of Press Drying on Paper Structure.' *Paperi Ja Puu-Paper and Timber* **65**(12): 798–804.

Narter, M. A., S. K. Batra and D. R. Buchanan (1999). 'Micromechanics of three-dimensional fibrewebs: constitutive equations.' *Proceedings of the Royal Society of London Series a-Mathematical Physical and Engineering Sciences* **455**(1989): 3543–3563.

Ogston, A. G. (1958). 'The Spaces in a Uniform Random Suspension of Fibers.' *Trans. Faraday Soc.* **54**: 1754–1757.

Page, D. H. (1993). 'A Quantitative Theory of the Strength of Wet Webs.' *Journal of Pulp and Paper Science* **19**(4): J175–J176.

Page, D. H. (2002). 'The Meaning of Nordman Bond Strength.' *Nordic Pulp & Paper Research Journal* **17**(1): 39–44.

Page, D. H. and R. C. Howard (1992). 'The Influence of Machine Speed on the Machine-direction Stretch of Newsprint.' *Tappi Journal* **75**(12): 53–54.

Page, D. H., R. S. Seth, *et al.* (1979). 'Elastic Modulus of Paper. 1. Controlling Mechanisms.' *Tappi* **62**(9): 99–102.

Page, D. H. and R. S. Seth (1980a). 'The Elastic Modulus of Paper. 2. The Importance of Fiber Modulus, Bonding, and Fiber Length.' *Tappi* **63**(6): 113–116.

Page, D. H. and R. S. Seth (1980b). 'The Elastic Modulus of Paper 3. The Effects of Dislocations, Microcompressions, Curl, Crimps, and Kinks.' *Tappi* **63**(10): 99–102.

Page, D. H. and R. S. Seth (1980c). 'Structure and the Elastic Modulus of Paper.' *Abstracts of Papers of the American Chemical Society* **179**(MAR): 27–CELL.

Page, D. H. and R. S. Seth (1988). 'A Note on the Effect of Fiber Strength on the Tensile Strength of Paper.' *Tappi Journal* **71**(10): 182–183.

Pan, N. (1993a). 'Development of a Constitutive Theory for Short-fiber Yarns, Part III: Effects of Fiber Orientation and Fiber Bending Deformation.' *Textile Research Journal* **63**: 565–572.

Pan, N. (1993b). 'A Modified Analysis of the Microstructural Characteristics of General Fiber Assemblies.' *Textile Research Journal* **63**(6): 336–345.

Pan, N. (1993c). 'Theoretical Determination of the Optimal Fiber Volume Fraction and Fiber–Matrix Property Compatibility of Short-fiber Composites.' *Polymer Composites* **14**(2): 85–93.

Pan, N. (1994). 'Analytical Characterization of the Anisotropy and Local Heterogeneity of Short-fiber Composites – Fiber Fraction as a Variable.' *Journal of Composite Materials* **28**(16): 1500–1531.

Pan, N. (1995). 'Fiber Contact in Fiber Assemblies.' *Textile Research Journal* **65**(10): 618–618.

Pan, N. and G. A. Carnaby (1989). 'Theory of the Shear Deformation of Fibrous Assemblies.' *Textile Research Journal* **59**(5): 285–292.

Pan, N., J. Chen, M., Seo, and S. Backer (1997). 'Micromechanics of a Planar Hybrid Fibrous Network.' *Textile Research Journal* **67**(12): 907–925.

Pan, N. and W. Zhong (2006). 'Fluid Transport Phenomena in Fibrous Materials.' *Textile Progress*: in press.

Parkhouse J. and A. Kelly (1995). 'The Random Packing of Fibers In Three Dimensions.' *Proc: Math. and Phy. Sci. Roy. Soc.* **A 451**: 737.

Perkins, R. W. and R. E. Mark (1976). 'Structural Theory of Elastic Behavior of Paper.' *Tappi* **59**(12): 118–120.

Perkins, R. W. and R. E. Mark (1983a). 'Effects of Fiber Orientation Distribution on the Mechanical Properties of Paper.' *Paperi Ja Puu-Paper and Timber* **65**(12): 797–797.

Perkins, R. W. and R. E. Mark (1983b). 'A Study of the Inelastic Behavior of Paper.' *Paperi Ja Puu-Paper and Timber* **65**(12): 797–798.

Perkins, R. W. and M. K. Ramasubramanian (1989). *Concerning Micromechanics Models for the Elastic Behavior of Paper*. New York, The American Society of Mechanical Engineering.

Peterson, I. (1998). 'Cracking Kepler's Sphere-packing Problem.' *Science News* **154**(7): 103.

Pourdeyhimi, B. and H. S. Kim (2002). 'Measuring Fiber Orientation in Nonwovens: The Hough Transform.' *Textile Research Journal* **72**(9): 803–809.

Pourdeyhimi, B. and R. Ramanathan (1995). 'Image-analysis Method for Estimating 2-D Fiber Orientation and Fiber Length in Discontinuous Fiber-reinforced Composites.' *Polymers and Polymer Composites* **3**(4): 277–287.

Pourdeyhimi, B., R. Ramanathan, *et al.* (1996). 'Measuring fIber Orientation in Nonwovens.1. Simulation.' *Textile Research Journal* **66**(11): 713–722.

Ramasubramanian, M. K. and R. W. Perkins (1988). 'Computer Simulation of the Uniaxial Elastic–Plastic Behavior of Paper.' *Journal of Engineering Materials and Technology–Transactions of the ASME* **110**(2): 117–123.

Sayers, C. M. (1992). 'Elastic Anisotropy of Short-fiber Reinforced Composites.' *Int. J. Solids Structures* **29**: 2933–2944.

Schaffnit, C. and C. T. J. Dodson (1994). 'A New Analysis of Fiber Orientation Effects on Paper Formation.' *Paperi Ja Puu-Paper and Timber* **76**(5): 340–346.

Scharcanski, J. and C. T. J. Dodson (1997). 'Neural Network Model for Paper-forming Process.' *IEEE Transactions on Industry Applications* **33**(3): 826–839.

Scharcanski, J. and C. T. J. Dodson (2000). 'Simulating Colloidal Thickening: Virtual Papermaking.' *Simulation* **74**(4): 200–206.

Scharcanski, J., C. T. J. Dodson, *et al.* (2002). 'Simulating Effects of Fiber Crimp, Flocculation, Density, and Orientation on Structure Statistics of Stochastic Fiber Networks.' *Simulation – Transactions of the Society for Modeling and Simulation International* **78**(6): 389–395.

Schulgasser, K. and D. H. Page (1988). 'The Influence of Transverse Fiber Properties on the Inplane Elastic Behavior of Paper.' *Composites Science and Technology* **32**(4): 279–292.

Seth, R. S. and D. H. Page (1975). 'Fracture Resistance – Failure Criterion for Paper.' *Tappi* **58**(9): 112–117.

Seth, R. S. and D. H. Page (1996). 'The Problem of Using Page's Equation to Determine Loss in Shear Strength of Fiber–fiber Bonds upon Pulp Drying.' *Tappi Journal* **79**(9): 206–210.

Stewart, I. (1992). 'Has the Sphere Packing Problem Been Solved.?' *New Scientist* **134**: 16.

Strumillo, C. and T. Kudra (1986). *Drying: Principles, Applications and Design*. New York, Gordon and Breach Publishers.

Tournier, J. D., F. Calamante, *et al.* (2004). 'Direct Estimation of the Fiber Orientation Density Function from Diffusion-weighted MRI Data using Spherical Deconvolution.' *Neuroimage* **23**(3): 1176–1185.

van Wyk, C. M. (1946). 'Note on the Compressibility of Wool.' *Journal of Textile Institute* **37**: 282.

Weitz, D. A. (2004). 'Packing in the Spheres.' *Science* **303**: 968–969.

2

Understanding the three-dimensional structure of fibrous materials using stereology

---

D. LUKAS and J. CHALOUPEK, Technical University of Liberec, Czech Republic

Stereology is a unique mathematical discipline used to describe the structural parameters of fibrous materials found in textiles, geology, biology, fibrous composites, and in corn-grained solids, where fibre-like structures are created by the edges of grains in contact with each other. This chapter is compiled from lectures delivered to post-graduate students taking ‘Stereology of Textile Materials’ at the Technical University of Liberec (Lukas, 1999), and is relevant to students and researchers involved in interpreting flat images of fibrous materials in order to explain their behaviour, or to design new fibrous materials with enhanced properties. There are a number of excellent monographs on stereology, ranging from the basic to the expert. This chapter outlines an elementary technique for deriving most of the stereological formulae, avoiding those demanding either lengthy explanations or a specialised mathematical background. The chapter concentrates on the set of tools needed for a geometrical description of fibrous mass, and provides comprehensive references for further information on this relatively new field.

2.1 Introduction

Stereology was developed to solve various problems in understanding the internal structure of three-dimensional objects, such as fibrous materials, and especially textiles. The relevant geometrical features are mainly expressed in terms of volume, length, surface area, etc. (detailed in Section 2.1.1), and there are three main obstacles facing efforts to quantify these features. The first two difficulties are practical in nature and the third theoretical.

(i) The internal structure of an opaque object can only be examined in thin sections, comprising projections of its fibres. Sections of textile materials may be cut using sharp tools, or created virtually by applying the principles of tomography, confocal microscopy, etc.

(ii) The dimensions of an object under investigation are usually proportionately much greater than the characteristic dimensions of its internal structure; for instance, fibre diameters will be orders of magnitude smaller that the width and the length of the fabric they form. Hence, it is not practicable to study an entire object in detail.

(iii) Occasionally, investigators must determine an appropriate set of geometrical parameters to describe real structures and their properties. Specific parameters will be associated with either mechanical or adsorption properties of fibrous materials.

Various disciplines require information on the internal structures of objects, including biology, medicine, geology, material engineering and mathematics itself. The evolution of methods to quantify structural features laid the foundation for what is now known as stereology, and the concept has continued to evolve since it was proposed in 1961 by a small group of scientists at Feldberg in Germany, under the leadership of Hans Elias (Elias, 1963).

For the purposes of this chapter, the following definition of stereology is used:

> *Stereology is a mathematical method of statistical selection and processing of geometrical data to estimate geometrical quantities of an* n*-dimensional object through measurements of its sections and projections, which have dimensions less than* n.

The relationship between the geometrical quantities of an n-dimensional object and measurements of its sections and projections is quite logical and familiar. Figure 2.1 reminds us of the procedure for ascertaining the volume of a three-dimensional body. The volume of a three-dimensional body K, say $V(K)$, may be expressed by a definite integral, laid out as:

$$V(K) = \int_0^H a(z)dz \tag{2.1}$$

where $a(z)$ is the area of a planar cross-section of the body K and is perpendicular to the z-axis. H is the longitudinal length of the projection of the body on the z-axis. The left-hand side of the formula, i.e. the volume $V(K)$, represents a parameter of the three-dimensional object. The right-hand side reveals another parameter of the body in question, $a(z)$, which results from an analysis of its flat cross-section. The two-dimensional parameter $a(z)$ symbolises the area of the flat section cut in the body K by a plane, normal to the z-axis, thus, expressing its cross-sectional area as a function of z. Thus the relationship between three- and two-dimensional parameters is established through integration.

The above relationship may also be demonstrated through Cavalieri's principle. The conceptualisation was framed by Cavalieri, a student of Galileo in the 17th century (Naas and Schmidt, 1962; Russ and Dehoff, 2000), for two- and three-dimensional objects. For two dimensions, the principle states

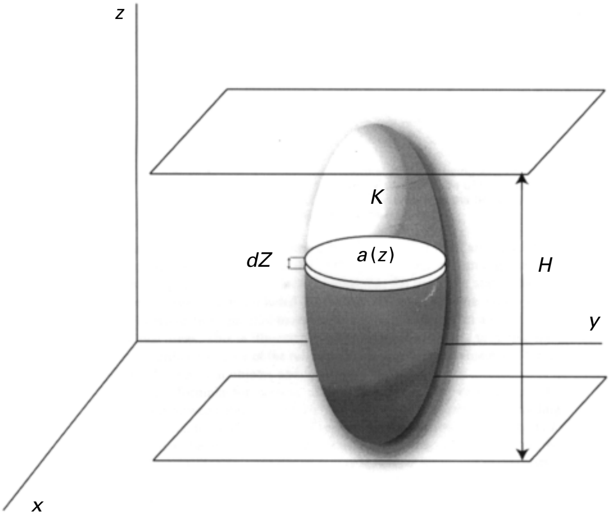

2.1 Volume, *V*(*K*), of a three-dimensional body, *K*, being expressed as a sum of the volumes of its elementary thin sections of thickness, *dz*, that are parallel to the *x*–*y* plane. *H* is the length of the body *K*, perceived as its upright projection on the *z*-axis.

that the areas of two figures included between parallel lines are equal if the linear cross-sections parallel to and at the same distance from a given base line have equal lengths. For three dimensions, the principle states that the volumes of two solids included between parallel planes are equal if the planar cross-sections parallel to and at the same distance from a given plane have equal areas. This is illustrated in Fig. 2.2. Cavalieri's principle thus provides further evidence of the relationship between the parameters of three- and two-dimensional objects and their sections.

Cauchy's formula for surface area also supports the existence of the relationship between objects and their lower-dimension projections. According to this formula, the surface area $S(K)$ of a three-dimensional convex body K is four times the mean area of its planar projection. This can easily be verified by considering a sphere of radius R, whose surface area S is $4\pi R^2$, and each of its planar projections has an area of πR^2. These quantities are proportional to each other, being related by a factor of 4. A similar relationship for two-dimensional convex bodies will be established in Section 2.3.4. The definition of a convex body will be specified in Section 2.1.1.

However, these attempts to colligate the dimensional aspects of objects with their sections and projections are based only on geometry. Stereology involves statistical methodology in combination with geometry and gives us the ability to model geometrical relations where measurement is impractical or even impossible. To understand the effectiveness of this method, it is necessary to review an interesting experiment carried out in the 18th century.

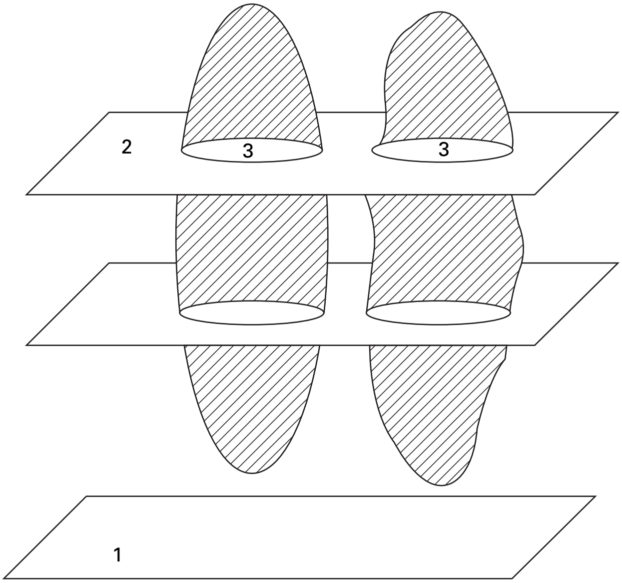

2.2 Illustration of Cavalieri's principle: Volumes of the two solid bodies included between parallel planes are equal if the corresponding planar cross-sections (shown as 3) at any position are equal and parallel to a given plane (shown as 1).

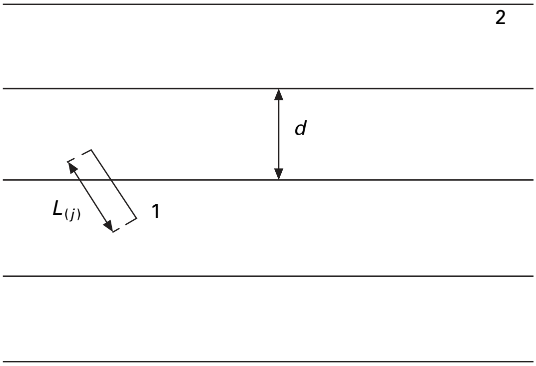

2.3 Buffon's needle (shown as 1) of length $L(j)$ is located on a warp of parallel lines (2), which are separated by a distance d.

In 1777, the French naturalist Buffon was attracted by the probability, P, that a randomly thrown needle, j, of length $L(j)$ will hit a line among a given set of parallel lines in a plane with each of the neighbouring lines separated by a distance d, so as to conform to a precondition of $d > L(j)$. The situation is depicted in Fig. 2.3. Buffon (1777) deduced P as $2L(j)/(\pi * d)$. The estimated value $[P]$ of probability P, from a large number of throws, N, could be estimated through a relative frequency of hits. Precisely, the value of P equalled the limiting value of $[P]$, while N tended to infinity, i.e. $P = \lim_{N\to\infty} [P]$. The relative frequency, $[P]$, was defined as:

$$[P] = \frac{n}{N} \tag{2.2}$$

where n is the number of positive trials, and N the total number of throws. From this relationship, an unbiased estimation of the distance between parallel lines, $[d]$ can be obtained. The concept of 'estimators' will be detailed in sub-section 2.3.1.

$$[d] = \frac{2L(j)}{\pi[P]} = \frac{2L(j)N}{\pi n} \tag{2.3}$$

The above relation [2.3] will be used in Section 3.3.2 to estimate the lengths of curves or fibrous materials in a plane.

Equation [2.3] can be verified by imagining a series of random needle throws. The needle has to be thrown in such a way as to ensure equal probabilities of its landing at various locations on the parallel lines in all possible orientations. This can be done by throwing the needle repeatedly in the same way, while rotating the parallel lines by an angle $k\pi/M$. For each particular orientation of the lines, groups of equal number of trials are carried out. Here, k is the sequence number of a particular group of trials and M the total number of groups of trials. Equation [2.3] shows that the one-dimensional geometrical parameter d may be estimated from the number of times Buffon's needle intersects a line. Since the intersection points are zero-dimensional, the connection between dimensions of an object with those of its sections is confirmed.

The next point noteworthy in the context of the Buffon's needle problem, concerns the Ludolf number π, which may be estimated statistically after rearranging Equation [2.3] to obtain an expression of $[\pi]$ as $2L(j) * N/(d * n)$ and, subsequently, using known values of the other parameters. The value of d has to be known exactly to estimate π. The Ludolf number is therefore estimated using a known set of parameters of $L(j)$, N, d, and n.

There are three different classes of analysis for investigating the internal structures of a material, and the most appropriate method or combination of methods is chosen for the particular problem at hand.

(i) The first class of analysis comprises estimations of the global geometrical parameters of a structure or the total values of its individual components, such as total volume, total length, and total numbers of particles. The geometrical parameters do not depend on the shape or distribution of the structure or its components in space. Accordingly, the corresponding stereological methods are independent as far as shapes and spatial distribution of the structural features are concerned. This class of study is characterised by estimations of total volumes, areas, lengths and densities.

(ii) The second class of study involves estimating the properties of individual parts and elements of a structure; for instance, estimating the distribution function of a chosen particle parameter. Sizes of particles and their projections are the most commonly measured parameters in this case.

(iii) The last class covers analyses of mutual spatial positions of structural features. The above two classes of study are not influenced in any way by the scatter of features in space. An analysis typical of this third class involves evaluating the planar anisotropy of fibrous systems, and this is described in more detail in Section 2.3.5. The importance of this area of study was highlighted by Pourdeyhimi and Koehl (2000a), who dealt with methods to examine the uniformity of a non-woven web. An understanding of the mutual spatial location of fibres and yarns is vital for the automatic recognition of fabric patterns, as described by Jeon (2003). Inter-fibre distances in paper and non-wovens have been studied by Dent (2001).

2.1.1 Structural features and their models

Textile engineering began with a classification of the various types of textiles, either according to their corresponding technologies or according to their most meaningful structural attributes, as described by Jirsak and Wadsworth (1999). Stereology provides the scientific basis for describing structures and their features, and these structural features are described below.

The notion of a 'feature' may be explained with reference to a complex structure, such as that of a non-woven textile. Figure 2.4 shows a point-bonded non-woven fabric made of thermoplastic fibres. The figure shows rectangular regions where many fibres adhere together. These regions are generally formed by the impacts of the rollers when the surface screen reaches the temperature at which the thermoplastic fibres melt and bond to form the fabric. These types of non-wovens are referred to as 'point-bonded'. Although the fibres are apparently randomly oriented, a deeper investigation reveals their preferred orientation. Some of the fibres have more crimp than others, and the distribution of the intra-rectangular bonded areas is nearly regular. Inside the squares, however, there are holes, or pores. Pores are found among the fibres as well, and the spatial distribution of the pores is irregular, as is the distribution of fibres.

The internal components of fibrous materials show morphological and dimensional variations along with a wide range of mutual spatial organisations, and a reasonable simplification of the complexity of such a structure appears unattainable. From a purely practical standpoint, a perfect description of the

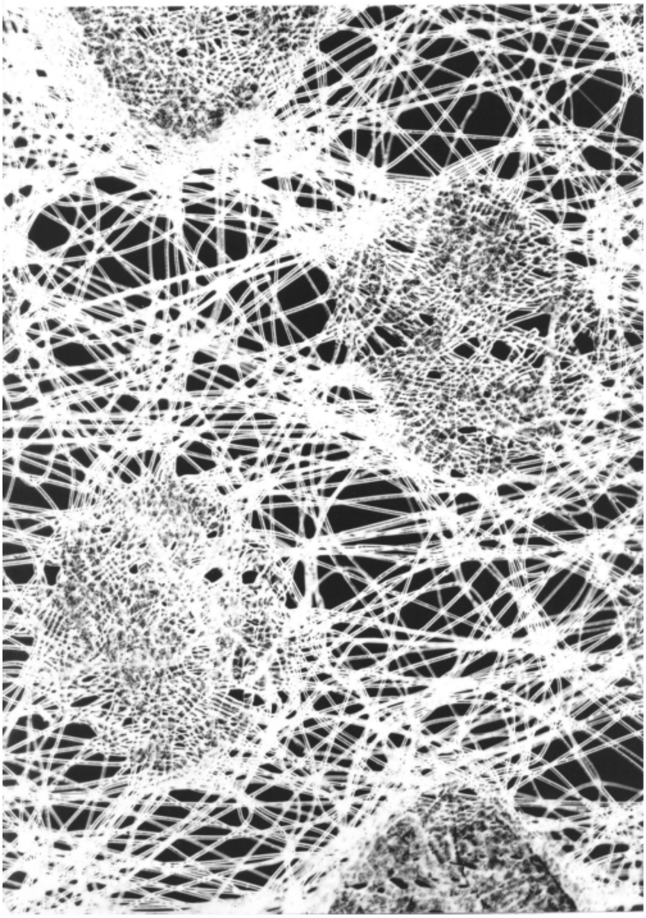

2.4 A point bonded nonwoven fabric, reinforced with thermoplastic fibers. The square-form spots were created by a regular grid of projections on one of the calender rollers. The projections, when they reached the melting temperature of fibers, bonded the nonwoven material in the predetermined pattern of spots with the thermoplastic fibres.

entire structure is unlikely to be helpful; it is more useful to examine the components that are responsible for the property under examination. The elements of the structure to be studied have to be spatially limited and experimentally distinguishable, otherwise quantitative measurements are not possible. The components that satisfy these conditions are called 'structural features', or simply 'features', and the combination of these features makes up the 'internal structure' of an object (Saxl, 1989).

The property(ies) of an object depend on its structure, which is studied or explained in terms of measurements of structural parameter. Properties such as textile permeability are studied without reference to the types of materials involved, as all materials trap gases and liquids, thus hindering their movement. On the other hand, the tensile strength of a fibrous material is related to the types of fibres and how they are bound.

The classification of structural elements as features also depends on how a sample is processed for stereological measurements. Figure 2.5 shows two different situations. Both diagrams display the same part of a blended fibrous mass, the right-hand image (b) differing with respect to shades. While it is not easy to distinguish between the two kinds of features in image a, it is possible in b. An exact recognition of structural features is important for processing images digitally. Koehl *et al.* (1998) developed a method for extracting geometrical features from digitised cross-sectional images of yarns.

Researchers must select the features that will enable them to investigate effectively the property of the object that is of interest. Features are mostly three-dimensional formations, distributed in three-dimensional space, but sometimes lower dimensions are more appropriate. One example of a lower-dimension investigation is for extremely thin textiles, where the investigation is restricted to their planar projections. Fibres may even be considered as one-dimensional features, and thus zero-dimensional points, such as centres of tiny dust particles in a fibrous filter, are features pertinent to the study of their distribution. Cross-sections or projections of three-dimensional objects may also be regarded as objects with their own intrinsic structure. In this chapter, such cross-sections and projections will be regarded as 'induced structures'.

Mathematical descriptions of internal structures are necessary to create a model of the feature that is both powerful enough to describe real objects

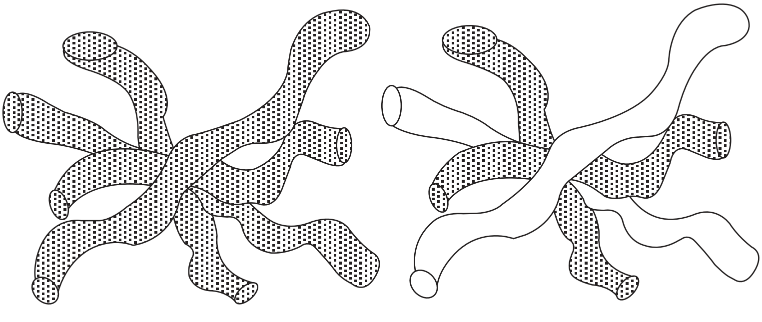

(a) (b)

2.5 Images of a fibrous object can have different kinds of features with different colour combinations. As the fibrous structure in (a) cannot be differentiated with respect to colour, it has only one type of feature. On the other hand, different shades of colours of the fibres in image (b) characterize it as a two-featured one.

and simple enough to model based on standard rules and regulations. The necessary attributes for this rarely coexist. The more generalised the model, the fewer the regulations, and therefore a rather careful choice of the feature model has to be carried out. Three models of features are described below, including some of the conceivable mathematical complications related to their usage, and their pertinence for describing fibrous materials.

(i) Compact sets

A compact set is a generalised model of structural features, and is discussed here in the context of fibrous features. Fibrous features are limited in space due to their well-defined boundaries, which therefore allow the existence of an n-dimensional cube with finite edge lengths that contains the chosen feature entirely. Therefore, fibrous features may also be referred to as closed sets, and thus a general model of structural features consists of limited and closed sets. Sets of points in Euclidian space obeying these properties are called ‘compact sets’.

Some compact sets have rather curious properties, as demonstrated by their characteristic finite volumes or areas, where determination of surface areas or boundary lengths causes a range of problems. An example of such a peculiar set is the von Koch flake. The base for its construction is an abscissa, $< 0, 1 >$, known as the ‘initiator’. It is divided into three equal sections, with the mid-section substituted by two line segments of equal lengths. Each of the segments has a length identical to that of the removed middle section. As shown in Fig. 2.6 (b), the segments meet together at an angle to form the vertex of an equilateral triangle. Subsequent repetitions of these steps produce the results shown in Fig. 2.6 (c). The basic unit, comprising a buckled line with four sections of equal lengths, is called the ‘generator’. Each of the four parts of the generator is replaced with a unit that is a diminished version of the generator in the ratio of 1:3. The resulting pattern has 16 sections of equal length. If the same procedure is repeated infinitely and each successive step ensures a reduction of the generator unit with respect to the previous step by the same ratio, a von Koch’s curve is obtained in the interval $< 0,1 >$. Using three initiators, joined together in a triangle form, a similar process will result in the von Koch’s flake. One of its construction stages is shown in Fig. 2.6 (d).

If the flake’s boundary is observed with a gradual increment of magnification, newer details will start emerging in stages. This unique feature, common to both von Koch’s curve and flake, is why determining their length and area is problematic. Similarly, three-dimensional sets can be constructed with very complex boundaries whose surface areas and volumes are not easily determined. These unique objects are called ‘fractals’, as described by Mandelbrot (1997). To exclude sets with

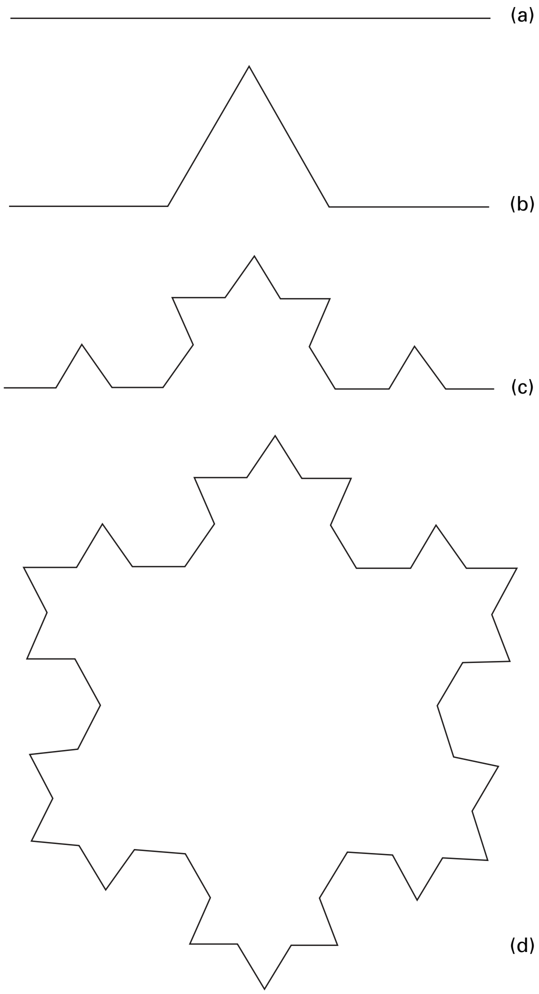

2.6 Von Koch curve and von Koch flake: Shows the initiator (a), and the generator (b) to enable constructions of the curve (c) and the flake (d). The parts (c) and (d) represent early stages of both the constructions.

complex boundaries, the ‘convex body’, a more specific class of model of feature, is used (see below).

Kang *et al.* (2002) investigated fibrous mass from the point of view of fractals, to model fabric wrinkle. Summerscales *et al.* (2001) explored Voronoi tessellation and fractal dimensions for the quantification of microstructures of woven fibre-reinforced composites.

(ii) Convex bodies

Convex bodies are characterised by the shortest link connecting two arbitrary points. If the straight line linking the points is enclosed fully inside the body, the body is then considered to be convex. Figure 2.7 illustrates three-dimensional convex and two-dimensional non-convex bodies. This model of convex bodies is inadequate to describe fibrous materials because the loops in the fibrous structure violate the model.

The concept of convex bodies, nevertheless, is significant in stereology because simple rules govern their properties. Figure 2.8 shows intersections of convex (a) and non-convex (b) two-dimensional bodies

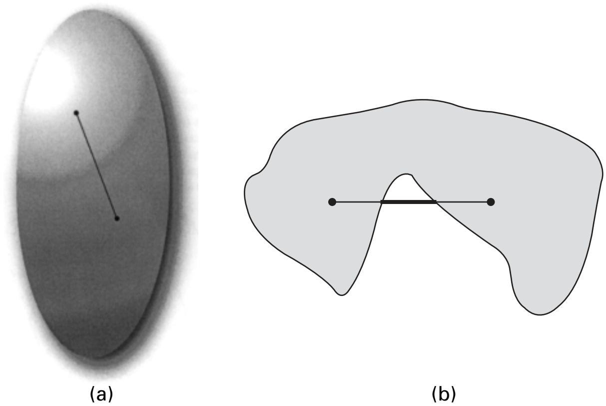

2.7 A three-dimensional convex body (a), and a two-dimensional non-convex body (b), obey the mutual relationship of the body and the shortest line connecting two of its arbitrary points. The straight link in-between the points has to lie fully inside the body to make it a convex one.

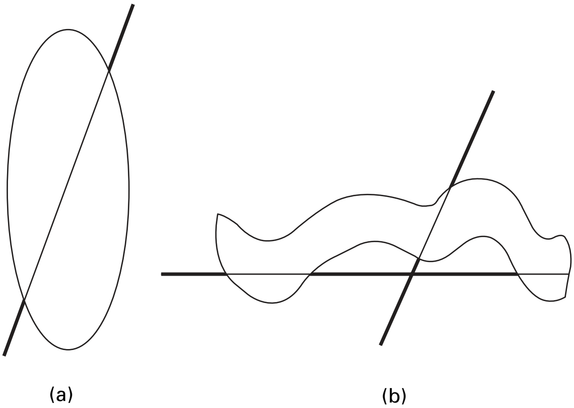

2.8 Intersections of a convex (a) and a non-convex two-dimensional body (b) with straight lines. Number of intersections for a non-convex body with such a line depends on the mutual position of the body and the line.

with straight lines. A convex body can be intersected by a straight line only once, and the intersection is itself convex. For a non-convex body, the number of intersections depends on the mutual orientation and position of the body and the straight line. For a non-convex body, an intersection may not be convex, but may be composed of several isolated parts. In other words, it is impossible to correlate the numbers of non-convex bodies and intersections from only knowing the number of intersections. The shortcomings of using convex bodies in describing fibrous structures must be overcome by an additional model, the 'convex ring', as described below.

(iii) Convex rings

A convex ring is defined as the union of a finite number of convex bodies. Figure 2.9 shows some two-dimensional bodies that demonstrate this concept, illustrating that not all convex rings are suitable for describing real fibrous structures. For our purposes, features pertinent to fibrous structures will be visualised in the context of convex rings.

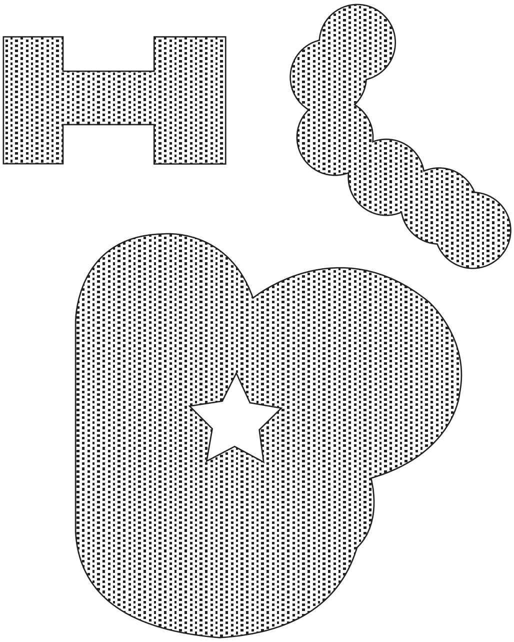

2.9 Two-dimensional bodies, so-called figures, belong to the set of the convex ring. Using more and more appropriately chosen convex bodies, one can create fibre-like objects either in two- or three-dimensional space.

2.2 Basic stereological principles

This section examines the geometrical characteristics of the volume of three-dimensional bodies, in the context of mapping the volume of a three-dimensional geometrical object with a set, R, of real numbers. A characterization theorem demonstrates how many groups there are of geometrical characteristics with the same set of attributes as the volume. Finally, we cite a generalised notion of section, which will be used as a tool to open opaque three-dimensional structures.

2.2.1 Content of convex ring sets and characterization theorem

One of the most frequently used parameters of features is their n-dimensional content, which generally refers to volume, surface area, and length. Accordingly, volume is regarded as a three-content, area two-content, and length as one-content in the parlance of stereology.

Now let us examine the generic properties of contents, along with the parameters that define n-dimensional objects of a convex ring and have the characteristic set of properties of content, using the example of the volume, or the three-content, of a three-dimensional prism h. The volume, $V(h)$, for any element, h, of the set of all possible prisms, H, is defined simply by a product of a, b and c, which exactly represent the lengths of the prism's perpendicular edges. As the set, H, of all prisms is connected to the set of real numbers, representing volume, $V(h)$, by means of 'onto mapping', the volume may be deemed as a functional. Generally, a functional is defined as the mapping of any set to a set of numbers. The well-known properties of functional, $V(h)$, are listed below:

(i) The functional, $V(h)$, does not depend on the location and the orientation of the prism, h, in space. This property is known as translational invariance.
(ii) If splitting the original prism, h, gives rise to two non-intersecting prisms, A and B, with at the most one common edge or side, then their corresponding volumes, $V(A)$ and $V(B)$, fulfil the relation $V(h) = V(A \cap B) = V(A) + V(B)$, where the functional $V(h)$ has its usual significance. The relation expresses a simple additivity of the volume functional.
(iii) The functional, $V(h)$, is positively defined, i.e., $V(h) \geq 0$ for each prism, h, from the set of prisms, H.
(iv) The functional, $V(h)$, is normalised. Thus for each $V(h)$, the properties (i), (ii), and (iii) satisfy a functional $V'(h) = \alpha \cdot a \cdot b \cdot c$, where α is the normalisation factor and $\alpha > 0$. When the value of α attains unity, then $V(h)$ has a unit value for a unit cube, with each of its edges, a, b and c

having unit length. Commonly, the normalization parameter α is taken to be one.

A fascinating theorem pertaining to convex bodies and convex ring sets gives a solution for the total number of linearly independent functionals of n-dimensional bodies in n-dimensional spaces that fulfil the same list of properties (i)–(iv) as does the volume V. A detailed explanation of the solution was given by Hadwiger (1967). Sera (1982) brought in a characterization theorem to state that every such body had just $(n + 1)$ linearly independent invariant characteristics, so-called 'invariant measures'. Saxl (1989) listed a specially chosen set of such measures for convex bodies and bodies from convex rings. An edited version of the list for convex ring bodies is provided in Table 2.1. The only characteristic that will not be discussed in this chapter is the integral of the mean curvature of the surface of three-dimensional bodies. In Table 2.1, this characteristic is highlighted in italics. Euler–Poincaré characteristics will be described in Section 2.3.3.

2.2.2 Sections and ground sections

Usually, the terms 'section' and 'ground section' refer to a two-dimensional section of a three-dimensional body. This concept can, however, be generalised. Using different kinds of sections to investigate various materials is highly advantageous, because they help us to analyse the internal structure of objects that are otherwise imperceptible. Taking care to prepare the sections appropriately preserves the original mutual positions of the features in different materials.

The notion of a section can be generalised as the intersection of a three-dimensional object with a two-dimensional space, i.e. the plane of a section made by a cutting tool or by the movement of a grindstone in the case of a

Table 2.1 List of linearly independent and invariant structural characteristics, also known as invariant measures, for objects of various dimensions from the convex ring

Dimension of object		Linearly independent invariant structural characteristics (invariant measures)			
		n-content	(n-1)-content	(n-2)-content	(n-3)-content
	3	Volume	Surface area	*Integral of the mean curvature of the surface*	Euler–Poincaré characteristics
	2	Area	Perimeter length	Euler–Poincaré characteristics	
	1	Length	Euler–Poincaré characteristics		
	0	Euler–Poincaré characteristics			

ground section. Two-dimensional sections may also be generated on the focal plane of a confocal microscope (Lukas, 1997). Therefore, the general definition of a section may be based on the intersection of an object under investigation, with another body having dimensions equal to or less than that of the investigated object. By choosing the dimensions of the different bodies, various types of sections can be obtained.

Sections obtained from the intersection of two three-dimensional bodies are called three-dimensional sections or, more frequently, thin sections. Normally, this kind of section has the shape of a layer between two parallel planes, as shown in Fig. 2.10 (a). Section 2.4.4 uses thin sections to evaluate the average values of curvature and torsions of linear features. Block-like three-dimensional sections, which will be described in detail in Section 2.4.5, are used as dissectors for counting isolated parts of internal structures.

A two-dimensional section is obtained by intersecting a three-dimensional body with a plane, as shown in Fig. 2.10 (b). The intersection of a three-dimensional body with a straight line results in a one-dimensional section, as is depicted in Fig. 2.11 (a). The intersection of a three-dimensional body with a point located on a line, as shown in Fig. 2.11 (b), produces a section of zero dimensions. Figures can have two-, one- and zero-dimensional sections, while curves can have only one and zero-dimensional sections.

Figure 2.12, where a part of fibrous structure is embedded in a block of region Ω, demonstrates the kinds of information about three-dimensional structures that is available from various sections. According to the

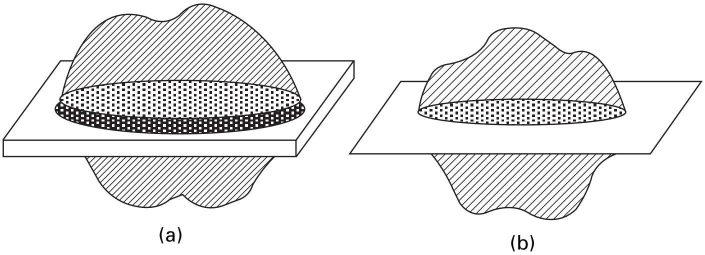

2.10 Three-dimensional (a) and two-dimensional (b) cross-sections of a three-dimensional object.

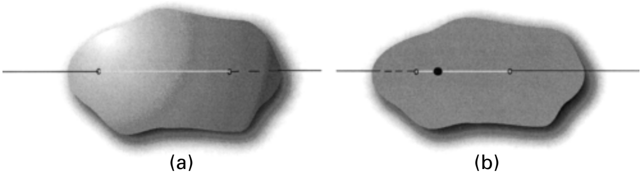

2.11 One-dimensional (a) and zero-dimensional cross-sections (b) of a three-dimensional body.

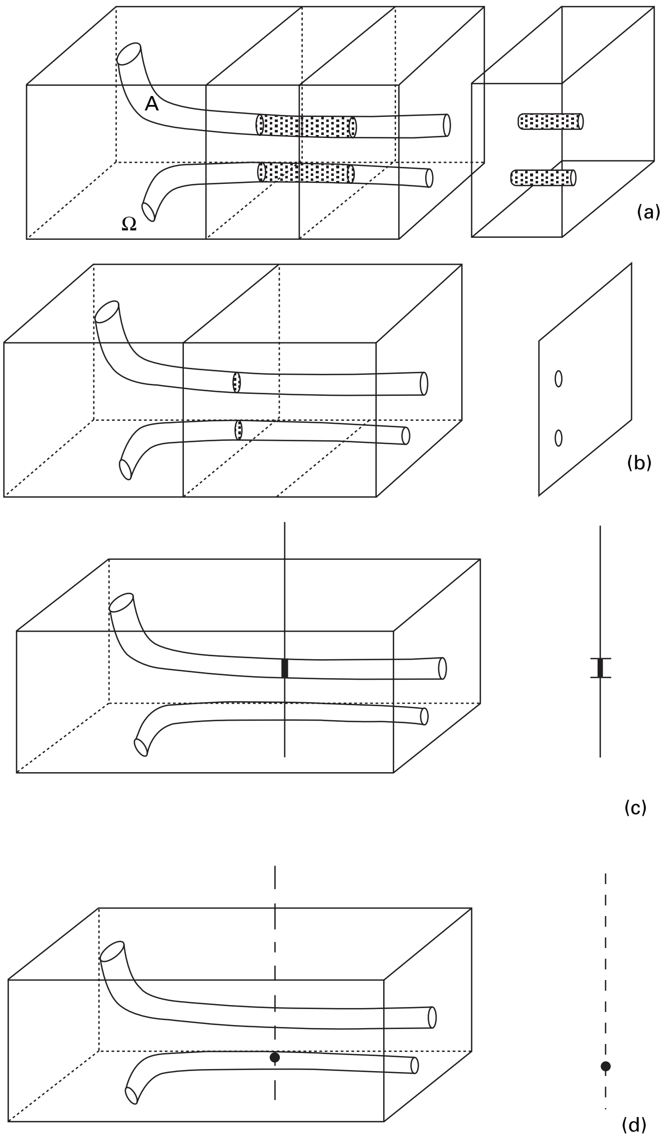

2.12 A three-dimensional object *A* in a region Ω and its various cross-sections: (a) shows a three-dimensional cross-section with the induced structure embedded in it; (b) shows a two-dimensional cross-section with the induced structure; (c) shows a one-dimensional cross-section to which belongs the induced structure composed of a piece of a line; (d) shows a zero-dimensional cross-section represented by a point.

characterization theorem and Table 2.1, four common characteristics can be assigned to the structure in this figure. The characteristics are the volume, surface area, the integral of the mean curvature of the surface expressed in terms of length, and the Euler–Poincaré characteristic taken here for convenience as the number of isolated convex parts of the object.

The three-dimensional section is also a three-dimensional structure and contains information about all four aforementioned characteristics of the structure. The fewer the dimensions of the section, the less information it contains. The correspondence between information conveyed by a section and the geometrical parameters of the original structure can be shown using a three-dimensional fibrous object enclosed in a three-dimensional region Ω such as that in Fig. 2.12(a). The set of independent parameters of the structure A comprises the volume, surface area, length of the very thin fibres (because thin fibres have only length as their physical dimension, they play a role very similar to the integral of the mean curvature of the surface. More information about integrals of curvature can be found in Saxl (1989)), and the number of isolated parts of the structure. The independence of the parameters implies that none of them can be expressed using linear combinations of the remaining ones. This independency can be explained using their dissimilar physical dimensions. Denoting the physical dimension of the length as L^1, dimensions of the volume, the surface area, and the number of isolated structural parts take the form of L^3, L^2 and L^0, respectively. The three-dimensional section of A, as depicted in Fig. 2.12(a), contains the induced structure of the three-dimensional object, and so contains information about all four independent parameters.

The two-dimensional section carries information about only three parameters, because its induced structure is described using only the three independent measures of surface area, boundary length and number of isolated parts. Since the number of isolated non-convex bodies of a convex ring cannot be estimated from their sections of lower dimensions, it is impossible to determine the number of isolated parts of an original structure with this type of section. This is because the number of intersections in a convex ring is manifold and does not depend solely on the total number of bodies there. It also depends on the position and orientation of the section, as was indicated in Fig. 2.8 for two-dimensional convex bodies.

One-dimensional sections contain information about length and the number of isolated line segments described on them as induced structures. As before, it is not possible to estimate the number of isolated bodies of the original structure from this type of section. Zero probability of an intersection of a straight line with a line or a curve cannot be used also to estimate the feature length of an original structure. The one-dimensional fibre here represents all parameters with a physical dimension L^1 including integrals of the surface main curvature.

Finally, the zero-dimensional section, or point, contains information only about the volume of an original structure because the probability of a point section intersecting with points, curves and surfaces embedded in a three-dimensional space, is zero.

The above statements concerning the information contained in various sections of a three-dimensional object are summarised in Table 2.2. Guidelines for interpreting Table 2.2 are given below:

(i) The second row in the table shows the three-dimensional structural parameter, which is volume with a physical dimension of L^3. The row expresses that each type of section can be used to estimate this parameter.
(ii) The fourth row includes sections specifically used to measure one-dimensional parameters, such as length with the physical dimension L^1. As has been observed before, the probability of a one-dimensional body intersecting with a line or a point section in three-dimensional space is nil. Hence, such a parameter can only be estimated from three and two-dimensional sections.
(iii) The fourth column corresponds to sections of one dimension. This type of section provides intersections among two- and three-dimensional features with a non-zero probability. Thus, one-dimensional sections are useful for estimating the volumes and surface areas of three-dimensional bodies.

The above analysis may be extended to any object of arbitrary dimensions through Equation [2.4]. This equation associates the dimension of an induced structure, the dimension of a structural feature, and the dimension of a body used to create sections, with that of an investigated body. Here, the dimension of an investigated body is the same as that of the space occupied by it. The term $d(\alpha)$ stands for the dimension of a structural feature, α, of an investigated body, A, having dimension $d(A)$. The structural feature, α, under consideration occasionally stands for the surface of a three-dimensional body. Therefore, $d(\alpha)$ and $d(A)$ have values of 2 and 3, respectively. Structural features and

Table 2.2 Dimensions of structural parameters of a three-dimensional object and dimensions of bodies from which their sections are created to determine the dimensions of induced structures on sections. For three-dimensional objects, the dimensions of the body used to carry out sectioning are equal to dimensions of the corresponding sections

Structural parameters of three-dimensional objects (and their dimensions)	Dimension of the sectioning bodies			
	3	2	1	0
Volume (**3**)	3	2	1	0
Surface area (**2**)	2	1	0	
Length (**1**)	1	0		
Euler–Poincaré characteristics (**0**)	0			

their structural parameters have the same dimensions. This principle has already been used in Table 2.2. The term $d(\beta)$ denotes the dimension of a body, β, from which sections of the investigated body, A, are created. For instance, β may be considered as a straight line with a dimension, $d(\beta)$, of 1. Finally, $d(\alpha \cap \beta)$ describes the dimension of the induced structure created out of an intersection of the structural feature, α, and the surface of the body, β. The dimensional terms $d(\alpha)$, $d(A)$, $d(\beta)$ and $d(\alpha \cap \beta)$ are related by the following formula, as introduced by Wiebel (1979). All the data in Table 2.2 can be derived from it.

$$d(\alpha \cap \beta) = d(\alpha) + d(\beta) - d(A) \qquad [2.4]$$

The above relation is easily verified in the context of this chapter. The three-dimensional body, A, with the dimension, $d(A)$, of 3, has the dimension of the surface area of its relevant feature, α, as $d(\alpha)$, having a value of 2. If the feature is examined with the one-dimensional body, β, having the dimension, $d(\beta)$, ascribed with a value of 1, the induced structure $\alpha \cap b$, which is created by the intersection of the surface, α, of the three-dimensional body, A, and the straight-line, β, takes the form of a point. Consequently, its dimension is $d(\alpha \cap b) = 0$. By assigning the above-mentioned values for the corresponding terms on the right-hand side, the relationship is verified.

The above relationship may be extended to objects having fewer than three dimensions. If A is any two-dimensional area embedded with a fibrous system (material) α, then the relevant term $d(A)$, has a value of 2. Accordingly, the internal structure consists of a one-dimensional fibrous system, α, characterised by a value of $d(\alpha)$ as 1. A body, β, with a dimension, $d(\beta)$, of 0, may be used, hopefully, to estimate the length as a geometrical parameter of the internal structure, which consists of one-dimensional fibrous material α. Fitting the values into the equation gives the value of $d(\alpha \cap \beta)$ as –1, which is ignored due to its physical insignificance. A similar argument explains the empty box of the row for the surface area in Table 2.2.

2.2.3 Lattices and test systems

Measuring part of an object, X, can be facilitated by incorporating a test system that is composed of a regular lattice of fundamental regions along with a regular distribution of probes. A lattice of fundamental regions consists of regions $\alpha_0, \alpha_1, \alpha_2, \ldots, \alpha_n$ with the following attributes:

(i) Each of the fundamental regions, α_i, contains at the most one point of an n-dimensional space.

(ii) All fundamental regions are distributed regularly in space with respect to translational symmetry. Thus each fundamental region, α_i, can be exactly displaced to any other region, α_j, and the displacement vector consists of a linear combination of basic lattice vectors. Multiplication constants in this linear combination are integers.

The most common lattices of fundamental regions consist of squares, oblongs, triangles, hexagons, etc. According to the attribute (i), tightly packed lattices in a plane comprise fundamental regions whose boundaries are partly open, to preclude overlapping of the boundary points. Lattices of fundamental regions are illustrated in Fig. 2.13.

Test systems are constructed so that set *B* is encompassed by each fundamental region, where *B* is distributed in the lattice with the same translational symmetry as that of the spatial distribution of the fundamental regions in the lattice. This means that the local view for each fundamental region is identical with the others. The set *B* is known as a probe, and is generally represented as points, curves or figures. As described in Section

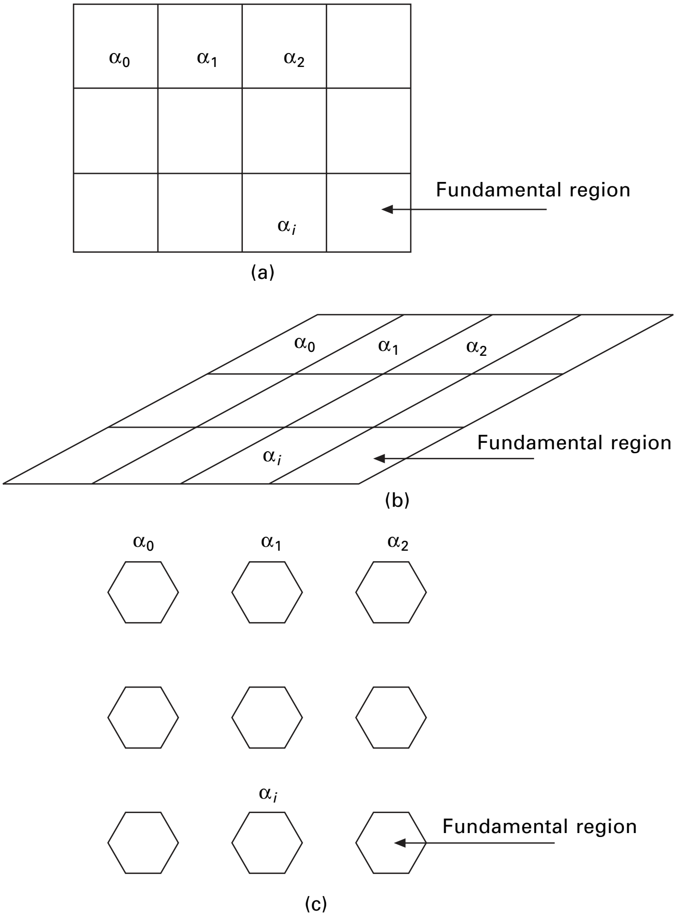

2.13 Three examples of two-dimensional lattices of fundamental regions: a square lattice (a), a lattice with the fundamental region of parallelogram type (b), and a hexagonal lattice (c).

3.4.5, dissectors are the only systems that are based on the use of three-dimensional probes.

To model a probe on a transparent sheet or a foil, marking tools leave behind trails and spots whose respective widths and diameters are significantly thick; therefore, these spots and trails do not correspond to points or one-dimensional lines. The same argument is valid for grids, lines, and points created by graphics software on monitor screens. An uncertainty therefore persists about the precision of the presumed intersections of the probes used to study structural features. Figure 2.14 demonstrates this imprecision. To counter this problem, a pointed probe in a testing system is expressed as an intersection of the edges of two mutually perpendicular trails. A one-dimensional curvilinear probe is represented by the chosen edge of a trail.

The positions of the probes must be in a uniform random distribution with respect to the object under examination, in order to arrive at an unbiased estimation of the selected structural parametric value. In other words, stereological measurements are carried out in a series of uniform random and isotropic sections. Pertaining to a body, A, and a test section, T, there are uniform random sections $A \cap T$ corresponding to a point, $X \in T$, randomly located in A with the same probability of appearing at each region of A, provided that the isotropic orientation of T in three-dimensional space remains unaffected by the position of X in A. An analogous definition may be framed for two-dimensional space, whereas for one-dimensional space the only condition is the uniform randomness. Two of uniform random and isotropic cross-sections of three-dimensional object are portrayed in Fig. 2.15(a).

Uniform random and isotropic sections are, in fact, obtained by micro-photographs or micro-images. These are subsequently used to measure the chosen parameters of the internal structures, using testing systems as sketched in Fig. 2.15(b). The position of the testing system in the section has to be

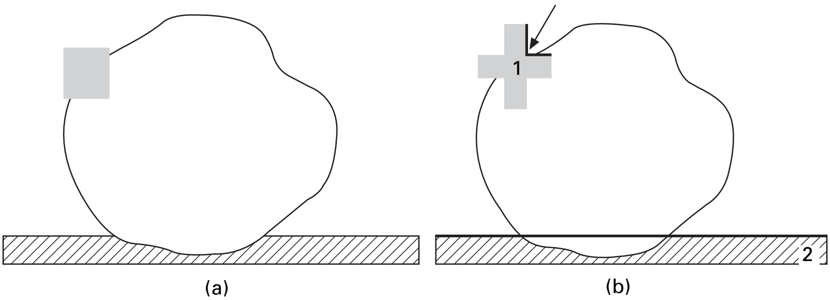

2.14 Inaccuracy of a point and a curve probe using a pencil trail, where thickness of trails hinder clarity of intersection of a point or a line with an object or its boundary, is depicted (a). The point (1) and the line probe (2) can be more sharply represented by edges of trails, as is highlighted in (b) using bold lines.

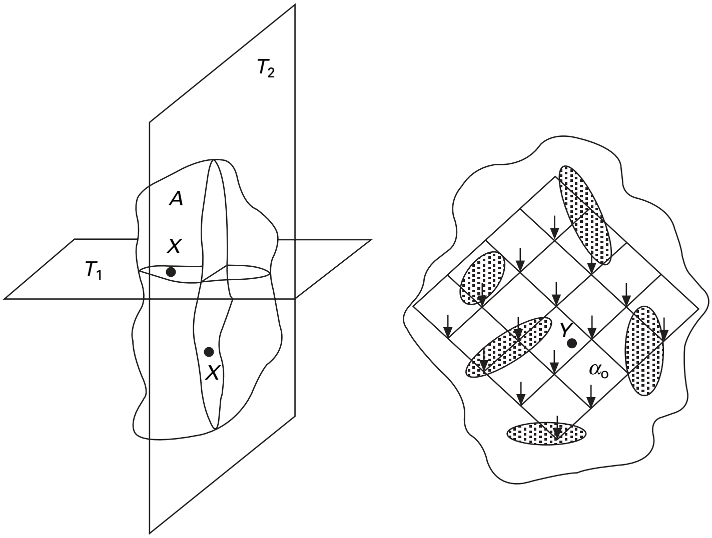

(a) (b)

2.15 Application of uniform random and isotropic sections for measurements of geometrical parameters of internal structure of the object *A*. Two such sections, $A \cap T_1$ and $A \cap T_2$, created by two plains T_1 and T_2, are depicted in (a). Cross-sections $A \cap T_i$ are used for measurements with test systems that are uniform random and isotropic in their locations on these sections. One such instance with respect to a cross-section of object *A* is shown in the part (b). Dark gray objects in (b) represent cross-sections of the inner structure of *A*.

uniform random and isotropic. Due to the translational symmetry of the test system, a point *Y*, chosen from the object section, can be displaced in a uniform random manner on a selected fundamental area, $\alpha_{0,}$ of the test system. For each new position of the point *Y*, a rotation of the testing system, with respect to the section, may be carried out simultaneously. The angular positions of the testing system must be isotropic.

In some cases, the efficacy of a stereological measurement is enhanced by integral testing systems (Jensen and Gundersen, 1982). In this chapter, integral testing systems will be used for estimating the surface areas of three-dimensional objects and the lengths of curves in three-dimensional space in Sections 2.4.2 and 2.4.3. The word 'integral' here implies the simultaneous usage of several types of probes (points, lines, figures) in a test system. An example of a fundamental region of an integral test system is shown in Fig. 2.16. A synopsis of various kinds of testing systems and their notations is included in Wiebel (1979).

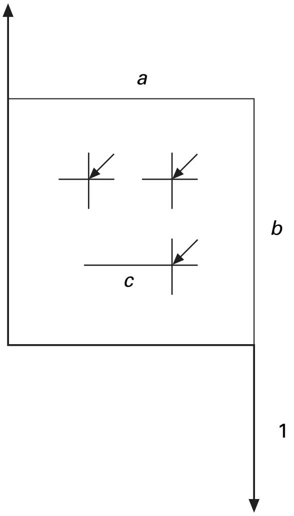

2.16 Fundamental region of an integral test system containing three point probes (arrows are pointing towards them): A curve probe of the length *c*, an excluding line (1), see Section 2.3.3, and a two-dimensional probe of oblong shape with edge lengths *a* and *b*.

2.3 Stereology of a two-dimensional fibrous mass

Here we describe selected methods for stereological measurements of two-dimensional fibrous materials. In particular, we estimate the geometrical parameters of an entire structure according to the area, length, and count of selected structural features, and define the Euler–Poincaré characteristic. Circular granulometry is introduced as a typical example of the second class of tasks for structural analysis. We will focus on one property of the individual parts of the structure, namely the distribution of particles using a typical length scale. The last example introduced in this section concerns the planar anisotropy of plain fibrous systems, which is a typical example of the third group of structure analysis problems, describing the mutual space distribution of structural features. This distribution will be represented by mutual fibre orientation, not taking into account the distances between them.

2.3.1 Point counting method for area and area density measurement

Volumes and volume densities of fibrous masses determine several of their properties, including air permeability, tensile strength and filtration efficiency. Glagolev (1933) and Thompson (1930) demonstrated that the cross-sectional area of a three-dimensional object is related to a random point counting procedure conducted on its two-dimensional section. Glagolev and Thompson worked in the field of geology. A similar method was independently introduced in biology by Chalkley (1943). Two-dimensional parameters of two-dimensional objects, the areas of figures, can be estimated using their zero-dimensional sections. The probe has to be a point or a finite set of points in a test system. For such sections, the following example shows a point counting method.

Using a two-dimensional reference region Ω and a two-dimensional object *B* that is embedded fully or partly in Ω, we will solve the question of how to estimate the area of *B* inside Ω using uniform random zero-dimensional sections. As a reference region, we can consider a microphotograph or a part of it. The situation is shown in Fig. 2.17. We start with the probability *p* that a uniform random point in Ω intersects the object *B*.

$$p = \frac{S(B)}{S(\Omega)} \qquad [2.5]$$

The area of the region Ω is here denoted as $S(\Omega)$ and the particular area of the object *B* that is embedded in the region Ω is $S(B)$. The probability *p* is expressed as the ratio of two surfaces and hence it is called a geometrical probability. Carrying out *n* measurements with the point probe we derive from Equation [2.5] $np = nS(B)/S(\Omega)$. The number of non-empty intersections, denoted as *I*, is equal to *np*. Then we obtain

$$\frac{I}{n} \cong \frac{S(B)}{S(\Omega)} \qquad [2.6]$$

Due to the finite number of trials, we only estimate the probability *p* as I/n, so the left-hand side of Equation [2.6] does not represent the exact value of *p* but a very good estimation of the fraction $S(B)/S(\Omega)$ that is equal to *p*. From Equation [2.6] we can draw two conclusions. Knowing the area $S(\Omega)$

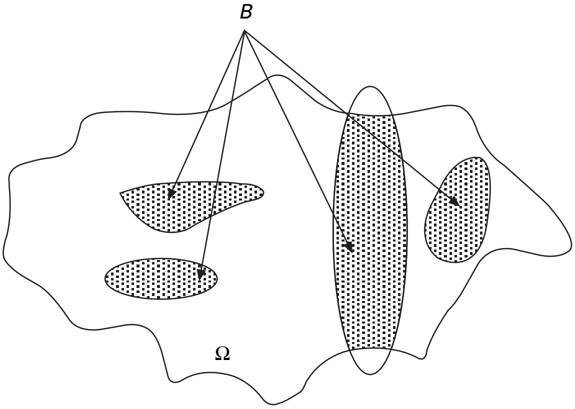

2.17 A two-dimensional space containing a region Ω, within which parts of an object *B* are embedded.

exactly, we can estimate the area $S(B)$, or we can estimate the area density $S(B)/S(\Omega)$ of the object B inside Ω directly. But first we will state the notation for estimating a feature parameter value.

We have mentioned that, for instance, p is estimated using the fraction I/n. This can be expressed as $p \cong I/n$. Without additional explanation, however, this does not tell the reader which quantities in the relationship are measured with complete or high accuracy, and which of them are estimated. Here the estimated quantity is p while I and n are measured accurately. To underline these facts, we write $[p] = I/n$ which we understand as – p is estimated as the fraction of known values I and n, and the symbol $[p]$ denotes the estimator of p.

Let us return to Equation [2.6]. If we know exactly the area of the reference region Ω, which is, as a rule, the area of our micro-photograph or monitor screen, we can express from Equation [2.6] the estimator $[S(B)]$ of the area $S(B)$ inside Ω as:

$$[S(B)] = \frac{I}{n} S\{\Omega) \qquad [2.7]$$

When our interest is focused on the B area density $S(B)/S(\Omega)$ inside region Ω, we can state from Equation [2.6] its estimator in the following form:

$$\frac{[S(B)]}{[S(\Omega)]} = \frac{I}{n} \qquad [2.8]$$

We have written the left-hand side of Equation [2.8] in the form $[S(B)]/[S(\Omega)]$ rather than $[S(B)/S(\Omega)]$ because $S(B)$ is in fact estimated with I and $S(\Omega)$ is estimated using n. The measurement procedure can be improved using a test system with zero-dimensional probes. When we wish to estimate the total area of B inside the region Ω, or the area density of B within Ω, we have to cover Ω with the test system as sketched in Fig. 2.18. The number of hits I on the figure B by test system point probes is equal to 4 in this example. These hits are denoted using empty squares. The total number n of point probes falling into Ω is 14 in this case, and these hits are marked either by empty squares or by black circles. The situation in Fig. 2.18 leads to the approximate value of the area density $[S(B)]/[S(\Omega)] = 0.286$, a poor estimate from only one particular position of the test system. We can enhance the accuracy of our measurement significantly by increasing the number of uniform random and isotropic trials.

The point counting method for estimating area and area density of figures in the reference region is in fact a direct extension of the well-known method based on square grids and counting the number of squares that are fully contained within B, as shown in Fig. 2.19. However, this method is less accurate than the point counting method. Increasing the accuracy of the grid method by measuring squares that are only partly contained in B is more laborious than using the Glagolev and Thompson point counting method.

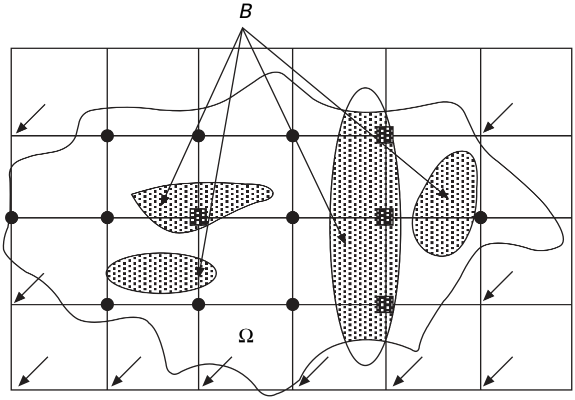

2.18 A test system having one point probe at left bottom corner of each of its fundamental regions (indicated by arrows), covering the region Ω completely with embedded objects, *B*. Hits of probes with *B* are denoted with squares and residual probes in Ω are encircled in black. A very rough estimation of area density of *B* in Ω may be calculated here as $[S(B)]/[S(\Omega)] = 4/14 = 0.286$.

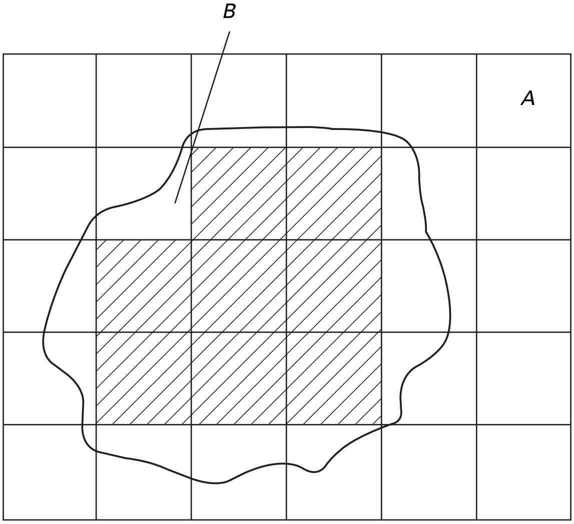

2.19 A simple estimation of area covered by *B* using a square grid and counting the areas of fundamental squares fully embedded in *B*. If the area of a grid cell is *A*, then *S*(*B*) stands for the particular case shown in the figure, having an estimated value of 8*A*.

2.3.2 Buffon's needle and curve length estimation

A thorough investigation of a fibrous mass often requires information about total fibre length or fibre length density. The influence of fibre length and fibre distribution on the strength of fibres in yarns, and the relation between cross-sectional counts of fibres and their length, have been investigated by Zeidman and Sawhney (2002). This subsection examines how to estimate the length $L(C)$ of one-dimensional linear features, i.e. curves, embedded into two-dimensional space, or into a plane. It will be shown, based on Buffon's needle problem, that $[L(C)] = (\pi/2)dI$, where d is the distance between equidistantly spaced parallels and I is the number of intersections between the curve and the system of parallels.

Buffon's needle, as described in Section 2.1, identifies the probability p with which a uniform random and isotropic abscissa j, the so-called Buffon's needle, of length $L(j)$, touches the warp of equidistant parallels under the condition that the needle falls on it and nowhere else. The relation $L(j) < d$ ensures, at maximum, one hit for each trial. Figure 2.20 shows this in more detail. If the mutual orientation of the needle and the warp is fixed, this suggests that the needle is uniformly random, but anisotropic. We initially select its orientation perpendicular to the warp lines. The probability P of the anisotropic needle hitting one of the parallel lines is given as the fraction $L(j)/d$, which follows from the concept of geometrical probability given as the ratio of the areas of two point sets. The first set is composed of the locations of a chosen fixed point on the needle for all possible trials when the needle hits the warp, and the second consists of the area of the point set created by all locations of the same selected point on the needle for all possible trials. Thanks to the warp periodicity, we can restrict our attention to the region between two pairs of neighbouring parallel warp lines, so we consider nothing outside such bands. Both bands are parallel with the warp lines. The first has width equal to the needle length $L(j)$ and the latter has the width d that fills the entire space between neighbouring parallel lines. The lengths of both bands can be taken as equal, so we only need to take the widths into account. With the aid of Fig. 2.20 we can conclude that $P = L(j)/d$.

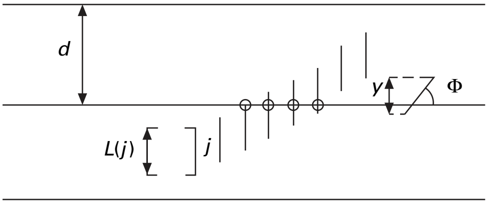

2.20 Buffon's needles are anisotropically distributed and are all perpendicular to the parallel warp lines. The distance between parallels is *d* and the Buffon's needle length is *L*(*j*). A hit of a needle with one of the warp lines is denoted by a small circle. The probability of the hit is evaluated from the ratio *L*(*j*)/*d*. On the right part of the figure is depicted a declined needle that makes an angle *θ* with parallels. Its projection on the normal to the warp lines is *y*.

Repeating the process for a needle with some chosen fixed angle θ to the parallel warp lines, as shown in Fig. 2.20, instead of the needle's length, we will be concerned with its parallel projection y on the direction perpendicular to the straight lines that make up the warp. For $y = L(j) \sin(\theta)$ we can write the probability P_θ of hits by the angled needle as:

$$P_\theta = \frac{y}{d} = \frac{L(j)\sin(\theta)}{d} \qquad [2.9]$$

The last step in solving Buffon's needle problem is to consider isotropic orientations of a uniform random needle. Here we need to calculate the average value for $L(j) \sin(\theta)/d$, where $L(j)$ and d are constants. Using the well-known formula for the mean value $\bar{f}_{<a,b>}$ of a function $f(x)$ on an interval $< a, b >$ written as $\bar{f}_{<a,b>} = \frac{1}{b-a}\int_a^b f(x)dx$, we obtain the final relation for the probability of hits of a uniform random and parallel needle as:

$$p = \frac{L(j)}{\pi d}\int_0^\pi \sin\theta d\theta = \frac{L(j)}{\pi d}[-\cos\theta]_0^\pi = \frac{2L(j)}{\pi d} \qquad [2.10]$$

where $b - a = \pi - 0 = \pi$ is the length of the interval in question.

Before we extend Buffon's problem to the estimation of curve length in a plane, let us look at the formula for the mean value of a function on an interval. We have introduced geometrical probability as a generally accepted approach and now we can describe the geometrical interpretation of the mean value of a function. Imagine a very thin aquarium containing fine sand. We will arrange the sand into the shape of $\sin\theta$ on the interval $< 0, \pi >$. The volume of the sand pile is proportional to $\int_0^\pi \sin\theta d\theta$ (see Fig. 2.21). Tapping the aquarium gently will produce a flat block of sand from the previously sinusoidal heap. We have destroyed our original curve but the height of the sand in the aquarium is now equal to the average value of the function in question and, moreover, the volume of sand (which is conserved) is now easily expressed as $\pi\bar{f}_{<a,b>}$. Equilibrating both formulae for the volume of the sand, we obtain a formula from which the average function value $\bar{f}_{<a,b>}$ on the interval $< 0, \pi>$ can be easily derived as $\pi\bar{f}_{<a,\pi>} = \int_0^\pi \sin\theta d\theta$.

We will now investigate a curve in a plane of total length $L(C)$. Imagine the curve is divided into very short straight segments of equal length; these segments can be taken as Buffon's needles with uniform lengths $L(j)$. Unlike previous discussions of the Buffon's needle problem, here j denotes the j-th piece from the total number of n linear pieces composing the curve. Length

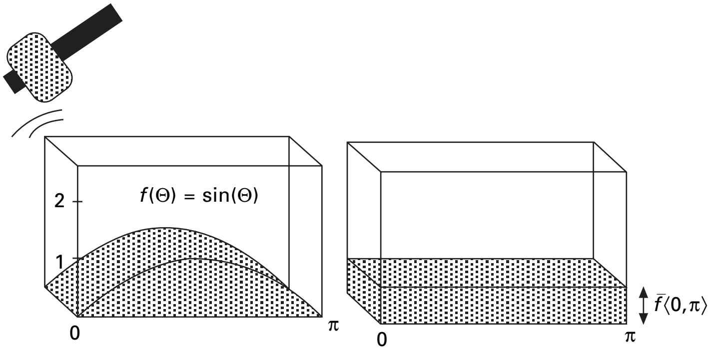

2.21 A sinusoidal sand pile in a narrow aquarium is streamed using a gentle percussion to create a flat block. The sand volume is conserved during the motion.

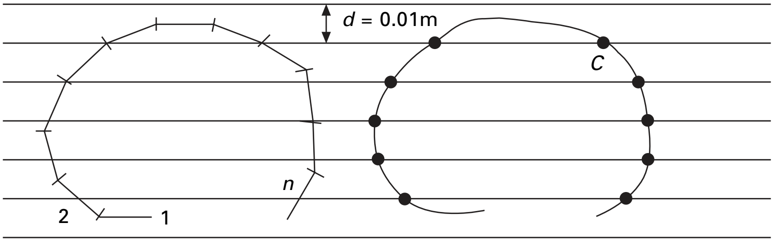

2.22 A curve *C* is approximated using a set of straight pieces. Their lengths are assumed nearly equal. The number of hits *I* of the curve *C* and the warp lines in this case is 10. Hence a rough estimation of the curve length *L*(*C*) from a single trial is *πd*10/2, as given by Equation [2.11].

$L(j)$ is shorter than the distance d between parallel straight lines. The warp now represents our test system. We overlap the curve with this test system as shown in Fig. 2.22. As the curve is composed of n Buffon's needles, it means $nL(j) = L(C)$, and the number of hits I of the curve in the uniform random and isotropic system of parallels will be equal to the n-multiple of the probability p in Equation [2.10]:

$$I = n[p] = n\frac{2[L(j)]}{\pi d} = \frac{2[L(C)]}{\pi d} \qquad [2.11]$$

The only measurement done with the curve overlapping the test system provides us with a very pure estimation of $L(C)$ from a single trial. The derivation of the formula [2.10] for p was based on uniform random and isotropic needles, so we have to carry out a lot of measurements to ensure this condition by rotating and shifting the warp and by counting and averaging all the hits. These experiments provide us with a more exact estimation of

$[L(C)]$. From Equation [2.11], the final formula for curve length estimation in two-dimensional space can be easily derived as:

$$[L(C)] = \frac{\pi d\bar{I}}{2} \qquad [2.12]$$

where $\bar{I}$ is the average number of hits per single measurement calculated from numerous uniform random and isotropic trials of test system position with respect to a curve.

The equidistant and parallel system of lines represents a lattice of fundamental regions, each of them being oblong in shape as the lines are restricted to a plane. The area of a particular oblong between neighbouring parallels represents a fundamental region. In each fundamental region, there is only one piece of a line as a probe, represented by one of the parallels.

2.3.3 Feature count in two-dimensional space and the Euler–Poincaré characteristic

Feature count is useful for instance in identifying an economic wool fibre where scale frequency plays an important role, as shown by Wortham *et al.* (2003). The count of fuzz and pill formation on knitted samples as a function of enzyme dose for treatment has been investigated by Jensen and Carstensen (2002) and is another example of the importance of feature count techniques for fibrous materials. Before we discuss the stereological method for estimating feature count in two-dimensional space, we will describe the Euler–Poincaré characteristic $\nu(A)$. This characteristic is the functional that evaluates the connectivity of compact sets, which is why it can also be used for convex ring sets. The connectivity of a set A can be defined in various ways that reflect an intuitive view. We will use an approach similar to that described by DeHoff and Rhines (1968), Wiebel (1979) and Saxl (1989), aiming at a visual and rigorous introduction of the Euler–Poincaré characteristic. We take the position that a set composed of two disjoined cubes has the same value of connectivity as another set consisting of two disjoined spheres. In addition, we note that connectivity does not depend on the size of the bodies involved. On the contrary, it depends on the numbers of holes and cavities in the bodies and on their nature, which is consistent with the number of isolated parts of the body boundaries. We distinguish between open holes, for example a hole created by a perforation of a sphere, and a closed cavity, which results in the sphere having a boundary composed of two isolated parts.

The degree of connectivity depends on the behaviour of a body with respect to a section. If we draw a curve that lies in a plane on the body's surface, then we can extract the part of the body that lies within this plane and is restricted by the curve on the boundary. A sphere without holes or a sphere with a closed cavity are both broken up by such a section. A sphere with an open hole only breaks in some cases, and is hence the more connected set. These situations are sketched schematically in Fig. 2.23. The numerical value of the Euler–Poincaré characteristic ν depends also on the dimension of the set.

Generalising the above leads us to the following rules for the determination of Euler–Poincaré characteristic values:

(i) For a one-dimensional set A composed of N isolated curves, $\nu(A) = N$.
(ii) The two-dimensional set B consisting of N isolated parts with total number of N' cavities (in two-dimensional space cavities are always closed) has the Euler–Poincaré value $\nu(B) = N - N'$.
(iii) For the three-dimensional set C of N isolated parts with the total number of N'' open holes and N' closed cavities, $\nu(C) = N + N' - N''$.

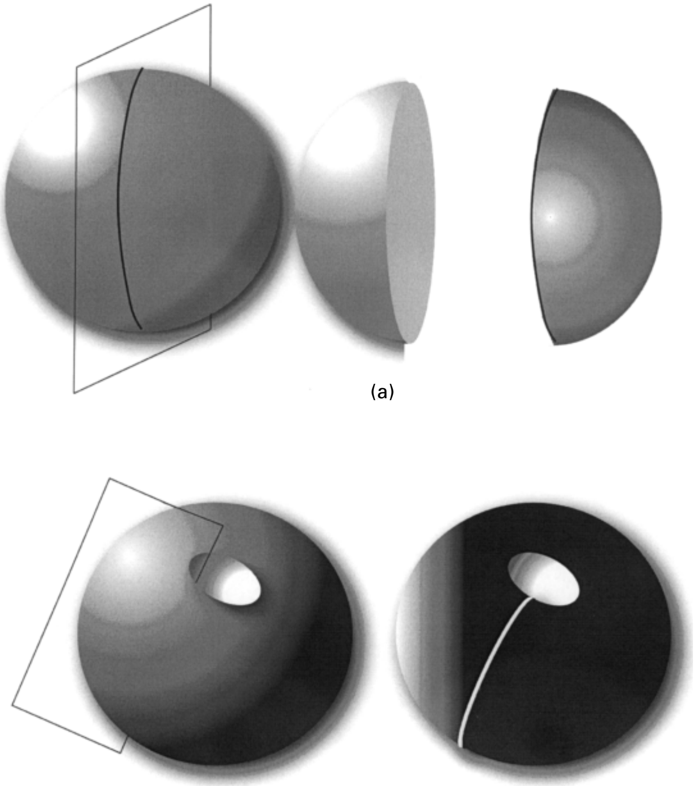
(a)

(b)

2.23 The sphere without an open hole detaches into two parts after each cutting, followed by withdrawal of the sphere part lying within this section and restricted by its planar curve on the spherical surface (a). The sphere with an open hole does not disintegrate after such cutting (b).

This gives us the result that, for a circle with a cavity and for a sphere with an open hole, $\nu = 0$. An arbitrary single body or figure without holes or cavities has a Euler–Poincaré characteristic equal to one, which is why the Euler–Poincaré characteristic is identical to the feature count for objects without any holes. The connectivity of a sphere with a closed cavity is evaluated as $\nu = 2$.

Saxl (1989) introduces the Euler–Poincaré characteristic by having the boundary of a half space in such a position that the origin of the coordinate system lies within it, and the investigated structure *A* lies fully in the right-hand of the half space as drawn in Fig. 2.24. The boundary is swept from the left to the right side along the perpendicular axis. The boundary is plane in three-dimensional space, a line in two-dimensional space and a point in one-dimensional space. We count the values of the left-hand side limit

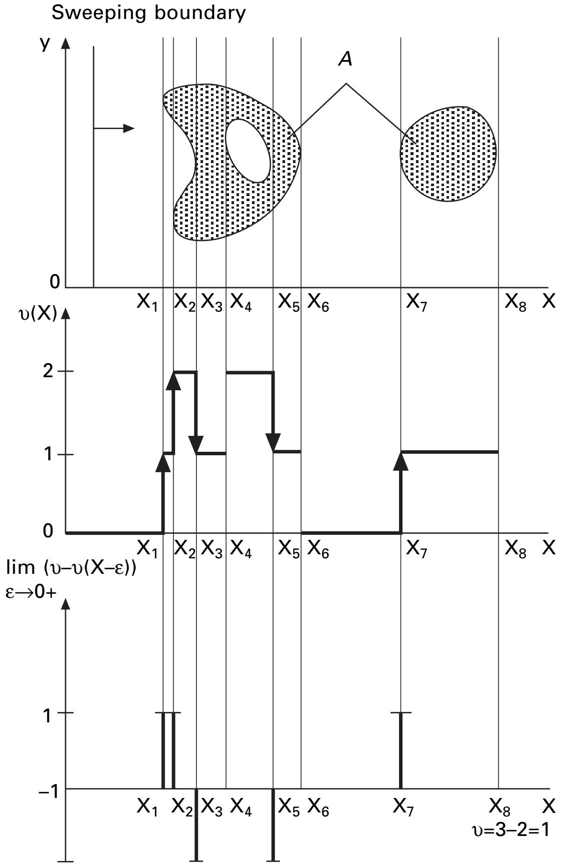

2.24 Euler–Poincaré characteristics as introduced by Serra (1976) and Saxl (1989). The Euler–Poincaré characteristic value of the object *A* is equal to 1.

$\lim_{\varepsilon \to 0+} (\nu(x) - \nu(x - \varepsilon))$ composed of the subtraction of the Euler–Poincaré characteristic values of the induced structure in sections of the moving boundary with the investigated structure, in cases where the limit values are non-zero. The subsequent stages of this method are shown in Fig. 2.24.

Now to discuss the problems of counting features notwithstanding the number and the nature of the holes they contain. To estimate features in a selected area of a two-dimensional structure, we use a test system with the so-called excluding line introduced by Gundersen *et al.* (1988). A probe A in this system is two-dimensional and as a rule it has an oblong shape. Its area will be denoted here as $S(A)$. The excluding line is an infinite straight line running along a portion of the boundary of probe A which changes direction twice. The excluding line falls particularly on two neighbouring sides of the oblong A. The mutual position of probe A and the excluding line is shown in Fig. 2.25. This probe is inserted into a lattice of fundamental regions to create a test system. The estimation of the feature count N_A in a certain area of the object is conducted according to the following procedure:

- (i) Count all figures (i.e. all isolated parts of the object) that have non-empty intersections with a chosen probe A and at the same time have no hits with the excluding line. Their count is denoted as Q.
- (ii) Repeat this measurement for each probe in the test system and for all its uniform random and isotropic positions with respect to the fixed object.

The estimation of the total count of features N in the reference region Ω is then:

$$[N] = \frac{QS(\Omega)}{S(A)} \qquad [2.13]$$

where Q is the feature count per probe of area $S(A)$ and $S(\Omega)$ is the area of the reference region.

The estimator of the feature count area density $[N]/[S(\Omega)]$ in the object is simply:

$$\frac{[N]}{[S(\Omega)]} = \frac{Q}{S(A)} \qquad [2.14]$$

The estimation accuracy increases with the number of uniform random and isotropic trials conducted in different test system positions.

2.3.4 Linear characteristics of convex ring sets and circular granulometry

For many practical applications, it is valuable to introduce a numerical linear parameter that estimates the representative size of structural features. For

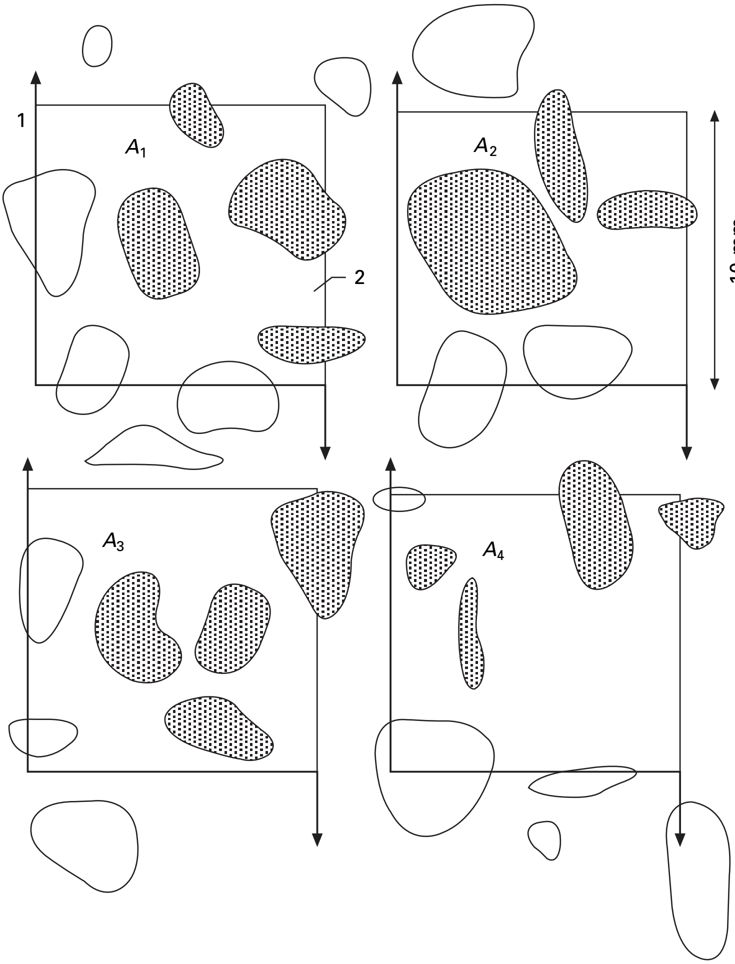

2.25 Test system for estimation of particle numbers: The grey particles are counted exclusively. The residual ones either hit the excluding lines or have no intersection with fundamental regions and are not counted, according to the counting procedure. Excluding lines are in bold (1). Two-dimensional probes (2) are arranged in a lattice of fundamental regions. The rough estimation of the feature count density $[N]/[S(\Omega)]$ from this particular trial comes out to be $Q/S = 15/(4S(A))$, where $S = \sum S(A_i) = 4S(A)$ is the area of all the oblong probes used for the purpose.

example, Neckar and Sayed (2003) described pores between fibres in general fibre assemblies with particular focus on their linear characteristics, such as pore dimension, perimeter and length. Pore length and radius were used by Miller and Schwartz (2001) as critical parameters for a forced flow percolation model of liquid penetration into samples of fibrous materials. Lukas *et al.*

(1993a) compared the breadth and diameter of maximal pores in thin non-woven fabric with their radius values measured using the bubble counting method. Cotton fibre width and its distribution using image analysis was measured by Huang and Xu (2002). Farer *et al.* (2002) studied fibre diameter distribution in melt-blown non-woven webs. Brenton and Hallos (1998) investigated the size distribution, morphology, and composition of dust particles gathered from the vicinity of various commonly performed processes in industrial wool fibre preparation. Here we discuss the estimation of breadth w, diameter d and width t of structural features, and then introduce the effective method for estimating diameter known as circular granulometry.

Consider an n-dimensional body A, part of a convex ring, and an arbitrary direction $\vec{u}$ as is sketched in Fig. 2.26. The support plane is taken as that which creates the boundary of the 'smallest' half space that contains the body A in the direction $\vec{u}$, hence it touches A. Since this half-space unfolds from the support plane in the direction $\vec{u}$, there is no part of A in the residual half-space. For each support plane perpendicular to the chosen direction $\vec{u}$, there is a parallel twin for the opposite direction $-\vec{u}$. We will denote the distance between the two support planes as the breadth $w(A, \vec{u})$ of a body A in the direction $\vec{u}$, and consequently also in the direction $-\vec{u}$. The isotropic average of breadths $w(A, \vec{u})$ is denoted as $\overline{w}(A, \vec{u})$, where all $\vec{u}$ directions have the same weight.

$$w(A) = \overline{w}(A, \vec{u}) \qquad [2.15]$$

The maximum breadth value is diameter $d(A)$ and the minimum is width $t(A)$. Extending this to $n < 3$ dimensions is straightforward.

As an example, we will calculate the average breadth $\overline{w}(S)$ of the square S with side length a (see Fig. 2.27). For the breadth w of square S we have:

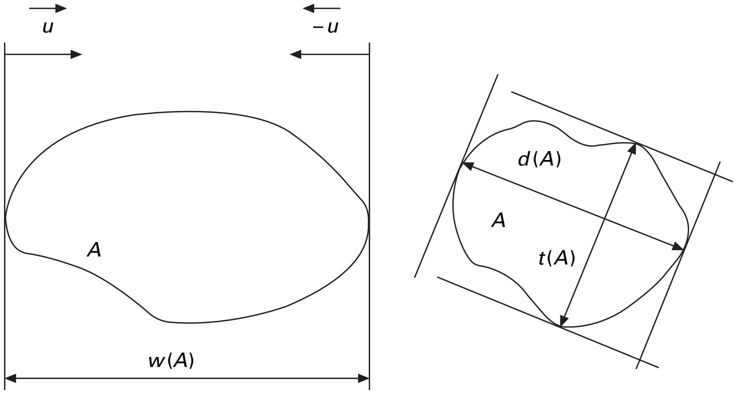

2.26 Linear characteristics of a set A of a convex ring having breadth $w(A)$, width $t(A)$, and diameter $d(A)$. Supporting planes are perpendicular to $\vec{u}$ and $-\vec{u}$.

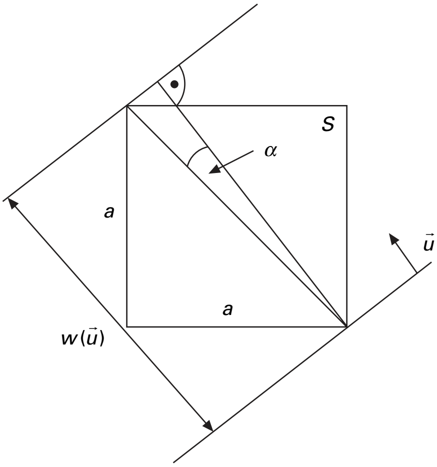

2.27 The breadth $w(S, \vec{u})$ of a square *S*.

$$w(S, \vec{u}) = a\sqrt{2}\cos\alpha \qquad [2.16]$$

Taking periodicity into account, we will consider only $\pi/2$ rotations of the twin support lines with respect to the square. The isotropic average value of $w(S, \vec{u})$ in the interval of $\vec{u}$ directions $< 0, \pi/2 >$ is:

$$w(S) = \frac{2}{\pi}\int_{-\pi/4}^{\pi/4} a\sqrt{2}\cos\alpha d\alpha = \frac{2\sqrt{2}a}{\pi}[\sin\alpha]_{-\pi/4}^{\pi/4}$$

$$= \frac{2\sqrt{2}a}{\pi}\frac{2}{\sqrt{2}} = \frac{4a}{\pi} \qquad [2.17]$$

Noting the above relationship between square *S* perimeter $O(S) = 4a$ and its average breadth $w(S)$, then for a square, $O(S) = \pi\, w(S)$. The same relation holds for a circle *C* with perimeter $O(C) = 2\pi r$ and with average breadth $w(C) = 2r$. The general relation:

$$O(B_2) = \pi w(B_2) \qquad [2.18]$$

is valid for all two-dimensional convex sets B_2; hence their average breadths are commonly calculated from their perimeters.

Circular granulometry is a simple method for estimating diameter *d* in the distribution of two-dimensional particles or projections of three-dimensional ones. The method is based on a special type of test system consisting of circles of various diameters. Stereotypes of circles are commonly used, with diameters expanding equidistantly in steps of one millimetre. Then we select at random a particle from the magnified image and assign to it the smallest circle that can fully contain that particle. We count the numbers of particles assigned to circles of various diameters and we plot their total relative counts

p_d as a histogram that estimates the probability densities or probability distribution function. The probability density histogram expresses the appearance of the particle diameter in the interval ($d_i - \Delta d$, d_i), where Δd is the incremental step used for the construction of the circle stereotypes. An example of circular granulometry analysis is indicated in Fig. 2.28.

2.3.5 Analysis of planar anisotropy of two-dimensional fibrous structures

Fibrous materials often present as thin, nearly planar fibrous systems; for instance thin webs, sheets, some yarn tangles, woven and knitted textiles,

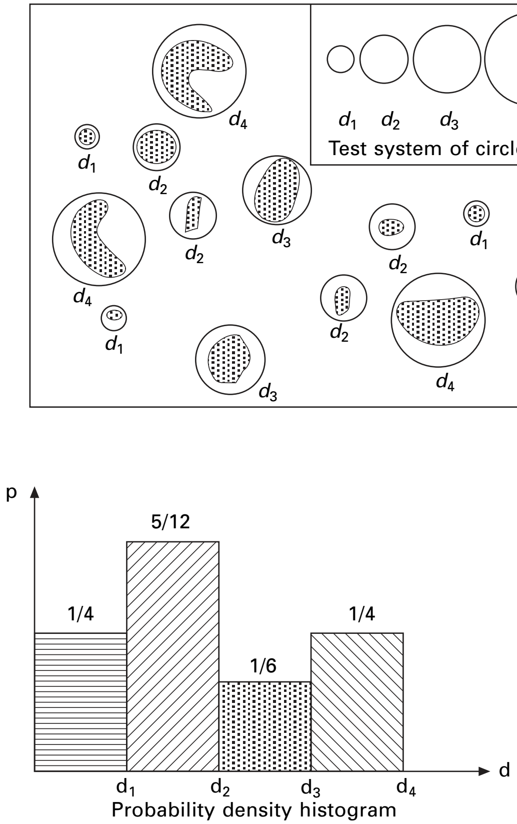

2.28 Circular granulometry: To randomly chosen particles of an investigated structure are assigned the smallest circles from the test system that can circumscribe the chosen particles completely. The special test system, represented here by stereotypes of circles with various diameters, is shown in the right upper corner. The histogram relates the frequencies of estimated particle diameters with the diameters.

and vessels in bladders. Planar fibre systems can also be projections of three-dimensional fibrous materials. The intensity of light scattering and its distribution in non-woven fabric as a function of fibre mass arrangement in space has been studied by Zhou *et al.* (2003). Pourdeyhimi and Kim (2002) outlined the theory and application of the Hough transform (Hough, 1962) in determining fibre orientation distribution in a series of simulated and real non-woven fabrics. Farer and colleagues (2002) studied fibre orientation in melt-blown non-woven webs. A general model of directional probability in homogeneous, anisotropic non-woven structures was presented by Mao and Russel (2000), in which fibre diameter, porosity and particularly fibre-orientation distribution were considered as structural parameters. A method for non-destructive fibre tracing in a three-dimensional fibre mass using X-ray microphotography was developed by Eberhardt and Clarke (2002). Karkkainen and colleagues (2002) developed stereological formulae based on the scaled variation of grey shades in digital images of fibrous materials to estimate the rose of directions. Thin fibrous systems can also be modelled and analysed using established theory of fibre processes, as is described thoroughly in Stoyan *et al.* (1995).

In this section, we describe the simple graphical method for evaluating planar fibre mass anisotropy introduced by Rataj and Saxl (1988), beginning with a discussion of planar anisotropy.

Imagine a curve or a thread of total length L fully embedded in a plane thanks to its negligibly small diameter. It is understood for anisotropy that equal angle intervals (β_i, $\beta_i + \Delta\beta$) do not contain equal lengths of thread elements pointing to the corresponding directions (see Fig. 2.29). A parameter of anisotropy is therefore the angular density of the thread $f(\beta)$ governing

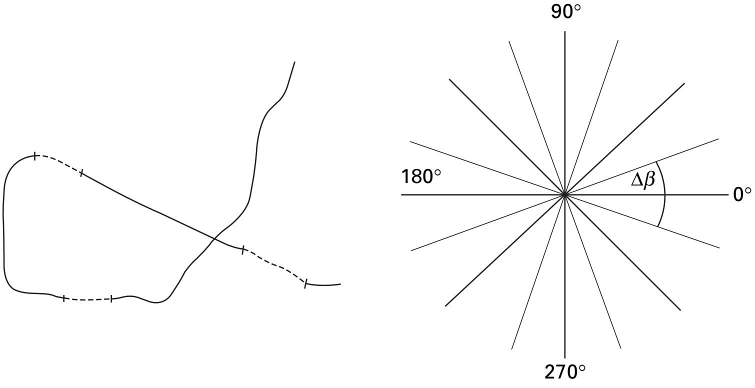

2.29 The left-hand side of the figure represents a thread of a total length *L*. The broken segments of the thread have an orientation within an angular interval ($-\Delta\beta$, $+\Delta\beta$) of an equidistant net of angles as shown on the right-hand side.

the particular length of the thread $L(\beta, \beta + \Delta\beta)$ leading up to the interval $(\beta, \beta + \Delta\beta)$:

$$L(\beta, \beta + \Delta\beta) = L \int_{\beta}^{\beta+\Delta\beta} f(\beta)\,d\beta \qquad [2.19]$$

where L is the total thread length. The density function $f(\beta)$ is known as the rose of directions or the texture function.

There are additional experimental methods that enable us to estimate the rose of directions $f(\beta)$. The direct method, as indicated in Fig. 2.29, was described by Sodomka (1981). According to this procedure, we first identify the part of the thread with the highest curvature. Inside this part, we demarcate a piece of the thread for which tangent directions vary within the interval $\pm \frac{1}{2}\Delta\beta$. The remaining part of the thread is then divided into elements of equal length, this length being determined by the length of the section in the most curved part of the thread. Each such thread element will be counted to a corresponding angular interval $(\beta_\iota, \beta_\iota + \Delta\beta)$. The fractions N_β/N, where N_β are the counts inside the interval $(\beta_\iota, \beta_\iota + \Delta\beta)$ and N is the total number of counts, give the estimations for values of the rose of directions.

It is clear that experimental implementation of this procedure would be laborious and time-consuming. Its advantage, however, is the clarity with which it helps us introduce the notion of the rose of directions. More effective methods for estimating fibrous planar anisotropy are based on measuring a rose of intersections (Rataj and Saxl, 1988). The rose of intersections is obtained using the method shown in Fig. 2.30(a, b) and in Table 2.3. The rose of directions is constructed from rose of intersection data by a simple graphical construction using a Steiner compact in the following five steps:

(i) Place a net of angles drawn on a transparent foil over the structure being studied, or a computer-aided net over the image on a monitor screen. An example of such a net is shown in Fig. 2.30(a). The net consists of arms of equal length that intersect each other at their central points, and the number of arms has to be equal to or smaller than 18, otherwise the method does not produce sufficiently stable, or reproducible, results. The angular distance among all arms is equal to π divided by the number of arms. The example in Fig. 2.30(a) has four arms with the angular distance $\pi/4$.

(ii) Count the intersections of the fibrous features with each arm separately, as shown in Fig. 2.30(b). Repeat this measurement in uniform randomly chosen parts of the fibrous structure, keeping the orientation of the angular net strictly fixed. Take the direction of a line in the object and its images and denote it as direction 0°. One of the arms of the net of angles must then be parallel with this line for each measurement. Put together the total number of intersections for each arm into a table such

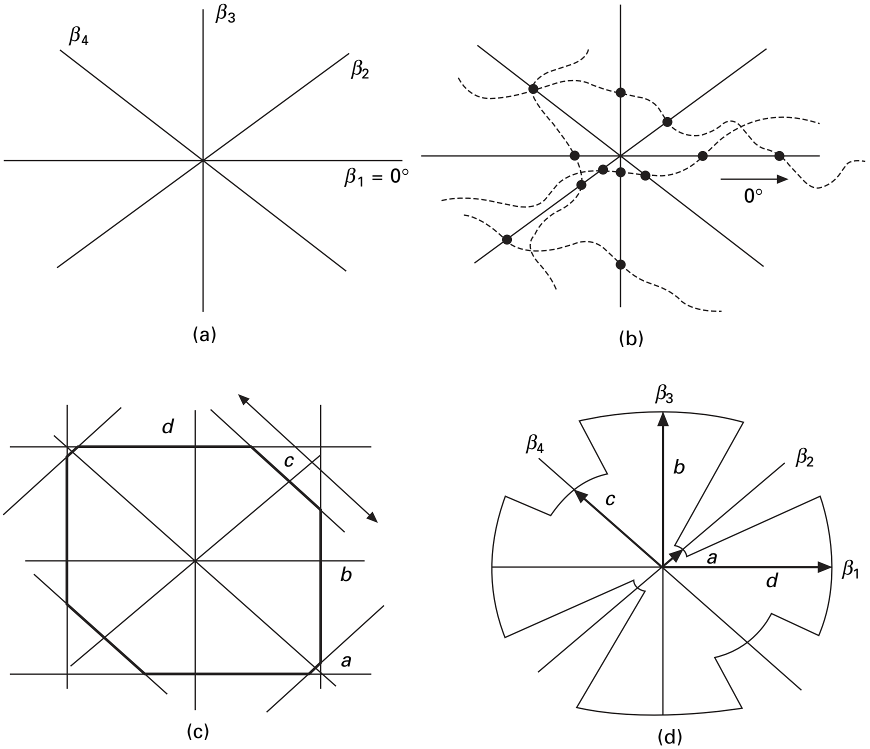

2.30 Construction of a rose of directions using a simple graphical method: A net of angles is composed of equal arm lengths (a); intersections of a net of angles with a planar fibrous structure and a chosen direction in it (b); Steiner compact of side lengths *a*, *b*, *c*, *d* with arrow pointing towards β_i, belonging to the side *c* (c); a rose of directions (d).

Table 2.3 The values of the rose of intersections for the fibrous system as depicted in Fig. 2.30(b). The last column of the figure contains values of this rose after rotation by $\pi/2$, used for construction of the Steiner compact in Fig. 2.30(c)

Angle	Rose of intersections values	$\pi/2$ rotated values
0°	3	3
45°	4	3
90°	3	3
135°	3	4

as Table 2.3. The intersection count data can then be expressed graphically in a polar diagram, known as the rose of intersections. Rotate the rose of intersections by the angle $\pi/2$ clockwise or anticlockwise or shift values in the table. The fibres are not orientated up or down, so it is not important to distinguish between those fibre segments that point in direction β or $\beta + \pi$. Hence the angular density $f(\beta)$ is the periodic function with the period π. Clockwise and anticlockwise rotations of the rose of intersections differ by $\pi/2 + \pi/2 = \pi$, and this periodicity provides us with the same information about $f(\beta)$.

(iii) Plot the count number from the rotated rose of intersection data into a polar diagram, using an appropriate scale, to obtain the $\pi/2$ rotated geometrical interpretation of a rose of intersections.

(iv) Raise verticals from each point of the $\pi/2$ rotated rose of intersections to obtain a polygon restricted to containing the origin of the polar diagram. This polygon must be convex and centrally symmetric, and is known as the Steiner compact (see Fig. 2.30(c)). The distance between neighbouring vertices, i.e. the Steiner compact side length, is the estimation of the angular density $f(\beta_i)$ of the rose of directions value for a direction identical to the direction of the side in question. Hence, using the length of the side pointing in the direction β_i we can estimate the angular density $f(\beta_i)$ within the interval $\beta_i \pm 1/2 \cdot \Delta\beta$.

(v) Construct arcs with their centres in the polar graph to finish the rose of directions. Each arm of these arcs is proportional to the length of the corresponding side of the Steiner compact. Similarly, like the Steiner compact, the rose of directions must also be centrally symmetric. The resultant rose of directions for our example is depicted in Fig. 2.30(d). To normalise the construction, we have used a scale where the total length value of the arms of the rose of directions is equal to 1.

Figure 2.31 shows us various simple planar curve systems, a regular square grid, a grid of rectangles and a system of circles. Each grid is shown with its rose of directions. The reader is invited to estimate them using the simple graphical method described above. We should point out that, for each measurement, the net of angles must be fully embedded into the fibrous system. The reader will probably observe some nearly negligible angular density values estimated for directions that are not present in the system. That is the cost paid for the method's simplicity.

2.4 Stereology of a three-dimensional fibrous mass

Adding a dimension helps us to fully appreciate the power of using stereological methods to estimate three-dimensional parameters of features from measurements of their two- and lower dimensional sections. Here, we introduce methods for estimating volumes, surfaces, lengths and their densities in three-dimensional reference regions. We then describe methods for estimating average curvature and torsion of fibrous materials in three-dimensional space. Finally we discuss feature counts.

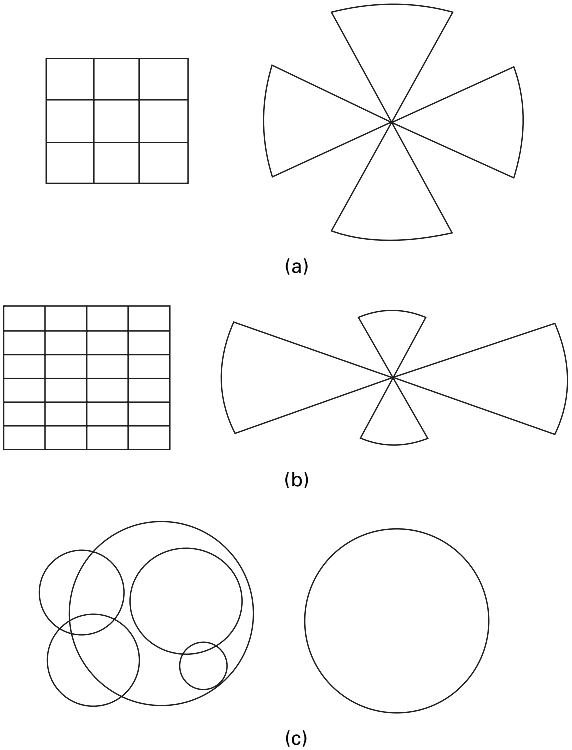

2.31 Roses of directions belonging to various fibre structures: a regular square grid (a); a rectangular frame (b); a system of circles (c).

2.4.1 Estimation of volume and volume density

To illustrate the importance of volume estimations, we refer to the fact that pore volume or pore volume density are critical parameters in the air permeability of fibrous materials, as has been shown for instance by Mohammadi *et al.* (2002). Fibre bulk density heavily influences the compressibility of fibrous materials, as shown by Taylor and Pollet (2002) or in classic work on this topic by Van Wyck (1964). The porosity of a fabric and the volume fraction of fibres were considered critical parameters for coupled heat and liquid moisture transfer in porous textiles by Li and colleagues (2002). The point counting method introduced by Glagolev and Thompson to estimate the areas of figures was actually aimed at ultimately estimating volumes, and we will now extend the results discussed above to three-dimensional space in order to estimate volumes and volume densities of real fibrous objects.

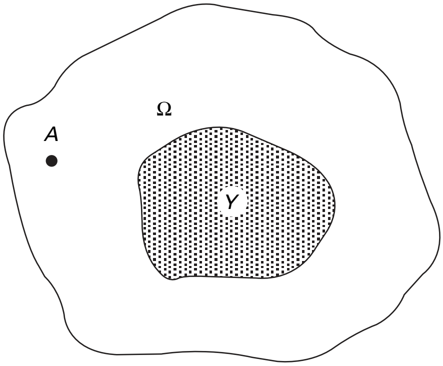

2.32 In a reference region is embedded a three-dimensional object *Y*. A point *A* represents a zero-dimensional section in the region Ω that does not strike the object *Y*.

Imagine a three-dimensional reference region Ω and an object Y embedded in it, as shown in Fig. 2.32. The conditional probability p with which a uniform random point A in Ω has a non-empty intersection with the object Y is given by the relation:

$$p = \frac{V(Y)}{V(\Omega)} \qquad [2.20]$$

where $V(\Omega)$ is the volume of the reference region Ω and $V(Y)$ is the volume of the object Y to be estimated. The geometrical probability p of the hit is equal to the fraction of the aforementioned volumes $V(Y)/V(\Omega)$. When we carry out n measurements with the uniform random point in the three-dimensional region Ω, it will hit the object I times, where I is close to the product pn; in other words I/n estimates p. Hence, by knowing the volume $V(\Omega)$ with sufficient accuracy, we can express the estimation of the volume $[V(Y)]$ of the object Y as:

$$[V(Y)] = \frac{I}{n} V(\Omega) \qquad [2.21]$$

The volume fraction is hence estimated by:

$$\frac{[V(Y)]}{[V(\Omega)]} = \frac{I}{n} \qquad [2.22]$$

To improve the efficiency of three-dimensional volume and volume fraction measurements, as a rule we use uniform random two-dimensional sections on which we carry out zero-dimensional sections, i.e. point hit trials, using test systems. This procedure is indicated in Fig. 2.33 for a single measurement. To enhance the accuracy of our measurements, we have to take further two-

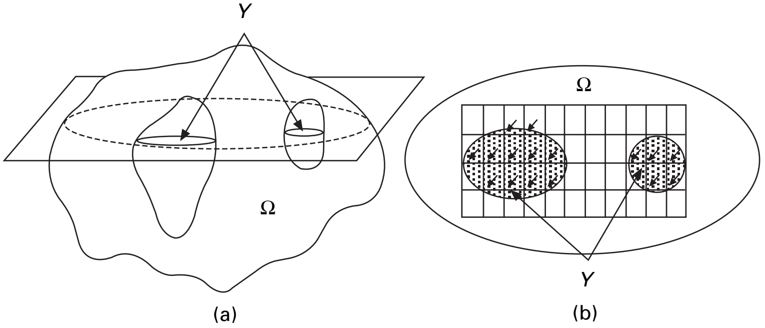

2.33 A two-dimensional section of a reference region Ω with embedded objects, *Y* (a), consists of two parts of the two-dimensional section (b). The cross-section is overlapped with a test system containing zero-dimensional probes at the bottom right-hand corner of the fundamental zones, as highlighted by arrows. The total number, *N*, of probes in the test system is 44 and the number of hits with *Y* as *I* = 16. The volume density can be roughly estimated as $[V(Y)/V(\Omega)]$ to be $I/n = 16/44 = 0.364$ from this measurement.

dimensional sections of the body and apply more trials on them using the test system. All trials must be uniform, random and isotropic.

Measurements of volume density correspond with a fundamental principle of stereology that was proved long before this mathematical discipline was established in 1961. The French geologist Delesse (1847) showed that the volume densities of various components making up rocks can be estimated from random ground sections by measuring the relative areas of their profiles. The same statement is contained in Equation [2.22] because the right-hand side is identical with the right-hand side of Equation [2.8] for area density estimation, and we claimed that with the test system of point probes we made our measurements on planar, i.e. two-dimensional, sections. That is why:

$$\frac{[V(Y)]}{[V(\Omega)]} = \frac{[S(Y_2)]}{[S(\Omega_2)]} = \frac{I}{n} \qquad [2.23]$$

where $[S(Y_2)]/[S(\Omega_2)]$ is taken as the average value from a series of measurements carried out on a sufficient number of uniform random two-dimensional sections of Ω and *Y*. Quantities Y_2 and Ω_2 represent induced structures of *Y* and Ω on the two-dimensional sections. Symbols *I* and *n* have the same meanings as before.

Another approach for deriving the Delesse principle is based on integration, as introduced in the integral relation [2.1] commenting on the definition of stereology. Having a function of both cross-sectional areas $S_Y(z)$ and $S_\Omega(z)$ for *Y* and Ω using the same incremental step Δz, we obtain:

$$\frac{V(Y)}{V(\Omega)} = \frac{\int_0^H S_Y(z)\,dz}{\int_0^H S_\Omega(z)\,dz} \cong \frac{\sum_{i=1}^{H/\Delta z} S_Y(z_i)\Delta z}{\sum_{i=1}^{H/\Delta z} S_\Omega(z_i)\Delta z} = \sum_{i=1}^{H/\Delta z} \frac{S_Y(z_i)}{S_\Omega(z_i)} = \frac{\overline{S(Y_2)}}{S(\Omega_2)} \tag{2.24}$$

The term of the left of Equation [2.24] is the mean value of the fraction of areas. Integrals in Equation [2.24] have been estimated using a finite number $H/\Delta z$ of sections, where H is the total height of the reference region Ω and Δz is the step, i.e. the constant distance between parallel and neighbouring sections. For more details see Fig. 2.34. The relation [2.24] is independent of the choice of z-axis direction and hence estimation of volumes and volume densities can be carried out on one series of parallel sections, which is unusual in stereology since sections must normally be isotropic.

2.4.2 Surface area and surface area density of three-dimensional features

Surface and surface area density estimations are critical for explaining the sorption characteristics of a fibrous mass. Kim and colleagues (2003) carried out research on fibre structure and pore size in wiping cloths. The filtration properties of fibrous materials with respect to their surface areas were investigated by Lukas (1991).

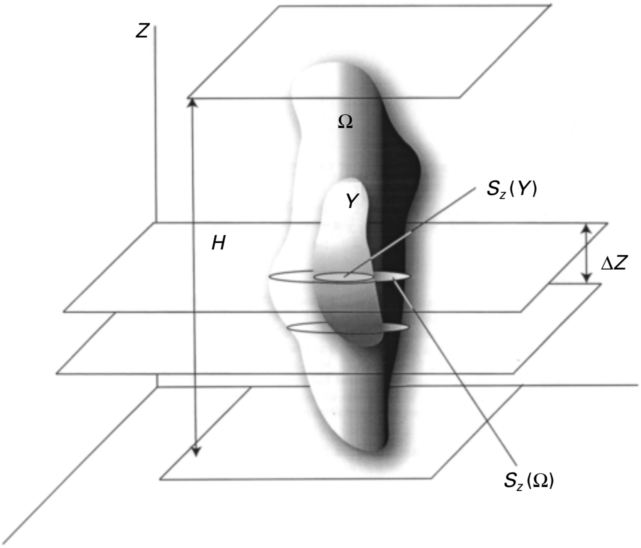

2.34 Delesse's principle: The volume density $V(Y)/V(\Omega)$ is estimated through the average value of area densities $S_z(Y)/S_z(\Omega)$.

To describe a stereological method for surface area estimation, we start with the three-dimensional reference region Ω of volume $V(\Omega)$. In this volume is placed a three-dimensional body with surface Y and of surface area $S(Y)$. We will use a test needle T of length $L(T)$ to estimate the surface area $S(Y)$. Assume the needle is uniform, random and isotropic in Ω, being the region to which the appearance of the needle is restricted. The isotropy of the needle means that if we moved its lower point to the origin of a coordinate system, the upper point hits the small area $d\mu$ on a sphere with radius $r = L(T)$ with the probability p_1 for which:

$$p_1 = \frac{d\mu}{2\pi r^2} \qquad [2.25]$$

Taking one small, flat piece y on the surface Y with the area $S(y)$, then the whole area $S(Y)$ is built of n such elementary surface pieces y. The probability p_2 with which the uniform random and completely anisotropic needle T, i.e. a needle with fixed orientation, hits y in a region Ω will be expressed as a geometrical probability. The probability of the hit p_2 is now given by the fraction of two volumes. The first is the volume of a point set composed of locations of the needle fixed point (let it be located on its lower edge) for all cases when the needle hits the small area y. The second volume is that of Ω. This volume is proportional to all possible locations of the fixed point of the needle. The first volume, the small area y, and the needle, are depicted in Fig. 2.35. For p_2, the following is true:

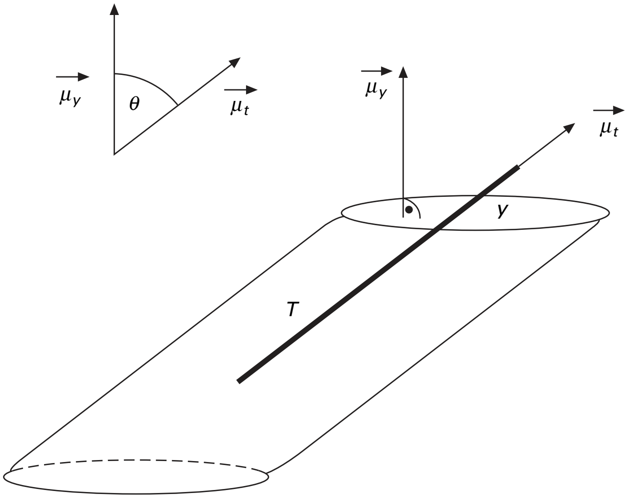

2.35 The probability of intersection of the needle T (having a fixed orientation in space) and a small surface piece y is proportional to the volume $V = S(y)L(T)/\cos\Theta$. $\vec{u}_y$ is perpendicular to y and $\vec{u}_t$ of unitary length lies in the needle direction.

$$p_2 = \frac{S(y)\,L(T)/\cos\theta/}{V(\Omega)} \qquad [2.26]$$

where $S(y)L(T)/\cos\theta/$ is the volume of the first point set when T hits y. Straight brackets denote the absolute value of the cosine of angle θ that contains the needle and the normal perpendicular to the small area y. All we have to do now is to express the average value of p for uniform random positions and isotropic orientations of the needle, which means we have to express the average value of the function $/\cos\theta/$, where all needle directions will have equal weight. To do that we return to the area $d\mu$ on the sphere and consider the sphere radius $r = 1$. Envisage the situation depicted in Fig. 2.36, which helps us to obtain the relation $d\mu = \sin\theta\, d\Phi\, d\theta$. The total area covered by all $d\mu$'s for various needle orientations is one half of the unit sphere surface area 2π. One half of the sphere surface is used here because we do not wish to distinguish between up and down orientation of the needles. The $d\mu$ elements are of various areas for various θ as can be seen in Fig. 2.36. The area $d\mu$ is much smaller near the sphere's apex than in the vicinity of the sphere's equator. Considering the geometrical interpretation of a function average value on a chosen interval; here we have a two-dimensional interval 2π which has the shape of one half of the unitary sphere surface. In the interval value, r^2 is implicit because $r = 1$. This interval is determined using angles Φ and θ in Fig. 2.36. The function for which the average is sought is $/\cos\theta/$. The factor $\sin\theta$ in the relation $d\mu = \sin\theta\, d\Phi\, d\theta$ tells us how the area $d\mu$ varies with various values of the angle θ, representing various attitudes on the sphere. The interval for θ is $<0, \pi/2>$ and Φ is from $<0, 2\pi>$. The

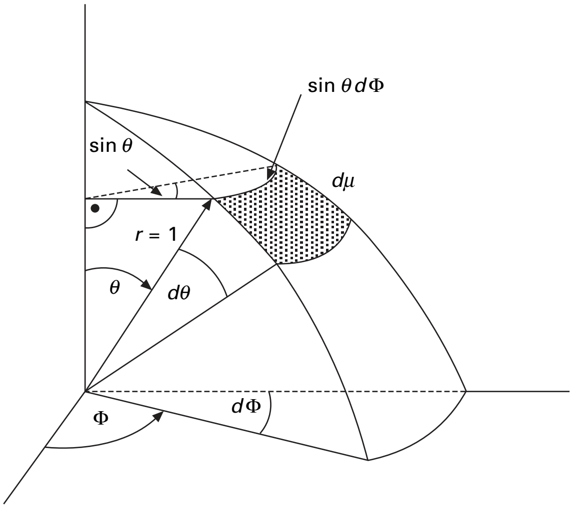

2.36 A small piece of surface $d\mu$ on a sphere has its area expressed in terms of angles Φ and θ.

average value of /cos θ/ for an isotropic needle on the interval 2π is then given by:

$$\overline{/\cos\theta/} = \frac{1}{2\pi}\int_A /\cos\theta/\, d\mu$$

$$= \frac{1}{2\pi}\int_0^{2\pi} d\Phi \int_0^{\pi/2} /\cos\theta/ \sin\theta d\Phi d\theta$$

$$= \int_0^{\pi/2} /\cos\theta/ \sin\theta d\theta = \left[\frac{1}{2}\sin^2\theta\right]_0^{\pi/2} = \frac{1}{2} \qquad [2.27]$$

The first integral in the relation is taken over one half of the unitary sphere surface denoted here as A.

Now we substitute this result into Equation [2.26] to obtain p as the average value of p_2 with respect to the isotropic orientation of the needle:

$$p = \frac{S(y)L(T)\overline{/\cos\theta/}}{V(\Omega)} = \frac{S(y)L(T)}{2V(\Omega)} \qquad [2.28]$$

The relation [2.28] is valid for each surface piece y. All y's cover the whole surface Y. To sum the probability p for the total number n of y's we obtain:

$$np = I = \frac{L(T)}{2V(\Omega)}\sum_{i=1}^{n} S(y_i) = \frac{L(T)S(Y)}{2V(\Omega)} \qquad [2.29]$$

where the product of the probability p and the number N of elementary areas y is expressed as the number of hits I between the needle of length $L(T)$ and surface Y. We estimate p from a finite number of measurements. That is why the estimation of the surface $S(Y)$ for known volume $V(\Omega)$ has the shape:

$$[S(Y)] = \frac{2IV(\Omega)}{L(T)} \qquad [2.30]$$

For the surface density $[S(Y)]/[V(\Omega)]$ of Y in the three-dimensional reference region Ω we can write:

$$\frac{[S(Y)]}{[V(\Omega)]} = \frac{2I}{L(T)} \qquad [2.31]$$

For measurements using a test system containing the total length L of all needles, I is the total number of all hits belonging to the total length L of all needles. Hence the formula [2.31] is valid for test systems after the substitution of L for $L(T)$ according to this new meaning of I.

We will now demonstrate the use of an integral test system to estimate the surface area $S(Y)$ of a surface Y that is embedded in a three-dimensional region Ω. We prepare uniform random and isotropic sections from our specimen and then we place over them the integrated test system as shown in Fig. 2.37.

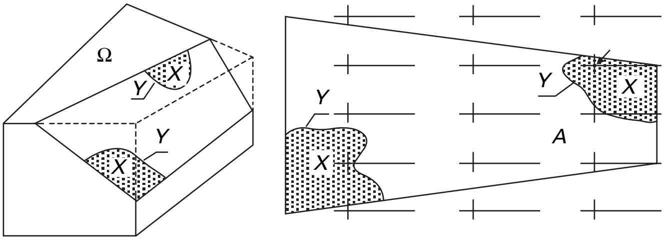

2.37 A three-dimensional object *X*, e.g. a fibrous mass, has its surface denoted here as *Y* (right side of the figure). The number of intersections between test needles and the surface *Y* of the object *X* to estimate the surface area *S*(*Y*) can be realised through two-dimensional sections (left-hand side of the figure). The number of intersections of point probes with cross-section of the region Ω is denoted by *Q* (*Q* = 9 in this case). *Q* estimates the total needle length *L* in a particular section as $L = Q \cdot L(T)$. The number of hits of test needles with *Y* is $I = 2$. Hence, a rough estimation of the surface density from the measurement is $[S(Y)]/[V(Y) = 2I/(QL(T) = 4/(9L(T))$.

The total length L of the needles inside Ω is estimated by the count Q of needle reference points that fall inside Ω rather than by time-consuming measurements of the needle length if they are only partly involved in Ω. The estimation of the total needle length in Ω is then $L = L(T)Q$.

We can also estimate $S(Y)$ from two-dimensional sections of Y, denoted Y_2, using Buffon's needle. We simply substitute the distance d between parallels in Equation [2.12] with $S(\Omega_2)/L$, where Ω_2 is now the reference area of the two-dimensional section of Ω and L is the total length of parallel lines lying in Ω_2. The substitution into [2.12] gives us $[L(Y_2)] = \pi S(\Omega_2)I/(2L)$. Here, $L(Y_2)$ is the perimeter length of Y_2. The surface area $S(Y)$ is then estimated according to [2.30], using the following formula for known $V(\Omega)$:

$$[S(Y)] = \frac{4[L(Y_2)]}{\pi[S(\Omega_2)]}V(\Omega) \qquad [2.32]$$

or the surface density $S(Y)/V(\Omega)$ in the reference region Ω can be estimated as:

$$\frac{[S(Y)]}{[V(\Omega)]} = \frac{4[L(Y_2)]}{\pi[S(\Omega_2)]} \qquad [2.33]$$

The surface area $S(\Omega_2)$ can be measured by point counting methods using zero-dimensional probes in an appropriate test system.

2.4.3 Length and length density in three-dimensional space

Linear, fibre-like structures in biological tissues support a wide variety of physiological functions, including membrane stabilisation, vascular perfusion, and cell-to-cell communication; thus stereological estimations of the parameters of fibre-like three-dimensional structures are of primary interest. Smith and Guttman (1953) demonstrated a stereological method to estimate the total length density of linear objects based on random intersections with a two-dimensional sampling probe. The method presented by Mouton (2002) uses spherical probes that are inherently isotropic to measure the total length of thin nerve fibres in the dorsal hippocampus of the mouse brain. Hlavickova *et al.* (2001) studied bias in the estimator of length density for fibrous features in a three-dimensional space using projections of vertical slices. Cassidy (2001) estimated the total length of fibres in a fibrous mass simultaneously with the count of fibres, providing an estimation of average fibre length that was used to investigate fatigue breaks in wool carpets.

Consider a fibre mass composed of negligibly thin fibres. We treat this fibrous system as a curve C of a total length $L(C)$ in the three-dimensional reference region Ω, having the volume $V(\Omega)$. To estimate the curve length, we will use a test tablet T of known area $S(T)$. This test tablet T will sit inside Ω uniform random and isotropic positions. For T this means, accordingly with remarks in Section 2.2.3:

(i) the chosen fixed point X of T is uniform random in the reference region Ω; and

(ii) the orientation of the testing surface T is isotropic independent of the position of T in Ω, which means in this case that the normal vector $\vec{u}_T$ perpendicular to T is isotropic in three-dimensional space. This situation is shown in Fig. 2.38.

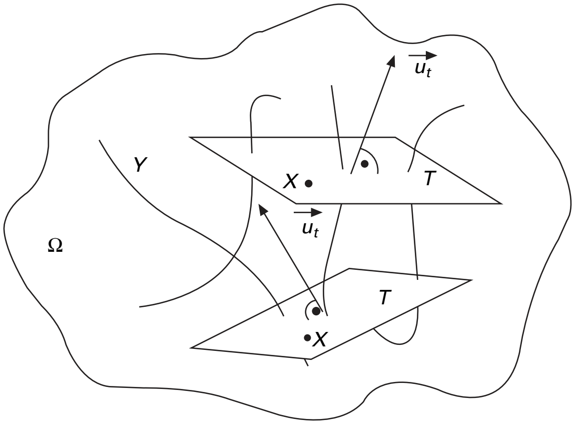

2.38 A reference region Ω of volume, $V(\Omega)$, contains a fibrous system Y of a total length, $L(Y)$. The length, $L(Y)$, is estimated from the number of intersections, I, between Y and a test piece of a plane, whose surface area is $S(T)$. Two uniform random and isotropic positions of T are indicated in the figure.

Imagine an element c of the curve C of length $L(c)$ which is so short that it can be considered to be straight, appearing together with the uniform random and isotropic tablet T in Ω. The probability p that T will be hit by c is the same as in the subsection below dealing with the estimation of a three-dimensional object and its surface area. For the current example, we exchange $S(T)$ for $S(Y)$, and $L(c)$ for $L(T)$ in Equation [2.28]. In other words, the testing probe becomes the measured object and *vice versa*. Using these substitutions, we obtain the following formula for the hit probability:

$$p = \frac{S(T)L(c)}{2V(\Omega)} \qquad [2.34]$$

From this relation we derive the formula for estimating the length $L(C)$ of the curve C using the sum over all its elements c_i. We suppose that there are n such elements constituting C, thus:

$$I = \frac{S(T)}{2V(\Omega)} \sum_{i=1}^{n} L(c_i) \qquad [2.35]$$

where I is the number of hits represented by the product np and $\sum_{i=1}^{n} L(c_i)$ is equal to the total curve length $L(C)$. We estimate $L(C)$ from a finite number of measurements, and hence we can write from Equation [2.35] the relation:

$$[L(C)] = \frac{2IV(\Omega)}{S(T)} \qquad [2.36]$$

This relation is desirable for known volumes $V(\Omega)$ of the reference region. The length density of the curve C in the reference region Ω is then estimated as:

$$\frac{[L(C)]}{[V(\Omega)]} = \frac{2I}{S(T)} \qquad [2.37]$$

To estimate the curve length or the curve length density in a three-dimensional reference region Ω using testing systems, we first have to prepare uniform random and isotropic sections of a three-dimensional sample, as suggested in Fig. 2.39. We then use test systems with two-dimensional probes and the excluding line. For these measurements, I is the total number of cross-sections of the curve in all two-dimensional probes, and $S(T)$ is estimated as count Q of the fixed points in each probe that hits the section of Ω under investigation. The area of the two-dimensional probe is denoted a. We can then write:

$$\frac{[L(C)]}{[V(\Omega)]} = \frac{2I}{aQ} \qquad [2.38]$$

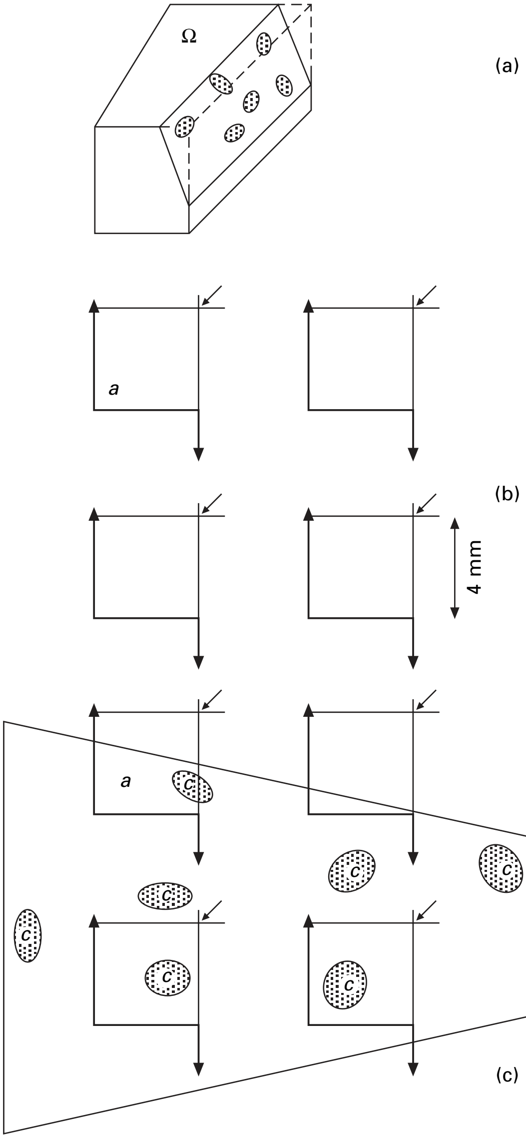

2.39 An isotropic and uniform random two-dimensional section of a reference region Ω is sketched (a) while the used test system with excluding lines is given by (b). The area of each two-dimensional probe of the test system is *a*. The total number of objects, counted by the test system is denoted as *I* while *p* is the total number of two-dimensional probes with area *a* used to count particles, as shown in (c). A rough estimation of the length density from only one measurement in a particular case is $[L(C)]/[V(\Omega)] = 2I/S(T) = 4/(2S(T))$.

2.4.4 Average curvature and average torsion of linear features in three-dimensional space

Understanding torsion and curvature values in three-dimensional space is important where the compression behaviour of fibrous materials is critical, for instance in some furniture and automotive applications. The method described here was first introduced by DeHoff (1975). Wool fibre curvatures were calculated by Munro and Carnaby (1999) from their internal geometry and shrinkage. We introduce the notions of curvature and torsion of fibres in three-dimensional space, and then describe the count method for estimating average values, without deriving the respective formulae. Curvature is usually considered in studies of the compression behaviour of a fibrous mass (Beil *et al.*, 2002), while torsion is generally ignored. Changes in both these values during the compression of a very small fibrous mass were estimated in Lukas *et al.* (1993).

Curvature and torsion are local characteristics of curves in three-dimensional space. The latter vanishes when the curve is fully embedded in a plane. Our definitions of the curve and its torsion are based on the osculation plane, the osculation circle, the tangent, the normal and the binormal. We start by investigating the vicinity of a point A on a curve in three-dimensional space as shown in Fig. 2.40. As well as point A, two points B and C are located on the same curve so that A is between them. These three points determine the circle going through all of them. The limit circle for $B \rightarrow A$ and $C \rightarrow A$ is the

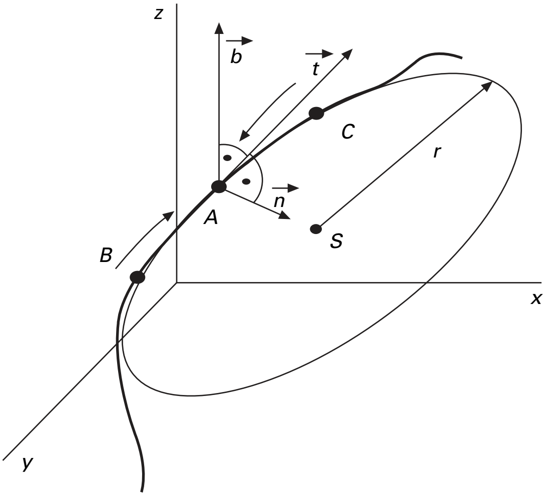

2.40 A curve in three-dimensional space with three points A, B, C that determines the osculation circle with centre at S. The tangent $\vec{t}$ and the normal vector $\vec{n}$ lie in the osculation plane whilst the binormal vector $\vec{b}$ is perpendicular to it.

osculation circle to the curve in the point A. This osculation circle determines the osculation plane. The normal vector $\vec{n}$ to the curve is embedded in this plane, which is unitary, has its origin in the point A and points in the direction A to S, where S is the centre of the osculation circle.

The unitary vector lying in the osculation plane that is perpendicular to the normal $\vec{n}$ is the tangent vector $\vec{t}$ of the curve in point A. Both these orthogonal vectors $\vec{n}$ and $\vec{t}$ determine the next unitary vector $\vec{b}$ which is perpendicular to them. This vector is denoted as binormal of the curve in point A. By shifting point A along the curve by distance $d\lambda$, the orientation of all these three vectors $\vec{n}$, $\vec{t}$ and $\vec{b}$ can be changed. The new vectors between the shifted point and the original one generally contain non-zero angles. We will denote the angle between tangents as $d\theta$ and the angle that contains binormals as $d\gamma$. The curvature k at point A is defined as

$$k = \frac{d\theta}{d\lambda} \qquad [2.39]$$

and is equal to $1/r$ where r is the radius of the osculation circle belonging to point A on the curve. The torsion τ at point A has the defining relation:

$$\tau = \frac{d\gamma}{d\lambda} \qquad [2.40]$$

From the definitions, it is clear that the curvature relates to orientation changes of the tangent while torsion is related to orientation changes of the binormal. The average values of curvature $\bar{k}$ and torsion $\bar{\tau}$ along a curve of total length L are then expressed as average values of functions on the interval $(0, L)$ in the following manner:

$$\bar{k} = \frac{1}{L}\int_0^L k(\lambda)\,d\lambda \quad \bar{\tau} = \frac{1}{L}\int_0^L \tau(\lambda)\,d\lambda \qquad [2.41]$$

Stereological estimations and measurements of these average values are based on the investigation of projections of thin sections of a fibrous mass as depicted in Fig. 2.41. The average value of torsion $\bar{\tau}$ is estimated from the relation:

$$[\bar{\tau}] = \frac{\pi I_A}{2N_L} \qquad [2.42]$$

where I_A is the number of inflex points in a unit area of the projection. The inflex points are marked as squares in Fig. 2.41 and they represent those points on the curve where the centre of the osculation circle belonging to the planar projection of the curve jumps from one side of the curve to the other. For instance, the letter '*S*' has one such point in its centre while '*C*' and '*O*' have no inflection points. The quantity N_L is the average number of intersections between the testing line and the curve per unit length of the testing line, as

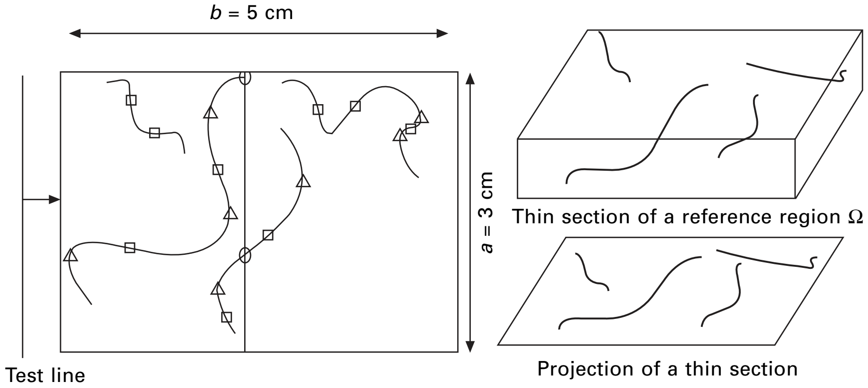

2.41 Projection of a thin section containing linear features, i.e. fibres. The tangential positions of a test line, moved along the fibres, are denoted by triangles. Inflection points are marked with small squares and hits of the fibres with the test line are denoted using empty circles. A rough estimation of the average torsion from one particular measurement is $[\vec{\tau}] = \pi I_A/(2N_L) = (\pi\, 9/(ab))/(4/a)$, while that of the average curvature is $[\bar{k}] = \pi T_A/(2N_L) = (\pi\, 7/(ab))/(4/a)$.

shown in Fig. 2.41. These testing lines have to be uniform random and isotropic.

The average value of curvature $\bar{k}$ is estimated using the formula:

$$[\bar{k}] = \frac{\pi T_A}{2N_L} \tag{2.43}$$

The symbol T_A denotes the average count of the tangential positions of a sweeping testing line per projection unit area. We refer to a tangential position as that where the sweeping line first touches the curve. The sweeping line is moved slowly across the projection, perpendicular to a previously chosen direction. The average number of counts is then calculated from all isotropic orientations and directions along which the sweeping line has moved. The count of tangential positions for each orientation of the sweeping line is then divided by the area of the sample projection (across which the line has swept), to obtain T_A. Some tangential positions of the sweeping line are shown in Fig. 2.41.

2.4.5 Feature count and feature count density: dissectors

The introduction of dissectors into stereology represents a major turning point for this discipline. Dissectors, described by Gundersen (1988b), can, without exaggeration, be considered a methodological conception as significant as the contributions of Delesse, and Glagolev and Thompson.

Table 2.1 (Section 2.2.2) shows that only three-dimensional probes can measure the feature count in three-dimensional space. Unlike the methods described above, dissectors consist of three-dimensional probes and hence they cannot be expressed using two-dimensional test systems.

The use of dissectors is demonstrated in Fig. 2.42. The dissector can be envisaged as a prism-shaped three-dimensional probe. The base of this prism A has surface area $S(A)$, and it has height h. The volume of the dissector D is then $V(D) = S(A)h$. Critical parts of the dissector are the so-called excluding walls. In Fig. 2.42, parts of these excluding walls are shown using different shades. The excluding walls are infinite plains that involve three mutually perpendicular walls of the prism. Using the dissector consists of determining an object count N_V belonging to the dissector's volume $V(D)$. The decision procedure for counting concrete features is similar to the feature count method in two-dimensional space, viz. that given in Section 2.3.3, where we used test systems with the excluding line. Here, we count only features that fulfil the following requirements:

(i) The object has a non-empty intersection with the dissector's prism.
(ii) The object does not touch any of the three excluding walls.

The unbiased estimation of object count volume density N_V is then:

$$[N_V] = \frac{I}{V(D)} \qquad [2.44]$$

where I is the number of counted objects in the dissector D that respect the conditions (i) and (ii).

In the example in Fig. 2.42, we count only particles 1, 2, 3 and 4 because the others have either an empty intersection with the dissector's prism or

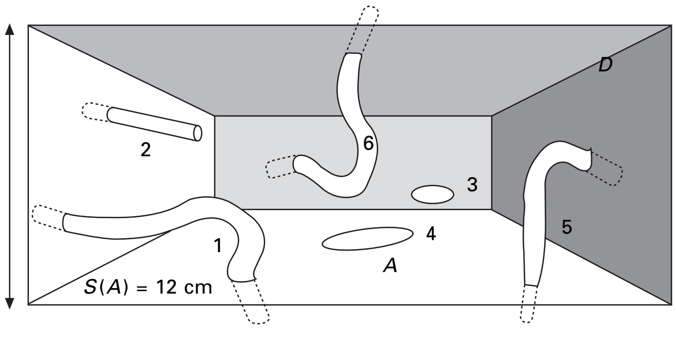

2.42 The dissector D on the figure of volume $V(D) = hS(A)$ has height h and base A of area $S(A)$. Parts of three excluding walls are shaded grey. Only particles No. 1, 2, 3 and 4 are counted in D as the rest hit the excluding walls. The volume density of the object count for this particular case may be estimated as $[N_V] = I/V(D) = 4/V(D)$.

they touch at least one of the excluding walls. Measurements have to be repeated using a number of uniform random dissectors. Counting long fibrous features is extremely arduous as we have to follow an entire fibre outside the dissector prism to make sure that the fibre does not hit one of the excluding walls. The best way to count fibres is to count their origins and divide the final count by two, because each fibre has two ends.

2.5 Sources of further information and advice

We have introduced a number of stereological methods useful for investigating fibrous materials, focusing mostly on explaining the basic stereological tools. We have not covered the statistical side of processing experimental data, which is broadly described in Russ (2000), Saxl (1989) and Elias and Hyde (1983). Recent information about stereology and its application regarding fibrous materials can be found in the *Journal of Microscopy*, the official journal of the International Society for Stereology, and in the *Textile Research Journal* and *The Journal of The Textile Institute*.

We refer the reader to the following recent works for a greater understanding of stereology: Baddeley (2005), Coleman (1979), Ambartzumian (1982), Russ (1986), Hilliard (2003), Mouton (2002), Underwood (1981), Vedel Jensen (1998) and DeHoff (1968).

Stereological methods could be also useful for identifying fabric defects in a dynamic inspection process. A dynamic inspection system for fast image acquisition with a linear scan digital camera is described by Kuo (2003). Changes in appearance due to mechanical abrasion may be evaluated with respect to changes in image texture properties, as has been shown by Berkalp *et al.* (2003).

2.6 References

Ambartzumian R V (1982), *Combinatorial Integral Geometry: with Applications To Mathematical Stereology*, New York, Chichester, Wiley.

Baddeley A (2005), *Stereology for Statisticians*, Boca Raton, Chapman & Hall/CRC.

Beil N B, William W and Roberts J (2002), 'Modeling and computer simulation of the compressional behavior of fibre assemblies', *Textile Res. J.*, 72(5), 375–382.

Berkalp O B, Pourdehimi B, Seyam A and Holmes R (2003), 'Texture retention of the fabric-to-fabric abrasion', *Textile Res. J.*, 73(4), 316–321.

Brenton J R and Hallos R S (1998), 'Investigation into the composition, size, and morphology of dust generated during wool processing', *J. Text. Inst.*, 89(2), 337–353.

Buffon G L L (1777), 'Essai d'arithmetique morale', *Suppl. A l'Histoire Naturale*, Paris, 4.

Cassidy B D (2001), 'Type and location of fatigue breaks in wool carpets, Part II: Quantitative examination', *J. Text. Inst.*, 92(1), 88–102.

Chalkley H W (1943), 'Methods for quantitative morphological analysis of tissue' *J. Nat. Cancer Inst.*, 4, 47.

Coleman R (1979), *An Introduction to Mathematical Stereology*, Aarhus, University of Aarhus.

DeHoff R T (1975), 'Quantitative microscopy of linear features in three dimensions', *4th Int. Congress of Stereology*, Goithersburg, p. 29.

DeHoff R T and Rhines F N (1968), *Quantitative Microscopy*, New York, McGraw Hill.

Delesse M A (1847), 'Procede mecanique pour determiner la composition des roches', *C.R. Acad. Sci.*, Paris, 25, 544.

Dent R W (2001), 'Inter-fibre distances in paper and non-wovens', *J. Text. Inst.*, 92(1), 63–74.

Eberhardt C N and Clarke A R (2002), 'Automated reconstruction of curvilinear fibres from 3D datasets acquired by X-ray microphotography', *J. Microsc.*, 206(1), 41–53.

Elias H (1963), 'Address of the President', *1st Int. Congress for Stereology*, Wien, Congressprint, p. 2.

Elias H and Hyde D M (1983), *A Guide to Practical Stereology*, New York, Krager Continuing Education Series, Switzerland.

Farer R *et al.* (2002), 'Meltblown structures formed by robotic and meltblowing integrated systems: impact of process parameters on fibre orientation and diameter distribution', *Textile. Res. J.*, 72(12), 1033–1040.

Glagolev A A (1933), 'On the geometrical methods of quantitative mineralogic analysis of rocks', *Trans. Ins. Econ. Min.*, Moscow, 59, 1.

Gundersen H J G *et al.* (1988a), 'Some new single and efficient stereological methods and their use in pathological research and diagnostics', *APMIS*, 96, 379–394.

Gundersen H J G (1988b), 'The new stereological tools: dissector, fractionator, nucleator and point sampled intercepts, and their use in pathological research and diagnostics', *APMIS*, 96, 857–881.

Hadwiger H (1967), *Vorlesungen uber Inhalt, Oberflache und Isoperimetrie*, Berlin, Heidelberg, New York, Springer Verlag.

Hilliard J E (2003), *Stereology and Stochastic Geometry*, Boston, Kluwer Academic Publishers.

Hlavickova M, Gokhale A M and Benes V (2001), 'Bias of a length density estimator based on vertical projections', *J. Microsc.*, 204(3), 226–231.

Hough R V (1962), Method and means for recognizing complex patterns, U.S. Patent 306954.

Huang Y and Xu B (2002), 'Image analysis for cotton fibres; Part I: longitudinal measurements', *Textile Res. J.*, 72(8), 713–720.

Jensen E B and Gundersen H J G (1982), 'Sterological ratio estimation based on counts from integral test systems', *J. Microscopy*, 125, 51–66.

Jensen K L and Carstensen J M (2002), 'Fuzz and piles evaluated on knitted textiles by image analysis, *Textile Res. J.*, 72(1), 34–38.

Jeon B.S. (2003), 'Automatic recognition of woven fabric patterns by a neural network', *Textile Res. J.*, 73(7), 645–650.

Jirsak O and Wadsworth L C (1999), *Non-woven Textiles*, Durham, North Carolina, Carolina Academic Press.

Kang T J, Cho D H and Kim S M (2002), 'Geometric modeling of cyber replica system for fabric surface property grading', *Textile Res. J.*, 72(1), 44–50.

Karkkainen S, Jensen E B V and Jeulin D (2002), 'On the orientational analysis of planar fibre system', *J. Microsc.*, 207(1), 69–77.

Kim S H, Lee J H and Lim D Y (2003), 'Dependence of sorption properties of fibrous assemblies on their fabrication and material characteristics' *Textile Res. J.*, 73(5), 455–460.

Koehl L, Zeng X, Ghenaim A and Vasseur C (1998), 'Extracting geometrical features from a continuous-filament yarn by image-processing techniques', *J. Text. Inst.*, 89(1), 106–116.

Kuo C H J, Lee C J and Tsai C C (2003), 'Using a neural network to identify fabric defects in dynamic cloth inspection', *Textile Res. J.*, 73(3), 238–244.

Lukas D (1991), 'Hodnocení filtračních vlastností vlákenných materiálů pomocí stereologických metod', *1st Conf. Filtračné a Absorbčné Materiály*, Starý Smokovec, 25–33.

Lukas D, Hanus J and Plocarova M (1993), 'Quantitative microscopy of non-woven material STRUTO', *6th European Conference of Stereology*, Prague, p. iv–13.

Lukas D, Jirsak O and Kilianova M (1993a), 'Stanoveni Maximální Velikosti Pórů Textilních Filtračních Materiálů Omocí Přístroje Makropulos 5', *Textil*, 7, 123–125.

Lukas D (1997), 'Konfokální mikroskop TSCM', *3rd Conf. STRUTEX'97*, Liberec, Nakladatelství Technická Univerzita v Liberci, 18–19.

Lukas D (1999), *Stereologie Textilnich Materialu*, Liberec, Technicka Univerzita v Liberci.

Mandelbrot B B (1997) *Fractals, Form, Chance and Dimensions*, San Francisco, W.H. Freeman and Co.

Mao N and Russel S J (2000), 'Directional probability in homogeneous non-woven structures; Part I: The relationship between directional permeability and fibre orientation', *Textile Res. J.*, 91(2), 235–243.

Miller A and Schwartz P (2001), 'Forced flow percolation for modeling of liquid penetration of barrier materials', *J. Text. Inst.*, 92(1), 53–62.

Mohammadi M and Banks-Lee P (2002), 'Air permeability of multilayered non-woven fabrics: comparison of experimental and theoretical results', *Textile Res. J.*, 72(7), 613–617.

Mouton P R (2002), *Principles and Practices of Unbiased Stereology :An Introduction for Bioscientists*, Baltimore, Johns Hopkins University Press.

Mouton P R, Gokhale A M, Ward N L and West M J (2002a), 'Stereological length estimation using spherical probes', *J. Microsc.*, 206(1), 54–64.

Munro W A and Carnaby G A (1999), 'Wool-fibre crimp; Part I: The effects of microfibrillar geometry', *J. Text. Inst.*, 90(2), 123–136.

Naas J and Schmidt H L (1962), *Mathematics Worterbuch, Band I A-K*, Berlin, Akademie Verlag Gmbh.

Neckar B and Sayed I (2003), 'Theoretical approach for determining pore characteristics between Fibres', *Textile Res. J.*, 73(7), 611–619.

Pourdeyhimi B and Kim H S (2002), 'Measuring fibre orientation in non-wovens: The Hough transform', *Textile Res. J.*, 72(9), 803–809.

Pourdeyhimi B and Kohel L (2002a), 'Area based strategy for determining web uniformity', *Textile Res. J.*, 72(12), 1065–1072.

Rataj J and Saxl I (1988), 'Analysis of planar anisotropy by means of Steiner compact: a simple graphical method', *Acta Stereologica*, 7(2), 107–112.

Russ J C (1986), *Practical Stereology*, New York, Plenum Press.

Russ J C and Dehoff R T (2000), *Practical Stereology*, New York, Kluwer Academic/ Plenum Publishers.

Saxl I (1989), *Stereology of Objects with Internal Structure*, Amsterdam, New York, Elsevier.

Sera J (1982), *Image Analysis and Mathematical Morphology*, London, Academic Press.

Smith C S and Guttman L (1953), 'Measurement of internal boundaries in three-dimensional structures by random sectioning', *Trans AIME*, 197, 81–92.

Sodomka L (1981), ‘Studium textury pavucin, rouna a netkane textilie’, *Textil*, 36, 129.

Stoyan D, Kendall W S and Mecke K R (1995), *Stochastic Geometry and its Applications*, Chichester, J. Wiley.

Summer scales J, Peare N R L, Russell P and Guld F J (2001). ‘Vornonoi cells, fractal dimensions and fibre composites, *Journal of Microscopy*, 201(2), 153–162.

Taylor P M and Pollet D M (2002), ‘Static load lateral compression of fabrics’, *Textile Res. J.*, 72(11), 983–990.

Thompson E (1930), ‘Quantitative microscopic analysis’, *J. Geol.*, 38, 193.

Underwood E E (1981), *Quantitative Stereology*, Addison-Wesley Pub. Co.

Van Wyck C M (1964), ‘A study of the compressibility of wool with special reference to South African Merino wool’, *Ondersteoort J. Vet. Sci. Anim. Ind.*, 21(1), 99–226.

Vedel Jensen E B (1998), *Local Stereology*, Singapore, World Scientific.

Wiebel E R (1979), *Stereological Methods; Vol. 1 Practical Methods for Biological Morphometry*, New York, Academic Press.

Wortham F J, Phan K H and Augustin P (2003), ‘Quantitative fibre mixture analysis by scanning electron microscopy, *Textile Res. J.*, 73(8), 727–732.

Yil, Zhu Q and Yeung K W (2002), ‘Influence of thickness and porosity on coupled heat and liquid moisture transfer in porous textiles’, *Textile Res. J.*, 72(5), 435–446.

Zhou S, Chu C and Yan H (2003), ‘Backscattering of light in determining fibre orientation distribution and area density of non-woven fabrics’, *Textile Res. J.*, 73(2), 131–138.

Ziedman M and Sawhney P S (2002), ‘Influence of fibre length distribution on strength efficiency of fibres in yarn’, *Textile Res. J.*, 72(3), 216–220.

3

Essentials of psychrometry and capillary hydrostatics

N. PAN and Z. SUN, University of California, USA

3.1 Introduction

From the general engineering approach, water flow in solid porous media should be treated as a problem of hydromechanics. Thus the fundamental laws, such as the continuity or conservation equations, the rheological conditions and the Navier–Stokes equations supposedly govern the phenomena. However, several unique characteristics of fluids transport in fibrous materials render these tools nearly irrelevant or powerless. For instance, except during the wet processing period where higher speed flow may be encountered, low speed, low viscosity and small influx of the fluids make such issues as the interactions between fluids and solid media much more prevalent over the fluids flow problem itself; the pore size, often so tiny as to be on the same scale level as the free molecular path length in the fluid, highlights the need for consideration of the so-called molecular flow, where problems such as absorption and capillary action dominate. In other words, a more microscopic view and associated approaches become indispensable.

Further, if our focus is mainly on fluid transport in porous media during static or quasi-static conditions, it raises another question related to the phase change. The solid fibrous media may cause some of the fluids (e.g. moist air) to condense back to liquid phase, which in turn brings out other issues such as capillary condensation, moisture absorption, associated change of the properties and behaviors of the fibrous materials, and generation of sorption heat.

The above issues and discussions in fact dictate the content and focus of this chapter.

3.2 **Essentials of psychrometry** (Skaar, 1988; Siau, 1995; Morton and Hearle, 1997)

3.2.1 Atmosphere and partial pressures

Our unique ambient environment conditions provide a proper combination of such factors as air, moisture, temperature, and pressure indispensably suitable for life on earth. The whole system is a dynamic one in which every physical entity constantly interacts with others, yet maintains the equilibrium most of the time for our survival and prosperity. Moisture is one of the three states in which water manifests itself and its existence and behavior in the atmosphere is one of the fundamental issues in our discussion.

It is common knowledge that the dry air surrounding us comprises a mixture of gases, the approximate percentages of which are shown in Table 3.1; these are known as the dry gases of the atmosphere. Based on this composition, the molecular mass of dry air is calculated as 28.9645. For a given atmospheric conditions, the dry gases will inevitably absorb water moisture and become a humid mixture termed the moist air. Psychrometrics deals with the thermodynamic properties of moist air and uses these properties to analyze conditions and processes involving moist air.

In dealing with the connection of behaviors between the system and its constituents, our problem here is rare where the Rule of Mixtures is actually valid – that is, the water vapor is completely independent of the dry atmospheric gases in that its behavior is not affected by their presence or absence. For instance, in moist air, the dry gases and the water vapor behave according to Dalton's law of Partial Pressures, i.e. they act independently of one another and the pressure each exerts combines to produce an overall 'atmospheric pressure' p_{atm}.

$$p_{\text{atm}} = p_g + p_v$$

where p_g and p_v are termed the partial pressures of the dry gases and of the water vapor, respectively. From the ideal gas laws, the partial pressures are

Table 3.1 The approximate percentage (composition) of dry air

Nitrogen	78.0840%
Oxygen	20.9476%
Argon	0.9340%
Carbon dioxide	0.0314%
Neon	0.001818%
Helium	0.000524%
Methane	0.0002%
Sulfur dioxide	0 to 0.0001%
Other	0.0002%

related to other thermodynamic variables such as the volume V and temperature T of the constituent i as

$$p_iV_i = n_iRT_i = N_ikT_i \tag{3.1}$$

where the subscript i = atm, g or v, respectively.

- n = number of moles
- R = universal gas constant
- N = number of molecules
- k = Boltzmann constant = 1.38066×10^{-23} J/K
  = R/N_A, N_A – Avogadro's number = 6.0221×10^{23}/mol

Since the mole fraction (x_i) of a given component in a mixture is equal to the number of moles (n_i) of that component divided by the total number of moles (n) of all components in the mixture, then the mole fractions of dry air and water vapor are, respectively:

$$x_g = \frac{n_g}{n_g + n_v} = \frac{p_g}{p_g + p_v} = \frac{p_g}{p_{\text{atm}}} \tag{3.2}$$

and

$$x_v = \frac{n_v}{n_g + n_v} = \frac{p_v}{p_g + p_v} = \frac{p_v}{p_{\text{atm}}} \tag{3.3}$$

By definition, $x_a + x_v = 1$.

However, upon the changing of environment conditions, the mass of water vapor will change due to condensation or evaporation (also known as dehumidification and humidification respectively), but the *mass of dry air will remain constant.* It is therefore convenient to relate all properties of the mixture to the mass of the dry gases rather than to the combined mass of dry air and water vapor.

The evaporation of water is a temperature-activated process and, as such, the saturated vapor pressure p_{sv} (the maximum of p_v) may be calculated with relatively good precision using an Arrhenius-type (Skaar, 1988; Siau, 1995) equation:

$$p_{sv} = A \exp\left(-\frac{E}{RT}\right) \tag{3.4}$$

where p_{sv} = saturated water vapor pressure, A = constant; E = escape energy. The equation in fact offers the relationship between vapor saturation and the ambient temperature, and increasing temperature will lead to a greater saturated vapor pressure p_{sv}.

For instance, with increasing temperature there is an increase in molecular activity and thus more water molecules can escape from the liquid water and be absorbed into the gas. After a while, however, even at this increased temperature, the air will become fully saturated with water vapor so that no more water can evaporate unless we again increase the temperature. The pressure produced by the water vapor in this fully saturated condition is known as the saturated vapor pressure (p_{sv}) and, since at a given temperature the air cannot absorb more water than its saturated condition, the saturated vapor pressure is the maximum pressure of water vapor that can occur at any given temperature.

3.2.2 Percentage saturation and relative humidity

To describe the water vapor concentration in the atmosphere, the most natural way is to determine its volume or weight in a given volume of the air. However, the obvious difficulties in actually handling the vapor volume or weight prompt other more feasible measures for the purpose. The first one is the Percentage Saturation *PS*

$$PS(\%) = \frac{h_v}{h_{sv}} \times 100 \tag{3.5}$$

where h_v is the actual mass of vapor in a unit volume of the air and h_{sv} is the saturated vapor mass. So the *PS* value indicates the degree of saturation of the atmosphere at a given temperature.

Another more frequently used measure is the relative humidity (RH), defined based on the ratio of the partial vapor pressures

$$\mathrm{RH}(\%) = \frac{p_v}{p_{sv}} \times 100 \tag{3.6}$$

For most practical purposes, the ratio of the partial vapor pressures is very close to the ratio of the humidities, i.e.

$$\frac{h_v}{h_{sv}} \approx \frac{p_v}{p_{sv}} \tag{3.7}$$

or

$$\mathrm{RH} \approx PS \tag{3.8}$$

Although the relative humidity and the percentage saturation have been treated as interchangeable in many applications, it is often useful to remember their differences.

3.2.3 Dew-point temperature (T_{dp})

Since the molecular kinetic energy is greater at higher temperature, more molecules can escape the surface and the saturated vapor pressure is correspondingly higher. Besides the two characteristic temperatures which

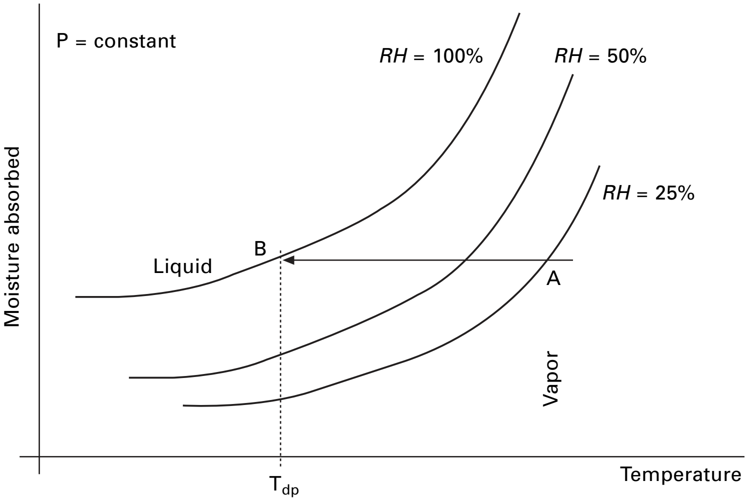

3.1 Dew temperature and relative humidity.

affect the state of water, namely, the ice point and boiling point, the dew point temperature is yet another one. This is the temperature at which the saturation state (RH = 100%) of the mixture of air and water vapor during a cooling process, at constant pressure and without any contact with the liquid phase, is reached. If the temperature drops lower than this point, water vapor will begin to condense back into liquid water as indicated by the arrow A in Fig. 3.1.

3.3 Moisture in a medium and the moisture sorption isotherm

3.3.1 Moisture regain and moisture content

Similar to the case of vapor in the atmosphere, we need to find a way to specify the amount of total moisture in a material. If we can determine the weight D of dry material and weight W of moisture in the material, there are two definitions commonly used in the textile and fiber industries (Morton and Hearle, 1997).

Moisture regain (R)

$$R(\%) = \frac{W}{D} \times 100 \qquad [3.9]$$

Moisture content (M)

$$M(\%) = \frac{W}{(W + D)} \times 100 \qquad [3.10]$$

It is obvious that $R > M$ and relation between R and M:

$$R(\%) = \frac{M(\%)}{\left(1 - \frac{M(\%)}{100}\right)}$$

and

$$M(\%) = \frac{R(\%)}{\left(1 + \frac{R(\%)}{100}\right)} \qquad [3.11]$$

Note that in literature, as well as in our discussion hereafter, the terms of both moisture regain and moisture content are *often treated as interchangeable*.

Equilibrium moisture content (EMC) is the moisture content at which the water in a medium is in balance with the water in the surrounding atmosphere. Although the temperature and relative humidity of the surrounding air are the principal factors controlling EMC, it is also affected by species, specific gravity, extractives content, mechanical stress, and previous moisture history. The curve relating the equilibrium moisture content of a material with the relative humidity at constant temperature is called the *sorption isotherm*. A collection of moisture *sorption isotherms* of several fibers is provided in Fig. 3.2 (Morton and Hearle, 1997). At a given set of standard atmospheric

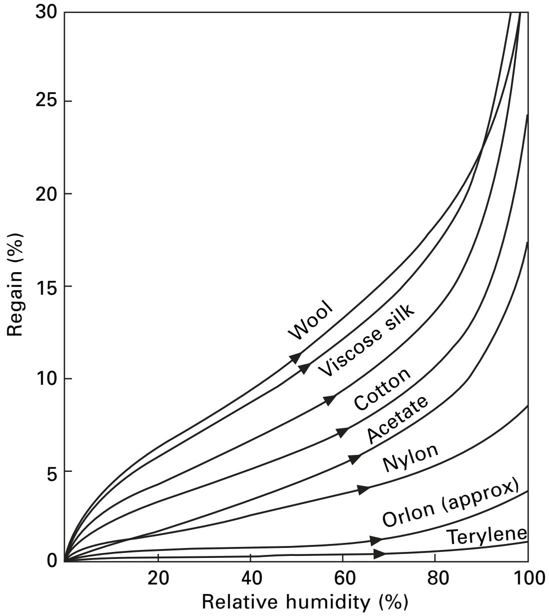

3.2 Sorption isothermals for various fibers. From Morton, W. E. and J. W. S. Hearle (1997). *Physical Properties of Textile Fibers*. UK, The Textile Institute.

conditions, the EMC for each fiber type is a constant, and hence is termed as ‘official’ or ‘commercial’ regain for trading purpose (Morton and Hearle, 1997). Table 3.2 shows the data including the ‘commercial’ regains for some common textile fibers (Morton and Hearle, 1997).

3.3.2 Moisture sorption isotherm

The relationship between the moisture content in a material and the ambient relative humidity at a constant temperature yields a moisture sorption isotherm when expressed graphically. Determination of a moisture sorption isotherm is the general approach for characterizing the interactions between water and solids. This isotherm curve can be obtained experimentally in one of two ways (see Fig. 3.3).

(i) An *adsorption isotherm* is obtained by placing a completely dry material into various atmospheres of increasing relative humidity and measuring the weight gain due to water uptake;

Table 3.2 Moisture sorption data for major fibers

Moisture absorption of fibres			
Material	Recommended allowance or commercial regain or conventional allowance* (%)	Absorption regain (%) (65% R.H., 20°C)†	Difference in desorption and absorption regains (65% R.H., 20°C)†
Cotton	8.5	7–8	0.9
Mercerized cotton	–	Up to 12	1.5
Hemp	12	8	–
Flax	12	7	–
Jute	13.75	12	1.5
Viscose rayon	13	12–14	1.8
Secondary acetate	9	6, 6.9	2.6
Triacetate	–	4.5	–
Silk	11	10	1.2
Wool	14–19	14, 16–18	2.0
Casein	–	4.1	1.0
Nylon 6.6, nylon 6	$5^{3}/_{4}$ or $6^{1}/_{4}$	4.1	0.25
Polyester fibre	1.5 or 3	0.4	–
Acrylic fibre	–	1–2	–
Modacrylic fibre	–	0.5–1	–
Poly(vinyl chloride)	–	0	–
Poly(vinyl alcohol)	–	4.5–5.0	–
Glass, polyethylene	–	0	–

Adapted from Morton and Hearle (1997)

* As given in B.S. 4784:1973; other standardizing organizations may quote different values.

† The earlier measurements were at 70°F (21.1°C).

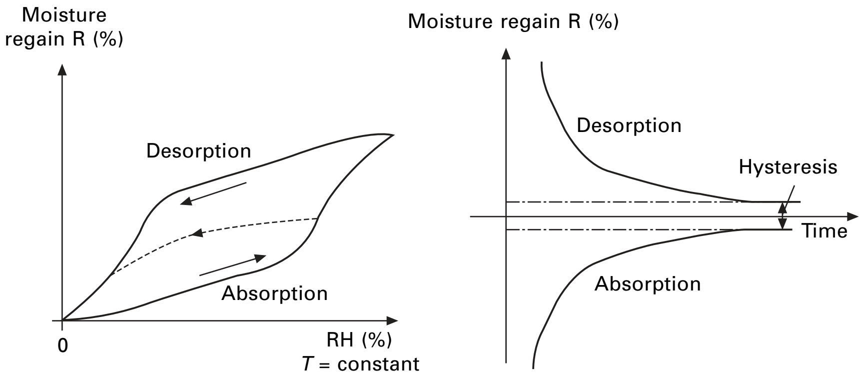

3.3 Two ways of depicting the sorption isotherms and hysteresis. From Morton, W. E. and J. W. S. Hearle (1997). *Physical Properties of Textile Fibers*. UK, The Textile Institute.

(ii) A *desorption isotherm* is found by placing an initially wet material under the same relative humidities, and measuring the loss in weight.

The adsorption and desorption processes are both referred to as the sorption behavior of a material, and are not fully reversible; a distinction can be made between the adsorption and desorption isotherms by determining whether the moisture levels within the material are increasing, indicating wetting, or whether the moisture is gradually lowering to reach equilibrium with its surroundings, implying that the product is being dried.

On the basis of the van der Waals adsorption of gases on various solid substrates, Brunauer *et al.* (1938) classified adsorption isotherms into five general types (see Fig. 3.4). Type I is termed the Langmuir, and Type II the sigmoid-shaped adsorption isotherm; however, no special names have been attached to the other three types. Types II and III are closely related to Types V and IV, respectively. For the same adsorption mechanisms, if they occurred in ordinary solids, Types II and III depict two typical isotherms. If, however, the solid is porous so that it has an internal surface, then the thickness of the adsorbed layer on the walls of the pores is necessarily limited by the width of the pores. The form of the isotherm is altered correspondingly; Type II turns into Type V and Type III corresponds to Type IV (Gregg and Sing, 1967). Moisture sorption isotherms of most porous media are nonlinear, generally sigmoidal in shape, and have been classified as Type II isotherms. Caurie (1970), Rowland (in Brown, 1980), Rao and Rizvi (1995) and Chinachoti and Steinberg (1984) explained the mechanisms and material types (mainly foods) leading to different shapes of the adsorption isotherms. Morton and Hearle have collected most comprehensive experimental results regarding the moisture sorption behaviors (e.g. Fig. 3.3) of fibrous materials including moisture sorption isotherms for various fibers. Al-Muhtaseb *et al.* published

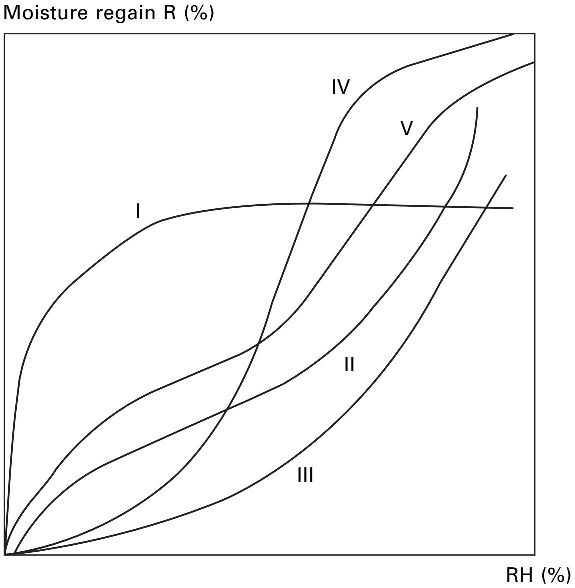

3.4 Different moisture sorption behaviors. Reprinted from Brunauer, S., P. H. Emmett, *et al.* (1938). 'Adsorption of gases in multimolecular layers.' *Journal of the American Chemical Society* 60: 309. With permission from American Chemical Society.

a comprehensive review on moisture sorption isotherm characteristics (Al-Muhtaseb *et al.* 2002). For interpretation purposes, a generalized moisture sorption isotherm for a hypothetical material system may be divided into three main regions, as detailed in Fig. 3.5 (Al-Muhtaseb, *et al.* 2002).

Region A represents strongly bound water with an enthalpy of vaporization considerably higher than that of pure water. A typical case is sorption of water onto highly hydrophilic biopolymers such as proteins and polysaccharides. The moisture content theoretically represents the adsorption of the first layer of water molecules. Usually, water molecules in this region are un-freezable and are not available for chemical reactions or as plasticizers.

Region B represents water molecules that are less firmly bound, initially as multi-layers above the monolayer. In this region, water is held in the solid matrix by capillary condensation. This water is available as a solvent for low-molecular weight solutes and for some biochemical reactions. The quantity of water present in the material that does not freeze at the normal freezing point usually is within this region.

In region C or above, excess water is present in macro-capillaries or as part of the liquid phase in high moisture materials. It exhibits nearly all the properties of bulk water, and thus is capable of acting as a solvent. The variation in sorption properties of materials reported in the literature is caused

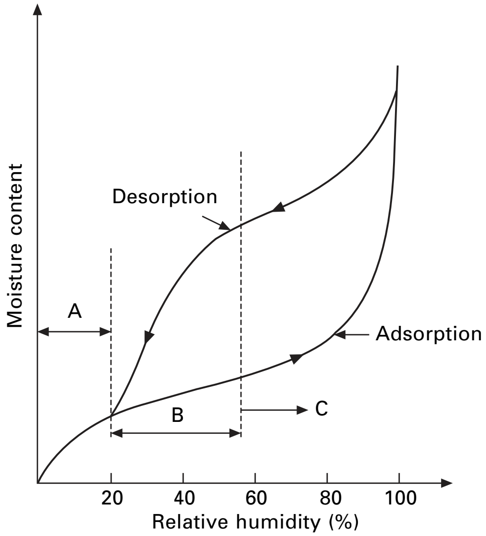

3.5 Three main regions in a generalized moisture sorption isotherm. Reproduced with permission from Al-Muhtaseb, A. H., McMinn, W. A. M. and Magee, T.R.A. (2002). 'Moisture sorption isotherm characteristics of food products: a review.' *Trans. IChemE*, Part C, 80: 118–128.

by property variations, pretreatment, and differences in experimental techniques adopted (gravimetric, manometric or hygrometric) (Saravacos, *et al.* 1986).

The mechanisms of moisture sorption, especially in hydrophilic fiber materials, are further complicated by a continuous change of the structure of the fibers owing to swelling (Preston and Nimkar, 1949). High internal temperature change caused by heat of sorption with large amounts of moisture also introduces more difficulties to the kinetics of the moisture sorption (Urquhart and Williams, 1924).

3.3.3 Water activity and capillary condensation

In describing the state of any medium, the free energy (ΔG) of the system is one of the most important parameters along with temperature T, volume V, concentration c and pressure p. On a molar basis, the free energy becomes the chemical potential F (cal/mole), and is defined as

$$F = F_o + RT \ln a \qquad [3.12]$$

where R = gas constant and T = absolute temperature in °K. The dimensionless variable a is termed the thermodynamic activity of the medium, which as reflected clearly in the equation, determines the system energy at a given temperature. A substance with a greater *a* value is thermodynamically more active.

The water activity a_w is a measure of the energy status of the water in a specific system such as in the air or in a fiber mass. Different materials systems will generate different a_w values. As a potential energy measurement a_w is a driving force for water movement from regions of high water activity to regions of low water activity. In other words, the water activity is the cause for water (liquid or moisture) transport in porous media (Berlin, 1981; Luck, 1981; Van den Berg and Bruin, 1981).

There are several factors that control water activity in a system, and they have been summarized mathematically in the well known Kelvin equation (McMinn and Magee, 1999) as

$$a_w = \frac{p_v}{p_{sv}} = e^{\frac{-2\gamma M}{r\rho RT}} \qquad [3.13]$$

where M = molecular weight of water, γ = surface tension; ρ = density of water, T the absolute temperature and r the capillary radius. Although there have been questions on the validity of the Kelvin equation, it has been proven (Powles, 1985) that the equation is valid to a few per cent even for temperatures approaching the critical temperature and for microscopic drops insofar as homogeneous thermodynamics is valid. One word of caution is that according to Equation [3.13], $a_w \to 0$ when $r \to 0$, i.e. an adequately low a_w would require a capillary radius too small to be practical; a lower boundary should thus be observed in specific cases.

On open surfaces, moisture condensation sets in when saturation vapor pressure has been reached. However, it follows from the Kelvin equation that the vapor saturation pressure reduces inside capillaries of narrower sizes. As a result, for the same vapor pressure, the saturation point becomes lower in smaller pores so that water condenses inside the pores. This means that the tightest pores will be filled first with condensed liquid water. This 'pre-matured' condensation in pores is termed the capillary condensation. This is an extremely important phenomenon widely observable in our daily life. The process of such condensation continues until vapor pressure equilibrium is reached, i.e. up to the point at which the vapor pressure of the water in the surrounding gaseous phase is equal to the vapor pressure inside the pores.

Further, from Equation [3.13], several major factors which can lower the water activity a_w value are identified. *Temperature* is an obvious one and there is a special section later in this chapter on its influence.

Next, the *nature of the material system* the water is in; including the impurities or dissolved species (e.g. salt or dyestuff) in liquid water which interact in three dimensions with water through dipole–dipole, ionic, and hydrogen bonds, leading to the associated colligative effects which will alter such properties as the boiling or freezing point and vapor pressure. Raoult's Law (Labuza, 1984) sometimes is used to account for these factors. In a solution of N_w moles water as the solvent and N_s moles of dissolved solute,

$$a_w = \alpha \frac{N_w}{N_w + N_s} \qquad [3.14]$$

where α is termed the activity coefficient and $\alpha = 1$ for an ideal solute. The presence of the solute N_s reduces the water activity a_w and thus leads to the colligative effects.

Also the *surface interactions* in which water interacts directly with chemical groups on un-dissolved solid ingredients (e.g. fibers and proteins) through dipole–dipole forces, ionic bonds (H_3O^+ or OH^-), van der Waals forces and hydrogen bonds, as reflected by the change of the surface tension (Taunton, Toprakcioglu *et al.*, 1990; Duran, Ontiveros *et al.*, 1998).

Finally, the *structural influences*, which are reflected through the capillary size r where water activity is less than that of pure water because of changes in the hydrogen bonding between water molecules.

It is a combination of all these factors in a material that reduces the energy of the water and thus reduces the water activity as compared to pure water (Al-Fossail and Handy, 1990; Hirasaki, 1996; Reeves and Celia, 1996; Tas, Haneveld *et al.*, 2004).

3.3.4 Water activity and sorption types

As described in the Kelvin equation, moisture trapped in the small pores exerts a vapor pressure less than that of pure water at the given temperature. In other words, water has a lower activity once trapped inside a material system. The solids in which this effect can be observed exhibit so-called hygroscopic properties. The phenomenon of hygroscopicity can be interpreted by a sorption model such as the Brunauer, Emmett and Teller (BET) Equation (Brunauer, Emmett *et al.*, 1938) which proposes a multi-molecular sorption process as shown in Fig. 3.6, based on the different levels of the water activity a_w.

- $a_w \leq 0.2$, formation of a monomolecular layer of water molecules on the pore walls
- $0.2 < a_w < 0.6$, formation of a multi-molecular layers of water molecules building up successively on the monolayer;
- $a_w \geq 0.6$, the process of capillary condensation takes place as described by the Kelvin equation.

3.3.5 Pore size effects

Just as indicated in the Kelvin equation, the wetting mechanisms change with the pore sizes r.

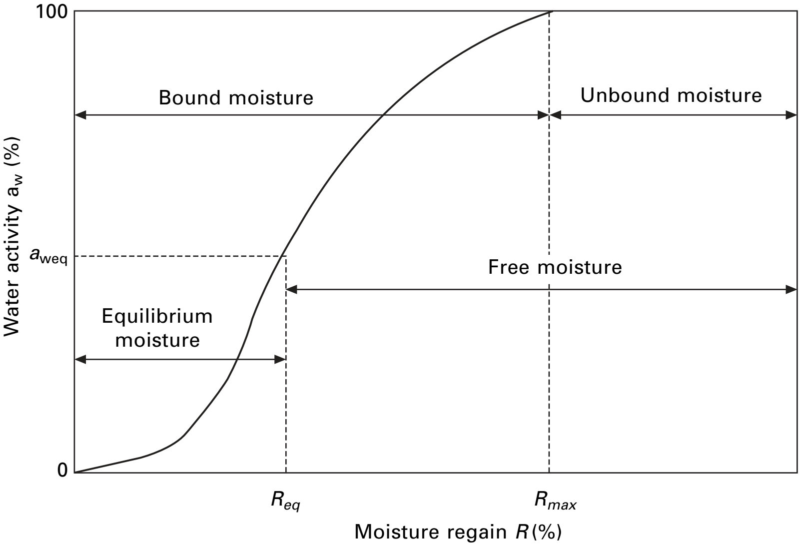

3.6 Various kinds of moisture in a material. Reprinted from Brunauer, S, P. H. Emmett *et al.* (1938). 'Adsorption of gases in multimolecular layers.' *Journal of the American Chemical Society* 60: 309. With permission from American Chemical Society.

- Pore size < 10^{-7}m – capillary-porous bodies within which the moisture is maintained mainly through surface tension
- Pore size >10^{-7}m – porous bodies within which the gravitational forces have to be considered, apart from the capillary forces

On the other hand, taking into consideration the mechanism of liquid and gaseous phase motion, the assumed value of 10^{-7}m is of the same order as the mean free path of water vapor under atmospheric pressure. Luikov (Luikov, 1968; Strumillo and Kudra, 1986) divided capillaries into micro-capillaries with radii less than 10^{-7}m.

Therefore, in the micro-capillaries in which the free path is larger than the capillary radius, gas is transported by means of ordinary diffusion, i.e. chaotic particle motion. In micro-capillaries, the capillary tubes filled up with liquid due to capillary condensation on capillary walls, with a mono-molecular liquid layer of about 10^{-7}m thick formed. In the case of polymer adsorption, the layers formed on the opposite capillary walls can be joined and the whole capillary volume is filled with a liquid phase.

Macro-capillaries with radii bigger than 10^{-7}m are, on the other hand, filled up with liquid phase only when they are in a direct contact with liquid – no more capillary condensation. Such a division into macro- and micro-capillaries has been confirmed by Kavkazov (Kavkazov, 1952; Luikov, 1968; Strumillo and Kudra, 1986) who observed that capillary-porous bodies of

$r > 10^{-7}$ m did not absorb moisture from humid air, but on the contrary released the moisture into atmosphere.

It is worth mentioning that when vapor and temperature equilibrium are obtained, the water activity in the atmosphere is now equal to the relative humidity of surrounding air, i.e.

$$a_w = \frac{p_v}{p_{sv}} \approx \frac{h_v}{h_{sv}} = \frac{\mathrm{RH}(\%)}{100} \qquad [3.15]$$

This equation connects a material property, the water activity, with the ambient condition. The more tightly water is bound with the material, the lower its activity a_w becomes. Equation [3.15] has wide implications and applications. For instance, the moisture sorption isotherm can be expressed in two ways; moisture regain ~ relative humidity presents how the ambient condition affects the moisture in the material, as in many fiber related cases (Morton and Hearle, 1997); whereas moisture regain ~ water activity reveals the interconnection between the two material properties.

3.4 Wettability of different material types

Leger and Joanny (1992), Zisman (1964) and de Gennes (1985) have each written an extensive review on the liquid wetting subject. The following is just a brief summary of what been dealt with by them. Based on the cohesive energy or surface tension, there are two types of solids (de Gennes, 1998).

- Hard solids – covalent, ionic or metallic bonded, high-energy surfaces with surface tension γ_{SO} ~ 500 to 5000 erg/cm^2;
- Weak molecular crystals – van der Waals (VW) forces, or in some special cases, hydrogen bonds bonded, low-energy surfaces, with γ_{SO} ~ 50 erg/cm^2.

3.4.1 Typical behaviors of high-energy surfaces

Most molecular liquids achieve complete wetting with high-energy surfaces. Assuming that chemical bonds control the value of γ_{SO}, while physical ones control the liquid/solid interfacial energies, when there is no contact between the solid and liquid, the total energy of the system is $\gamma_{SO} + \gamma$ where γ is the surface tension of the liquid. However, once the solid and liquid are in contact, the interfacial energy becomes

$$\gamma_{SL} = \gamma_{SO} + \gamma - V_{SL} \qquad [3.16]$$

Here the term $-V_{SL}$ describes the attractive van der Waals interactions at the *S/L* interface. Similarly, when bringing two portions of the same liquid together, the system energy changes from 2γ to

$$\gamma_{LL} = 2\gamma - V_{LL} = 0 \qquad [3.17]$$

where $-V_{LL}$ represents the L/L interfacial attractions. Thus the spreading parameter S, which measures the energy difference between the bare solid and the solid covered with the liquid, is defined as (de Gennes, 1985)

$$S = \gamma_{SO} - (\gamma_{SL} + \gamma) = -2\gamma + V_{SL} = V_{SL} - V_{LL} \qquad [3.18]$$

and the complete wetting ($S > 0$) occurs when

$$V_{SL} > V_{LL} \qquad [3.19]$$

That is, the high energy surfaces are wetted by molecular liquids, not because γ_{SO} is high, but rather because the interfacial attraction between the solid and liquid V_{SL} is higher than the attraction between the liquid and liquid V_{LL}.

3.4.2 Low-energy surfaces and critical surface tensions

For solids of low-energy surface, wetting is not complete. A useful way of representing these results is to plot the contact angle cos θ versus the liquid surface tension γ (See Fig. 3.7 for example). Although in many cases we never reach complete wetting so that cos $\theta = 1$, we can extrapolate the plot down to a value $\gamma = \gamma_c$ when cos $\theta = 1$; $\gamma > \gamma_c$ indicates a partial wetting and $\gamma < \gamma_c$ a total wetting (de Gennes *et al.*, 2003).

In general, we expect γ_c to be dependent on both the solid and liquid.

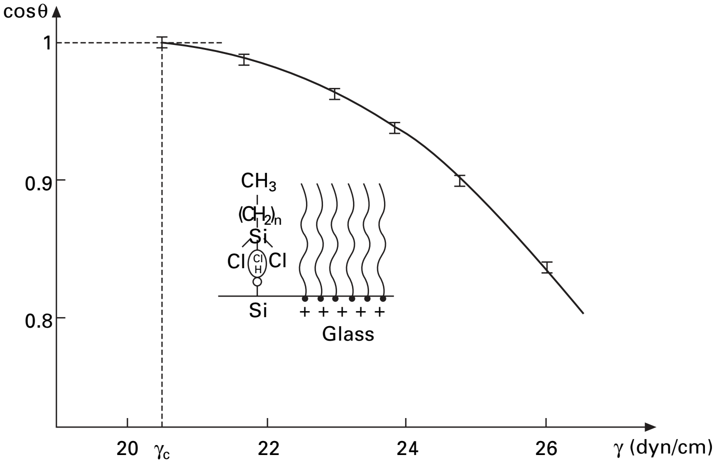

3.7 The contact angle versus the liquid surface tension; From Brochard-Wyart, F., 'Droplets: Capillarity and Wetting', in *Soft Matter Physics*, M. Daoud, C.E. Williams, Editors. 1999, Springer: New York. p. 1–45. With kind permission of Springer Science and Business Media.

However, when dealing with simple molecular liquids (where VW forces are dominant), Zisman (1964) observed that γ_c is essentially independent of the nature of the liquid, and is a characteristic of the solid alone. Typical values of γ_c are listed in Table 3.3. So if we want to find a molecular liquid that wets completely a given low energy surface, we must choose a liquid with surface tension $\gamma \leq \gamma_c$. This critical surface tension γ_c is clearly an essential parameter for many practical applications.

In general, the chemical constitutions of both the solid *S* and liquid *L* affect the wetting behavior of the *S/L* system (Zisman, 1964), and some concluding remarks are listed below.

(i) Wettability is proportional to the polarity of a solid;
(ii) The systems of high γ_c (Nylon, PVC) are those wettable by organic liquids.
(iii) Among systems controlled by VW interactions, we note that CF_2 groups are less wettable (less polar) than CH_2 groups. In practice, many protective coatings (antistain, waterproofing etc.) are based on fluorinated systems.

Usually, glassy polymers, when exposed to a range of relative humidities, show differing absorption behavior at low and high relative humidities (i.e. low or high activities of the penetrant species) (Karad and Jones, 2005). At low activities, sorption of gases and vapors into glassy polymers is successfully described by a dual mode sorption theory, which assumes a combination of Langmuir-type trapping within pre-existing holes and Henry's Law type dissolution of penetrant into the glassy matrix. At high activities, strong positive deviations from Henry's Law are observed, which indicated that the sorbed molecules diffuse through the macromolecular array according to a different mechanism (Jacobs and Jones, 1990).

In fact, the high cohesive energy of water leads to a phenomenon of cluster forming in nonpolar polymers. The water molecule is relatively small and is strongly associated through hydrogen bond formation. This combination of features distinguishes it from the majority of organic penetrants. As a result, strong localized interactions may develop between the water molecules and suitable polar groups in the polymer. On the other hand, in relatively nonpolar materials, clustering or association of the sorbed water is encouraged. Rodriquez *et al.* (2003) confirmed that polymers having strong interactions

Table 3.3 The critical surface tension γ_c for some polymers

	Nylon	PVC	PE	PVF_2	PTFE
γ_c (mN/m)	46	39	31	28	18

Reprinted from Capillarity and Wetting Phenomena: Drops, Bubbles, Pearls, Waves. pp. 21, de Gennes, P. G., Brochard-Wyart, F. and Quere, D. Copyright (2003), with kind permission of Springer Science and Business Media with water have negligible degrees of water clustering, while the more hydrophobic polymers exhibit a higher degree of clustering.

The quantitative description of penetrant diffusion into micro-heterogeneous media has evolved over the last three decades and has become known as the dual mode sorption theory. Based on Meares' (1954) concept of microvoids in the glassy state, Barrer *et al.* (1958) suggested two concurrent mechanisms of sorption – ordinary dissolution and 'hole-filling'.

Brown (1980) concluded through an extensive study that, at low partial pressures or relative humidities, water is distributed uniformly throughout the polymers, but probably preferentially where hydrogen bonding is possible. At higher pressures, chains of water molecules form at hydrogen bonding sites. The initial sorption process can be described by a conventional solution theory and the enhancement process can be viewed as one of occupancy of sites.

3.4.3 Retention of water inside a sorbent

All the natural fibers have groups in their molecules that attract water, referred to as the hydrophilic groups (Morton and Hearle, 1997). However, after all the hydrophilic groups have absorbed water molecules directly, the newly arrived water molecules may form further layers on top of the water molecules already absorbed. These two groups of water molecules are termed the directly and indirectly attached water, as shown in Fig. 3.8. The former is firmly bonded with the sorbent and hence is limited in movement and exhibits physical properties significantly different from those of free, or bulk, water (Berlin, 1981).

According to Luck (1981), bound water has a reduced solubility for other compounds, causing a reduction in the diffusion of water-soluble solutes in

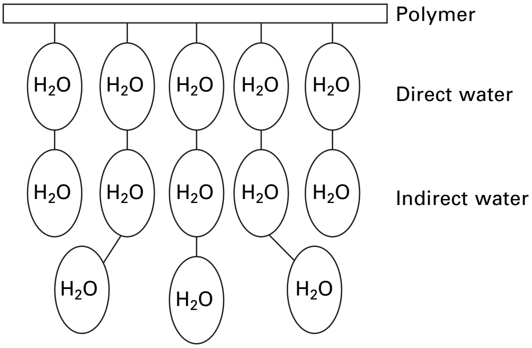

3.8 Direct and indirect water. Adapted from Morton, W. E. and J. W. S. Hearle (1997). *Physical Properties of Textile Fibers*. UK, The Textile Institute.

the sorbent, and a decrease in diffusion coefficient with decreasing moisture content. The decreased diffusion velocity impedes drying processes because of slower diffusion of water to the surface. Some of the characteristics of bound water include a lower vapor pressure, high binding energy as measured during dehydration, reduced mobility as seen by nuclear magnetic resonance (NMR), non-freezability at low temperature, and unavailability as a solvent (Labuza and Busk, 1979). Although each of these characteristics has been used to define bound water, each gives a different value for the amount of water which is bound. As a result of this, as well as the complexities and interactions of the binding forces involved, no universal definition of bound water has been adopted. Indirectly attached water groups whose activity is in between those of the directly attached water and the free liquid water are held relatively loosely. In fact, this division of two water groups inside a sorbent forms the basis on which the first theory on moisture sorption was constructed in 1929 by Peirce (1929).

3.5 Mathematical description of moisture sorption isotherms

Water transport in porous material systems can be classified into three categories (Rizvi and Benado, 1984).

(i) Structural aspects: to describe the mechanism of hydrogen bonding and molecular positioning by spectroscopic techniques;
(ii) Dynamic aspects: to study molecular motions of water and their contribution to the hydrodynamic properties of the system;
The use of these two approaches is restricted by the limited information on the theory of water solid interactions.
(iii) Thermodynamic aspects: to understand the water equilibrium with its surroundings at a certain relative humidity and temperature. Since thermodynamic functions are readily calculated from sorption isotherms, this approach allows the interpretation of experimental results in accordance with a statement of theory (Iglesias *et al.* 1976).

Various theories have been proposed and modified in the past centennial to describe the sorption mechanisms of individual fiber materials (Barrer, 1947; Hill, 1950; Taylor, 1954; Al-Muhtaseb *et al.*, 2002). Langmuir (1918) developed the classical model for adsorption isotherms which is applicable for gases adsorbed in a monolayer on material surfaces. Largely based on Langmuir's work, Brunauer *et al.* (1938) derived a widely used model for multi-layer adsorption. Independently, Peirce introduced in 1929 a model which is based on the assumption of direct and indirect sorption of water molecules on attractive groups of the fibrous materials (Peirce, 1929); and a theory also dealing with fibrous materials, in which the interaction between water and the binding sites was classified into three types of water with different associating strengths, was later proposed by Speakman (1944). Young and Nelson (1967) developed a complete sorption–desorption theory, starting from the assumption of a distinct behavior of bound and condensed water.

The moisture uptake leads to swelling of hygroscopic cellular fibers, a dimensional change due to breaking of inter- and intra-molecular hydrogen bonds between the cellular molecules (Gruber, Schneider *et al.*, 2001). Also the equilibrium moisture isotherms show a distinct hysteresis between the sorption and desorption cycle, indicating structural changes of the fiber caused by the interaction with water (Hermans, 1949).

Labuza (1984) noted that no single sorption isotherm model could account for the data over the entire range of relative humidity, because water is associated with the material by different mechanisms in different water activity regions. Of the large number of models available in the literature (Van den Berg and Bruin, 1981), some of those more commonly used are discussed below, a most recent account referring to Sánchez-Montero *et al.* (2005).

3.5.1 Selected theories on sorption isotherm

Amongst several brilliant pieces of work, Peirce proposed in 1929 one of the earliest mathematical models to describe the absorption process. Given the simplicity of his treatment, the model is surprisingly robust in comparison with the more sophisticated models that followed. Peirce first divided the absorbed water molecules into two parts, directly and indirectly attached water molecules:

$$C = C_a + C_b \qquad [3.20]$$

where C, C_a and C_b are the total, direct and indirect water molecules absorbed per available absorption site. The value C in fact is related to the moisture regain R by

$$R = \frac{CM_w}{\kappa M_o} \qquad [3.21]$$

where M_w, M_o are the molecular weights of water and of per absorption site, respectively, and $\kappa = \frac{W_t}{W_o}$, and W_t, W_o are the total masses of the material and of all absorption sites. Peirce then derived the expressions for both C_a and C_b

$$C_a = 1 - e^{-C} \qquad [3.22]$$

and

$$C_b = C - C_a = C - 1 + e^{-C} \qquad [3.23]$$

So that

$$C = \frac{3\kappa R}{100} \qquad [1.24]$$

By replacing the moisture regain with the ratio of pressures, and working out the result for the coefficient κ for a case of soda-boiled cotton, Equation [3.20] was turned into

$$1 - \frac{p_v}{p_{sv}} = (1 - 0.4\,C_a)e^{-5.4\,C_b} \qquad [3.25]$$

A comparison between the experiments and predictions is shown in Fig. 3.9 (Peirce 1929).

The Brunauer–Emmett–Teller (BET) model (Brunauer, Emmett *et al.*, 1938) has been the most widely used method for predicting moisture sorption by solids. An important application of the BET isotherm is the surface area evaluation for solid materials. In general, the BET model describes the isotherms well up to a relative humidity of 50%, depending on the material and the type of sorption isotherm. The range is limited because the model cannot describe properly the water sorption in multilayers due to its three rather crude assumptions (Al-Muhtaseb *et al.* 2002):

(i) the rate of condensation on the first layer is equal to the rate of evaporation from the second layer;

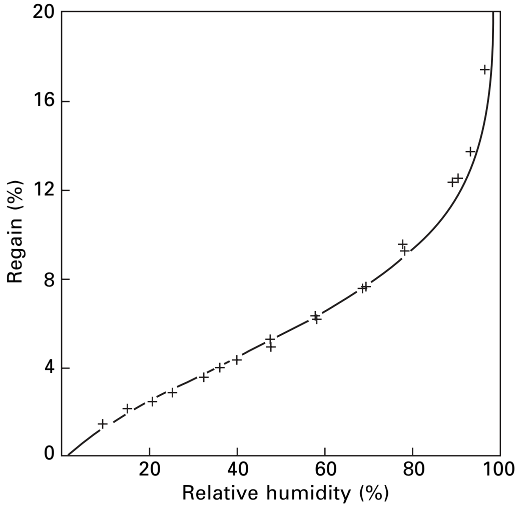

3.9 Comparison of Peirce's theory with experiment. Soda-boiled cotton at 110°C. From Peirce, F. T. (1929). 'A two-phase theory of the absorption of water vapor by cotton cellulose.' *Journal of Textile Institute* 20: 133T.

(ii) the binding energy of all of the adsorbate on the first layer is equal;
(iii) the binding energy of the other layers is equal to those of the pure adsorbate.

However, the equation has been useful in determining an optimal moisture content for drying and storage stability of materials, and in the estimation of the surface area of a material (Van den Berg, 1991). The BET equation is generally expressed in the form:

$$\frac{a_w}{R(1 - a_w)} = \frac{1}{\alpha R_o} + \frac{\alpha - 1}{\alpha R_o} a_w \qquad [3.26]$$

where R is the moisture regain, R_o is the monolayer moisture regain, a_w is the water activity, and α is approximately equal to the net heat of sorption. The advantage of this expression is that the RHS of the equation is a linear function of a_w or the relative humidity. A plot of the equation in comparison with experimental data of various fibers is seen in Fig. 3.10 (Morton and Hearle, 1997). Dent in 1977 proposed a revised theory in which he improved the BET model by lifting the assumption that the binding energy of the other layers is equal to those of the pure adsorbate: this led to a better prediction (Dent, 1977).

Hailwood and Horrobin (1946) developed a model in which the first vapor layer of water molecules was treated as being chemically bonded with the polymer groups and the successively absorbed water was viewed as solution inside the polymer. Their final result yielded:

$$\frac{RM}{1800} = \frac{HK}{1 - HK} + \frac{HKK_1}{1 + HKK_1} \qquad [3.27]$$

where R is the moisture regain of the polymer; M the molecular weight of the polymer group; K_1 is the equilibrium constant; and K is the ratio of the masses of the water solution and water vapor. By choosing the last three constants for best fitting with experimental data, they achieved a close agreement between the theoretical predictions and the testing data for both wool and cotton fibers, as illustrated in Fig. 3.11 (Hailwood and Horrobin, 1946).

In order to analyze the sorption isotherm over a wider range of relative humidities, a model, known as the Guggenheim–Anderson–de Boer (GAB) theory, was also proposed by Guggenheim (1966), Anderson (1946) and de Boer (1968), based on some modified assumptions of the BET model, including the presence of an intermediate adsorbed layer having different adsorption and liquefaction heats and also the presence of a finite number of adsorption layers. The GAB equation provides the monolayer sorption values and could also be used for solid surface area determinations. At the same time, the equation covers a broader range of humidity conditions (Timmermann, 2003).

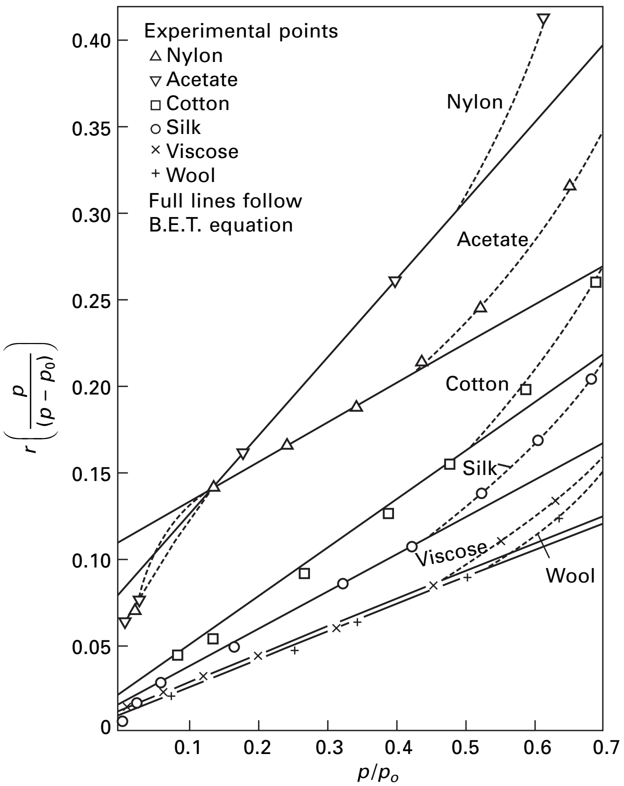

3.10 Comparison between the experiments and BET model. From Morton, W. E. and J. W. S. Hearle (1997). *Physical Properties of Textile Fibers*. UK, The Textile Institute.

Both BET and GAB methods have become very popular in food science, where the theory of mono and multilayer adsorption is applied to the sorption of water by a wide variety of dehydrated foods. The two theories are often expressed in the same format; the BET equation

$$W = \frac{W_m cp/p_o}{(1 - p/p_o)/(1 - p/p_o + cp/p_o)} \qquad [3.28]$$

and the GAB equation

$$W = \frac{W_m ckp/p_o}{(1 - kp/p_o)/(1 - kp/p_o + ckp/p_o)} \qquad [3.29]$$

where W is the weight of adsorbed water, W_m the weight of water forming a monolayer, c the sorption constant, p/p_o the relative humidity and k the additional constant for the GAB equation. Using gravimetrically obtained data, the constants in the two equations were obtained by an iterative technique,

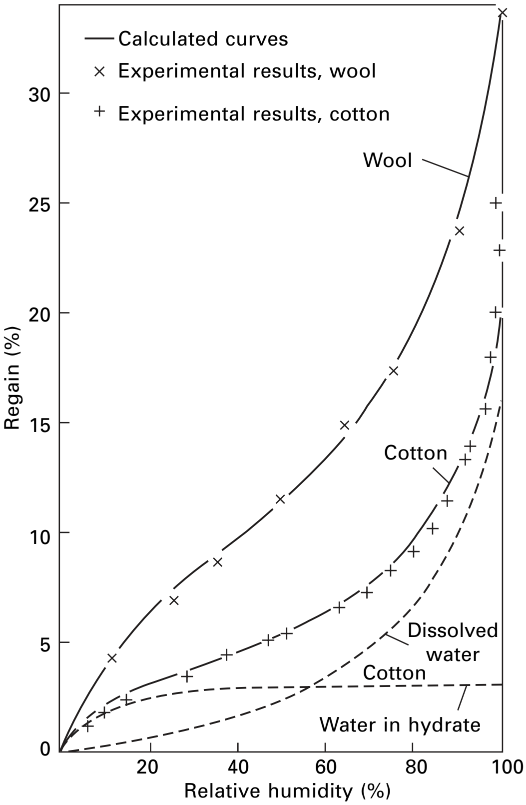

3.11 Comparison between the experiments and predictions. Reproduced by permission of the Royal Society of Chemistry from Hailwood, A. J. and S. Horrobin (1946). 'Absorption of water by polymers: analysis in terms of a simple model.' *Trans. Faraday Soc.* 42B: 84.

so that both methods were applied in Roskar and Kmetec (2005) to evaluate the sorption characteristics of several excipients. Microcalorimetric analysis was also performed in order to evaluate the interaction between water and the substances. As shown in Fig. 3.12 from (Roskar and Kmetec, 2005), the experiments showed excellent agreement between data and the BET model up to 55% RH, confirming the previous conclusion and the GAB model over the entire humidity range, indicated also by high values of the statistical correlation coefficients in Roskar and Kmetec (2005). Furthermore, microcalorimetric measurements suggested that the hygroscopicity of solid materials could be estimated approximately using these approaches.

A kinetic study of moisture sorption and desorption on lyocell fibers was recently conducted by Okubayashi *et al.* (2004). The authors summarized the various moisture sorption modes as shown in Fig. 3.13 and discussed the

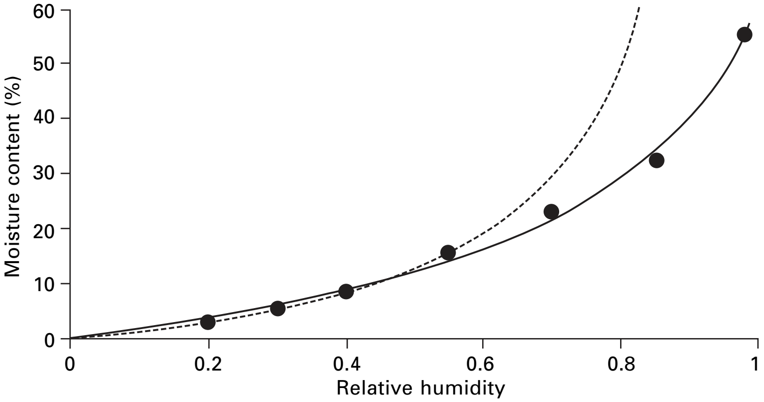

3.12 Moisture sorption isotherms of Kollidone CL fitted by the BET (dotted line) and GAB (solid line) models to the experimental data (Roskar and Kmetec, 2005). With kind permission from the Pharmaceutical Society of Japan.

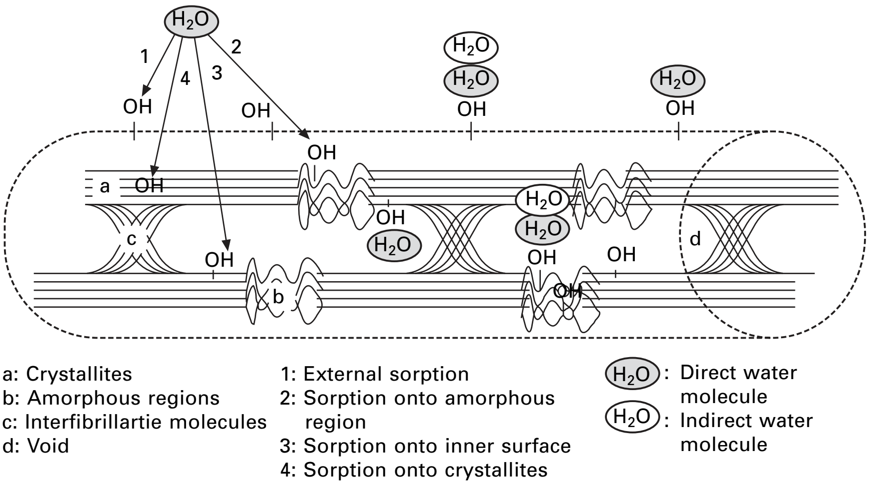

3.13 A schematic diagram of direct and indirect moisture sorption onto external surface (1), amorphous regions (2), inner surface of voids (3), and crystallites (4). Reprinted from *Carbohydrate Polymers*, 58, Okubayashi, S., U.J. Griesser, and T. Bechtold, 'A kinetic study of moisture sorption', 293–299, Copyright (2004), with permission from Elsevier.

results of quantitative and kinetic investigations of moisture adsorption in a man-made cellulose lyocell fiber by using a parallel exponential kinetics (PEK) model proposed by Kohler, Duck *et al.* (2003). A mechanism of water adsorption into lyocell is applied by considering the BET surface area, water retention capacity and hysteresis between the moisture regain isotherms and is compared to those of cotton fibers. The simulation curves showed good fits with the experimental data of moisture regain in both sorption isotherms (Fig. 3.14) and sorption hysteresis (Fig. 3.15).

The enthalpy change (ΔH) provides a measure of the energy variations

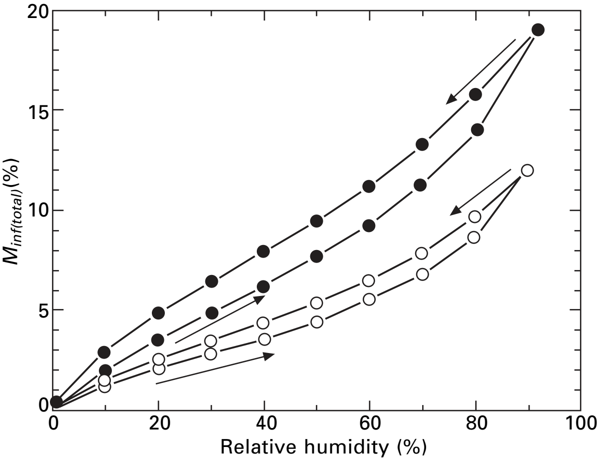

3.14 Equilibrium moisture sorption and desorption isotherms of lyocell (black) and cotton (white) at 20 °C. Reprinted from *Carbohydrate Polymers*, 58, Okubayashi, S., U.J. Griesser, and T. Bechtold, 'A kinetic study of moisture sorption', 293–299, Copyright (2004), with permission from Elsevier.

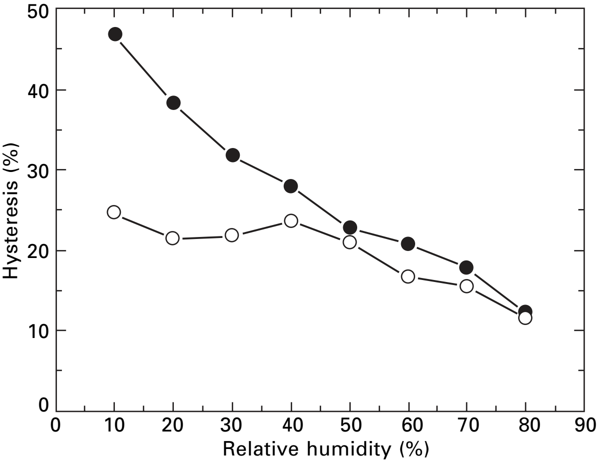

3.15 Effects of relative humidity on hysteresis between sorption and desorption isotherms for lyocell (black) and cotton (white) at 20 °C. Reprinted from *Carbohydrate Polymers*, 58, Okubayashi, S., U.J. Griesser, and T. Bechtold, 'A kinetic study of moisture sorption, 293 – 299, Copyright (2004), with permission from Elsevier.

occurring on mixing water molecules with sorbent during sorption processes, whereas the entropy change (ΔS) may be associated with the binding, or repulsive, forces in the system and is associated with the spatial arrangements at the water–sorbent interface. Thus, entropy characterizes the degree of order or randomness existing in the water-sorbent system and aids interpretation of processes such as dissolution, crystallization and swelling. Free energy (ΔG), based on its sign, is indicative of the affinity of the sorbent for water, and provides a criterion as to whether water sorption is a spontaneous ($-\Delta G$) or non-spontaneous process ($+\Delta G$) (Apostolopoulos and Gilbert, 1990).

The relation between differential enthalpy (ΔH) and differential entropy (ΔS) of sorption is given by the equation (Everett, 1950):

$$\ln a_w = -\frac{\Delta H}{RT} + \frac{\Delta S}{R} \qquad [3.30]$$

where a_w is water activity; R is universal gas constant (8.314 J mol^{-1}K^{-1}) and T is temperature (K). From a plot of ln (a_w) versus $1/T$ using the equilibrium data, ΔH and ΔS values were determined from the slope and intercept, respectively. Applying this at different moisture contents (X) allowed the dependence of ΔH and ΔS on moisture content to be determined (Aguerre, *et al.* 1986).

3.5.2 Moisture sorption hysteresis

As in many nonlinear complex phenomena, there is hysteresis in the moisture sorption process, typically depicted by the different paths on a regain–time curve between absorption and desorption isotherm processes. Taylor (1952, 1954) has shown that hysteresis occurs even in cycles at low relative humidities.

The interpretations proposed for sorption hysteresis can be classified into one, or a combination, of the following categories (Arnell, 1957; Kapsalis, 1987):

(i) Hysteresis in porous solids: for instance in polymers, the uneven breaking and reforming of the cross-links due to capillary pressure during the absorption and desorption processes causes the hysteresis (Urquhart and Eckersall, 1930; Hermans, 1949; Morton and Hearle, 1997).
(ii) Hysteresis in non-porous solids: this is observed in materials such as protein, where the theory is based on partial chemisorption, surface impurities, or phase changes (Berlin, 1981);
(iii) Hysteresis in non-rigid solids: this is observed in materials such as in single fibers, where the theory is based on changes in structure due to swellings which hinder the further penetration of the moisture (Meredith, 1953; Ibbett and Hsieh, 2001).

Given the complexity of the issue, a more effective way to analyze the sorption hysteresis is to investigate the hysteresis in the contact angle during sorption processes. Any wetting process is extremely sensitive to heterogeneities or chemical contamination and one of the most spectacular manifestations of the inhomogeneity is the contact angle hysteresis (Leger and Joanny, 1992).

On a real solid surface one almost never measures the equilibrium contact angle given by Young's law, but a static contact angle that depends on the history of the sample. If the liquid–vapour interface has been obtained by advancing the liquid, (after spreading of a drop, for example) the contact angle has a value θ_A larger than the equilibrium value; if, on the contrary, the liquid–vapour interface has been obtained by receding the liquid (by retraction or aspiration of a drop), the measured contact angle θ_R is smaller than the equilibrium contact angle in Fig. 3.16. Even when the solid surface is only slightly heterogeneous, the difference $\theta_A - \theta_R$ can be as large as a few degrees; in more extreme situations, when the spreading liquid is not a simple liquid but a solution, differences of the order of 100 degrees have been observed (Leger and Joanny, 1992).

Contact angle hysteresis explains many phenomena observed in everyday life. A raindrop attached to a vertical window should flow down under the action of its weight; on a perfect window the capillary force exactly vanishes. On a real window, in the upper parts of the drop the liquid has a tendency to recede and the contact angle is the receding contact angle; in the lower parts of the drop, the liquid has a tendency to advance and the contact angle is the advancing contact angle; the difference in contact angles creates a capillary force directed upwards that can balance the weight (Leger and Joanny, 1992).

The most common heterogeneities that are invoked to explain contact angle hysteresis are roughness and chemical heterogeneities due to contamination that we discuss in more detail below. Any kind of heterogeneity of the solid may, however, create contact angle hysteresis: examples are the porosity of the solid or the existence of amorphous and crystalline regions at the surface of a polymeric solid. Another source of contact angle hysteresis may come from the liquid itself; when it is not a simple liquid but a solution, the irreversible adsorption of solutes leads to strong hysteretsis effects. The following are just two examples of various models proposed for specific surfaces.

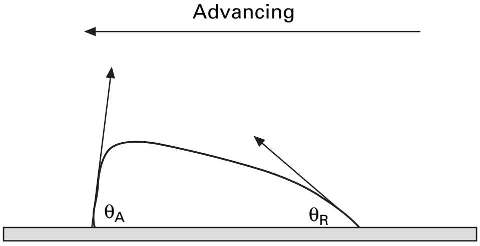

3.16 Advancing and receding contact angles.

(i) *Contact angle hysteresis on a rough surface* The early models to describe contact angle hysteresis considered surfaces with parallel or concentric groves (Mason, 1978). The simplest example is that of a surface with a periodic roughness in one direction $u = u_o \sin qx$ when the contact line is parallel to the groves in the y direction. In this geometry, Young's law can be applied locally and leads to a contact angle between the liquid–vapour interface and the local slope of the solid θ_o. The apparent contact angle θ is, however, the angle between the liquid–vapour interface and the average solid surface. If $qu_o < 1$:

$$\theta = \theta_o - \frac{du}{dx} \qquad [3.31]$$

For stability reasons, in an advancing experiment, the contact angle must increase; θ thus reaches its maximum value $\theta = \theta_o + qu_o$ and the contact line must then jump one period towards the next position where this value can be attained; the advancing contact angle is thus

$$\theta_A = \theta_o + qu_o \qquad [3.32]$$

Similarly, in a receding experiment, the contact angle must decrease and the receding contact angle is the lowest possible contact angle

$$\theta_R = \theta_o - qu_o \qquad [3.33]$$

This very simple model thus leads to contact angle hysteresis $\Delta\theta = \theta_A - \theta_R = 2qu_o$ and predicts jumps of the contact line between equilibrium positions. It, however, contains some unrealistic features.

(ii) *Surface with a single defect* Far away from the contact line, the liquid–vapour interface is flat and shows a contact angle θ_A. Following Young's arguments, the extra force due to the defects on the contact line is $\gamma_{LV}(\cos \theta_o - \cos \theta_A)$. The dissipated energy for one defect is

$$D = U\gamma_{LV} (\cos \theta_o - \cos \theta_A) \qquad [3.34]$$

where U is the advancing speed. This dissipated energy is due to the jump of the contact line on the defects and may be thus calculated directly. The number of defects swept per unit time and unit length of the contact line is nU and W_A is the surface energy

$$D = nUW_A \qquad [3.35]$$

Comparing these two expressions we obtain the advancing angle as

$$\gamma_{LV} (\cos \theta_o - \cos \theta_A) = nW_A \qquad [3.36]$$

Similarly in a receding experiment,

$$\gamma_{LV} (\cos \theta_o - \cos \theta_R) = nW_R \qquad [3.37]$$

The contact angle hysteresis is then

$$\gamma_{LV}\,(\cos\theta_R - \cos\theta_A) = n(W_A + W_R) \qquad [3.38]$$

For a smooth defect we thus predict a contact angle hysteresis γ_{LV} $(\cos\theta_R - \cos\theta_A)$

This dilute defect model has several important limitations; it is restricted to small contact angles, to small distortions of the contact lines (that we have assumed approximately flat) and to extremely dilute defects.

3.5.3 Heat and temperature effects on sorption isotherm

When a material absorbs water, heat is released, depending on the state of the water. For liquid water, this heat is denoted as Q_l, or Q_v for vapor. The two differ by the condensation heat Q_c at constant temperature, i.e.

$$Q_v = Q_l + Q_c \qquad [3.39]$$

There are two ways to describe or calculate the heat released (Watt and McMahon, 1966; Morton and Hearle, 1997; Mohamed, Kouhila *et al.*, 2005).

(i) The differential heat of sorption Q(J per gram of water absorbed): Heat evolved for l gram water to be completely absorbed by a material of infinite mass at a given moisture regain level R. Data for some fibers are shown in Table 3.4 (Morton and Hearle, 1997).

(ii) The integral heat of sorption W (J per gram of dry material): Heat evolved for l gram dry mass to be completely wet (absorption from the liquid state) at a given moisture regain level R as shown in Fig. 3.17 for several fibers (Morton and Hearle, 1997).

$$W \times 100(\%) = \int_R^{R_s} Q_l\,dR \qquad [3.40]$$

where R_S is the saturation moisture regain at the constant temperature;

Table 3.4 The differential heat of sorption for some fibers

Differential heats of sorption (kJ/g)						
	Relative humidity (%)					
Material	0	15	30	45	60	75
Cotton	1.24	0.50	0.39	0.32	0.29	–
Viscose rayon	1.17	0.55	0.46	0.39	0.32	0.24
Acetate	1.24	0.56	0.38	0.31	0.24	–
Mercerized cotton	1.17	0.61	0.44	0.33	0.23	–
Wool	1.34	0.75	0.55	0.42	–	–
Nylon*	1.05	0.75	0.55	0.42	–	–

Adapted from Morton and Hearle (1997)
*From sorption isotherms.

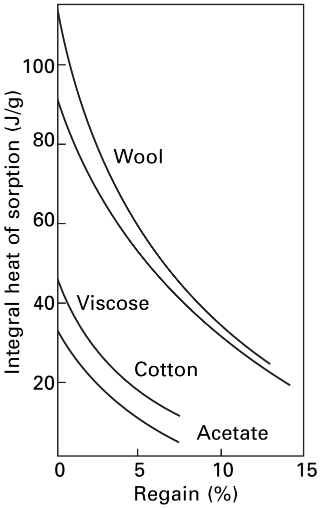

3.17 The integral heat of sorption for some fibers. From Morton, W. E. and J. W. S. Hearle (1997). *Physical Properties of Textile Fibers*. UK, The Textile Institute.

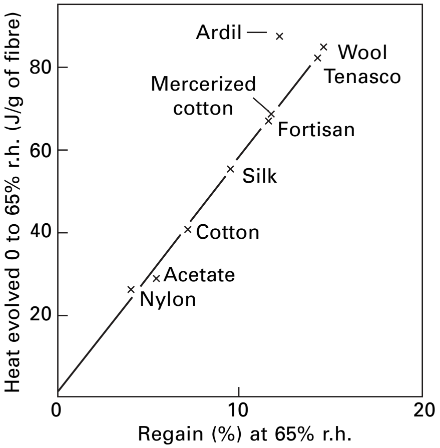

3.18 Heat evolved from 0 to 65% RH for major fibers. From Meredith, R. (1953). From *Fiber Science*. J. M. Preston. Manchester, The Textile Institute: p. 246.

or

$$Q_l = -100\,\frac{dW}{dR} \qquad [3.41]$$

Heat evolved from 0 to 65% RH for major fibers is provided in Fig. 3.18 (Meredith, 1953).

The differential heat of sorption is the amount of energy above the heat of water vaporization associated with the sorption process. This parameter is used to indicate the state of absorbed water by the solid particles. Free energy and differential heat of sorption are commonly estimated by applying the Clausius–Clapeyron equation to sorption isotherms (Kapsalis, 1987; Yang and Cenkowski, 1993):

$$\ln \frac{a_2}{a_1} = \frac{Q_s}{R}\left[\frac{1}{T_1} - \frac{1}{R_2}\right] \qquad [3.42]$$

where a_i is the water activity at temperature T_i °K, Q_s the heat of sorption in cal/mole, a function of the moisture content. There is no analytical way to determined Q_s other than to conduct tests at two temperature levels to determine the moisture sorption isotherms, from which Q_s can be derived (Labuza, 1984). R the gas constant = 1.987 cal/mole °K, a_w value increases as T increases at a constant moisture content. In describing a moisture sorption isotherm, one must specify the temperature and hold it constant. Morton and Hearle (1997) have shown by using the equation that an increase in moisture regain Δa of 0.6 causes the temperature to increase by 10.3 °C.

Although, in theory, this sorption heat can serve as a thermal buffer for clothing materials (for evaporation of sweat from a hot body absorbs the heat to more or less chill the body), in practice, sweat often blocks the air flow channels in the clothing, and causes fiber swelling which in turn reduces the free pores in the clothing. Both hinder the 'breath-ability' of the clothing. Furthermore, the sorption heat can be a safety hazard for materials storage. The collective sorption heat can raise the temperature to the burning point!

3.6 References

Aguerre, R. J., Suarez, C. and Viollaz, P. E. (1986). 'Enthalpy–entropy compensation in sorption phenomena: application to the prediction of the effect of temperature on food isotherms.' *Journal of Food Science* **51**: 1547–1549.

Al-Fossail, K. and Handy L. L. (1990). 'Correlation between capillary number and residual water saturation.' *J. Coll. Interface Sci.* **134**: 256–263.

Al-Muhtaseb, A. H., McMinn, W. A. M. and MaGee, T.R.A. (2002). 'Moisture sorption isotherm characteristics of food products: a review.' *Trans IChemE, Part C*, **80**: 118–128.

Anderson, R. B. (1946). 'Modifications of the Brunauer, Emmett and Teller equation.' *J. Am. Chem. Soc.* **68**: 686–691.

Apostolopoulos, D. and Gilbert, S. (1990). 'Water sorption of coffee solubles by frontal inverse gas chromatography: Thermodynamic considerations.' *Journal of Food Science* **55**: 475–477.

Arnell, J. C. and McDermot, H. L. (1957). Sorption hysteresis. *Surface Activity*. J. H. Schulman. London, Butterworth. Vol. 2.

Barrer, R. M. (1947). 'Solubility of gases in elastomers.' *Transactions of Faraday Society* **43**: 3.

Barrer, R. M., Barrie, J. A. and Slater, J. (1958). 'Sorption and diffusion in ethyl cellulose. Part III. Comparison between ethyl cellulose and rubber.' *J. Polym. Sci.* **27**: 177.

Berlin, E. (1981). Hydration of milk proteins. *Water Activity: Influences on Food Quality*. L. B. Rockland and G. F. Stewart (eds). New York, Academic Press: 467.

Brown, G. L. (ed.) (1980). *Water in Polymers*. Rowland S.P. (ed) Washington, DC, American Chemical Society: 441.

Brunauer, S. and Emmett, P. H. *et al.* (1938). 'Adsorption of gases in multimolecular layers.' *Journal of the American Chemical Society* **60**: 309.

Caurie, M. (1970). 'A practical approach to water sorption isotherms and the basis for the determination of optimum moisture levels of dehydrated foods.' *J. Food Technol.*, **6**: 853.

Chinachoti, P. and Steinberg, M. P. (1984). 'Interaction of sucrose with starch during dehydration as shown by water sorption.' *J. Food Sci.*, **49**: 1604.

de Boer, J. H. (1968). *The Dynamical Character of Adsorption*. Oxford, Clarendon Press.

de Gennes, P. G. (1985). 'Wetting: Statics and dynamics.' *Re. Mod. Phys.* **57**: 827–863.

de Gennes, P. G. (1998). 'The dynamics of reactive wetting on solid surfaces.' *Physica a-Statistical Mechanics and its Applications* **249**(1–4): 196–205.

de Gennes, P. G., Brochard-Wyart, F. and Quere, D. (2003). *Capillarity and Wetting Phenomena: Drops, Bubbles, Pearls, Waves*. New York, Springer.

Dent, R. (1977). 'A multilayer theory for gas sorption I. Sorption of a single gas.' *Textile Res. J.* **47**: 145.

Duran, J. D. G., Ontiveros, A. *et al.* (1998). 'Kinetics and interfacial interactions in the adhesion of colloidal calcium carbonate to glass in a packed-bed.' *Applied Surface Science* **134**(1–4): 125–138.

Everett, D. H. (1950). 'The thermodynamics of adsorption. Part II. Thermodynamics of monolayers on solids.' *Transactions of the Faraday Society* **46**: 942–957.

Gregg, S. J. and Sing K. S. W. (1967). *Adsorption Surface Area and Porosity*. New York, Academic Press.

Gruber, E., Schneider, C. *et al.* (2001). 'Measuring the extent of hornification of pulp fibers.' *Das Papier*: 16–21.

Guggenheim, E. A. (1966). *Application of Statistical Mechanics*. Oxford, Clarendon Press.

Hailwood, A. J. and Horrobin S. (1946). 'Absorption of water by polymers: analysis in terms of a simple model.' *Trans. Faraday Soc.* **42B**: 84.

Hermans, P. H. (1949). *Physics and Chemistry of Cellulose Fibers*. Amsterdam, Netherlands, Elsevier.

Hill, T. L. (1950). 'Statistical mechanism of adsorption X. Thermodynamics of adsorption on an elastic adsorbent.' *Journal of Chemical Physics* **18**: 791.

Hirasaki, G. J. (1996). 'Dependence of waterflood remaining oil saturation on relative permeability, capillary pressure, and reservoir parameters in mixed-wet turbidite sands.' *SPERE* **11**: 87.

Ibbett, R. N. and Hsieh Y. L. (2001). 'Effect of fiber swelling on the structure of lyocell fabrics.' *Textile Research Journal* **71**(2): 164–173.

Iglesias, H. A., Chirife, J. and Viollaz, P. (1976). 'Thermodynamics of water vapour sorption by sugar beet root.' *J. Food Technology* **11**: 91–101.

Jacobs, P. M. and Jones, F. R. (1990). 'Diffusion of moisture into two-phase polymers: Part 3 Clustering of water in polyester resins.' *J. Mater. Sci.* **25**: 2471.

Kapsalis, J. G. (1987). Influence of hysteresis and temperature on moisture sorption isotherms. *Water Activity: Theory and Application to Food*. Rockland, L. R. and Beuchat, L. R. (eds) New York, Marcel Dekker, Inc.: pp. 173–213.

Karad, S. K. and Jones, F. R. (2005). 'Mechanisms of moisture absorption by cyanate ester modified epoxy resin matrices: The clustering of water molecules.' *Polymer* **46**(8): 2732–2738.

Kavkazov, J. L. (1952). *Leather and Moisture Interaction*. Moscow (in Russian), Gizlegprom.

Kohler, R., Duck, R. *et al.* (2003). 'A numeric model for the kinetics of water vapor sorption on cellulosic reinforcement fibers.' *Composite Interfaces* **10**(2–3): 255–276.

Labuza, T. P. (1984). *Moisture Sorption: Practical Aspects of Isotherm Measurement and Use*. St. Paul, Minnesota, American Association of Cereal Chemists.

Labuza, T. P. and Busk C. G. (1979). 'An analysis of the water binding in gels.' *J. Food Sci.*, **44**: 379.

Langmuir, I. (1918). 'The sorption of gases on plane surfaces of glass, mica and platinum.' *Journal of American Chemical Society* **40**: 1361.

Leger, L. and Joanny J. F. (1992). 'Liquid Spreading.' *Rep. Pro. Phys.* **431**.

Luck, W. A. P. (1981). Structure of water in aqueous systems. *Water Activity: Influences on Food Quality*. L. B. Rockland and G. F. Stewart (eds). New York, Academic Press: 407.

Luikov, A. V. (1968). *Drying Theory*. Moscow (in Russian), Energia.

Mason, S. (1978). *Wetting Spreading and Adhesion*. J. F. Padday (ed). New York, Academic.

McMinn, W. A. M. and Magee, T. R. A. (1999). 'Studies on the effect of temperature on the moisture sorption characteristics of potatoes.' *J. Food Proc. Engng*, **22**: 113.

Meares, P. (1954). 'The diffusion of gases through polyvinyl acetate.' *J. Am. Chem. Soc.* **76**: 3415.

Meredith, R. (1953). *Fiber Science*. J. M. Preston (ed.). Manchester, Textile Institute: p. 246.

Mohamed, L. A., Kouhila, M. *et al.* (2005). 'Moisture sorption isotherms and heat of sorption of bitter orange leaves (*Citrus aurantium*).' *Journal of Food Engineering* **67**(4): 491–498.

Morton, W. E. and Hearle J. W. S. (1997). *Physical Properties of Textile Fibers*. Manchester, UK, The Textile Institute.

Okubayashi, S., Griesser, U. J. *et al.* (2004). 'A kinetic study of moisture sorption and desorption on lyocell fibers.' *Carbohydrate Polymers* **58**(3): 293–299.

Peirce, F. T. (1929). 'A two-phase theory of the absorption of water vapor by cotton cellulose.' *Journal of Textile Institute* **20**: 133T.

Powles, J. G. (1985). 'On the validity of the Kelvin equation.' *J. Phys. A: Math. Gen.* **18**: 1551–1560.

Preston, J. M. and Nimkar, M. V. (1949). 'Measuring swelling of fibres in water.' *Journal of Textile Institute* **40**: P674.

Rao, M. A. and Rizvi S. S. H. (1995). *Engineering Properties of Foods*. New York, Marcel Dekker Inc.

Reeves, P. C. and Celia M. A. (1996). 'A functional relationship between capillary pressure, saturation and interfacial area as revealed by a pore-scale network model.' *Water Resources Research* **32**: 2345–2358.

Rizvi, S. S. H. and Benado A. L. (1984). 'Thermodynamic properties of dehydrated foods.' *Food Technology* **38**: 83–92.

Rodriquez, O., Fornasiero, F., Arce, A., Radke C. J. and Prausnitz, J. M. (2003). 'Solubilities and diffusivities of water vapor in poly(methylmethacrylate), poly(2-hydroxyethylmethacrylate), poly(*N*-vinyl-2-pyrrolidone) and poly(acrylonitrile).' *Polymer* **44**: 6323.

Roskar, R. and Kmetec, V. (2005). 'Evaluation of the moisture sorption behaviour of several excipients by BET, GAB and microcalorimetric approaches.' *Chemical & Pharmaceutical Bulletin* **53**(6): 662–665.

Sánchez-Montero, M. J., Herdes, C., Salvador, F. and Vega, L.F. (2005). 'New insights into the adsorption isotherm interpretation by a coupled molecular simulation – experimental procedure.' *Applied Surface Science*, **25**: 519.

Saravacos, G. D., Tsiourvas, D. A. and Tsami, E., (1986). 'Effect of temperature on the water adsorption isotherms of sultana raisins.' *J Food Sci,* **51**: 381.

Siau, J. F. (1995). *Wood: Influence of Moisture on Physical Properties*. Blacksburg, VA., Virginia Polytechnic Institute and State University.

Skaar, C. (1988). *Wood–Water Relations*. New York, Springer-Verlag.

Speakman, J. B. (1944). 'Analysis of the water adsorption isotherm of wool.' *Transactions of Faraday Society* **40**: 60.

Strumillo, C. and Kudra, T. (1986). *Drying: Principles, Applications and Design*. New York, Gordon and Breach Publishers.

Tas, N. R., Haneveld, J. *et al.* (2004). 'Capillary filling speed of water in nanochannels.' *Applied Physics Letters* **85**(15): 3274–3276.

Taunton, H. J., Toprakcioglu, C. *et al.* (1990). 'Interactions between surfaces bearing end-adsorbed chains in a good solvent.' *Macromolecules* **23**: 571–580.

Taylor, J. B. (1952). 'Sorption of water by viscose rayon at low humidities.' *J. Textile Inst.* **43**: T489.

Taylor, J. B. (1954). 'Sorption of water by soda-boiled cotton at low humidities and some comparisons with viscose rayon.' *Journal of Textile Institute* **45**: 642T.

Timmermann, E. O. (2003). 'Multilayer sorption parameters: BET or GAB values?' *Colloids Surf., A Physicochem. Eng. Asp.* **220**: 235–260.

Urquhart, A. R. and Eckersall N. (1930). 'The moisture relations of cotton. VII. A study of hysteresis.' *Journal of Textile Institute* **21**: T499.

Urquhart, A. R. and Williams A. M. (1924). 'The moisture relations of cotton.' *Journal of Textile Institute* **17**: T38.

Van den Berg, C. (1991). Food–water relations: progress and integration, comments and thoughts. *Water Relations in Foods*. H. Levine and L. Slade (eds). New York, Plenum Press: 21– 28.

Van den Berg, C. and Bruin, S. (1981). Water activity and its estimation in food systems. *Water Activity: Influences on Food Quality*. L. B. Rockland and G. F. Stewart (eds). New York, Academic Press: 147.

Watt, I. C. and McMahon, G. B. (1966). 'Effects of heat of sorption in the wool–water sorption system.' *Textile Research Journal* **36**(8): 738.

Yang, W. H. and Cenkowski S. (1993). 'Latent heat of vaporization for canola as affected by cultivar and multiple drying–rewetting cycles.' *Canadian Agricultural Engineering* **35**: 195–198.

Young, J. H. and Nelson, G. H. (1967). 'Theory of hysteresis between sorption and desorption isotherms in biological materials.' *Transactions of the American Society of Agricultural Engineering* **10**: 260.

Zisman, W. (1964). *Contact Angle, Wettability and Adhesion*. F. M. Fowkes. Washington, D.C., ACS: 1.

4

Surface tension, wetting and wicking

W. ZHONG, University of Manitoba, Canada

4.1 Introduction

Surface tension, wicking and wetting are among the most frequently observed phenomena in the processing and use of fibrous materials, when water or any other liquid chemical comes into contact with and is transported through the fibrous structures.

The physical bases of surface tension, wetting and wicking are molecular interactions within a solid or liquid, or across the interface between a liquid and a solid.

Wetting/wicking behaviors are determined by surface tensions (of solid and liquid) and liquid/solid interfacial tensions. Curvature and roughness of contact surface are two other critical factors for wetting phenomena, especially in the case of wetting in fibrous materials. These factors and their effects on wetting phenomena in fibrous materials will also be discussed.

4.2 Wetting and wicking

4.2.1 Wetting

The term ‘wetting’ is usually used to describe the displacement of a solid–air interface with a solid–liquid interface. When a small liquid droplet is put in contact with a flat solid surface, two distinct equilibrium regimes may be found: partial wetting with a finite contact angle θ, or complete wetting with a zero contact angle (de Gennes, 1985), as shown in Fig. 4.1.

The forces in equilibrium at a solid–liquid boundary are commonly described by the Young’s equation:

$$\gamma_{SV} - \gamma_{SL} - \gamma_{LV} \cos \theta = 0 \qquad [4.1]$$

where γ_{SV}, γ_{SL}, and γ_{LV} denotes interfacial tensions between solid/vapor, solid/liquid and liquid/vapor, respectively, and θ is the equilibrium contact angle.

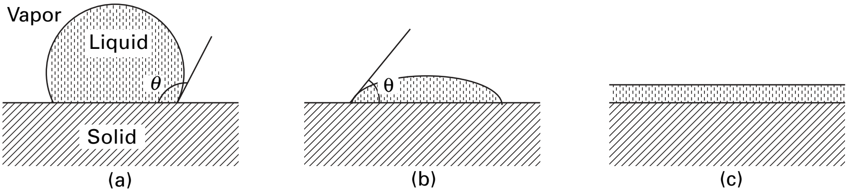

4.1 A small liquid droplet in equilibrium over a horizontal surface: (a) partial wetting, mostly non-wetting, (b) partial wetting, mostly wetting, (c) complete wetting.

The parameter that distinguishes partial wetting and complete wetting is the so-called spreading parameter S, which measures the difference between the surface energy (per unit area) of the substrate when dry and wet:

$$S = [E_{\text{substrate}}]_{\text{dry}} - [E_{\text{substrate}}]_{\text{wet}} \tag{4.2}$$

or

$$S = \gamma_{So} - (\gamma_{SL} + \gamma_{LV}) \tag{4.3}$$

where γ_{S_o} is surface tension of a vapor-free or 'dry' solid surface.

If the parameter S is positive, the liquid spreads completely in order to lower its surface energy ($\theta = 0$). The final outcome is a film of nano-scale thickness resulting from competition between molecular and capillary forces.

If the parameter S is negative, the drop does not spread out, but forms at equilibrium a spherical cap resting on the substrate with a contact angle θ. A liquid is said to be 'mostly wetting' when $\theta \leq \pi/2$, and 'mostly non-wetting' when $\theta > \pi/2$ (de Gennes *et al.*, 2004). When contacted with water, a surface is usually called 'hydrophilic' when $\theta \leq \pi/2$, and 'hydrophobic' when $\theta > \pi/2$.

4.2.2 Wicking

Wicking is the spontaneous flow of a liquid in a porous substrate, driven by capillary forces. As capillary forces are caused by wetting, wicking is a result of spontaneous wetting in a capillary system (Kissa, 1996).

In the simplest case of wicking in a single capillary tube, as shown in Fig. 4.2, a meniscus is formed. The surface tension of the liquid causes a pressure difference across the curved liquid/vapor interface. The value for the pressure difference of a spherical surface was deduced in 1805 independently by Thomas Young and Pierre Simon de Laplace, and is represented with the so-called Young–Laplace equation (Adamson and Gast, 1997):

$$\Delta P = \gamma_{LV}\left(\frac{1}{R_1} + \frac{1}{R_2}\right) \tag{4.4}$$

For a capillary with a circular cross-section, the radii of the curved interface R_1 and R_2 are equal. Thus:

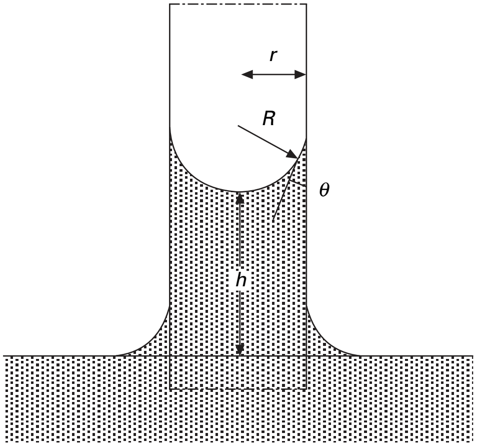

4.2 Wicking in a capillary.

$$\Delta P = 2\gamma_{LV}/R \qquad [4.5]$$

where $R = r/\cos\,\theta \qquad [4.6]$

and r is the capillary radius. As the capillary spaces in a fibrous assembly are not uniform, usually an indirectly determined parameter, effective capillary radius r_e is used instead.

4.3 Adhesive forces and interactions across interfaces

The above discussions show that both wicking and wetting behaviors are determined by surface tensions (of solid and liquid) and liquid/solid interfacial tensions. These surface/interfacial tensions, in macroscopic concepts, can be defined as the energy that must be supplied to increase the surface/interface area by one unit. In microscopic concepts, however, they originate from such intra-molecular bonds as covalent, ionic or metallic bonds, and such long-range intermolecular forces as van der Waals forces and short range acid–base interactions. Therefore, the physical bases of wetting and wicking are those molecular interactions or adhesive forces within a solid or liquid, or across the interface between a liquid and a solid. These adhesive forces include Lifshitz–van de Waals interactions and acid–base interactions.

4.3.1 Lifshitz–van der Waals forces

Molecules can attract each other at a moderate distances and repel each other at a close range, as denoted by the Lennard–Jones potential:

$$w(r) = \frac{A}{r^{12}} - \frac{C}{r^{6}} \qquad [4.7]$$

where $w(r)$ is the interactive potential between two molecules at distance r, and A and C are intensities of the repellency and attraction, respectively.

The attractive forces, represented by the second term at the right-hand side of Equation [4.7], are collectively called 'van der Waals forces'. They are some of the most important long-range forces between macroscopic particles and surfaces. They are general forces which always operate in all materials and across phase boundaries. Van der Waals forces are much weaker than chemical bonds. Random thermal agitation, even around room temperature, can usually overcome or disrupt them. However, they play a central role in all phenomena involving intermolecular forces, including those interactions between electrically neutral molecules (Israelachvili, 1991; Good and Chaudhury, 1991).

When those intermolecular forces are between like molecules, they are referred to as cohesive forces. For example, the molecules of a water droplet are held together by cohesive forces. The cohesive forces between molecules inside a liquid are shared with all neighboring atoms. Those on the surface have no neighboring atoms beyond the surface, and exhibit stronger attractive forces upon their nearest neighbors on the surface. This enhancement of the intermolecular attractive forces at the surface is called surface tension, as shown in Fig. 4.3.

Intermolecular forces between different molecules are known as adhesive forces. They are responsible for wetting and capillary phenomena. For example, if the adhesive forces between a liquid and a glass tube inner surface are larger than the cohesive forces within the liquid, the liquid will rise upwards along the glass tube to show a capillary phenomenon, as shown in Fig. 4.2.

To derive the van der Waals interaction energy between two bodies/surfaces from the pair potential $w(r) = -C/r^6$, Hamaker (1937) introduced an additivity assumption that the total interaction can be seen as the sum over all pair

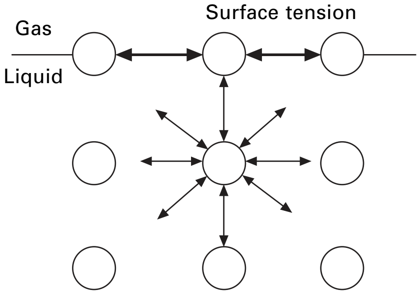

4.3 Liquid surface tension caused by cohesive forces among liquid molecules.

interactions between any atom in one body and any atom in the other, thus obtaining the ‘two-body’ interaction energy, such as that for two spheres (Fig. 4.4(a)), for a sphere near a surface (Fig. 4.4(b)), and for two flat surfaces (Fig. 4.4(c)) (Israelachvili, 1991). And the Hamaker constant A is given as a function of the densities of the two bodies:

$$A = \pi^2 C \rho_1 \rho_2 \tag{4.8}$$

Hamaker’s theory has ever since been used widely in studies of surface–interface interactions and wetting phenomena, although there have been concerns about its additivity assumption and ignorance of the influence of neighboring atoms on the interaction between any atom pairs (Israelachvili, 1991; Wennerstrom, 2003).

The problem of additivity is completely avoided in Lifshitz’s theory (Garbassi *et al.*, 1998; Wu, 1982; Wennerstrom, 2003; Israelachvili, 1991). The atomic structure is ignored, and interactive bodies are regarded as dielectric continuous media. Then the van der Waals interaction free energies W between large bodies can be derived in terms of such bulk properties as their dielectric constants and refractive indices. And the net result of a rather complicated calculation is that Lifshitz regained the Hamaker expressions in Fig. 4.4, but with a different interpretation of the Hamaker constant A. An approximate expression for the Hamaker constant of two bodies (1 and 2) interacting across a medium 3, none of them being a conductor (Israelachvili, 1991; Wennerstrom, 2003), is

$$A_{1,2} = \frac{3h\nu_e (n_1^2 - n_3^2)(n_2^2 - n_3^2)}{8\sqrt{2}\,(n_1^2 + n_3^2)^{1/2}(n_2^2 + n_3^2)^{1/2}[(n_1^2 + n_3^2) + (n_2^2 + n_3^2)^{1/2}]} + \frac{3}{4}kT\,\frac{\varepsilon_1 - \varepsilon_3}{\varepsilon_1 + \varepsilon_3}\,\frac{\varepsilon_2 - \varepsilon_3}{\varepsilon_2 + \varepsilon_3} \tag{4.9}$$

where h is the Planck’s constant, ν_e is the main electronic adsorption frequency in the UV (assumed to be the same for the three bodies, and typically around $3 \times 10^{15}\ \mathrm{s}^{-1}$), and n_i is the refractive index of phase i, ε_i is the static dielectric constant of phase i, k is the Boltzmann constant, and T the absolute temperature.

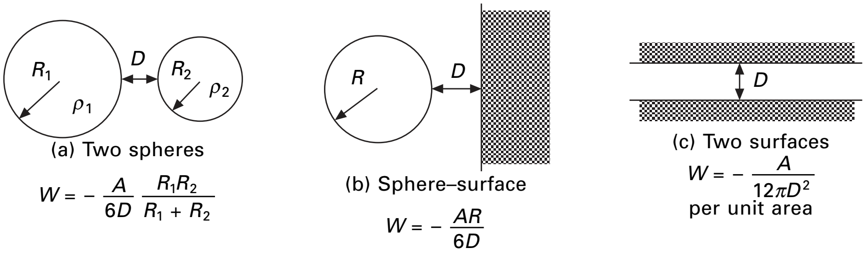

(a) Two spheres

$W = -\frac{A}{6D}\frac{R_1R_2}{R_1 + R_2}$

(b) Sphere–surface

$W = -\frac{AR}{6D}$

(c) Two surfaces

$W = -\frac{A}{12\pi D^2}$

per unit area

4.4 Van der Waals interaction free energies between selected bodies.

Alternatively, from a macroscopic view, the creation of an interface with interfacial free energy γ_{12} by bringing together two different phases from their infinitely separately states, characterized by their surface energies γ_1 and γ_2, results in a molecular reorganization in the surface layers of each phase, as well as in interphase molecular interactions. These effects can be expressed thermodynamically as the work of adhesion, W_a:

$$W_a = \gamma_1 + \gamma_2 - \gamma_{12} \tag{4.10}$$

It was suggested by Fowkes that the equilibrium work of adhesion between two surfaces for a system involving only apolar interactions (Fowkes, 1962) is:

$$W_a = 2(\gamma_1\gamma_2)^{1/2} \tag{4.11}$$

Combining Equations [4.10] and [4.11], we obtain:

$$\begin{aligned}\gamma_{12} &= \gamma_1 + \gamma_2 - 2(\gamma_1\gamma_2)^{1/2},\ i \text{ and } j \text{ apolar}\\ &= (\sqrt{\gamma_1} - \sqrt{\gamma_2})^2\end{aligned} \tag{4.12}$$

For greater generality, polar components should be taken into consideration. This will be examined in the following section.

4.3.2 Acid–base interactions

While Lifshitz–van der Waals (LW) interactions (γ^{LW}) represent the apolar component of interfacial forces, acid–base (AB) interactions (γ^{AB}) account for the polar component. Hydrogen bonds constitute the most important subclass of acid–base interactions. The Lifshitz–van der Waals/acid–base approach, or acid–base approach for short claimed that, for any liquid or solid, the total surface tension γ can be uniquely characterized by these two surface tension components (van Oss, 1993; Good, 1992; Good *et al.*, 1991):

$$\gamma = \gamma^{LW} + \gamma^{AB} \tag{4.13}$$

This approach came into existence when the thermodynamic nature of the interface was re-examined by van Oss *et al.* (1987a) in the light of Lifshitz theory. The apolar interaction between a protein and a low energy surface solid is repulsive and hence solely the apolar interaction cannot explain the strong attachment of biopolymer on the low energy solid. A polar term, short-range interaction, later called Lewis acid–base (AB) interaction, was introduced to explain the attraction.

The LW component in Equation [4.13] can be derived by Equation [4.12]. AB interactions, on the other hand, are not ubiquitous as are LW interactions. They occur when an acid (electron acceptor) and a base (electron donor) are brought close together. Accordingly, the acid–base surface tension component comprises two non-additive parameters: acid surface tension parameter γ^+ and base surface tension parameter γ^-:

$$\gamma^{AB} = 2\sqrt{\gamma^+\gamma^-} \qquad [4.14]$$

The *AB* interactions across an interface may be expressed in the form

$$\gamma_{12}^{AB} = (2\sqrt{\gamma_1^+} - \sqrt{\gamma_2^+})(\sqrt{\gamma_1^-} - \sqrt{\gamma_2^-}) \qquad [4.15]$$

The existence of acid–base interactions can substantially improve wetting and adhesion. The high energy associated with acid–base interactions is due to their short range (2–3A) Coulombic forces.

The interfacial tension for solid/liquid systems, therefore, can be obtained through a combination of Equations [4.12]–[4.15] (van Oss, 1993; Kwok *et al.*, 1994):

$$\gamma_{SL} = \gamma_S + \gamma_L - 2(\gamma_S^{LW}\gamma_L^{LW})^{1/2} - 2(\gamma_S^+\gamma_L^-)^{1/2} - 2(\gamma_S^-\gamma_L^+)^{1/2} \qquad [4.16]$$

It is well known that surface tensions of liquids may readily be measured directly by force methods such as the Wilhelmy plate or the du Nouy ring. However, there is no well-accepted direct method to measure the surface tensions of solid polymers. When using the Young's equation [4.1] to derive the solid surface tension from liquid surface tension and contact angle, a valid approach to determine interfacial tensions between liquid and solid is very important. The acid–base approach has therefore been used frequently to estimate the solid surface tensions (Kwok *et al.*, 1994, 1998; van Oss *et al.*, 1990) or interfacial adhesion (Greiveldinger and Shanahan, 1999; Chehimi *et al.*, 2002).

In order to calculate the solid surface tension components from the acid–base approach, Equation [4.16] combined with Young's Equation [4.1] yields (Lee, 1993):

$$\gamma_L(1 + \cos\theta) = 2(\gamma_S^{LW}\gamma_L^{LW})^{1/2} + 2(\gamma_S^+\gamma_L^-)^{1/2} + 2(\gamma_S^-\gamma_L^+)^{1/2} \qquad [4.17]$$

under the assumption that vapor adsorption is negligible.

From Equation [4.17], the solid surface tension components, γ_S^{LW}, γ_S^+ and γ_S^- can be calculated by simultaneous solution of three equations if the measurement of contact angles with respect to three different liquids is known on the solid substrates. Three liquids of known surface tension components (γ_L^{LW}, γ_L^+ and γ_L^-) are also required. Usually, the van der Waals component γ_S^{LW} can be first determined by using an apolar liquid. Then two other polar liquids can be used to determine the acid–base components of the solid, γ_L^+ and γ_L^- (Kwok *et al.*, 1994; van Oss *et al.*, 1990).

4.4 Surface tension, curvature, roughness and their effects on wetting phenomena

There has been numerous research work published on the wetting process on solid surface, including several comprehensive reviews (Good, 1992; de Gennes, 1985), which cover topics from contact angle, contact line, liquid–solid adhesion, wetting transition (from partial wetting to complete wetting) and dynamics of spreading. However, wetting of fibrous materials becomes an even more complex process as it involves interaction between a liquid and a porous medium of *curved*, *intricate* and *tortuous* structure, yet with a *soft* and *rough* surface, instead of a simple solid, flat and smooth surface.

4.4.1 Surface tension and wettability

From studies on the bulk cohesive energy, we learn that there are two main types of solids: hard solids (bound by covalent, ionic or metallic) with so-called ‘high energy surfaces’, and weak molecular crystals (bound by van der Waals forces, or in some cases by acid–base interactions) with ‘low energy surfaces’. The surface tension, γ_{sv}, is in the range of 500 to 5000 mN/m for high energy surfaces, and 10 to 50 mN/m for low energy surfaces (Fowkes and Zisman, 1964). Most organic fibers belong to the ‘low energy surfaces’ category.

Most molecular liquids achieve complete wetting with high-energy surfaces (de Gennes, 1985). In the idealized case where liquid–liquid and liquid–solid interactions are purely of the van der Waals type (no chemical bonding nor polar interactions), solid–liquid energy could be deducted as follows:

If a semi-infinite solid and a semi-infinite liquid are brought together, they start with an energy $\gamma_{LV} + \gamma_{So}$, and end in γ_{SL}, as the van der Waals interaction energy V_{SL} between solid and liquid is consumed. This process can be expressed as:

$$\gamma_{SL} = \gamma_{So} + \gamma_{LV} - V_{SL} \qquad [4.18]$$

To a first approximation, the van der Waals couplings between two species are simply proportional to the product of the corresponding polarizabilities α (de Gennes, 1985):

$$V_{SL} = k\alpha_S\alpha_L \qquad [4.19]$$

Similarly, if two liquid portions are brought together, they start with energy $2\gamma_{LV}$, and end up with zero interfacial energy:

$$2\gamma_{LV} - V_{LL} = 0 \qquad [4.20]$$

The same applies to solids:

$$2\gamma_{So} - V_{SS} = 0 \qquad [4.21]$$

Equation [4.3] combined with [4.18]–[4.21] gives:

$$S = \gamma_{So} - (\gamma_{SL} + \gamma_{LV}) = V_{SL} - V_{LL} = k(\alpha_S - \alpha_L)\alpha_L \qquad [4.22]$$

Therefore, a liquid spreads completely if $\alpha_S > \alpha_L$ so as to make S positive.

Low-energy surfaces can give rise to partial or complete wetting, depending on the liquid chosen (de Gennes, 1985). The empirical criterion of Zisman (Zisman, 1964; de Gennes *et al.*, 2004) is that each solid substrate has a critical surface tension γ_C, and there is partial wetting when the liquid surface tension $\gamma > \gamma_C$ and total wetting when $\gamma < \gamma_C$.

The critical surface tension can be determined by the so-called Zisman plot. A series of homologous liquid (usually *n*-alkanes, with *n* the variable) is chosen for the study. Cos θ as a function of γ is plotted to give the critical surface tension, as shown in Fig. 4.5 (de Gennes *et al.*, 2004; de Gennes, 1985).

Equation [4.22] is an interpretation of spreading coefficient S in terms of van der Waals forces only. To extend the wetting criteria for liquid/solid interfaces to include both long-range and short-range interactions, two key parameters are used: the effective Hamaker constant A_{eff} and the spreading coefficient S (Brochard-Wyart *et al.*, 1991; Lee, 1993). The effective Hamaker constant describes the long-range interactions:

$$A_{eff} = A_{SL} - A_{LL} \qquad [4.23]$$

And the spreading coefficient S contains contributions from short-range interactions in its original expression [4.3]. It is also important to note that both S and A_{eff} are independent variables, and both can have positive or negatives values.

Using two parameters, S and A_{eff}, as wetting criteria, results in four possibilities of wetting behaviors:

(i) $S > 0$ and $A_{eff} > 0$, complete wetting. A small droplet put in contact with a flat solid surface spreads out and forms a thin 'pancake' film, as shown in Fig. 4.6(a).

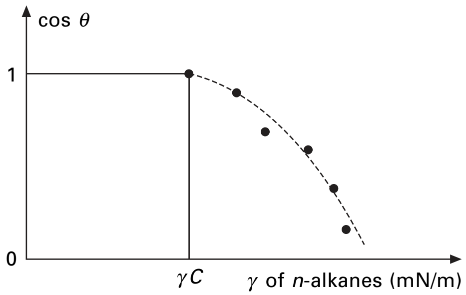

4.5 A typical Zisman plot to determine critical surface tension γC.

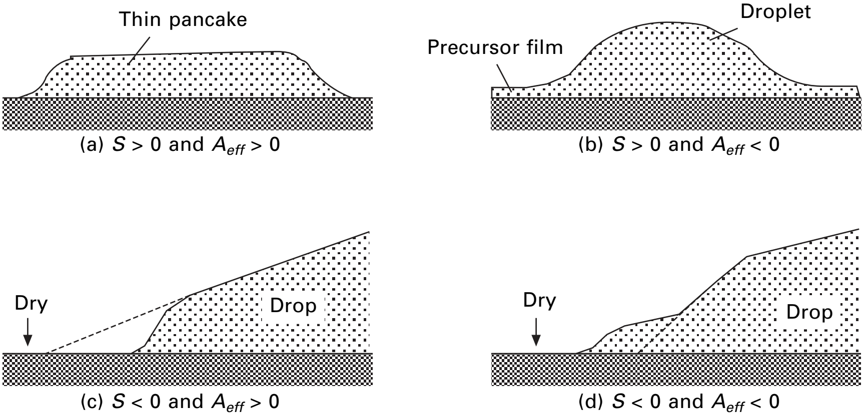

(a) $S > 0$ and $A_{eff} > 0$ (b) $S > 0$ and $A_{eff} < 0$

(c) $S < 0$ and $A_{eff} > 0$ (d) $S < 0$ and $A_{eff} < 0$

4.6 Various kinds of wetting.

(ii) $S > 0$ and $A_{eff} < 0$, pseudo partial wetting. The final equilibrium state of the liquid drop is a spherical cap with a precursor film, as shown in Fig. 4.6(b).

(iii) $S < 0$ and $A_{eff} > 0$, partial wetting. The solid around the droplet is dry. The liquid profile is hyperbolic and curved downward, as shown in Fig. 4.6(c).

(iv) $S < 0$ and $A_{eff} < 0$, partial wetting. The solid around the droplet is dry. The liquid profile is hyperbolic and curved upward, as shown in Fig. 4.6(d).

Over the past two decades, considerable interest has developed in the field of acid–base, or electron acceptor/donor theory and their applications in evaluating surface and interfacial tensions, as described in the previous section. One of the appealing features of the concept based on acid–base theory is that it introduces the possibility of negative interfacial tensions, as exist in spontaneous emulsification or dispersion phenomena. Negative interfacial tensions were impossible within the confines of van der Waals bonding (van Oss *et al.*, 1987b; Leon, 2000).

4.4.2 Curvature and wetting

Wetting of fibrous materials is dramatically different from the wetting process on a flat surface, due to the geometry of the cylindrical shape. A liquid that fully wets a material in the form of a smooth planar surface may not wet the same material when presented as a smooth fiber surface.

Brochard (1986) discussed the spreading of liquids on thin cylinders, and stated that, for nonvolatile liquids, a liquid drop cannot spread out over the cylinder if the spreading coefficient S is smaller than a critical value S_c, instead of 0. At the critical value S_c, there is a first-order transition from a droplet to a sheath structure ('manchon'). The critical value was derived as

$$S_c = \frac{3}{2}\gamma\left(\frac{a}{b}\right)^{2/3} \qquad [4.24]$$

where a is the molecular size, b is the radius of the cylinder.

There was also plenty of research work on the equilibrium shapes of liquid drops on fibers (Neimark, 1999; McHale *et al.*, 1997, 1999, 2001; Quere, 1999; Bauer *et al.*, 2000; Bieker and Dietrich, 1998; McHale and Newton, 2002). It was reported that two distinctly different geometric shapes of droplet are possible: a barrel and a clam shell, as shown in Fig. [4.7].

In the absence of gravity, the equilibrium shape of a drop surface is such that the Laplace excess pressure, across the drop surface is everywhere constant, as shown in Equation [4.4]. (McHale *et al.* (2001) solved this equation for the axially symmetric barrel shape subject to the boundary condition that the profile of the fluid surface meets the solid at an angle given by the equilibrium contact angle θ:

$$\Delta P = \frac{2\gamma_{LV}(n - \cos\theta)}{x_1(n^2 - 1)} \qquad [4.25]$$

where $n = x_2/x_1$, is the reduced radius as shown in Fig. 4.7(a).

Their (McHale *et al.*, 1999) solution for the barrel shape droplet was subsequently used to compute the surface free energy, defined as

$$F = \gamma_{LV}A_{LV} + (\gamma_{SL} - \gamma_{SV})A_{SL} \qquad [4.26]$$

where A_{LV} and A_{SV} are the liquid/vapor and solid/liquid interfacial areas, respectively.

In contrast to the barrel-shape droplet problem, no solution to Laplace's equation for the asymmetric clam-shell shape is reported except for such numerical approaches as finite element methods (McHale and Newton, 2002). There are, however, papers discussing the roll-up (barrel to clam-shell) transition (McHale *et al.*, 2001, McHale and Newton, 2002) in the wetting process on a fiber.

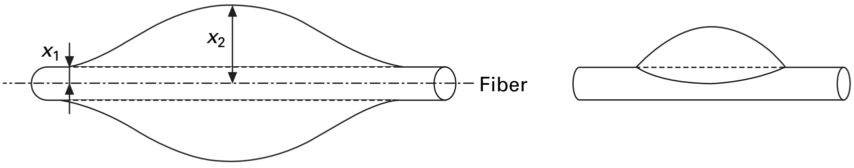

(a) Barrel shape (c) Clam-shell shape

4.7 Equilibrium liquid droplet shapes on a fiber.

In addition, there is work with respect to gravitational distortion of barrel-shape droplets on vertical fibers (Kumar and Hartland, 1990). To represent the heterogeneous nature of fibrous materials in the wetting process, Mullins *et al.* (2004) incorporated a microscopic study of the effect of fiber orientation on the fiber-wetting process when subjected to gravity, trying to account for the asymmetry of wetting behavior due to fiber orientation and gravity. The theory concerning the droplet motion and flow on fibers is based on the balance between drag force, gravitational force and the change in surface tension induced by the change in droplet profile as the fiber is angled. As a result, there comes out an angle where droplet flow will be maximized.

In reality, fibrous materials are porous media with *intricate*, *tortuous* and yet *soft* surfaces, further complicating the situation. As a result, a precise description of the structure of a fibrous material can be tedious. Therefore, much research work has adopted Darcy's law, an empirical formula that describes laminar and steady flow through a porous medium in terms of the pressure gradient and the intrinsic permeability of the medium (Yoshikawa *et al.*, 1992; Ghali *et al.*, 1994; Mao and Russell, 2003):

$$u = -\frac{K}{\mu}\nabla p \tag{4.27}$$

where u is the average velocity of liquid permeation into the fibrous material, μ the Newtonian viscosity of the liquid, K the permeability, and ∇p the pressure gradient. In the case of wetting, the driving pressure is usually the capillary pressure as calculated by the Laplace equation. The permeability K is either determined by experiments or by the empirical Kozeny–Carman relations as a function of fiber volume fraction (Mao and Russell, 2003).

Darcy's law reflects the relationship of pressure gradient and average velocity only on a macroscopic scale. To reach the microscopic details of the liquid wetting behavior in fibrous media, various computer simulation techniques have been applied in this field to accommodate more complexity so as to investigate more realistic systems, and to better understand and explain experimental results.

Molecular Dynamics (MD) and Monte Carlo (MC) are best-known, standard simulation formulae emerging from the last decades (Hoffmann and Schreiber, 1996) and, accordingly, most of the simulation for clarifying liquid wetting behaviors falls into these two categories.

Fundamentally, wetting behaviors of liquids in fibrous materials stem from interactions between liquid/solid and within the liquid at the microscopic level. The most important task for the various models and simulations is, therefore, to define and treat these interactions.

In Molecular Dynamics, all potentials between atoms, solid as well as liquid, are described with the standard pairwise Lennard–Jones interactions:

$$V_{ij}(r) = 4\varepsilon_{ij}\left(\left(\frac{\sigma_{ij}}{r}\right)^{12} - \left(\frac{\sigma_{ij}}{r}\right)^{6}\right) \qquad [4.28]$$

where r is the distance between any pair of atoms i and j, ε_{ij} is an energy scale (actually the minimum of the potential), and σ_{ij} is a length scale (the distance at which the potential diminishes to zero).

Large-scale MD simulations have been adopted to study the spreading of liquid drops on top of flat solid substrates (Semal *et al.*, 1999; van Remoortere *et al.*, 1999). If the system contains enough liquid molecules, the macroscopic parameters, such as the density, surface tension, viscosity, flow patterns and dynamic contact angle, can be 'measured' in the simulation.

However, the computational cost for MD simulations is huge, as they are dealing with the individual behaviors of a great number of single molecules. And, the application of MD simulations for liquid spreading on a fiber or transport in intricate fibrous structures is still pending, although there are already reports on microscopic understanding of wetting phenomena on cylindrical substrates for simple fluids whose particles are governed by dispersion forces and are exposed to long-ranged substrate potentials (Bieker and Dietrich, 1998). Based on a microscopic density functional theory, the effective interface potential for a liquid on a cylinder has been derived.

To solve the problem of huge computation, simulation techniques have been invented to cope with the so called 'cell', or small unit of the system, instead of single molecules. The statistical genesis of the process of liquid penetration in fibrous media can be regarded as the interactions and the resulting balance among the media and liquid cells that comprise the ensemble. This process is driven by the difference of internal energy of the system after and before a liquid moves from one cell to the other.

In the 1990s, Manna *et al.* (1992) presented a 2D stochastic simulation of the shape of a liquid drop on a wall due to gravity. The simulation was based on the so called Ising model and Kawasaki dynamics. Lukkarinen *et al.* (1995) studied the mechanisms of fluid droplets spreading on flat solids using a similar model. However, their studies dealt only with flow problems on a flat surface instead of a real heterogeneous structure. Only recently has the Ising model been used in the simulation of wetting dynamics in heterogeneous fibrous structures (Lukas *et al.*, 1997; Lukas and Pan, 2003; Zhong *et al.*, 2001a, 2001b).

As a 'meso-scale' approach, stochastic models and simulations deal with discrete and digitalized cells or subsystems instead of individual molecules. They lead to considerable reduction of computational cost, naturally.

4.4.3 Surface roughness and wetting

The Young's Equation [4.1] describes the mechanical balance at the triple line of the three-phase solid–liquid–vapor system. However, the equilibrium contact angle θ in the equation can be obtained only experimentally on a perfectly smooth and homogeneous surface. In the real world, the roughness and heterogeneity of the solid surface produces the contact angle hysteresis (de Gennes, 1985):

$$\Delta\theta = \theta_a - \theta_r \geq 0 \qquad [4.29]$$

The advancing angle θ_a is measured when the solid–liquid contact area increases, while the receding angle θ_r is measured when the contact area shrinks, as shown in Fig. 4.8. The equilibrium contact angle lies between them:

$$\theta_r < \theta < \theta_a \qquad [4.30]$$

The most important source of contact angle hysteresis is the surface roughness. Early studies on the effect of surface roughness concentrated on periodic surfaces, such as a surface with parallel grooves (Cox, 1983; Oliver *et al.*, 1977). In the simplest case where the triple line is parallel to the grooves, as shown in Fig. 4.9, the energy barrier for liquid spreading over a ridge of the rough surface can be computed numerically. When the grooves are rather deep, vapor bubbles may be trapped at the bottom of the grooves, as shown in Fig. 4.9(b). These vapor bubbles would lead to much smaller barriers, which was also observed in experimental work. With the increase of roughness, that is, with the increase of the depth of the grooves, there is first a corresponding decrease of receding angle θ_r; but when the grooves become deep enough, θ_r increases as the entrapped vapor bubbles reduce the barriers (de Gennes, 1985).

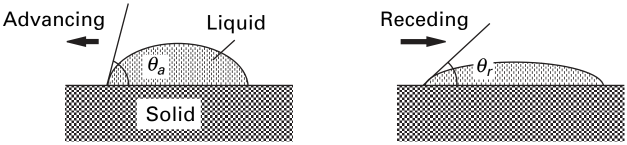

4.8 Advancing and receding contact angles for a liquid on a solid surface.

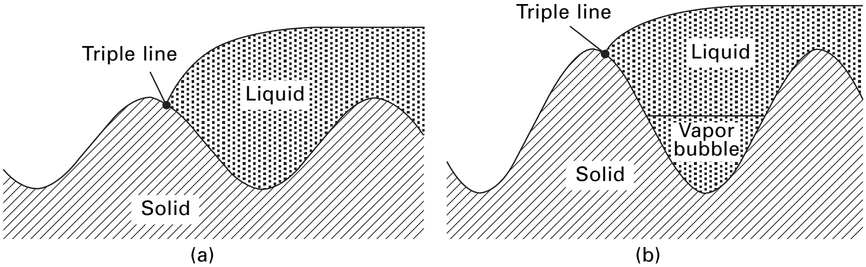

4.9 Wetting of rough surfaces without and with vapor bubbles.

A more realistic representation of a rough surface is a random surface (Joanny and de Gennes, 1984). The irregularities of the surface can be defined in a random function $h(x, y)$. Consider a single 'defect', which is defined as a perturbation $h(x, y)$ localized near a particular point (x_d, y_d) and with finite linear dimension d, as shown in Fig. 4.10. A triple line becomes anchored to the defect. Far from the defect, the line coincides with $y = y_L$. An approximation of the total force f exerted by the defect on the line is:

$$f(y_m) = \int_{-\infty}^{\infty} dxh(x, y_m) \tag{4.31}$$

Assuming a Gaussian defect,

$$h(x, y) = h_0 \exp\left[-\frac{(x - x_d)^2 + (y - y_d)^2}{2d^2}\right] \tag{4.32}$$

The force $f(y_m)$ is also Gaussian:

$$f(y_m) = (2\pi)^{1/2}\ h_0 d \exp\left[-\frac{(y_m - y_d)^2}{2d^2}\right] \tag{4.33}$$

In equilibrium, the force expressed in Equation [4.33] is balanced by an elastic restoring force f_e, which tend to bring y_m back to the unperturbed line position y_L. Assume that this has the simple Hooke form:

$$f_e = k(y_L - y_m) \tag{4.34}$$

Therefore:

$$k(y_L - y_m) = f(y_m) \tag{4.35}$$

The equation can be solved graphically in Fig. 4.11. When the magnitude of the defect h_0 is small, there is only one root y_m for any specified y_L, and no

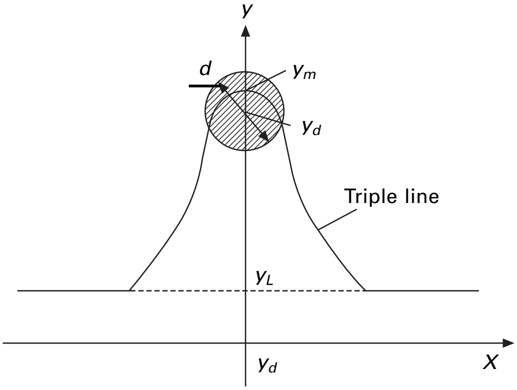

4.10 A triple line anchored in a defect.

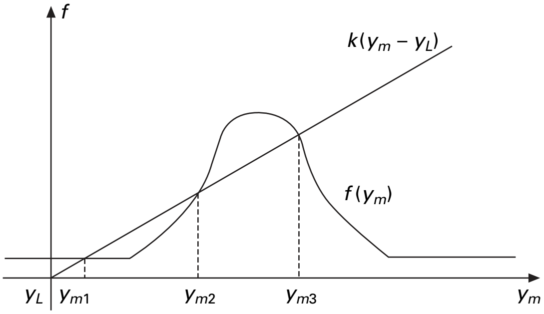

4.11 Equilibrium positions of a triple line in the presence of a local defect.

hysteresis. If h_0 reaches a certain threshold, there are three roots for a specified y_L, and hysteresis occurs. This means that weak perturbation create no hysteresis. Accordingly, for a good determination of equilibrium contact angle, a surface with irregularities below a certain threshold would be enough if an ideal surface is not available.

The above arguments can be further extended to a dilute system of defects. However, it only applies to defects with diffuse edges. The case of shaped edge defects, where the function $h(x, y)$ has step discontinuities, is a completely different story. Hysteresis can happen for very small h_0.

An alternative approach to study the influence of surface roughness on the contact angle hysteresis is to examine the Wenzel's roughness factor r^W, defined as (Wenzel, 1936):

$$r^W = \frac{A_{\text{real}}}{A_{\text{geom}}} = \frac{A_{\text{real}}}{bl} \geq 1 \qquad [4.36]$$

where A_{real} is the real area of the rough solid surface of width b and length l. And the measured contact angle, or Wenzel angle θ^W, is given by

$$\cos \theta^W = r^W \cos \theta \qquad [4.37]$$

Introducing equation [4.37] into the Young's equation [4.1]:

$$r^W(\gamma_{SV} - \gamma_{SL}) = \gamma_{LV} \cos \theta^W \qquad [4.38]$$

An empirical 'friction force' F was used by good (1952) to explain the contact angle hysteresis:

$$r^W(\gamma_{SV} - \gamma_{SL}) = \gamma_{LV} \cos \theta_a + F \qquad [4.39]$$

$$r^W(\gamma_{SV} - \gamma_{SL}) = \gamma_{LV} \cos \theta_r - F \qquad [4.40]$$

F reflects the influence of the surface roughness on the triple line. If F is assumed to be the same for both wetting and de-wetting processes, it is obtained that

$$2r^W(\gamma_{SV} - \gamma_{SL}) = \gamma_{LV}\,(\cos\,\theta_a + \cos\,\theta_r) \qquad [4.41]$$

Combining Equations [4.37], [4.38] and [4.41] gives an expression to derive the equilibrium contact angle from the advancing and receding angles:

$$\cos\,\theta = \frac{\cos\,\theta_a + \cos\,\theta_r}{2r^W} \qquad [4.42]$$

According to Equation [4.36], the Wenzel roughness factor r^W can be determined by appropriate scanning force microscopy (SFM) (Kamusewitz and Possart, 2003) or atomic force microscopy (AFM) (Semal *et al.*, 1999) measurement of the surface topography of the solid. In general, it is agreed that contact angle hysteresis increases steadily with the microroughness of the solid surface.

4.5 Summary

Surface tensions, wicking and/or wetting are among the most frequently encountered phenomena when processing and using fibrous materials. Wetting is a process of displacing a solid–air interface with a solid–liquid interface, while wicking is a result of spontaneous wetting in a capillary system.

The physical bases of surface tension, wetting and wicking are those molecular interactions within a solid or liquid, or across the interface between liquid and solid. These adhesive forces include the Lifshitz–Van de Waals interactions and acid–base interactions. The Lifshitz–Van de Waals (LW) interactions are general, long-range forces which always operate in all materials and across phase boundaries. The Lewis acid–base (AB) interactions are polar, short-range interactions that occur only when an acid (electron acceptor) and a base (electron donor) are brought close together. Existence of acid–base interactions can substantially improve wetting and adhesion between two surfaces.

Wetting and wicking behaviors are determined by surface tensions (of solid and liquid) and liquid/solid interfacial tensions. Curvature and roughness of contact surfaces are two critical factors for wetting phenomena, especially in the case of wetting in fibrous materials, which are porous media of intricate, tortuous and yet soft, rough structure. A liquid that fully wets a material in the form of a smooth planar surface may not wet the same material when presented as a smooth fiber surface, let alone a real fibrous structure. To reach the microscopic details of the liquid wetting behaviors in fibrous media, various computer simulation techniques have been applied in this field to accommodate more complexity so as to investigate more realistic systems, and to better understand and explain experiment results. On the other hand, the surface roughness is the most important source of contact angle hysteresis. In general, it is agreed that contact angle hysteresis increases steadily with microroughness of solid surface.

4.6 References

Adamson, A. W. and Gast, A. P. (1997) *Physical Chemistry of Surfaces*, New York, Wiley.

Bauer, C., Bieker, T. and Dietrich, S. (2000) Wetting-induced effective interaction potential between spherical particles. *Physical Review E*, **62**, 5324–5338.

Bieker, T. and Dietrich, S. (1998) Wetting of curved surfaces. *Physica A – Statistical Mechanics and Its Applications*, **252**, 85–137.

Brochard-wyart, F., Dimeglio, J. M., Quere, D. and de Gennes, P. G. (1991) Spreading of nonvolatile liquids in a continuum picture. *Langmuir*, **7**, 335–338.

Brochard, F. (1986) Spreading of liquid-drops on thin cylinders – the Manchon–Droplet transition. *Journal of Chemical Physics*, 84, 4664–4672.

Chehimi, M. M., Cabet-Deliry, E., Azioune, A. and Abel, M. L. (2002) Characterization of acid–base properties of polymers and other materials: relevance to adhesion science and technology. *Macromolecular Symposia,* **178**, 169–181.

Cox, R. G. (1983) The spreading of a liquid on a rough solid-surface. *Journal of Fluid Mechanics*, **131**, 1–26.

de Gennes, P.-G., Brochard-Wyart, F. and Quere, D. (2004) *Capillarity and Wetting Phenomena: Drops, Bubbles, Pearls, Waves* New York, Springer.

de Gennes, P. G. (1985) Wetting – statics and dynamics. *Reviews of Modern Physics*, **57**, 827–863.

Fowkes, F. M. (1962) Determination of interfacial tensions, contact angles, and dispersion forces in surfaces by assuming additivity of intermolecular interactions in surfaces. *Journal of Physical Chemistry*, **66**, 382.

Fowkes, F. M. and Zisman, W. A. (1964) *Contact Angle, Wettability and Adhesion: The Kendall Award Symposium Honoring William A. Zisman,* Washington, American Chemical Society.

Garbassi, F., Morra, M. and Occhiello, E. (1998) *Polymer Surfaces: From Physics to Technology*, Chichester, England; New York, Wiley.

Ghali, K., Jones, B. and Tracy, J. (1994) Experimental techniques for measuring parameters describing wetting and wicking in fabrics. *Textile Research Journal*, **64**, 106–111.

Good, R. J. (1952) A thermodynamic derivation of Wenzel's modification of Young's equation for contact angle, together with a theory of hysteresis. *Journal of the American Chemistry Society* **74**, 5041–5042.

Good, R. J. (1992) Contact angle, wetting, and adhesion – a critical review. *Journal of Adhesion Science and Technology*, **6**, 1269–1302.

Good, R. J. and Chaudhury, M. K. (1991) Theory of adhesive forces across interfaces: 1. The Lifshitz – van der Waals component of interaction and adhesion, in Lee, L. H. (Ed.) *Fundamentals of Adhesion* Plenum Press.

Good, R. J., Chaudhury, M. K. and Van OSS, C. J. (1991) Theory of adhesive forces across interfaces: 2. Interfacial hydrogen bonds as acid–base phenomena and as factors enhancing adhesion, in Lee, L. H. (Ed.) *Fundamentals of Adhesion*, Plenum Press.

Greiveldinger, M. and Shanahan, M. E. R. (1999) A critique of the mathematical coherence of acid base interfacial free energy theory. *Journal of Colloid and Interface Science*, **215**, 170–178.

Hamaker, H. C. (1937) The London van der Waals attraction between spherical particles. *Physica*, **4**, 1058–1072.

Hoffmann, K. H. and Schreiber, M. (1996) *Computational Physics: Selected Methods, Simple Exercises, Serious Applications,* Berlin; New York, Springer.

Israelachvili, J. N. (1991) *Intermolecular and Surface Forces,* London; San Diego, CA, Academic Press.

Joanny, J. F. and de Gennes, P. G. (1984) A model for contact-angle hysteresis. *Journal of Chemical Physics*, **81**, 552–562.

Kamusewitz, H. and Possart, W. (2003) Wetting and scanning force microscopy on rough polymer surfaces: Wenzel's roughness factor and the thermodynamic contact angle. *Applied Physics A – Materials Science and Processing*, **76**, 899–902.

KISSA, E. (1996) Wetting and wicking. *Textile Research Journal*, **66**, 660–668.

Kumar, A. and Hartland, S. (1990) Measurement of contact angles from the shape of a drop on a vertical fiber. *Journal of Colloid and Interface Science*, **136**, 455–469.

Kwok, D. Y., Lee, Y. and Neumann, A. W. (1998) Evaluation of the Lifshitz–van der Waals acid–base approach to determine interfacial tensions. 2. Interfacial tensions of liquid–liquid systems. *Langmuir*, **14**, 2548–2553.

Kwok, D. Y., Li, D. and Neumann, A. W. (1994) Evaluation of the Lifshitz–van der Waals acid–base approach to determine interfacial tensions. *Langmuir*, **10**, 1323–1328.

Lee, L. H. (1993) Roles of molecular interactions in adhesion, adsorption, contact-angle and wettability. *Journal of Adhesion Science and Technology*, **7**, 583–634.

Leon, V. (2000) The mechanical view of surface tension is false. *Journal of Dispersion Science and Technology*, **21**, 803–813.

Lukas, D., Glazyrina, E. and Pan, N. (1997) Computer simulation of liquid wetting dynamics in fiber structures using the Ising model. *Journal of the Textile Institute*, **88**, 149–161.

Lukas, D. and Pan, N. (2003) Wetting of a fiber bundle in fibrous structures. *Polymer Composites*, **24**, 314–322.

Lukkarinen, A., Kaski, K. and Abraham, D. B. (1995) Mechanisms of fluid spreading – Ising model simulations. *Physical Review E*, **51**, 2199–2202.

Manna, S. S., Herrmann, H. J. and Landau, D. P. (1992) A stochastic method to determine the shape of a drop on a wall. *Journal of Statistical Physics*, **66**, 1155–1163.

Mao, N. and Russell, S. J. (2003) Anisotropic liquid absorption in homogeneous two-dimensional nonwoven structures. *Journal of Applied Physics*, **94**, 4135–4138.

McHale, G., Kab, N. A., Newton, M. I. and Rowan, S. M. (1997) Wetting of a high-energy fiber surface. *Journal of Colloid and Interface Science*, **186**, 453–461.

McHale, G. and Newton, M. I. (2002) Global geometry and the equilibrium shapes of liquid drops on fibers. *Colloids and Surfaces a-Physicochemical and Engineering Aspects*, **206**, 79–86.

McHale, G., Newton, M. I. and Carroll, B. J. (2001) The shape and stability of small liquid drops on fibers. *Oil and Gas Science and Technology – Revue de L' Institut Français du Petrole*, **56**, 47–54.

McHale, G., Rowan, S. M., Newton, M. I. and Kab, N. A. (1999) Estimation of contact angles on fibers. *Journal of Adhesion Science and Technology*, **13**, 1457–1469.

Mullins, B. J., Agranovski, I. E., Braddock, R. D. and Ho, C. M. (2004) Effect of fiber orientation on fiber wetting processes. *Journal of Colloid and Interface Science*, **269**, 449–458.

Neimark, A. V. (1999) Thermodynamic equilibrium and stability of liquid films and droplets on fibers. *Journal of Adhesion Science and Technology*, **13**, 1137–1154.

Oliver, J. F., Huh, C. and Mason, S. G. (1977) The apparent contact angle of liquids on finely-grooved solid surfaces – a SEM study. *Journal of Adhesion*, **8**, 223–234

Quere, D. (1999) Fluid coating on a fiber. *Annual Review of Fluid Mechanics*, **31**, 347–384.

Semal, S., Blake, T. D., Geskin, V., de Ruijter, M. J., Castelein, G. and de Coninck, J. (1999) Influence of surface roughness on wetting dynamics. *Langmuir*, **15**, 8765–8770.

van OSS, C. J. (1993) Acid–base interfacial interactions in aqueous media. *Colloids and Surfaces A – Physicochemical and Engineering Aspects*, **78**, 1–49.

van OSS, C. J., Chaudhury, M. K. and Good, R. J. (1987a) Monopolar Surfaces. *Advances in Colloid and Interface Science*, **28**, 35–64.

van OSS, C. J., Giese, R. F. and Good, R. J. (1990) Reevaluation of the surface tension components and parameters of polyacetylene from contact angles of liquids. *Langmuir*, **6**, 1711–1713.

van OSS, C. J., Ju, L. K., Good, R. J. and Chaudhury, M. K. (1987b) Negative interfacial tensions between polar liquids and some polar surfaces 2. Liquid surfaces. *Abstracts of Papers of the American Chemical Society*, **193**, 172–COLL.

van Remoortere, P., Mertz, J. E., Scriven, L. E. and Davis, H. T. (1999) Wetting behavior of a Lennard–Jones system. *Journal of Chemical Physics*, **110**, 2621–2628.

Wennerstrom, H. (2003) The van der Waals interaction between colloidal particles and its molecular interpretation. *Colloids and Surfaces A – Physicochemical and Engineering Aspects*, **228**, 189–195.

Wenzel, R. N. (1936) Resistance of solid surface to wetting by water. *Industrial and Engineering Chemistry* **28**, 988.

WU, S. (1982) *Polymer Interface and Adhesion,* New York, Marcel Dekker.

Yoshikawa, S., Ogawa, K., Minegishi, S., Eguchi, T., Nakatani, Y. and Tani, N. (1992) Experimental study of flow mechanics in a hollow-fiber membrane module for plasma separation. *Journal of Chemical Engineering of Japan*, **25**, 515–521.

Zhong, W., Ding, X. and Tang, Z. L. (2001a) Modeling and analyzing liquid wetting in fibrous assemblies. *Textile Research Journal*, **71**, 762–766.

Zhong, W., Ding, X. and Tang, Z. L. (2001b) Statistical modeling of liquid wetting in fibrous assemblies. *Acta Physico-Chimica Sinica*, **17**, 682–686.

Zhong, W., Ding, X. and Tang, Z. L. (2002) Analysis of fluid flow through fibrous structures. *Textile Research Journal*, **72**, 751–755.

Zisman, W. A. (1964) Contact angle, wettability and adhesion, in Fowkes, F. M. (Ed.) *Advances in Chemistry Series.* American Chemical Society, Washington, D. C.

5

Wetting phenomena in fibrous materials

R. S. RENGASAMY, Indian Institute of Technology, India

5.1 Introduction

Wetting of fibrous materials is important in a diverse range of applications in textile manufacture such as desizing, scouring, bleaching, dyeing and spin-finish application, cleaning, coating and composite manufacture. Clothing comfort also depends on wetting behavior of fibrous structure. In fibre composites, the adhesion between the fibers and resin is influenced by the initial wetting of the fibers by resin, which governs the resin penetration into the voids between the fibers and subsequently the performance of the composites. On the other hand, surgical fabrics should not let liquid and solid particles pass through easily. Wetting processes are considered extremely important in the application of fibrous filters, where wetting of the fibre surface is the key mechanism for the separation of two different liquids from their mixture; for instance, in separating oil from sea-water during a cleaning process after an oil spillage. Wetting and wicking behavior of the fibrous structures is a critical aspect of the performance of products such as sports clothes, hygiene disposable materials, and medical items.

Wetting is a complex process complicated further by the structure of the fibrous assembly. Fibrous assemblies do not meet the criteria of ideal solids. Most practical surfaces are rough and heterogeneous to some extent. Fibers are no exception to this. In addition, curvature of fibers, crimps on fibers, and orientation and packing of fibers in fibrous materials make evaluation of wetting phenomena of fibrous assemblies more complicated.

5.2 Surface tension

A molecule on the surface of a liquid experiences an imbalance of forces due to the presence of free energy at the surface of the liquid which tends to keep the surface area of the liquid to a minimum and restrict the advancement of the liquid over the solid surface. This can be conceived as if the surface of a liquid has some kind of contractable skin. The surface energy is expressed per unit area. Precise measurement of surface energy is not generally possible; the term surface tension refers to surface energy quantified as force per length (mN/m or dynes/cm). For a liquid to wet a solid completely or for the solid to be submerged in a liquid, the solid surfaces must have sufficient surface energy to overcome the free surface energy of the liquid.

When a liquid drop is placed on an ideal flat solid surface (i.e. smooth, homogeneous, impermeable and non-deformable), the liquid drop comes to an equilibrium state corresponds to minimization of interfacial free energy of the system. The forces involved in the equilibrium are given by the well-known Young's equation:

$$\gamma_{SV} - \gamma_{SL} = \gamma_{LV} \cos \theta \qquad [5.1]$$

The terms γ_{SV}, γ_{SL}, and γ_{LV} represent the interfacial tensions that exists between the solid and vapor, solid and liquid and liquid and vapor respectively. The last term is also commonly referred as the surface tension of the liquid. θ is the equilibrium contact angle. The term '$\gamma_{LV} \cos \theta$', is the 'adhesion tension' or 'specific wettability'. Young's equation has been widely used to explain wetting and wicking phenomena.

Contact angle is the consequences of wetting, not the cause of it, and is determined by the net effect of three interfacial tensions. For a hydrophilic regime, γ_{SV} is larger than γ_{SL} and the contact angle θ lies between 0 and 90°, i.e. cos θ is positive. For a hydrophobic regime, γ_{SV} is smaller than γ_{SL}, and the contact angle lies between 90° and 180°. With increasing wettability, the contact angle decreases and cos θ increases. Complete wetting implies a zero contact angle, but equating $\theta = 0$ may lead to incorrect conclusions and it is better to visualize that, when the contact angle approaches zero, wettability has its maximum limit.[1] A lower contact angle for water wets the surface and at high contact angle water run off the surface. According to Adam,[2] equilibrium condition cannot exist when the contact angle is zero, and Equation [5.1] does not apply.

The equilibrium contact angle is the single valued intrinsic contact angle described by the Young equation for an ideal system. An experimentally observed contact angle is an apparent contact angle, measured on a macroscopic scale, for example, through a low-power microscope. On rough surfaces, the difference between the apparent and intrinsic contact angles can be considerable.[3]

Immersion, capillary sorption, adhesion, and spreading are the primary processes involved in wetting of fibrous materials. A solid–liquid interface replaces the solid–vapor interface during immersion and capillary penetration/sorption. For spontaneous penetration, the work of penetration has to be positive. Work of adhesion, W_A, is equal to the change of surface free energy of the system when the contacting liquid and the solid are separated:

$$W_A = \gamma_{SV} + \gamma_{LV} - \gamma_{SL} = \gamma_{LV} (1 + \cos \theta) \qquad [5.2]$$

During spreading, the solid–liquid and liquid–vapor interfaces increase, whereas the solid–vapor interface decreases. For spreading to be spontaneous, the work of spreading or the spreading coefficient, W_S, has to be positive, which is related as:

$$W_S = \gamma_{SV} - \gamma_{LV} - \gamma_{SL} \tag{5.3}$$

5.3 Curvature effect of surfaces

5.3.1 Wetting of planar surfaces

For a sufficiently small drop of a partial wetting or non-wetting liquid placed on a planar surface, gravity effects can be neglected. For such a drop, hydrostatic pressure inside the drop equilibrates and the drop adopts a shape to conform to the Laplace law:

$$\Delta P = \gamma_{LV}(1/R_1 + 1/R_2) \tag{5.4}$$

where ΔP is the pressure difference between two sides of a curved interface characterized by the principal radii of curvature R_1 and R_2. The drop shape would be spherical. For complete wetting of a flat surface, this pressure can be reduced towards zero by simultaneously increasing both R_1 and R_2 conserving the volume of the liquid.

5.3.2 Wetting of curved surfaces

A fluid that fully wets a material in the form of smooth planar surface may not wet the same material if it is presented as a smooth fiber form. On a flat surface, vanishing contact angle is a sufficient condition for the formation of a wetting film. On a chemically identical fiber surface, the indefinite spreading is inhibited and the equilibrium is not necessarily a thin sheathing film about the fiber, but can have a microscopic profile. This shows that vanishing contact angle is not a sufficient condition for the formation of a wetting film on a fiber. The Laplace excess pressure inside a liquid drop resting on a fiber is:

$$\frac{1}{R_\perp} + \frac{1}{R_{II}} = \frac{\Delta P}{\gamma} \tag{5.5}$$

The two radii of curvature $R_\perp$ and R_{II} of a drop, are measured normal to and along the fiber axis respectively. For a droplet on a fiber, the radii of curvature cannot both be increased while maintaining the volume of liquid. It is necessary to reduce one radius of curvature as the other is increased. Nevertheless, the excess pressure given by the Laplace law can still be reduced toward zero, although not to zero, by making R_{II} negative. The other radius $R_\perp$ cannot be reduced below the radius of curvature of the fiber; a minimization of the excess pressure can be obtained while maintaining finite values for the radii of curvature.

5.3.3 Wetting of fiber surfaces

In the case of fiber, three distinct droplet configurations are observed, as shown in Fig. 5.1: a series of axisymmetrical 'barrel' shaped (unduloid) droplets around the fiber, commonly connected by a film in the order of a nanometer (Configuration I); axially asymmetric 'clam-shell' shaped droplets around the fiber (Configuration II), the flow usually being broken into distinct droplets by Rayleigh instability; and a sphere for a non-wetting liquid (Configuration III). The droplet-on-fiber system becomes a droplet-on-a-plane-surface in the limiting case of an extremely large fiber radius (very low fiber curvature). It has been shown that barrel-shaped droplets, even under vertical fibers, becomes axially asymmetric under the influence of drag forces.[4]

On a fiber, the equilibrium shape of a barreling droplet is only approximately a spherical cap rotated about the axis of the fiber. Under certain conditions, the curvature goes through a point of inflexion as it approaches the solid surface at the three-phase interface, before then changing the sign of curvature as shown in Fig. 5.2.

For a high-energy fiber, when the diameter of the fiber reduces, the inflection angle increases and the transition to the lower value of contact angle occurs very rapidly as the drop profile nears the fiber surface. This makes the measurement of contact angle difficult. An improved estimation of the equilibrium contact angle can be obtained by measuring the inflection angle, and the reduced length and thickness of the droplets.

Transition or roll-up from one conformation to other can occur. It is reported that for large drops with contact angle < 90°, barrel shapes will be stable for any fiber radius.[7] The parameters that influence the roll-up process have been investigated by Briscoe *et al*.[5] Increasing the parameters of contact

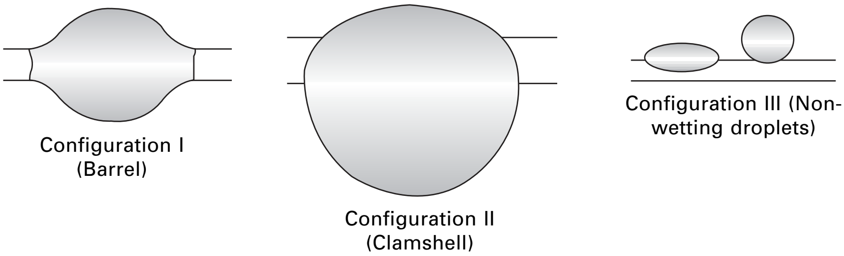

5.1 Droplets shapes on fiber. Reprinted from *Colloids and Surfaces*, Vol. 56, B. J. Briscoe, K. P. Galvin, P. F. Luckham, and A. M. Saeid, pp. 301–312, Copyright (1991), with permission from Elsevier.

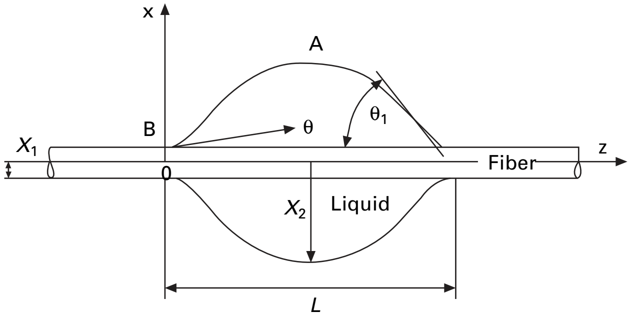

5.2 Geometrical parameters for the description of a drop on a single fiber. X_1 is the fiber radius; X_2, the maximum drop height; θ, the contact angle; θ_1 the inflection angle; and L the drop length 'Reprinted from *International Journal of Adhesion and Adhesives*, Vol. 19, S. Rebouillat, B. Letellier, and B. Steffenino, pp. 303–314, Copyright (1999), with permission from Elsevier'.

angle, surface tension of liquid and diameter of fibers, or reducing the volume of the droplets favors change of confirmation of droplets from Configuration I to III. Local surface anomalies due to chemical or physical heterogeneity can lead to two completely different droplet profiles on the same fiber.

5.3.4 Role of droplet shapes in wet fiber filtration

The formation of droplets of different shapes has a significant role in influencing the efficiency of wet-fiber filters in removing sticky and viscous particles. During wet filtration of solid or liquid aerosols, droplets attached to the fibers are observed to rotate under the influence of induced airflow. Barrel-shaped droplets, being smaller in size, rotate as a rigid body and the droplets laden with particles frequently flow down the fiber under gravity. The larger droplets, i.e. clamshells, have significant capacity to contain particulates, but rotate like less rigid bodies and can flow-off the fiber rather than flowing down with entrained particles. This is not advantageous in self-cleaning as it is likely to lead to re-entrainment of the particles back into the air stream.[8]

5.4 Capillarity

Transport of a liquid into a fibrous assembly may be caused by external forces or by capillary forces only. In most of the wet processing of fibrous materials, uniform spreading and penetration of liquids into pores are essential for the better performance of resulting products.[9] Capillarity falls under the general framework of thermodynamics that deals with the macroscopic and statistical behavior of interfaces rather than with the details of their molecular structure.[10] The interfaces are in the range of a few molecular diameters.

Wicking is one example of the more general set of phenomena termed 'capillarity'. For wicking to be significant, the ratio of solid–liquid (*SL*) interfacial area to liquid volume must be large. Wicking can only occur when a liquid wets fibers assembled with capillary spaces between them. The resulting capillary forces drive the liquid into the capillary spaces, increasing the solid–liquid interface and decreasing the solid–air interface. For the process to be spontaneous, free energy has to be gained and the work of penetration has to be positive, i.e. γ_{SV} must exceed γ_{SL}.

5.4.1 Capillary flow

When a liquid in a capillary wets the walls of the capillary, a meniscus is formed. The pressure difference ΔP across the curved liquid–vapor interface driving the liquid in a small circular capillary of radius r, is related as:

$$\Delta P = 2\gamma_{LV} \cos \theta / r \qquad [5.6]$$

For a positive capillary pressure, the values of θ have to be between 0° and 90°. Accordingly, the smaller the pore size, the greater is the pressure within the capillary, and so the smallest fill first. During draining of the capillary under external pressure, the smaller pores drain last. For most systems, wicking does not occur when the contact angle is between 90 to 180°. According to Marmur,[11] partial penetration of the capillary can occur even if the contact angle is 90°, provided the pressure within the bulk of the liquid is substantial enough to force the liquid into the capillary. This occurs only when the liquid reservoir is small, i.e. a drop of liquid. In a drop of liquid, the radius of curvature of the drop can be high enough such that the pressure directly outside of the capillary is increased, and thus the pressure difference, leading to penetration of liquid into the capillary.

The flow in a porous medium is considered as flow through a network of interconnected capillaries. The Lucas–Washburn equation[12] is widely used to describe this flow,

$$dh/dt = \frac{\gamma_{LV} r \cos \theta}{4\eta h} - r^2 \rho_L g / 8\eta \qquad [5.7]$$

The first term on the right side of the equation accounts for the spontaneous uptake of liquid into the material while the second term accounts for the gravitational resistance. The second term in the above equation is negligible if either the flow is horizontal or r is very small ($r^2 = 0$). The term h is the distance that the liquid has traveled at time t; and ρ_L and η are the density and viscosity of the liquid, respectively. When the capillary forces are balanced by the gravitational forces, liquid rise stops and equilibrium is reached as given by:

$$\gamma_{LV} \cos \theta \, 2\pi r = \pi r^2 \rho_L g h \qquad [5.8]$$

Hence, equilibrium wicking height is:

$$h_{eq} = 2\gamma_{LV} \cos \theta / r\rho_L g \qquad [5.9]$$

The linear rate of liquid flow (u) is:

$$u = dh/dt = r\gamma_{LV} \cos \theta / 4\eta\, h \qquad [5.10]$$

5.4.2 Wicking in fibrous materials

In the case of capillarity in fibrous assemblies, the term 'wicking' is used in a broader practical sense to describe two kinetically different processes: a spontaneous flow of a liquid within the capillary spaces accompanied by a simultaneous diffusion of the liquid into the interior of the fibers or a film on the fibers.[13] If the penetration of liquid is limited to the capillary spaces and the fibers do not imbibe the liquid, the wicking process is termed 'capillary penetration' or 'capillary sorption'. Swelling of the fibers caused by the sorption of the liquid into the fibers can reduce capillary spaces between fibers and change the kinetics of wicking. The interpretation of wetting results can be misleading if the effects of sorption in fibers or finishes on fibers are overlooked.[14]

For a theoretical treatment of capillary flow in fabrics, the fibrous assemblies are usually considered to have a number of parallel capillaries. The advancement of the liquid front in a capillary can be visualized as occurring in small jumps. The fibrous assembly is a non-homogeneous capillary system due to irregular capillary spaces having various dimensions and discontinuities of the capillaries leading to small jumps in the wetting front. The capillary spaces in yarns and fabrics are not uniform, and an indirectly determined effective capillary radius has to be used instead of the radius r.[15]

Fibers in textile assemblies form capillaries of effective radius r_e so the horizontal liquid transport rate becomes:

$$h^2 = \frac{\gamma_{LV} \cos \theta_a' r_e t}{2\eta} = k_s t \qquad [5.11]$$

where k_s is the capillary liquid transport constant for the penetration of a liquid into a definite fiber assembly.[16]

Equation [5.11] applies only to a system where the free surface of the liquid reservoir feeding the capillary tube is substantially flat, i.e. the capillary pressure on the reservoir surface is zero.[17] According to Lucas–Washburn, neglecting gravitational forces, the wicking height h is directly proportional to the square root of time t:[18]

$$h = (r\gamma_{LV} \cos \theta / 2\tau^2 \eta)^{1/2} t^{1/2} = kt^{1/2} \qquad [5.12]$$

where $h\tau$ is the actual distance traveled, τ is the tortuosity factor.

The Lucas–Washburn equation is used primarily to describe flow into vertically hung materials and it has been shown to be a good estimate of the flow rate within many textile materials. According to the Lucas–Washburn equation, the liquid uptake into the material is in direct correlation with the product of γ_{LV} and $\cos\theta$. If the contact angle is very large, use of surfactants will improve liquid uptake; on the other hand, if the initial contact angle before addition of surfactant is very low, adding surfactant only reduces the value γ_{LV} to a greater extent than it increases the $\cos\theta$ value. As a result, the product $\gamma_{LV}\cos\theta$ reduces, lowering the wicking rate.

The Lucas–Washburn equation has been extended for the case of radial expansion of a wicking liquid originating at the centre of a flat sample, relating liquid mass uptake m_A, the distance traveled by the liquid L and a constant K as[19]:

$$dm_A/dt = (K/m_A) - L \qquad [5.13]$$

Most textile processes are time limited, and often the rate of wicking is therefore very critical. However, the wicking rate is not solely governed by interfacial tension and the wettability of the fibers, but by other factors as well. The mechanisms of water transport for an isolated single fiber differs from water sorption in a fiber bundle or assembled fibers where capillary spaces exist.[20] Ito and Muraoka[21] have reported that water transport is suppressed as the number of fibers in the yarn decreases. When the number of fibers is greater, water moves along even untwisted fibers. But when the number of fibers is reduced, wicking occurs only for twisted fibers and, if reduced further, wicking may not occur at all. This indicates that sufficient number and continuity of pores are important for wicking.

5.4.3 Wicking in yarns

A yarn may be assumed to have oriented cylindrical fibers. Lord[22] has discussed a theory for yarn wicking. Using hydraulic radius theory for an assembly of parallel cylindrical fibers, the value of the hydraulic mean radius r_m is:

$$r_m = \frac{A_f}{2\pi r_f n} = (K_p K_c)\frac{r_f}{2} \qquad [5.14]$$

A correction factor K_c is applied in the above equation for cases when the fibers are not cylindrical or inclined to the axis of the yarn. In the above equation: A_f is area of fluid between fibers of a yarn, K_p is packing factor, r_f = radius of fiber, and n = number of fibers in the yarn cross-section. Equivalent wicking height is given by:

$$h' = \frac{2\gamma_{LV}\cos\theta}{\rho_L g K_c K_p r_f} \qquad [5.15]$$

For a given fiber and liquid, $2\gamma_{LV}$ cos $\theta/\rho_L g r_f$ is constant, and hence, $h\alpha(K_c K_p)^{-1}$

Both K_c and K_p are functions of twist multiple, fiber type, and packing and migration of fibers in the yarn, which are related to yarns produced by different technologies.

The presence of smaller pores at the core of the open-end yarn wicks dye solution to a greater height. The wicking rate and equilibrium height observed for ring yarn is higher than that of compact yarns. This indicates that the number of pores, pore size and continuity are important factors in yarn wicking.[23] The orientation of fibers in a yarn influences wicking. In air-jet textured yarns, the presence of long, drawn-out loops such as floats and arcs offers a less tortuous path for the liquid to travel; as a result, a greater percentage of floats and arcs leads to a higher wicking height. The equilibrium wicking height and wicking rate are higher for air-jet textured yarn than for the corresponding feeder yarn. Equilibrium wicking height initially increases and then decreases with increasing tension on the yarns during wicking. The initial increase in height is due to partial alignment of the filaments; further increase in tension may bring the filaments closer to each other, reducing the capillary radii and possibly discontinuity in the capillaries.[24] The packing density of the filaments influences more greatly the wicking in crenulated viscose filaments than in circular nylon filaments. Viscose filaments under loose condition show abnormally high wicking; when the packing of filaments increases, the crenulations mesh like gear teeth, the open space reduces greatly without any corresponding reduction in the yarn diameter, and thus the wicking rate diminishes.[17]

5.4.4 Wicking in fabrics

When a liquid drop is placed on a fabric, it will spread under capillary forces. The spreading process may be split conveniently into two phases: I liquid remains on the surface, and II liquid is completely contained within the substrate, as suggested by Gillespie.[25] For two-dimensional circular spreading in textiles during phase II, Kissa[26] developed Gillespie's equation to propose the following exponential sorption:

$$A = K(\gamma_{LV}/\eta)^u V^m t^n \qquad [5.16]$$

where A is the area covered by the spreading liquid, K is the capillary sorption coefficient, η is the viscosity of the liquid, V is the volume of the liquid, t is the spreading time.

Wicking occurs when a fabric is completely or partially immersed in a liquid or in contact with a limited amount of liquid, such as a drop placed on the fabric. Capillary penetration of a liquid can therefore occur from an infinite (unlimited) or limited (finite) reservoir. Wicking processes from an infinite reservoir are immersion, transplanar wicking, and longitudinal wicking. Wicking from a limited reservoir is exemplified by a drop placed onto the fabric surface.

5.4.5 Porosity of fabrics and spreading of liquids

The porosity ϕ of material is defined as the fraction of void space within the material.[27]

$$\phi = 1 - (\rho_F/\rho_f) \qquad [5.17]$$

where ρ_f is the density of the fiber and ρ_F is the density of the fabric; the latter is the ratio of fabric weight to thickness. The maximum liquid absorption capacity C_m is:

$$C_m = [(\rho_l\phi)/\rho_f(1 - \phi)] \qquad [5.18]$$

where, ρ_l is the liquid density.

The pores within the structure are responsible for the liquid flow through a material and the size and connectivity of the pores in the fabric influence how fast and how much liquid is transported through the material. Hsieh *et al.*, [28,29] reported that, in the case of woven, non-woven and knitted fabrics, a distribution of pore sizes along any planar direction is expected. Hsieh[27] has also shown that with poor wetting, many pores in fabrics are not filled by water due the effect of reduced cos θ in driving the water into the pores, e.g. with polyester fabric.

When liquid moves into a fiber assembly, the smaller pores are completely filled and the liquid then moves to the larger pores. The sizes and shapes of fibers as well as their alignment will influence the geometric configurations and topology of the pores, which are channels with widely varying shape and size distribution and may or may not be interconnected.[29–31]

The shape of fibers in an assembly affects the size and geometry of the capillary spaces between fibers and consequently the wicking rates. The flow in capillary spaces may stop when geometric irregularities allow the meniscus to reach an edge and flatten.[15] The distance of liquid advancement is greater in a smaller pore because of the higher capillary pressure, but the mass of liquid retained in such a pore is small. A larger amount of liquid mass can be retained in larger pores but the distance of liquid advancement is limited. Therefore, fast liquid spreading in fibrous materials is facilitated by small, uniformly distributed and interconnected pores, whereas high liquid retention can be achieved by having a greater number of large pores or a high total pore volume.[27]

Wicking is affected by the morphology of the fiber surface, and may be affected by the shape of the fibers as well. Fiber shape does not affect the wetting of single fibers. However, the shape of the fibers in a yarn and fabric affects the size and geometry of the capillary spaces between the fibers, and consequently the rate of wicking.[3] Randomness of the arrangement of the fibers in the yarns considerably influences the amount of water and transport rate of the fabrics. The same factor also seems to control the ease of wetting of the surface of fabrics.

Non-woven fabrics are highly anisotropic in terms of fiber orientation, which depends greatly on the way in which the fibers are laid (random, cross-laid and parallel-laid) during web formation and any further processing. The in-plane liquid distribution is important in spreading the liquid over a large area of the fabric for faster evaporation of perspiration in clothing or maximum liquid drawing capacity of the secondary layer of baby diapers.

Classical capillary theory, based on equivalent capillary tubes applied for yarns and woven fabrics, is inadequate to study the liquid absorption in non-wovens.[32] The former structures are compact with a porosity in the range of 0.6–0.8 and have better defined fiber alignment, whereas non-wovens have porosity generally above 0.8 and as high as 0.99 in some high-loft structures. Further, wicking in woven fabrics is mainly concerned with liquid movement in between the fibers in the yarn[33] and the larger pores that exist between the yarns are therefore less important[34]. The structure of non-wovens is markedly different from the traditional structures in that they have larger spaces between fibers, and high variation of size, shape and length of capillary channels.[32] Orientation of fibers in non-wovens is found to influence the in-plane liquid transportation in different directions.

To characterize the capillary pressure during liquid transportation in non-woven fabrics, instead of using the pore size, an alternative theory was developed by Mao and Russell[35,36] based on hydraulic radius theories proposed by Kozeny[37] and Carman.[38] In hydraulic radius theories the channels usually have a non-circular shape and the hydraulic radius is defined by the surface area of the porous medium. Mao and Russell employed Darcy's law[39] to quantify the rate of liquid absorption in non-woven fabrics. Based on Darcy's law, they related specific or directional permeability of sample $k(\theta)$ in m^2 in the direction θ from reference and angle of fiber with respect to reference α as:

$$k(\theta) = -\frac{1}{32}\frac{\delta^2}{\phi}\left[\frac{ST}{\int_0^{\pi} \Omega(\alpha)\{T\cos^2(\theta-\alpha) + S\sin^2(\theta-\alpha)\}d\alpha}\right] \tag{5.19}$$

where δ is the fiber diameter, ϕ is the volume fraction of solid material, Ω is the fiber orientation distribution probability function that defines the arrangement of fibers within the fabric. S and T are functions in terms of ϕ.

By assuming that the capillary pressure in the fabric plane is hydraulically equivalent to a capillary tube assembly in which there are a number of cylindrical capillary tubes of the same hydraulic diameter, the equivalent hydraulic diameter $D_H(\theta)$ was formulated. Using the equivalent hydraulic diameter $D_H(\theta)$ in the Laplace equation, the capillary pressure in the direction θ in the fabric was calculated. For a given contact angle β, wicking rate $V(\theta)$ was shown as:

$$V(\theta) = -\frac{1}{32}\frac{\delta^2}{\phi}\left[\frac{ST}{\int_0^{\pi} \Omega(\alpha)\{T\cos^2(\theta-\alpha)+S\sin^2(\theta-\alpha)\}d\alpha}\right]$$

$$\times\frac{4\phi\int_0^{\pi}\Omega(\alpha)\,|\cos(\theta-\alpha)|d\alpha}{\delta(1-\phi)}\gamma_{LV}\cos\beta\frac{1}{\eta L} \qquad [5.20]$$

Fiber diameter, fiber orientation distribution and fabric porosity are the important structural parameters that influence the spreading rate of liquid in non-wovens. The anisotropy of liquid absorption in non-woven fabric largely depends on a combination of the fiber orientation distribution and the fabric porosity. Konopka and Pourdeyhimi[40] carried out experiments on non-woven fabrics to study in-plane liquid distribution using a modified GATS apparatus and found that fiber orientation factor is the dominant factor in determining where the liquid will spread in the material. Kim and Pourdeyhimi[41] simulated in-plane liquid distribution in non-wovens using the above equation and found reasonable agreement between the simulated and experimentally observed results.

Fiber orientation factor influences the rate of spreading in different directions as well as the mass of liquid transported in the dynamic state. The spreading of liquid in a thermally bonded non-woven is more elliptical than that in the woven, which is closer to isotropic.

5.5 Surface roughness of solids

The wetting of surfaces involves both chemistry and geometry. Geometry can be either local, in the form of rough or patterned surfaces, or it can be global, in the form of spheres, cylinders/fibers, etc. Amplification of hydrophobicity due to surface roughness is frequently seen in nature. Water droplets are almost spherical on some plant leaves and can easily roll off (lotus effect or super hydrophobic effect), cleaning the surface in the process. There are many applications of artificially prepared 'self-cleaning' surfaces. A drop placed on a rough surface can sit either on the peaks or wet the grooves, depending on how it is formed, determined by the geometry of the surface roughness. One that sits on the peaks will have a larger contact angle with higher energy. It has 'air pockets' along its contact with the substrate; hence it is termed a 'composite contact'. It is this type of surface that is desirable in applications such as 'self-cleaning' surfaces.

Wenzel[42] studied the wetting behavior of a rough substrate. The apparent contact angle of a rough surface θ^* depends on the intrinsic contact angle (Young's contact angle) θ, and the roughness ratio, r (called 'Wenzel's roughness ratio); the latter is the ratio of rough to planar surface areas.

$$\cos \theta^* = r \cos \theta \tag{5.21}$$

The underlying assumption of the above relationship is that hydrophilic surfaces that wet ($\theta < 90°$) if smooth will wet even better if rough. According to this relationship, if roughness is increased, the apparent contact angle will decrease. This much-quoted equation immediately suggests that:

if $\theta_s < \pi/2$ then $\theta_{ro} < \theta_s$; but if $\theta_s > \pi/2$ then $\theta_{ro} > \theta_s$

θ_s is the contact angle for a smooth or ideal surface and θ_{ro} the contact angle for a rough surface.

5.5.1 Heterogeneity of surfaces

In the case of chemically heterogeneous smooth surface consisting of two kinds of small patches, occupying fractions f_1 and f_2 of the surfaces, then the apparent contact angle is:[10]

$$\gamma_{LV} \cos \theta^* = f_1(\gamma_{S1V} - \gamma_{S1L}) + f_2(\gamma_{S2V} - \gamma_{S2L}) \tag{5.22}$$

Alternatively,

$$\cos \theta^* = f_1 \cos \theta_1 + f_2 \cos \theta_2 \tag{5.23}$$

In the case of microscopically heterogeneous surfaces, forces rather than surface tensions are averaged,[10] hence:

$$(1 + \cos \theta^*)^2 = f_1(1 + \cos \theta_1)^2 + f_2(1 + \cos \theta_2)^2 \tag{5.24}$$

In the case of a rough surface or a composite surface, such as a fabric, incompletely wetted by a liquid, if f_w is the area fraction of substrate that is wetted and f_u is the fraction of unwetted (open area of fabric) surface (i.e. $1 - f_w$), then in Equation [5.22] γ_{S2V} is zero (due to air entrapment) and γ_{S2L} is simply γ_{LV}; wettability of such surfaces is then expressed by Equation [5.37][43]:

$$\cos \theta^* = f_w \cos \theta - f_u \tag{5.25}$$

If the contact angle is large and the surface is sufficiently rough, the liquid may trap air so as to give a composite surface with the relation as given by Cassie:[44]

$$\cos \theta^* = rf_w \cos \theta - f_u \tag{5.26}$$

Alternatively, Cassie and Baxter[45] have shown that:

$$\cos \theta^* = \phi_s (1 + \cos \theta) - 1 \tag{5.27}$$

where ϕ_s is the surface fraction and, $1 - \phi_s$ is the air fraction. $\theta^* > \theta$ unless the roughness factor is relatively large.

Several workers have found that the apparent contact angle for water drops on paraffin metal screens, textile fabrics, and embossed polymer surfaces does vary with f_u in approximately the same manner predicted by Equation [5.25]. The Wenzel and Cassie states for a drop on a hydrophobic textured surface are shown in Fig. 5.3.

Shuttleworth and Bailey[47] have pointed out that a rough surface causes the contact line to distort locally, which give rise to a spectrum of micro-contact angles near the solid surface. Consequently, θ^*, will be less than or greater than θ according to the expression:

$$\theta^* = \theta \pm \alpha \tag{5.28}$$

where α is the maximum angle (±) of the local surface, representing the roughness. In contrast to Wenzel's relationship, the above equation predicts that the apparent contact angle will increase as roughness increases. This discrepancy in the predicted effects of roughness on wetting has been investigated experimentally by Hitchcock *et al.* They approximated Wenzel's roughness ratio and α as:

$$r = 1 + c_1(R/\lambda)^2 \quad \text{and} \quad \alpha = \tan^{-1}(c_2 R/\lambda) \tag{5.29}$$

where c_1 and c_2 are constants, and R and λ are RMS surface height and average distance between surface asperities, respectively.

For several liquids and a variety of solid substrates, they found agreement with the predictions of Shuttleworth and Bailey[47] in that wetting decreased

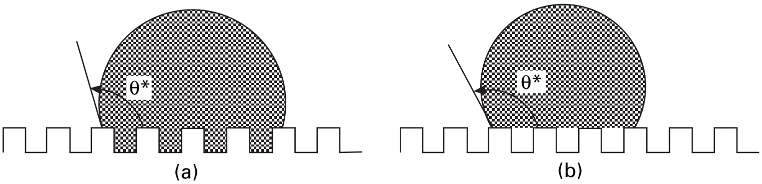

5.3 Two possible states for a drop on a hydrophobic textured surface: (a) Wenzel state; and (b) Cassie's state 'Reprinted from *Microelectronic Engineering*, Vol. 78–79, M. Callies, Y. Chen, F. Marty, A. Pépin, and D Quéré, pp. 100–105, Copyright (2005), with permission from Elsevier'.

with increased roughness ratio with the exception of a few examples (improved wetting with increased roughness, i.e. Wenzel's behavior). However, Johnson and Dettre[49] and Nicholas and Crispin[50] working on 'very well-wetting systems' found Wenzel's behavior.

5.5.2 Global geometry of surfaces

Nakae *et al.*[51] studied water wetting a paraffin surface made of hemispherical and hemi round-rod close-packed solids. The Wenzel's roughness factors were 1.6 and 1.9 for these surfaces, respectively, and were found to be independent of the radii of the spheres and cylinders. When the height roughness of the hemi-cylindrical surfaces was increased, the contact angle increased initially and then decreased when the roughness was increased beyond 50 μm.

5.5.3 Chemically textured surfaces

Shibuichi *et al.*[52] carried out experiments on the effect of chemical texturing of a surface on contact angle as a function of wettability of the solid. They plotted the measured cos θ^* as a function of cos θ determined on a flat surface of the same material and varied using different liquids. Their results are shown in Fig. 5.4.

As soon as the substrate becomes hydrophobic ($\theta > 90°$), cos θ^* sharply decreases, corresponding to a jump of contact angle θ^* to a value of the order of 160°. On the hydrophilic side, the behavior is quite different: in a first regime, cos θ^* increases linearly with cos θ, with a slope larger than 1,

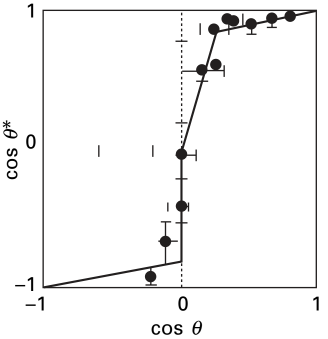

5.4 Experimental results of the Kao group (from Shibuichi *et al.* [52]. The cosine of the effective contact angle θ^* of a water drop is measured as a function of the cosine of Young's angle θ (determined on a flat surface of the same material and varied using different liquids). 'Reprinted from *Colloids Surfaces A: Physicochemical and Engineering Aspects*, Vol. 206, J. Bico, U. Thiele, and D. Quere, pp. 41–46, Copyright (2002), with permission from Elsevier'.

indicating improved wetting with a rough surfaces in agreement with Wenzel's relation. In a second regime (small contact angles), cos θ^* again increases linearly with cos θ, with a much smaller slope. Complete wetting of rough surfaces ($\theta^* = 0°$) is only reached if the substrate itself becomes wettable ($\theta = 0°$).

These successive behaviors have been modeled and explained by Bico *et al.*[53] In the super-hydrophobic regimes, when a liquid is deposited on a model surface, air is trapped below the liquid, inducing a composite interface between the solid and liquid as Cassie's state. The condition for stability for this state is:

$$\cos\,\theta < (f - 1)/(r - f) \qquad [5.30]$$

where f is the fraction of the solid–liquid interface below the drop (dry surface). For a very rough surface, r is very large, and cos $\theta < 0°$ expresses the usual condition for hydrophobicity. For a Young's contact angle θ between 90° and the threshold value given by the Equation [5.30], air pockets should be metastable.

For hydrophilic solids, the solid–liquid interface is likely to follow the roughness of the solid as $\gamma_{SV} > \gamma_{SL}$, which leads to a Wenzel contact angle as in Equation [5.21]. As $r > 1$ and $\theta < 90°$, Equation [5.21] implies $\theta^* < \theta$: the surface roughness makes the solid more wettable. The linear relation found in Equation [5.21] is in good agreement with the first part of the hydrophilic side.

5.5.4 Roughness and surface-wicking

A textured solid can be considered as a 2D porous material in which the liquid can be absorbed by hemi-wicking (surface wicking), which is intermediate between spreading and imbibitions ($0° < \theta < 90°$). When the contact angle is smaller than a critical value θ_{cr}, a film propagates from a deposited drop, a small amount of liquid is sucked into the texture, and the remaining drop sits on a patchwork of solid and liquid – a case very similar to the super-hydrophobic one, except that here the vapor phase below the drop is replaced by the liquid phase. In a partial wetting, as shown in Fig. 5.5, the top of the spikes remain dry as the imbibition front progresses.

If f is the solid fraction in dry state, then $\theta < \theta_{cr}$ with:

$$\cos\,\theta_{\mathrm{cr}} = (1 - f)/(r - f) \qquad [5.31]$$

For a flat surface, $r = 1$ and $\theta_{cr} = 0$, indicating spreading at vanishing of the contact angle. For a rough surface, $r > 1$ and $f < 1$, so that condition in the above equation defines the critical contact angle θ_{cr} in between 0° and 90°. The nature of the texture determined by r and f decides if condition in Equation [5.31] is satisfied or not. If the surface composition is such that $90° > \theta > \theta_{\mathrm{cr}}$, the solid remains dry beyond the drop, and Wenzel's relation

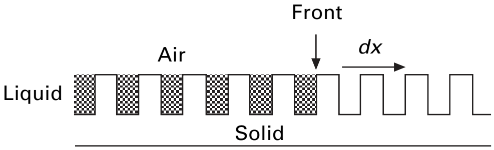

5.5 Liquid film invading the texture of a solid decorated with spikes (or micro channels). The front is marked with an arrow. In the case of partial wetting, the tops of the spikes remain dry. 'Reprinted from *Colloids Surfaces A: Physicochemical and Engineering Aspects*, Vol. 206, J. Bico, U. Thiele, and D. Quere, pp. 41–46, Copyright (2002), with permission from Elsevier'.

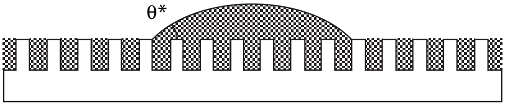

5.6 A film invades solid texture; a drop lies on a solid/liquid composite surface. The apparent contact angle θ^* lies between 0° and θ (contact angle on a flat homogeneous solid). 'Reprinted from *Colloids Surfaces A: Physicochemical and Engineering Aspects*, Vol. 206, J. Bico, U. Thiele, and D. Quere, pp. 41–46, Copyright (2002), with permission from Elsevier'.

applies. If the contact angle is smaller than θ_{cr}, a film develops in the texture and the drop sits upon a mixture of solid and liquid, as shown in Fig. 5.6.

For the hemi-wicking case:

$$\cos \theta^* = f(\cos \theta - 1) + 1 \qquad [5.32]$$

This shows that the film beyond the drop has improved wetting ($\theta^* < \theta$), but it does so less efficiently than with the Wenzel scenario. The angle deduced from Equation [5.32] is significantly larger than the one derived from Eq [5.21]. When the film advances, it smooths out the roughness, thus preventing the Wenzel effect from taking place.

Roughness of a surface can influence wicking on that surfaces. It is very common that fibrous materials encounter roughness on surfaces and walls of pores. The driving force for such surface wicking depends on the geometry of the grooves, the surface tension of the liquid, and the free energies of the solid–gas and solid–liquid interfaces.[54]

5.5.5 Hemi-wicking in fabrics

In a fabric, the distance between the most advanced and less advanced liquid front gets larger with time in most imbibition processes. In fabrics, the distances between the yarns are larger than the ones between the fibers. The liquid in between fibers propagates much faster than that between the yarns.

Fabric as a porous material can be modeled as a tube decorated with spikes, as shown in Fig. 5.7.

The observed phenomena in fabrics can be explained based on this model. Considering the length scales being much smaller than the capillary rise, the wetting liquid should invade both the tube itself (between yarns) and the texture (between fibers) if the condition of Equation [5.31] is satisfied. The texture acts as a reservoir for the film and hence the film propagates faster along the decorations than in the tube. Different capillary rises are likely to take place in such a tube. The film in between the fibers propagates faster than the main meniscus, which leads to a broadening of the front as times goes on. The main meniscus moves along a composite surface and the apparent contact angle for it is given by Equation [5.32]. The dynamics of the rise of the main meniscus are influenced by this contact angle. As the texture affects the value of the apparent contact angle, the value deduced from the dynamics of the rise can be different, and sometimes anomalously lower, than the one measured on the flat surface of the same material.

Pezron *et al.* [55] performed experiments on wicking in cotton woven fabrics to see the relationship between the mass of the liquid absorbed and square root of time, to test the validity of the Lucas–Washburn equation. The graph for m vs. $t^{1/2}$ displayed a non-linear relationship. The m vs. $t^{1/2}$ could be represented by two straight lines; one that wicks the liquid inside the fabric structure and the other, surface wicking due to alveoli which could not absorb liquid to a great height because of their large capillary size. When the fabric surface was coated with a gel to eliminate the alveoli, the m vs. $t^{1/2}$ displayed a linear relationship.

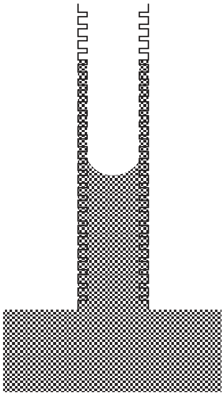

5.7 Tube decorated with spikes, as an example of the modeling of a porous material 'Reprinted from *Colloids Surfaces A: Physicochemical and Engineering Aspects*, Vol. 206, J. Bico, U. Thiele, and D. Quere, pp. 41–46, Copyright (2002), with permission from Elsevier'.

Liquid spreading rate in a non-woven is influenced by surface wicking during the in-plane wicking test using GATS (Grammetric Absorbency Test System), when plates are placed below, or on top of, or at both faces of, the fabric. The added capillaries increase the wicking rate due to surface wicking. The shape of the liquid spreading in a non-woven is not affected by the extra capillaries when material distribution is uniform throughout the non-woven fabric. However, non-uniform distribution of material influences the shape of the liquid spread.[40]

5.5.6 Roughness anisotropy and grooves

If the roughness geometry is isotropic, then the drop shape is almost spherical and the apparent contact angle of the drop is nearly uniform along the contact line. If the roughness geometry is anisotropic, e.g. parallel grooves, then the apparent contact angle and the shape of the drop is no longer uniform along the contact line[56]. For the case of a composite contact of a hydrophobic drop, the apparent contact angle in a plane normal to the grooves is larger than the one along the grooves. This is a consequence of the squeezing and pinning of the drop in the former and the stretching of the drop in the latter planes, respectively. Both these apparent contact angles are usually larger than the intrinsic values of the substrate material (i.e. the one for the smooth surface). Wenzel and Cassie's equations are insufficient to understand this anisotropy in the wetting of rough surfaces.

Yost *et al.*[57] demonstrated that, in extensive wetting, the arc length of wetting has a fractal character which is shown to arise from rapid flow into groove-like channels in the rough surface. This behavior is due to the additional driving force for wetting exerted by channel capillaries, resulting in flow into and along the valleys of the nodular structure. Several workers have shown that continuous paths of internodular grooves having $\alpha > \theta$ would explain the profuse wetting on rough surfaces. It has been shown that rough substrates having $\alpha < \theta$ do not show Wenzel behavior.

Flow in a straight V-shaped groove has been modeled. When the straight walls of the groove are oriented at an angle of α to the surface and the liquid fills the groove to a depth y, the curvature of the liquid surface ($1/R$) becomes:

$$1/R = \sin(\alpha - (\theta) \tan \alpha/y \qquad [5.33]$$

This shows that flow into the groove can only occur if $\alpha > \theta$. This clearly emphasizes that fluid is drawn only into grooves satisfying this inequality and provides an alternative path to its derivation originally provided by Shuttleworth and Bailey. Further, it was shown that the area of spreading of the liquid, $A(t)$ is related as:

$$A(t) = \beta D t \qquad [5.34]$$

where β is a proportionality coefficient including a tortuosity factor; the diffusion coefficient D is found to increase with α. This lends support to the notion that extensive wetting and spreading is driven by capillary flow into the valleys of rough surfaces.

5.5.7 Roughness of fibrous materials

Fabrics constructed from hydrophobic microfilament yarns have higher contact angles than others. Aseptic fabrics (sterilized) have mostly higher contact angles than non-aseptic fabrics.

Rough surfaces may facilitate fast spreading of liquid along troughs offered by the surface roughness**.** Alkaline hydrolysis causes pitting of the surface of polyester fibers and improves their wettability, as indicated by contact angle measurements.[58] The enhanced wettability is due to an increase in either the number or the accessibility of polymer hydrophilic groups to water and/or an increase in the roughness of the sample surfaces.

Hollies *et al.*,[16] reported that differences in yarn surface roughness give rise to differences in wicking of yarns and fabrics made from the yarns. Increase in yarn roughness due to random arrangement of its fibers gives rise to a decrease in the rate of water transport, and this is seen to depend on two factors directly related to water transfer by a capillary process: (i) the effective advancing contact angle of water on the yarn is increased as yarn roughness is increased; (ii) the continuity of capillaries formed by the fibers of the yarn is seen to decrease as the fiber arrangement becomes more random. The measurement of water transport rates in yarns is thus seen to be a sensitive measure of fiber arrangement and yarn roughness in textiles assemblies.[16]

Plasma-treated polypropylene melt-blown webs develop surface roughness as a result of chemical reactions and micro etchings on fiber surfaces. However, it has been pointed out that the improved water wettability after plasma treatment is due to the increased polarity of the surface; surface roughness is not a primary reason for improved wettability, but may increase it.[59]

5.5.8 Wetting of textured fabrics

The natural hydrophobicity of surfaces can be enhanced by creating texture on them, especially if the surfaces are microtextured. Surfaces that are rough on a nanoscale tend to be more hydrophobic than smooth surfaces because of the extremely reduced contact area between the liquid and solid, analogous to so-called ‘lotus-effect’ (repellency of lotus leaves).[60] This gives a self-cleaning effect to surgical fabrics, i.e. particles adhering to the fabric surface are captured by rolling water due to the very small interfacial area between the particle and the rough fabric surface.[61] Super hydrophobic surfaces can be created using a nanofiber web made from hydrophobic materials. In this kind of structure, the apparent contact angle θ^* will be very high since the fraction of the surface in contact with the liquid ϕ_s may be very low, coupled with a high intrinsic contact angle θ as evident from Equation [5.27]; a drop placed on them easily rolls-off without wetting the surface and subsequently hindering wicking in the material.

Electrospun nanofibrous webs have potential application as barriers to liquid penetration in protective clothing systems for agricultural workers. Research work is in progress to create microporous web made from nanofibers such as cellulose acetate and polypropylene laminated with conventional fabric for this application.[62] It is envisaged that the microporous web with small pore sizes will prevent liquid penetration, and the laminate will provide a selective membrane system that prevents penetration of pesticide challenged liquids while allowing the release of moisture vapor to provide thermal comfort.

5.6 Hysteresis effects

For an ideal surface wet by a pure liquid, the contact angle theory predicts only one thermodynamically stable contact angle. For many solid–liquid interactions, there is no unique contact angle and an interval of contact angles is observed. The largest contact angle is called ‘advancing’ and the smallest contact angle is called ‘receding’. The work of adhesion during receding is larger. Liquid droplets placed on a surface may produce an advancing angle if the drop is placed gently enough on the surface, or a receding angle if the deposition energy forces the drop to spread further than it would in the advancing case. Hysteresis occurs due to a wide range of metastable states as the liquid meniscus scans the surface of a solid at the solid–liquid–vapor interface. The true equilibrium contact angle is impossible to measure as there are free energy barriers between the metastable states. It is essential to measure both the contact angles and report the contact angle hysteresis to fully characterize a surface. The hysteresis effect can be classified in thermodynamic and kinetic terms. Roughness and heterogeneity of the surface are the sources of thermodynamic hysteresis. Kinetic hysteresis is characterized by the time-dependent changes in contact angle which depend on deformation, reorientation and mobility of the surface, and liquid penetration. Difference in hysteresis among fibers sheds light on the differences that exist in their chemical and physical structures.[63]

5.6.1 Characterization of hysteresis

Wetting hysteresis can be characterized in three different ways: the arithmetic difference between the values of the advancing and receding contact angles $\triangle\theta = \theta_a - \theta_r$; the difference between the cosines of the receding and advancing contact angles $\Delta\cos\theta = \cos\theta_r - \cos\theta_a$; and a dimensionless form,[64] referred to as 'reduced hysteresis' H,

$$H = (\theta_a - \theta_r)/\theta_a \qquad [5.35]$$

Wetting hysteresis is also characterized as the ratio of the work of adhesion in the receding mode to that in the advancing.

5.6.2 Hysteresis on micro-textured surfaces

On micro-textured surfaces, the contact angle hysteresis is affected by the state of the drop. The Wenzel state is characterized by a huge hysteresis in the range of 50° to 100° which makes it very sticky compared to the Cassie state, which is very slippery because of its low hysteresis (in the range of 5° to 20°). This is due to the fact the drop interacts with many defects on the surface in the first case, whereas it hardly feels the surface and can easily roll off in the second case.[46]

5.6.3 Hysteresis on fibrous materials

Since fibrous materials are complicated by surface roughness and heterogeneity, the measured (apparent) contact angle exhibits hysteresis and the advancing contact angle is usually employed in discussions of wicking.[65] Surface contamination, roughness, and molecular structure of fibers are the factors responsible for wetting hysteresis.[66] The wetting index while receding is governed mostly by the chemical make-up of the fiber; the index during advancing is affected additionally by the physical and morphological structures which include molecular orientation, crystallinity, roughness, and surface texture.

Whang and Gupta[67] tested wetting characteristics of chemically similar cellulosic fibers, *viz.* cotton, regular rayon (roughly round but crenulated shape), and trilobal-shaped rayon, using the Wilhelmy technique. The contact angles during receding for these fibers are similar due to their similar chemical structures. The wetting hysteresis for cotton, regular rayon and trilobal rayon were 1.06, 1.25 and 1.01, respectively. Very little or no hysteresis values for the trilobal rayon fiber and high values for regular rayon fiber may be explained on the basis of chemical purity, cross-sectional morphologies, and orientation of molecules in the fibers. The trilobal rayon fibers had high purity, were smoother and had more homogeneous surfaces than regular rayon fibers. These differences are partly responsible for the difference in the hysteresis values of the two rayon fibers. Pre-wetting and absorption can also influence hysteresis for some fibers.[63,68] Surface contamination of fibers can also cause hysteresis.[69]

5.7 Meniscus

When a fiber is dipped in a fluid, a meniscus is formed on it. When it is withdrawn, the meniscus is deformed, and a layer of fluid covers the fiber and is entrained with it. Two regions of meniscus can be described, as shown in Fig. 5.8. The dynamic region is high above the meniscus where the fluid layer is nearly constant and the hydrodynamic equations can be simplified and solved; and the static meniscus region is near the surface of the fluid bath, where the capillary equation of Laplace is integrated.

The Landau–Lavich–Derjaguin (LLD) theory forecasts the limit film thickness h_0, present on an inclined plate withdrawn from a liquid bath, by matching the curvature between the apex of the static meniscus and the bottom of the steady-state region of the dynamic regime using the expression:

$$h_0 = (0.945/(1 - \cos \alpha_0)^{1/2})(\eta v_0/\gamma_{LV})^{2/3}(\gamma_{LV}/\rho g)^{1/2} \qquad [5.36]$$

where α_0 is the inclination angle in degrees of the plate with the horizontal; v_0 is the plate velocity, and g is the gravity constant. The second term represents the capillary number and the final term is related to the inverse of the bond number.

5.7.1 Meniscus on single fiber

Rebouillat *et al.*[70] extended their work to a meniscus on an inclined fiber and showed that

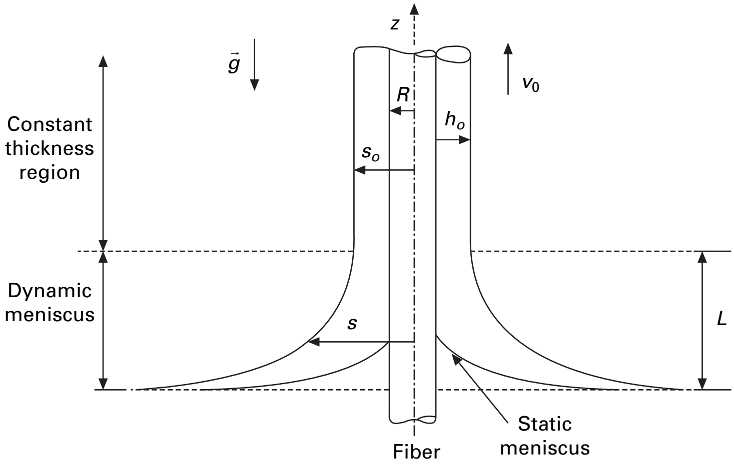

5.8 Withdrawal of a fiber from a bath of wetting liquid: the static meniscus is deformed and strained for a length L and a layer of constant thickness h_o covers the fiber above the meniscus. Reprinted from *Chemical Engineering Science*, Vol. 57, S. Rebouillat, B. Steffenino, and B. Salvador, pp. 3953–3966, Copyright (2002), with permission from Elsevier'.

$$h_0/(R + h_0) = 1.34C_a^{2/3}/\sqrt{1 - \cos\alpha_0} \qquad [5.37]$$

where R is the fiber radius and C_a is the capillary number expressed as $(\eta v_0/\gamma_{LV})$

The fluid radii in the dynamic meniscus region S and in the constant thickness region S_0 are related by the expression:

$$S = S_0 + B\exp(-z/E) \qquad [5.38]$$

where B and E are the parameters of the model and z is the distance along the fiber from the level of the liquid bath.

It is shown that, for a monofilament withdrawn from a bath of liquid, with increasing meniscus height, fluid radius decreases and for a given rise of liquid on the withdrawing fiber, the larger the withdrawal speed of the fiber, the larger is the fluid radii in the dynamic region.

5.7.2 Meniscus on multifilament

In the case of a multifilament, the complexity comes essentially from the influence of the porosity existing inside the structure between the filaments, which increases the surface of contacts as compared with a monofilament of the same size. Using images, it was shown that, at low velocity, the fluid seems to be dragged inside the fibers; that is to say, the structure seems to be swollen under the capillary suction effect. Nevertheless, at high speeds, the porous structure may become saturated and fluid is dragged around the cylinder composed of the multifilaments, internal fluid filling the porosity formed by the filament structure.

The ratio of fluid thickness on the fiber to radius of the fiber is found to be similar for monofilament and multifilament when the fiber is withdrawn at highspeeds, as if the multifilament fibers behave like a cylinder of apparent radius encompassing the majority of the filaments. The height of the dynamic meniscus L for velocities 20–120 m/min is expressed as:

$$L = \sqrt{(h_o(h_0 + R)} \qquad [5.39]$$

Wiener and Dejiová[30] modeled the curvature of the meniscus during wicking in multifilament yarns. The curvature of the liquid along the fibers is infinite and the radius of the curved meniscus between the fibers R, by simplifying the Laplace equation, yields $\Delta P = \gamma_{LV}/R$. When the capillary pressure driving the liquid front is balanced by the hydrostatic pressure, $\rho_L gh$, then R is:

$$R = \gamma_{LV}/\rho_L gh \qquad [5.40]$$

According to the above equation, the curvature of the liquid surface increases (or radius decreases) as the liquid rises to a greater height between the fibers. This is shown in Fig. 5.9.

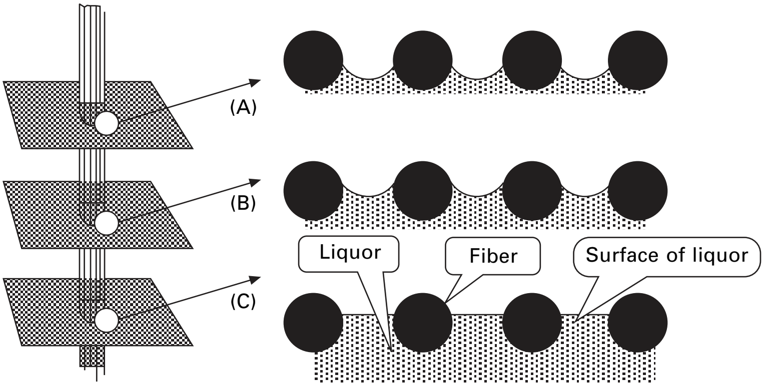

5.9 Influence of hydrostatic negative pressure or liquid height on the curvature of meniscus in a parallel fiber bundle. Height increases from *C* to *B* and then to a maximum height A (From Wiener and Dejiova, *Autex Research Journal.*[30]

5.8 Instability of liquid flow

Flow of liquid under certain conditions experiences instability. Instability of liquid flow influences the uniformity of coating of fibrous materials, including spin–finishes on synthetic filament yarns and filling of voids between fibers during fiber–composite production. Droplet formation occurs on fibers due to flow instability. During wet filtration, aerosol particles are captured by the liquid drops formed on the fibers rather than being directly captured by the fibers, and by providing sufficient liquid, the filter is self-cleaning and filtration efficiency is greatly increased.

5.8.1 Curvature of cylindrical surfaces

A uniform cylindrical bubble possesses a critical length beyond which it is unstable toward necking in at one end and bulging at the other. This length equals the circumference of the cylinder. A cylinder of length greater than this critical value thus promptly collapses into a smaller and a larger bubble. The same is true of a cylinder of liquid, i.e. a stream of liquid emerging from a circular nozzle.[10] A fluid film layer flowing either on the outside or inside of a vertical cylinder is more unstable than on a vertical plane wall. The stability of the flow on the cylindrical wall is characterized by the curvature of the free surface rather than that of the cylinder.[71] As the radius of the cylinder decreases, flow becomes more unstable. Even when the liquid is at rest, the layer of fluid is unstable because of the disturbance of the wave number beyond a certain critical value. With increasing curvature of the film, the range of unstable wave numbers and the wave number of the most amplified wave increase. For low curvature, the wave number of the most amplified wave decreases with the Reynolds number or Weber number, while for high curvatures it increases.

5.8.2 Fluid jets

A slow-moving, thin, cylindrical stream of water undergoes necking-in, becomes non-uniform in diameter and eventually breaks up into alternately smaller and larger droplets. This is an example of capillary break-up (a column of liquid in a capillary) and it is commonly known as Rayleigh instability.

A stream or jet of fluid emerging from a circular nozzle undergoes a process of necking-in, leading to break-up of the jet into alternate smaller and larger drops[72,73]. Weber[73] considered the break-up of a jet of fluid and, according to his theory, the most rapidly growing mode is given by:

$$2\pi a/\lambda = 0.707\ [1 + (9\eta^2/2\rho\gamma_{LV}a)^{1/2}]^{-1/2} \qquad [5.41]$$

where a is the initial radius of the liquid cylinder, η is the viscosity of the fluid, and λ is the wave length of the disturbance.

For a cylindrical jet, Rayleigh calculated that the most unstable disturbance wavelength, λ, is about nine times the radius of the jet. In the case of a thin annular coating of liquid on the inside of a capillary, the disturbance is much faster than the case where liquid completely fills in the capillary. The liquid film breaks up into droplets of equal length more quickly. A standing wave develops, which grows in amplitude until droplets are producted.[74]

Ponstein[75] studied jets of rotating fluids and observed that an increasing angular velocity decreases the stability of a solid jet and increases the stability of a 'hollow infinitely thick' jet. Investigations of annular jets with both surfaces free, showed that, in some cases, non-axially symmetric disturbances are more stable than axially symmetric ones, whereas in non-rotating jets, only axially symmetric disturbances are unstable. Tomotika[76] considered a cylinder of bi-component fluids (one liquid surrounded by the other). The most rapidly growing mode of disturbance is given by: $2\pi a/\lambda = 0$ if the ratio of viscosities is either zero or infinite and $2\pi a/\lambda \neq 0$ for finite values of the ratio.

5.8.3 Marangoni effect

Surface tension gradient on a liquid, known as the 'Marangoni effect', leads to an erratic and slow wicking rate of the liquid. Spin finishes are applied to synthetic fibers to control friction during downstream processes. Spin finishes are multicomponent liquid systems containing surfactant and are applied to yarns moving at high speeds. For uniform spreading of the finish within the yarn structure, it is important that the rate of wicking be high and the finish film not retract due to lack of adhesion as the carrier evaporates during the storage of yarn packages. It is observed that the absorption of surfactant molecules on the fiber surface at the wicking front results in a decrease in the surface energy of the fiber and an increase in the surface tension of the liquid, with a concomitant decrease in the cosine of the contact angle and capillary forces. Equilibrium conditions are re-established when the surfactant molecules diffuse from the more concentrated regions into less concentrated region (leading edge of the meniscus).[77] These effects, often termed transient effects, arise due to depletion and replenishment of surfactants at the liquid surface. The overall results of adsorption of surfactant molecules and surface tension gradient of liquid is erratic wicking behavior and a lower wicking rate. This depletion effect is more pronounced in dilute solutions and decreases as concentration of surfactant increases. The concentration of surfactant needed to overwhelm the depletion is equal to, or in excess of, critical micellar concentration.

5.8.4 Dewetting process

The rupture of a thin film on the substrate (liquid or solid) and formation of droplets, can be understood as dewetting: it is the opposite process of spreading of a liquid on a substrate, i.e. $S < 0$. Dewetting is one of the processes that can occur at a solid–liquid or liquid–liquid interface. Dewetting is an unwanted process in applications such as lubrication, protective coating and printing, because it destroys the applied thin film. Even in the case of $S < 0$, the film does not dewet immediately if it is in a metastable state, e.g. if the temperature of the film is below the Tg of the polymer forming the film. Annealing of the film above its Tg increases the mobility of the polymer chain molecules; dewetting starts from randomly formed holes (dry patches) in the film. These dry patches grow and the material is accumulated in the rim surrounding the growing hole, a polygon network of connected strings of material forming. These strings then can break-up into droplets by the process of ‘Rayleigh-instability’.

Dewetting of resin on glass fiber has to be controlled during composite manufacture. It has been shown that the presence of high surface energy components on the glass surface (treated with finishes) tends to resist dewetting of the receding fluid front, lowering the receding angle.[78]

5.8.5 Fiber coating

Droplet formation can occur in the case of coating of synthetic fibers with water for lubrication. Droplets can be formed on the inside of fiber assemblies from the thin liquid coating left behind either when the liquid drains from the tube or larger air bubbles pass through the tube.[79] In order to give cohesion between multifilaments to prevent them from being damaged in further operations or imparting lubrication and specific surface properties (hydrophilic, hydrophobic, functional etc.) in textile applications, fiber impregnation process is used. This process is usually done by passing the material through a liquid bath. The impregnation speed is of the order of 10 m s^{-1}. Rebouillat *et al.*[70] studied the high-speed fiber impregnation fluid layer formation on mono- and multifilaments. During high-speed impregnation, the predominant phenomenon is inertia followed by surface tension, viscosity and then gravity. At high speeds, the inertia effect tends to drag more quantities of fluid on the substrate and the meniscus takes a critical size; the capillary forces perpendicular to the fiber are no longer negligible and drops are formed as various forces tend to minimize the fluid surfaces. These formed drops are dragged under the effect of inertia.

5.9 Morphological transitions of liquid bodies in parallel fiber bundles

The fundamentals of non-homogeneous liquid flow dealing with thin films on flat surfaces, capillary instability and surface gradient effects have been well researched. A few attempts have been made to exploit non-homogeneous flow for practical applications involving fibrous materials in the areas of fiber coating, wet filters and development of liquid-barrier fabrics.

Wetting phenomena occurring between two or three equidistant, parallel cylinders have been studied.[62] By changing the ratio of spacing d between the cylinders and radii r of the cylinders, different morphologies can be observed for liquid shapes between the cylinders. As the ratio d/r is increased, one can observe that the morphology of the liquid changes from 'disintegrated column' to 'unduloid shape' through 'channel-filling column' (Fig. 5.10).

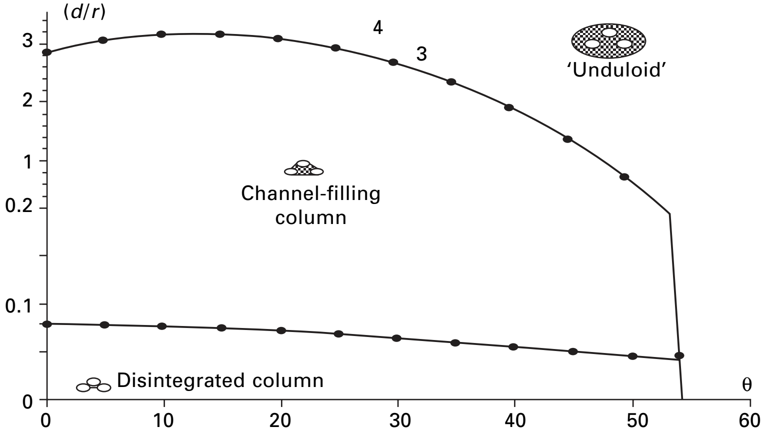

5.10 Morphology of liquid for three-cylinder system.[62]

This observation has a far-reaching impact on designing liquid-barrier fabrics by manipulating the pore size of nanofiber webs.

5.10 Sources of further information and advice

Many works of a significant nature have been published on the wetting of solids rather in the fiber wetting field. Little work has so far been done dedicated to the gas filtration of liquid aerosols using fiber filters. Most of the studies reported on wet filtration are on a macroscopic level investigating the efficiency of the wetted fiber filter without examining the actual processes occurring inside the filter. Microscopic works in the area of wet filters to enhance the understanding of the physical phenomena have been carried out by Mullins *et al.*[8] in developing the model for the oscillation of clamshell droplets in the Reynolds transition flow region; Mullins *et al.*[80] on dynamic effects of water build-up on the fiber, flow down the fiber leading to a self-cleaning effect, fiber rewetting and cake removal after evaporative drying; and Contal *et al.*[81] on a qualitative description of clogging of fiber filters by liquid droplets in terms of the change in the mass of deposit on fibers vs. pressure drop. Formation of barrel-shaped droplets is preferable to clamshell to improve the efficiency of the wet filter. Fine wettable fibers favor the barrel configuration for droplets. Future investigations should be directed towards selection of fibers and their fineness, surface modification of fibers by finishes/plasma treatment and the arrangement of these fibers in terms of angle and spacing to design efficient wet fiber filters.

Another promising area of research involving fibers is the development of liquid-barrier fabrics using nanofibers. Here again, little has been done except a work wherein the theory of liquid-instability is applied to develop a model for liquid instability between cylinder analogs to fibers.[62]

Methods of quantifying wetting of fibers, yarns and fabrics, effects of various parameters influencing wetting phenomena and modeling of wetting phenomena on fibrous materials including simulation are also very important and these are reviewed in a monograph 'Wetting and wicking in fibrous materials'.[82]

5.11 References

1. E. Kissa (1984) in *Handbook of Fiber Science and Technology Part II* (edited by B. M. Lewin and S. B. Sello), Marcel Dekker, NY, p. 144.
2. N. K. Adam (1968) *The Physics and Chemistry of Surfaces,* Dover, New York, p. 179.
3. A. Marmur (1992) in *Modern Approaches to Wettability*, (edited by M. E. Schrader and G. I. Loeb), Plenum Press, New York.
4. B. J. Mullins, I. E. Agranovski and R. D. Braddock (2004) *J. Colloid Interface Sci.*, **269** (2), 449–458.

5. B. J. Briscoe, K. P. Galvin, P. F. Luckham and A. M. Saeid (1991) *Colloids and Surfaces*, **56**, 301–312.
6. S. Rebouillat, B. Letellier and B. Steffenino (1999) *Int. J. Adh. Adhes.*, **19** (4), 303–314.
7. G. McHale, M. I. Newton and B. Carrol (2001) *Oil Gas Sci. Technol.*, **26** (1), 47–54.
8. B. J. Mullins, R. D. Braddock, I. E. Agranovski, R. A. Cropp and R. A. O' Leary, (2005) *J. Colloid Interface Sci.*, **284**, 245–254.
9. N. R. Bertoniere and S. P. Rowland (1985) *Text. Res. J.*, **55** (1), 57–64.
10. A. W. Adamson (1990) *Physical Chemistry of Surfaces*, Wiley-Inter Science, New York.
11. A. Marmur (1992) *Advances in Colloid and Interface Science*, **39**, 13–33.
12. R. Lucas (1918) *Kolloid Z.*, **23**, 15.
13. J. J. De Boer (1980) *Text. Res. J.*, **50** (10), 624–631.
14. C. Heinrichs, S. Dugal, G. Heidemann and E. Schollmeyer (1982) *Text. Prax. Int.*, **37** (5), 515–518.
15. E. Kissa (1996) *Text. Res. J.*, (1996) **66** (10), 660–668.
16. N. R. S. Hollies, M. M. Kaessinger and H. Bogaty, (1956) *Text. Res. J.*, **26**, 829–835.
17. F. W. Minor, A. M. Schwartz, E. A. Wulkow and L. C. Buckles (1959) *Text. Res. J.*, **29** (12), 931–939.
18. K. T. Hodgson and J. C. Berg (1988), *J. Coll. Interface Sci.*, **121**, (1), 22–31.
19. http:trc.ucdavis.edu/textiles/ntc%20projects/M02-CD03-04panbrief.htm.
20. B. Miller (1977) The Wetting of Fibers in *Surface Characteristics of Fibers and Textiles, Part II* (edited by M. J. Schick), Marcel Dekker, NY, USA, p. 417.
21. H. Ito and Y. Muraoka (1993) *Text. Res. J.*, **63** (7), 414–420.
22. P. R. Lord (1974) *Text. Res. J.*, **44**, 516–522.
23. K. K. Wong, X. M. Tao, C. W. M. Yuen and K. W. Yeung (2001) *Text. Res. J.*, **71** (1), 49–56.
24. A. K. Sengupta, V. K. Kothari and R. S. Rengasamy, (1991) *Indian J. Fiber Text. Res.*, **16** (2), (1991) 123–127.
25. T. Gillespie 1958 *J. Coll. Interface Sci.*, **13**, 32–50.
26. E. Kissa (1981) *J. Coll. Interface Sci.*, **83** (1), 265–272.
27. Y. -L. Hsieh (1995) *Text. Res. J.*, **65** (5), 299–307.
28. Y. -L. Hsieh, J. Thompson and A. Miller (1996) *Text. Res. J.*, **66** (7), 456–464.
29. Y. -L. Hsieh, A. Miller and J. Thompson (1996) *Text. Res. J.*, **66** (1), 1–10.
30. J. Wiener and P. Dejiová (2003) *AUTEX Res. J.*, **3** (2), 64–71.
31. Y. -L. Hsieh, B. Yu, and M. M. Hartzell (1992) *Text. Res. J.*, **62** (12), 697–704.
32. N. Mao and S. J. Russell, *J. Appl. Phy.*, **94** (6), 4135–4138.
33. N. R. Hollies M. M. Kaessinger, B. S. Watson, and H. Bogaty (1957) *Text. Res. J.*, **27** (1), 8–13.
34. D. Rajagopalan, A. P. Aneja and J. M. Marchal (2001) *Text. Res. J.*, **71** (9), 813–821.
35. M. Mao and S. J. Russell (2000) *J. Text. Inst.*, **91** Part 1(2), 235–243.
36. M. Mao and S. J. Russell (2000) *J. Text. Inst.*, **91** Part 1 (2), 244–258.
37. J. Kozeny (1997) *Proc. Royal Academy of Sci., Vienna, Class 1*, **136**, p. 271.
38. P. C. Carman (1956) Flow of Gases through Porous Media, Academic Press, New York.
39. H. D'Arcy (1856) Les Fontaines Publiques de la Ville de Dijon, Dalmont, Paris.
40. A. Konopka and B. Pourdeyhimi (2002) *Int. Non-wovens J.*, **11** (2), 22–27.

41. H. S. Kim and B. Pourdeyhimi (2003) *Int. Non-wovens J.*, **12** (2), 29–33.
42. R. N. Wenzel (1936) *Ind. Eng. Chem.*, **28**, 988.
43. S. A. Kulinich and M. Farzaneh (2005) *Vacuum*, **79**, 255–264.
44. A. B. D. Cassie (1948) *Discuss. Faraday Soc.*, **3**, 11.
45. A. B. D. Cassie and S. Baxter (1944) *Trans. Faraday Soc.* **40**, 546.
46. M. Callies, Y. Chen, F. Marty, A. Pépin and D Quéré (2005) *Microelectronic Engg.*, **78–79**, 100–105.
47. R. Shuttleworth and G. L. J. Bailey (1948) *Disc. Faraday Soc.*, **3**, 16.
48. S. J. Hitchcock, N. T. Carrol and M. G. Nicholas (1981) *J. Mater. Sci.*, **16**, 714.
49. R. E. Johnson and R. H. Dettre (1964) *Contact Angle, Wettability and Adhesion* (edited by R. F. Gould), Advances in Chemistry Series 43, ACS, Washington DC.
50. M. G. Nicholas and R. M. Crispin (1986) *J. Mater. Sci.*, **21**, 522.
51. H. Nakae, R. Inui, Y. Hirata and H. Saito (1998) *Acta Mater.*, **46** (7), 2313–2318.
52. S. Shibuichi, T. Onda, N. Satoh and K. Tsujii (1996) *J. Phys. Chem.*, **100**, 19512–19517.
53. J. Bico, U. Thiele and D. Quere (2002) *Colloids Surfaces A: Phy. Eng. Aspects*, **206**, 41–46.
54. J. C. Berg (1985) The Role of Surfactants in *Absorbency* (edited by P. K. Chatterjee), Elsevier, New York, p. 179.
55. I. Pezron, G. Bourgain and D. Quere (1995) *J. Colloid and Interface Sci.*, **173**, 319–327.
56. Y. Chen, B. He, J. Lee, and N. A. Patankar (2005) *J. Colloid Interface Sci.*, **281**, 458–464.
57. F. G. Yost, J. R. Michael and E. T. Eisenmann (1995) *Acta Metall. Mater.*, **43** (1), 299–305.
58. E. M. Sanders and S. H. Zeronian (1982) *J. App. Poly. Sci.*, **27** (11), 4477–4491.
59. P. P. Tsai, L. C. Wadsworth, and J. R. Roth (1997) *Text. Res. J.*, **67** (5), 359–369.
60. W. Barthlott and C. Neinhuis (1995) *Plant*, **202**, 1–8.
61. M. Pociūtė, B. Lehmann, and A. Vitakauskas (2003) *Mat. Sci.*, **9** (4), 410–413.
62. N. Pan, Y. L. Hsieh, K. Obendorf and S. Witaker, http://trc.ucdavis.edu/textiles/ntc%20projects/M02–CD03
63. B. Miller and R. A. Young (1975) *Text. Res. J.*, **45** (5), 359–365.
64. C. W. Extrand and Y. Kumagai (1995) *J. Colloid Interface Sc*i. **170**, 515.
65. R. H. Dettre and R. E. Johnson (1964) in '*Contact Angle, Wettability and Adhesion*' (edited by R. F. Gould), Advances in Chemistry Series, Vol. 43, ACS, Washington, D. C., p. 136.
66. P. Luner and M. Sandell (1969) *J. Poly. Sci. Part C*, **28**, 115–142.
67. H. S. Whang and B. S. Gupta (2000) *Text. Res. J.*, **70** (4), 351–358.
68. G. Giannotta, M. Morra, E. Occhiello, F. Garbassi, L. Nicolais, and A. D'Amore (1992) *J. Coll. Interface Sci.*, **148** (2), 571–578.
69. H. J. Barraza, M. J. Hwa, K. Blakley, E. A. O'Rear and B. P. Grady (2001) *Langmuir*, **17** (17), 5288–5296.
70. S. Rebouillat, B. Steffenino and B. Salvador, (2002) *Chemical Engg. Sci.*, **57**, 3953–3966.
71. E. Hasegawa and C. Nakaya (1970) *J. Phy. Soc. Japan*, **29** (6), 1634–1639.
72. L. Rayleigh (1879) *Appendix I Proc Roy. Soc. A*, **29**, 71.
73. C. Weber Z. (1931) *Angew Math. Mech.*, **11**, 136.
74. K. D. Bartle, C. L. Wooley, K. E. Markides, M. L. Lee and R. S. Hansen (1987) *J. High Resol. Chromatog. Chromatogr. Comm.*, **10**, 128.

75. J. Ponstein (1959) *Appl. Sci. Res. A*, 8, 425.
76. S. Tomotika (1935) *Proc. Roy. Soc. A*, **150**, 322.
77. Y. K. Kamath, S. B. Hornby, H. D. Weigmann and M. F. Wilde (1994) *Text. Res. J.*, **64** (1), 33–40.
78. K. Van de Velde and P. Kiekens (2000) *Indian J. Fiber Text. Res.*, **25** (1), 8–13.
79. S. L. Goren (1962) *J. Fluid Mech.*, **12**, 309–319.
80. B. J. Mullins, R.D. Braddock and I. E. Agranovski (2004) *J. Colloid Interface Sci.*, **279**, 213–227.
81. P. Contal, J. Simao, D. Thomas, T. Frising, S. Calle, J. C. Appert-Collin and D. Bémer (2004) *Aerosol Sci.*, 35, 263–278.
82. A Patnaik, R. S. Rengasamy, V. K. Kothari and A Ghosh (2006) ‘Wetting and Wicking in Fibrous Materials’, *Text Prog.*, **38** (1).

6

Interactions between liquid and fibrous materials

N. PAN and Z. SUN, University of California, USA

6.1 Introduction

The interaction of liquids with fibrous materials may involve one or several physical phenomena (Skelton, 1976; Leger and Joanny, 1992; Keey, 1995; Batch, Chen *et al.*, 1996; Kissa, 1996). On the basis of the relative amount of liquid involved and the mode of the liquid–fabric contact, the wicking processes can be divided into two groups: wicking from an infinite liquid reservoir (immersion, trans-planar wicking, and longitudinal wicking), and wicking from a finite (limited) liquid reservoir (a single drop wicking into a fabric). According to fiber–liquid interactions, the wicking processes can also be divided into four categories: capillary penetration only; simultaneous capillary penetration and imbibition by the fibers (diffusion of the liquid into the interior of the fibers); capillary penetration and adsorption of a surfactant on fibers; and simultaneous capillary penetration, imbibition by the fibers, and adsorption of a surfactant on fibers. When designing tests to simulate liquid–textile interactions of a practical process, it is essential to understand the primary processes involved and their kinetics (Batch, Chen *et al.*, 1996; Perwuelz, Mondon *et al.*, 2000; Baumbach, Dreyer *et al.*, 2001).

One of the fundamental parameters which dictates the liquid–solid interactions is the geometry of the solid, including the shape and relative positions of the structural components in the system, as explicitly reflected in the Laplace pressure law showing that the pressure drop is proportional to the characteristic curvatures. Consequently, for the same material, its wetting behavior will be different, in some cases drastically, when made into a film, a fiber, a fiber bundle or a fibrous material, as demonstrated in this chapter.

6.2 Fundamentals

Surface tension only occurs at the interface, and is therefore determined by both the media at the interface. Surface tension between two media (e.g. two non-miscible liquids) A and B is termed as γ_{AB}, except in the case of a water/

air interface where the surface tension is often denoted simply as γ. The following are some of the liquid/solid interfacial relationships fundamental to understanding the interactions between liquid and fibrous media. We will restrict our discussion to the case of non-volatile liquids.

6.2.1 A liquid drop on a fiber – in shape or not in shape

There has been much research work on the equilibrium shapes of liquid drops on fibers (Carroll 1976, 1984, 1992; McHale, Kab *et al.*, 1997; Bieker and Dietrich, 1998; McHale, Rowan *et al.*, 1999; Neimark, 1999; Quere, 1999; Bauer, Bieker *et al.*, 2000; McHale and Newton, 2002). In a complete wetting case, a liquid drop will form a barrel shape covering the fiber as shown in Fig. 6.1. Such a wetting liquid drop on a fiber of radius *b* has a profile $z(x)$ described by de Gennes *et al.* (2003) as

$$\frac{z}{\sqrt{1+\dot{z}^2}} - \frac{\Delta p}{2\gamma}(z^2 - b^2) = b \qquad [6.1]$$

The maximum radius of the drop $z_{\max} = R_m$ when $\dot{z} = \frac{dz}{dx} = 0$. The above equation gives

$$\frac{\Delta p}{2\gamma}(R_m^2 - b^2) = R_m - b \text{ or } R_m = \frac{\Delta\gamma}{\Delta p} - b \qquad [6.2]$$

Δp is the so-called over-pressure and roughly equals the Laplace capillary pressure $\frac{2\gamma}{R_m + b}$ for complete wetting (de Gennes *et al.*, 2003).

6.2.2 Meniscus on a fiber – what if the fiber is standing in water?

If a fiber is vertically inserted into a liquid bath, assuming the rise is very low so that the effect of gravity on the liquid is negligible and there is a complete wetting between fiber and the liquid, the liquid in the meniscus is in equilibrium with the liquid bath so that $\Delta p = 0$. Equation 6.1 hence becomes

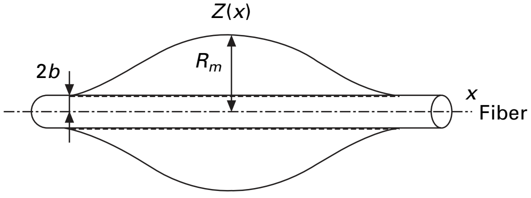

6.1 A liquid drop forming a barrel shape covering a fiber.

$$\frac{z}{\sqrt{1 + \dot{z}^2}} = b \qquad [6.3]$$

At a height x, the vertical projections of forces is balanced $2\pi zy\gamma \cos\theta = 2\pi b\gamma$ and $\tan\theta = \dot{z}$. Bringing both conditions into the above equation yields the solution of the profile of the meniscus

$$z = b\cosh\left(\frac{x}{b}\right) \qquad [6.4]$$

This is a hanging chain equation known as a centenary curve (see Fig. 6.2).

6.2.3 The capillary number and the spreading speed – dimensionless and dimensional

When a fiber is pulled out from a liquid at a speed V, the capillary force causes some liquid to move with the fiber, yet the liquid viscosity η resists any such movement. A dimensionless ratio of the two forces is called the capillary number C_a:

$$C_a = \frac{\eta V}{\gamma} \qquad [6.5]$$

A characteristic number with a dimension of speed

$$V_s = \frac{\eta}{\gamma} = C_a V \qquad [6.6]$$

is called the spreading speed.

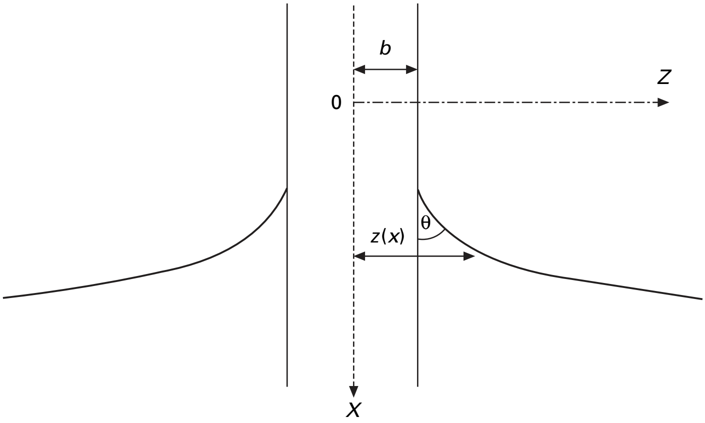

6.2 Liquid meniscus as a hanging chain or a centenary curve.

6.2.4 Capillary adhesion – water serving as glue

Two glass surfaces can adhere to each other if there is a liquid drop in between, as shown in Fig. 6.3. The Laplace pressure within the drop requires

$$\Delta p = p_o - p_w = \gamma\left(\frac{1}{R} + \frac{1}{R'}\right) = \gamma\left(\frac{1}{R} - \frac{\cos\theta}{H/2}\right) \qquad [6.7]$$

where p_o and p_w are the pressures in the air and water, respectively; γ is the liquid–air surface tension and $\theta < \pi/2$ to assure an attractive pressure $\Delta p < 0$. R and H are the radius of the liquid drop and the gap between the two surfaces, respectively. The capillary adhesion Δp reduces into

$$\Delta p \approx \frac{2\gamma\cos\theta}{H} \qquad [6.8]$$

if $H << R$. In the case of water as the liquid, with complete wetting $\theta = 0$, $R = 1$ cm, $H = 5$ µm. The total adhesive force

$$F \approx \pi R^2 \frac{2\gamma\cos\theta}{H} \sim 10N \qquad [6.9]$$

enough to support more than one kilogram of weight!

6.2.5 Capillary length – when liquid weight is negligible

The capillary length l_{cl} actually defines the ascending length of a liquid beyond which the gravity or the density ρ of the liquid has to be considered in analysis. Equating the Laplace pressure to the hydrostatic pressure,

$$\frac{\gamma}{l_{cl}} = \rho g l_{cl} \qquad [6.10]$$

or

$$l_{cl} = \sqrt{\frac{\gamma}{\rho g}} \qquad [6.11]$$

where g is the gravitational acceleration. For any length scale $< l_{cl}$, the liquid weight can be neglected. For water, $l_{cl} \approx = 2.7$ mm and for most other liquids, $l_{cl} \sim 1$ mm.

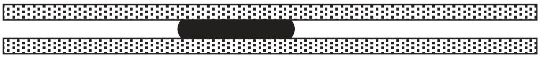

6.3 Two glass surfaces adhered to each other by a liquid drop in-between.

6.2.6 Capillary rise in tubes – water climbing in a very narrow tube

When a narrow tube of inner radius R is in contact with a liquid, the liquid rises in the tube by a height H in the tube. The imbibition (or impregnation) parameter defined by the solid–air and solid–liquid surface tensions

$$I = \gamma_{sa} - \gamma_{sl} \tag{6.12}$$

To assure capillary rise, $I > 0$; the liquid is then referred to as a wetting liquid. Based on Young's relation

$$\gamma_{sa} - \gamma_{sl} = \gamma \cos\theta \tag{6.13}$$

$I > 0$ is equivalent to $\theta < \pi/2$ as mentioned above. The factor I is closely related to the spreading parameter S (Brochard, 1986) by,

$$I = S + \gamma \tag{6.14}$$

Therefore, the capillary rising criterion is more restrictive than that of the spreading; if all other conditions remain the same, it is easier for a liquid to rise in a capillary tube than to spread.

When $H >> R$, a very thin tube, the total energy E of the liquid column due to the capillary rise can be calculated as

$$E = \frac{1}{2}\pi R^2 H^2 \rho g - 2\pi RHI \tag{6.15}$$

where the first term is the cost in terms of gravitational potential energy, and the second term is the surface energy. Minimizing the total energy (and note that $I = \gamma\cos\theta$) yields the equilibrium (or Jurin's) height:

$$H = \frac{2\gamma\cos\theta}{\rho g R} \tag{6.16}$$

(i) H is the height a liquid of density ρ can climb in a small tube due to the capillary effect. This value agrees with the experiments of Francis Hauskbee (1666–1713). H is inversely proportional to R, and is independent of the outer pressure and thickness of the tube wall.
(ii) $I = \gamma\cos\theta$ and H share the same sign, $I > 0$, $H > 0$ capillary rises, otherwise capillary descends.
(iii) H reaches maximum when $\theta = 0$. Further increase in $I > \gamma$ will lead to $S > 0$; a microscopic film forms ahead of the meniscus.
(iv) When the condition $H >> R$ is not true, corrections must be made in the equation (de Gennes *et al*, 2003). Equation [6.16] is often referred to as Jurin's Law.
(v) If $\theta \geq \pi/2$, $H < 0$, i.e. the liquid will not penetrate – a non-wetting situation; the secret for *Gore-Tex* and other waterproof finishes.

6.3 Complete wetting of curved surfaces

According to Brochard (1986) we define the complete wetting of a single fiber of radius b as the state when the fiber is covered by a liquid 'manchon' or barrel, as this liquid geometry is less energy demanding than the nearly spherical droplet sessile on the fiber. Let us denote by γ_{Sa}, γ_{SL} and γ the surface tensions of the solid fiber, the solid/liquid interface, and the liquid (or liquid/air), respectively. The liquid film thickness in the manchon is represented by a parameter e. This liquid manchon formation occurs when the so-called Harkinson spreading parameter S (Brochard, 1986), defined as

$$S = \gamma_{Sa} - \gamma_{SL} - \gamma \qquad [6.17]$$

reaches the critical value S_{CF} derived in Brochard (1986).

$$S_{CF} = \frac{e\gamma}{b} \qquad [6.18]$$

That is, the fiber will be covered by the liquid manchon in the case of the following inequality

$$S > S_{CF} = \frac{e\gamma}{b} \qquad [6.19]$$

Compared to the wetting of planes, the wetting of individual fibers is a more energy-consuming process according to the Young Equation (Young, 1805), as for complete wetting of a flat solid it only requires

$$S > 0 \qquad [6.20]$$

In other words, for a plane, the critical spreading parameter S_{CP} holds

$$S_{CP} = 0 \qquad [6.21]$$

From Equations [6.19] and [6.21] we see that it is obvious that liquids will wet a solid plane more promptly than wet a fiber.

Next, let us examine the case of a fiber bundle formed by n parallel fibers as seen in Fig. 6.4, each with a radius b. Let us focus on the less energy-demanding case and assume that the manchon is a cylindrically symmetric liquid body with an equivalent radius R, as shown in Fig. 6.5.

The equilibrium configurations of limited amounts of liquid in horizontal assemblies of parallel cylinders have been introduced and described in detail by Princen (Princen 1969, 1992; Princen, Aronson *et al.* 1980). The criterion of complete wetting of a vertical fiber bundle dipped partially in a liquid will be derived here by the comparison of the surface energy W_m of such a manchon liquid geometry with the surface energy W_b of a dry fiber bundle. For a length L of the dry fiber bundle,

$$W_b = 2\pi bnL\gamma_{Sa} \qquad [6.22]$$

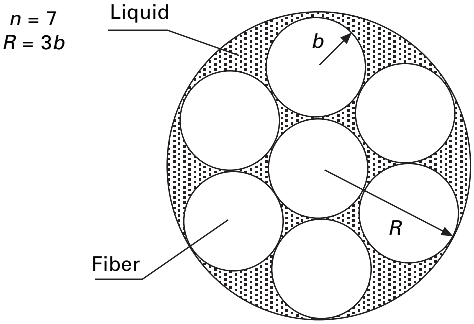

6.4 A fiber bundle formed by *n* parallel fibers; From Lukas, D. and N. Pan (2003). 'Wetting of a fiber bundle in fibrous structures.' *Polymer Composites* 24(3): 314–322 with kind permission of the Society of Plastics Engineers.

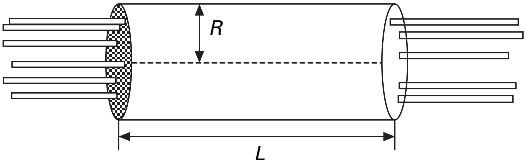

6.5 A liquid body with an equivalent radius *R* covering the fiber bundle; From Lukas, D. and N. Pan (2003). 'Wetting of a fiber bundle in fibrous structures.' *Polymer Composites* 24(3): 314–322 with kind permission of the Society of Plastics Engineers.

whereas the same length of liquid formed manchon on the fiber bundle has the surface energy

$$W_m = 2\pi bnL\gamma_{SL} + 2\pi RL\gamma \qquad [6.23]$$

That is, the energy W_m is composed of both terms of the solid/liquid interface and the liquid/air interface. The complete wetting sets in when the wet state of the system is energetically more favorable compared with the dry one, i.e. $W_b > W_m$. Or from previous equations

$$\gamma_{Sa} - \gamma_{SL} - \frac{R \cdot \gamma}{n \cdot b} > 0 \qquad [6.24]$$

Inserting Harkinson spreading coefficient from Equation [6.17] into Equation [6.24] yields

$$S = \frac{R - n \cdot b}{n \cdot b}\gamma \qquad [6.25a]$$

So the critical value S_{Cb} for the complete wetting of the bundle system is

$$S_{Cb} = \frac{R - n \cdot b}{n \cdot b}\gamma \qquad [6.25b]$$

The radius of the manchon *R* could be smaller than the total sum of fibers radii *nb*. Figure 6.4 shows us such an example when the cross-section of the seven-fiber bundle is covered by a liquid cylinder. The value of S_{Cb} is clearly only $-4/7\ \gamma$.

The above results show that it is highly probable to have a solid/liquid system in which, on one hand, the liquid will wet a solid plane but not a single fiber, and on the other hand, the liquid will wet a fiber bundle, even before it does the solid plane. This, of course, is attributable to the familiar capillary mechanism. However, the above simple analysis also explains the excellent wetting properties of a fiber mass in terms of energy changes: the consequence of the collective behavior of fibers in the bundle allows the manchon energy W_m to decrease more rapidly with the fiber number *n* in the bundle than the dry bundle energy W_b.

6.4 Liquid spreading dynamics on a solid surface

6.4.1 Fiber pulling out of a liquid – the Landau–Levich–Derjaguin (LLD) law

When a fiber is pulled out of a liquid pool, it drags a liquid film of thickness *e* along with it; a phenomenon resulting from several competing factors including the interfacial surface tensions, liquid viscosity and density. According to Derjaguin's law (Derjaguin and Levi, 1943), when $C_a << 1$:

$$e \approx l_{cl} C_a^{1/2} = \sqrt{\frac{\gamma}{\rho g}} \sqrt{\frac{\eta V}{\gamma}} = \sqrt{\frac{\eta V}{\rho g}} \qquad [6.26]$$

So the film thickness increases with the liquid viscosity and pulling out speed, decreases with the weight of liquid, and yet is independent of the liquid surface tension! Note the condition $C_a << 1$ to assure this is still in the LLD visco-capillary regime, instead of a visco-gravitional one characterized by $C_a \geq 1$ (de Gennes *et al.*, 2003).

The length of the dynamic meniscus l_{dm} can be derived from the Landau–Levich–Derjaguin (LLD) law to be related to both *e* and the capillary length l_{cl}

$$l_{dm} \propto \sqrt{e l_{cl}} \qquad [6.27]$$

When a drop of a liquid is put on top of a solid surface, there are two competing effects. The interactions with the solid substrate make it energetically favorable for the drop to spread such that it wets the surface. However, spreading increases the area of contact between the liquid and vapor, which also increases the surface energy between the drop and the vapor. When the interaction with the solid surface dominates, one gets complete wetting, and when the surface tension term dominates, one gets partial wetting (Seemann, Herminghaus *et al.*, 2005).

Curvature effects due to the cylindrical geometry also play an important role in the formation of liquid films from a reservoir on vertical fibers. Their static and dynamic properties have been studied in detail by Quere and co-workers (1988), both theoretically and experimentally.

6.4.2 Droplet spreading dynamics

Deposit a small drop of octane on a very clean glass, and record the change of the drop radius $R(t)$ as a function of time (see Fig. 6.6). Plot $R(t)$ on log/log paper. Check that $R \sim t^{\alpha}$, where $\alpha \approx 0.1$. If we replace the octane with a silicone oil, or even water, provided only that it can wet the glass, we find that all these liquids spread according to a universal law which does not depend on the liquid

$$R = (V_s t)^{0.1}\ \Omega^{0.3} \qquad [6.28]$$

where V_s is the spreading speed defined above and Ω is the liquid volume. We might have expected spreading speed to increase with spreading parameter S, but in fact on very clean glass, where S is large, or on silanized glass, where S is practically zero, a silicone oil will spread at seemingly the same speed! This mystery has recently been resolved by de Gennes. The spreading droplet comprises a macroscopic part which has the shape of a spherical cap, since the pressure reaches equilibrium very quickly in thicker regions. This is characterized by a contact angle θ_d. The measured spreading speed is independent of S! The effect of S is more subtle and passes unseen to the naked eye, for around the spreading droplet there is a microscopic film,

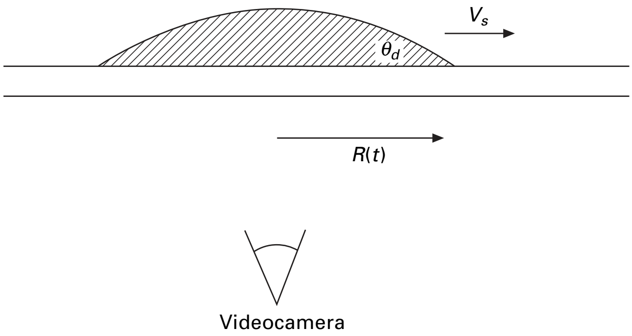

6.6 Recording change of a liquid drop radius *R*(*t*) as a function of time; From Brochard-Wyart, F., 'Droplets: Capillarity and Wetting', in *Soft Matter Physics*, M. Daoud, C.E. Williams, Editors. 1999, Springer: New York. pp. 1–45. With kind permission of Springer Science and Business Media.

known as the *precursor film* (see Fig. 6.7). This precursor film was first observed by Hardy in 1919 (Hardy, 1919) during his work on lubrication, when he noticed the motion of dust in front of a spreading droplet. However, the detailed study of its structure and profile, using high-precision optical techniques on the nanoscopic scale (ellipsometry), has been achieved only in the last decade or so. This has revealed a tiered structure, which gives us information about molecular forces (Heslot, Cazabat *et al.*, 1989; Cazabat, Gerdes *et al.*, 1997). A direct visualization of the droplet and its surrounding halo, obtained by an atomic force microscope, is shown in Fig. 6.8.

How can the spreading law be explained? The macroscopic force pulling on the droplet is the unbalanced Young's force

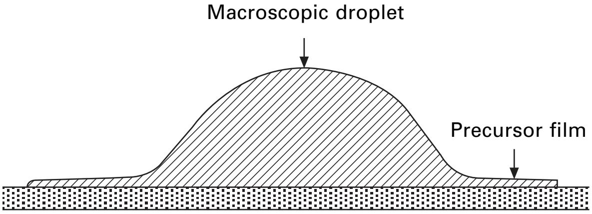

6.7 A close-up of a liquid precursor film; From Brochard-Wyart, F., 'Droplets: Capillarity and Wetting', in *Soft Matter Physics*, M. Daoud, C.E. Williams, Editors. 1999, Springer: New York. pp. 1–45. with kind permission of Springer Science and Business Media.

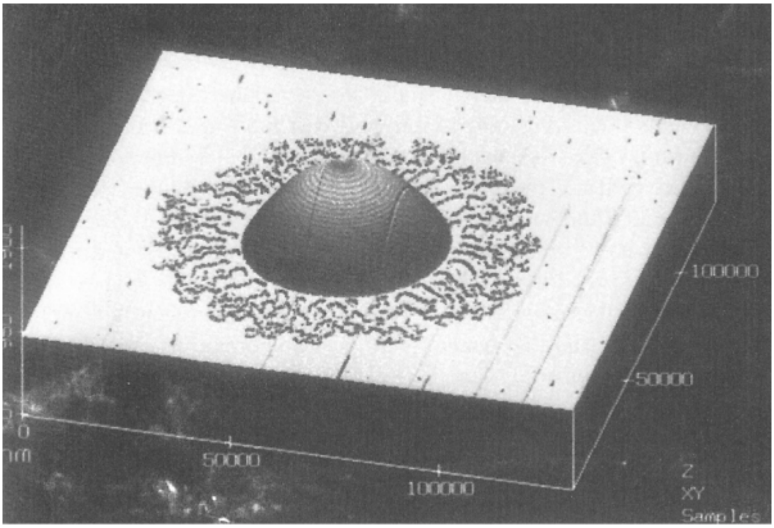

6.8 A direct visualization of the liquid droplet and its surrounding halo; From Brochard-Wyart, F., 'Droplets: Capillarity and Wetting', in *Soft Matter Physics*, M. Daoud, C.E. Williams, Editor. 1999, Springer: New York. pp. 1–45. With kind permission from Dr. Didier.

$$F_d = \gamma_{SO} - (\gamma_{SO} + \gamma \cos\ \theta) = S + \frac{1}{2}\gamma\theta_d^2 \qquad [6.29]$$

This force includes two terms: S (very large) and $\frac{1}{2}\gamma\theta_d^2$ (very small indeed; 10^4 times smaller than S for angles $\theta_d \approx 1°$). We will neglect S! We shall assume that the frictional force

$$F_f = \frac{\eta}{\theta_d} V \qquad [6.30]$$

on the fluid wedge balances the tiny contribution of $\frac{1}{2}\gamma\theta_d^2$ to the total force. We then obtain the experimentally established law for the spreading rate

$$V = \frac{\gamma}{\eta}\theta_d^3 \qquad [6.31]$$

By using the *capillary number*, the macroscopic spreading law is universal in reduced units:

$$C_a \approx \theta_d^3 \qquad [6.32]$$

One of the major contributions of de Gennes to wetting dynamics is the demonstration that the frictional force in the precursor film exactly balances S:

$$F_{fil} = S \qquad [6.33]$$

It is for this reason that, on a nanoscopic scale, S plays no role whatever in the spreading. On the other hand, the greater S is, the more the precursor film spreads out.

It is often said that we would have to wait as long as the age of the universe for a droplet to spread out. Indeed, since the spreading speed varies as θ_d^3, while the droplet is flattening out, it must spread more and more slowly. In consequence, it would take months for a micro droplet to spread spontaneously over several square centimeters, even if the liquid were of very low viscosity. It is thus easy to understand why spreading is forced in industrial processes, so as to cover surfaces more and more quickly (at rates of around the km/min).

Although liquids spread slowly in conditions of total wetting, they spread much more quickly in partial wetting, because the dynamical contact angle θ_d, which is always greater than the equilibrium one θ_e, remains large. The spreading time τ_e can be estimated using the dimensional law

$$R_e = \frac{\gamma}{\eta}\theta_e^3\tau_e \qquad [6.34]$$

where R_e is the radius of the deposited droplet at equilibrium.

$$R_e = 1\ mm,\ \frac{\gamma}{\eta} \approx 1 m/s,\ \theta_e \sim 1\ rad, \text{ and } \tau_e \sim 1\ ms.$$

6.5 Rayleigh instability

It is well known in the classical theory of capillarity that cylindrical jets are unstable and break into small droplets as seen in Fig. 6.9 (Rayleigh instability) (Sekimoto *et al.*, 1987). This is also true for macroscopic films deposited on fibers. The van der Waals interaction, however, stabilizes thin films on fibers of radius b. A linear stability analysis performed by Brochard (1986) shows that all films smaller than $e = (ab)^{1/2}$ are stable, where a is the liquid molecular size. This is particularly true both for the films in equilibrium with a reservoir and for the equilibrium sheaths.

6.5.1 A static analysis

A droplet will not spread out along a horizontal fiber, and this is true even for complete wetting ($S > 0$). Because of the cylindrical symmetry, the L/A interface is more dominant than the L/S interface, and a sleeve distribution is unstable (Brochard-Wyart, 1999). This is the reason for the so-called Rayleigh instability. Thus in Fig. 6.9 when a fiber is coated by a liquid film, the state is unstable and the film soon breaks down into small droplets, more or less regularly spaced along the fiber, leaving only an extremely thin liquid layer on the fiber owing to the intermolecular forces such as the van der Waals actions as mentioned above, if the disjoining pressure according to Derjaguin (Neimark, 1999) is negligible. The formation of such a droplet chain from the initially continuous liquid film occurs in the cases of either zero contact angle or complete wetting over a plane surface (Roe, 1957). In other words, wetting behavior of fibers is typified by the instability or breakdown of the liquid columns coating the fiber, first described by Plateau (1869) and Rayleigh (1878), hence the term of Rayleigh instability.

In general the disintegration of a liquid jet with radius r is attributed to the development of wave perturbations with various wavelengths λ on the surface of the liquid column, where λ has to be greater than $2\pi r$ according to Roe (1957). This perturbation will then trigger the disintegration of the liquid cylinder at an avalanching rate. This phenomenon was later studied by several

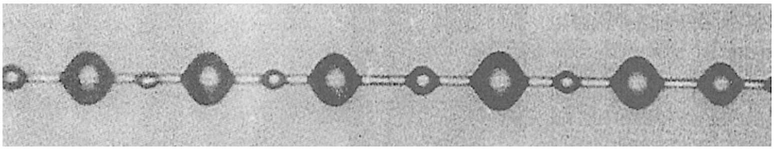

6.9 A typical example of liquid Rayleigh instability; From Brochard-Wyart, F., 'Droplets: Capillarity and Wetting', in *Soft Matter Physics*, M. Daoud, C.E. Williams, Editor. 1999, Springer: New York. pp. 1–45. With kind permission of Springer Science and Business Media.

other authors both theoretically and experimentally; for instance by Roe (1957), Tomotikav (1935) and Meister and Scheele (1967).

We will examine two parts of the process in the case of liquid coating a fiber (i) the breaking down of a continuous liquid cylinder covering a fiber and (ii) the detaching of the fragmented liquid droplets from the fiber. But first we have to investigate some geometrical surfaces of revolution with a constant mean curvature so as to establish a criterion at which liquid bodies remain stable, followed by a rough reasoning on the instability of the liquid film on a fiber, based on the energy conservation principle. Next, we will discuss the evolution of wave instability of a pure liquid jet according to Rayleigh (1878) so that the critical wavelength that sets off the liquid jet breakdown will be derived.

A rough analysis of the Rayleigh instability can be conducted by associating the initial shape of a liquid jet, a cylinder in our case, with the final shape of a chain of droplets each with identical volume. For an incompressible liquid

$$\pi r_0^2 \lambda_r = \frac{4}{3}\pi_d^3 \qquad [6.35]$$

where λ_r is the length of the cylinder with original radius r_o that is converted into one droplet of radius r_d. This λ_r value, obtainable from the volume and surface energy conservation laws, will be taken as the approximation of the Rayleigh wavelength λ. We then obtain

$$r_d^2 = \left(\frac{3}{4} r_o^2 \lambda_r\right)^{\frac{2}{3}} \qquad [6.36]$$

The energy of the liquid consists of the ones associated with the surface tension γF and the volume pressure $p_c V$; where F is the corresponding liquid surface area and V is the liquid volume, while p_c denotes the capillary pressure. The energy change before and after the disintegration of the liquid column clearly satisfies:

$$2\pi r_0 \lambda_r \gamma + \pi r_o \lambda_r \gamma \geq 4\pi r_d^2 \gamma + \frac{8}{3}\pi r_d^2 \gamma \qquad [6.37]$$

From Equation [6.37] we find λ_r

$$\lambda_r \geq \frac{20}{9}\frac{r_d^2}{r_o} \qquad [6.38]$$

Now we substitute for r_d^2 from Equation [6.36] into Equation [6.38] to obtain

$$\lambda_r \geq \frac{5^3 4}{3^4} r_0 \approx 1.96\pi \cdot r_o \qquad [6.39]$$

This result is consistent with the exact value obtained later for the Rayleigh wavelength $\lambda = 2.88\pi r_o$. A well-known similar inequality was first established experimentally by Plateau (1869), and he proceeded to the problem of oil drops in water mixed with alcohol forming into cylinders and determined that the instability starts to occur when the cylinder length, that is the wavelength λ, is between $1.99\pi r_o$ and $2.02\pi r_o$. There is another approach in the literature (de Gennes, 2003) that provides us with a similar inequality $\lambda > 2\pi r_o$. We can thus conclude that a drop with shorter wavelength than $2\pi r_o$ cannot be formed since the surface energy of the drop should always be lower than that of the original smooth cylinder.

We have to stress that the exact value for the wavelength of the Rayleigh instability cannot be derived based merely on the conservation of free energy, for the transformation of a liquid body shape is coupled with the mutation of its surface area, causing change of both energy and entropy at the liquid–gas interface as discussed in Grigorev and Shiraeva (1990).

6.5.2 A more dynamic approach

The Rayleigh instability of liquid jets is the consequence of a temporal development and magnification of the originally tiny perturbations, also known as the capillary waves (de Gennes *et al.*, 2003). We assume the perturbations to be harmonic with an exponentially growing amplitude. While such a perturbation is developing along a liquid jet, some of the liquid surface energy turns into the kinetic energy associated with a liquid flow, thus causing the cylindrical liquid column to be transformed into a chain of individual droplets. We anticipate the perturbations to develop with various speeds, depending on their wavelengths, and the perturbation that grows the most will quickly prevail so as to determine the wavelength, or distance between the neighboring droplets (Brochard, 1986). For practical purposes, we further assume that the resulting wavelength is entirely determined by the earliest state of the perturbations. We will develop more details of this idea below.

The perturbation wave propagates on the liquid column of the originally cylindrical shape. By coinciding the column axis with the axis z of the Cartesian coordinate system, the radius of the liquid body changes according to our assumption above in space and time as

$$r = r_o + ae^{qt}\cos(kz) \tag{6.40}$$

where r_o is a constant, and a denotes the initial amplitude of the perturbation. The growing parameter for the surface wave is q, and k is the wave vector ($k = 2\pi\lambda^{-1}$). For convenience, we will use in the following text a parameter $\alpha(t) = ae^{qt}$. Given the assumption that the whole process is determined by the early state of the perturbation, we take into account only the first non-zero term in the expansions of surface and kinetic energies of the developing perturbation.

Our further procedure will be a qualitative one, working with the following previously obtained findings. (i) The relevant parameters for the surface and kinetic energy changes are those involved in Equation [6.38], which is our first estimation of the Rayleigh wavelength. The relevant parameters include the radius of the original cylinder r_o, the wave vector k, and the amplitude $\alpha(t) = a\exp(-qt)$. (ii) According to the Plateau inequality [6.39] written in the form $r_ok < 0.996\sim1.012$, or approximately $r_ok < 1$, the dimensionless parameter r_ok, will play a critical role in changes of surface and kinetic energies. (iii) When the surface energy change is positive, there must be $r_ok > 1$, and the change is negative when $r_ok < 1$ as dictated by the Plateau inequality.

The surface energy change $\Delta W(t)$ per unit length of the liquid jet after some mathematical manipulations in de Gennes *et al.* (2003) can be written as

$$\Delta W(t) \approx \alpha^2(t)(1 - k^2r_o^2) \qquad [6.41]$$

The kinetic energy per unit length, $\Delta T = T_1 - T_2$, has to contain a relevant parameter proportional to the velocity squared. The only time-dependent relevant parameter is $\alpha(t) = ae^{qt}$ whose physical unit is length, and its time derivation

$$\frac{d}{dt}\alpha(t) = \dot{\alpha}(t) = aqe^{qt} = q\alpha(t) \qquad [6.42]$$

has the meaning of velocity. Therefore, we have ΔT proportional to $\dot{\alpha}^2(t)$. The dependence of ΔT with the remaining parameters k and r_o has to be estimated based on the kinetic energy required to transport an equal volume of liquid an equal distance in the same time. The flux in a tube is proportional to r^2v and its energy to r^2Lv^2 where r is the radius of the tube and L is the distance on which the liquid is transported through at average velocity v. From the equality of fluxes in tubes with various radii r_1 and r_2 follows $\frac{v_1}{v_2} = \frac{r_2^2}{r_1^2}$ and so the ratio of the kinetic energies T_1 and T_2 for different radii r_1 and r_2 is

$$\frac{T_1}{T_2} = \frac{r_2^2}{r_1^2} \qquad [6.43]$$

So, the kinetic energy estimated here has to be inversely proportional to r_o^2. The only way to incorporate the wave vector k into the equation so as to comply with the constraint on the kinetic energy by the condition (ii), the dependence on dimensional parameter r_ok, is to assume ΔT to be inversely proportional to the square of k as well. The resultant estimation of the kinetic energy of the perturbation is thus

$$\Delta T \approx \pi\rho r_o^2\dot{\alpha}^2(t)\frac{1}{(kr_o)^2} \qquad [6.44]$$

where ρ is the liquid mass density. The law of energy conservation, $\Delta T + \Delta W = 0$, leads to the relation

$$q^2 \frac{1}{(kr_o)^2} + [1 - (kr_o)^2] = 0 \qquad [6.45]$$

with its extreme value for the growing parameter q given as the function of the dimensionless product kr_o by the equation

$$\frac{d}{dx} \sqrt{(kr_o)^2 (k^2 r_o^2 - 1)} = 0 \qquad [6.46]$$

Equation [6.46] has the solution $kr_o \sqrt{1/2} = 0.707$, where $k = 2\pi\lambda^{-1}$, which provides us with the estimation of the Rayleigh wavelength $\lambda_{est} = 2\sqrt{2}\,\pi r_o = 2.83\pi r_o$. The exact result for the Rayleigh wavelength is achieved by means of Navier–Stokes such that Equation [6.46] can be expressed in terms of $(ikr_o)(J_o'(ikr_o))/J_o(ikr_o)$, where $J_o(ikr_o)$ is the Bessel function of zero order, and J_o' is its first-order derivative, r is the cylindrical coordinate, and i denotes the imaginary term. The maximum growing coefficient q then has the value of 0.69 and the Rayleigh wavelength thus obtained is $2.88\pi r_o$, in good agreement both with results from Equation [6.46] and from (Rayleigh, 1878).

6.6 Lucas–Washburn theory and wetting of fibrous media

6.6.1 Liquid climbing along a fiber bundle

Study of fiber wetting behavior is critical in prediction of properties and performance of fibrous structures such as fiber reinforced composites and textiles. On the other hand, the most often studied cases in physics for wetting phenomena are the wetting of solid planes. Compared to the plane wetting situation, the wetting of a fiber exhibits some unique features due to the inherent fiber curvature (Brochard, 1986; Bacri, Frenois *et al.*, 1988). Brochard, for instance, derived the critical spreading parameter S_{CF} for complete fiber wetting transition and proved that this parameter is greater than that for a plane of the same liquid/solid system. It means that liquids are more willing to wet planes than individual fibers of the same material, due to fiber curvature.

However, in spite of this higher inertia of wetting process of individual fibers, one of the best known and most frequently used materials for liquid absorption is fiber assemblies. Their excellent behavior during wetting processes could be intuitively explained by the capillary effect due to their collectively large inner surface area, but a more quantitative theory of fiber assembly wetting at the microscopic level has yet to be fully developed.

We attempt here to extend the approach presented by Brochard (Brochard, 1986; Brochard-Wyart and Dimeglio, 1987) and Bacri (Bacri, Frenois *et al.*, 1988; Bacri and Brochard-Wyart, 2000) obtained for single fiber wetting, to the spreading of a liquid along a fiber bundle. We then develop a theory to predict the ascension profile of a liquid along a vertical fiber bundle. The non-linear relationship between the liquid profile and the bundle properties observed experimentally will be predicted by the theoretical tool.

Brochard's deduction of a liquid body profile in a wetting regime for a single fiber is easily extendable to a small bundle of parallel fibers, with the assumption of axial symmetry of the sessile liquid body. Our goal here is to obtain the relationship between the liquid body profile $\Phi(x)$ measured from the bundle to the liquid/air interface. The equivalent radius of the fiber bundle is denoted above as R, and the bundle is vertically dipped into the liquid as shown in Fig. 6.10.

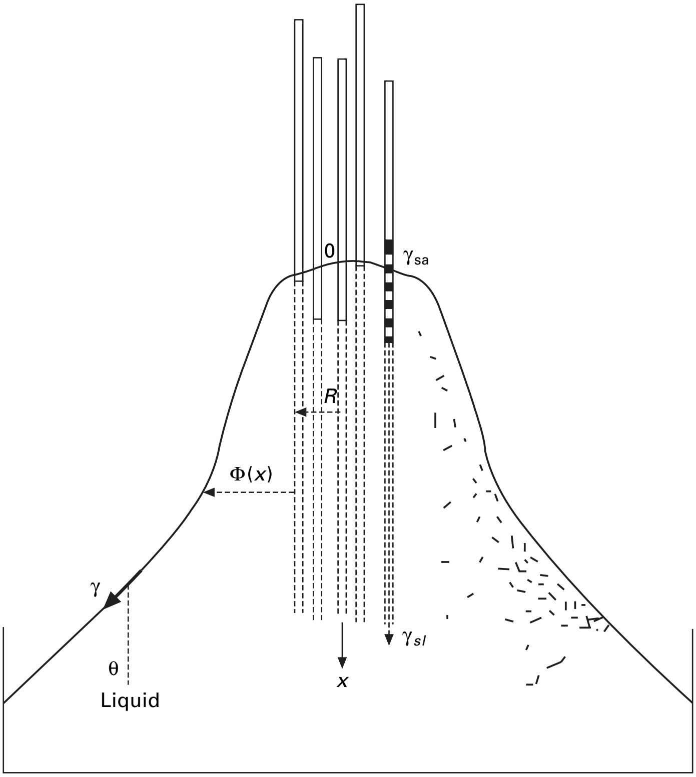

6.10 A fiber bundle vertically dipped into the liquid; From Lukas, D. and N. Pan (2003). 'Wetting of a fiber bundle in fibrous structures.' *Polymer Composites* 24(3): 314–322 with kind permission of the Society of Plastics Engineers.

The base for the derivation is the equilibrium of the projections onto the bundle axis x of the capillary forces (Brochard, 1986). The particular force projections taking part in the equilibrium include the one spreading the liquid on a fiber caused by γ_{SO}, parallel with the bundle axis, the force due to the fiber/liquid surface tension γ_{SL}, parallel with but opposite to γ_{SO}, and the third one in the direction with an angle θ from the x axis representing the liquid surface tension γ as illustrated in Fig. 6.10.

In Laplace force regime, the equilibrium of the capillary forces acting on the liquid spread on the fiber bundle is

$$2\pi n \cdot b\gamma_{SO} = 2\pi n \cdot b\gamma_{SL} + 2\pi(\Phi(x) + R) \cos \theta. \qquad [6.47]$$

In our consideration, we neglect the gravity effects, since addition of a gravitational term into Equation [6.47] will make it mathematically unsolvable. Yet it has been indicated (Manna *et al.*, 1992) that, for relatively short fibers ($\leq$ 10 cm), the effects of the gravitational force are negligible.

Using the following relations

$$\cos \theta = \frac{1}{\sqrt{1 + \tan^2\theta}} \qquad [6.48a]$$

and

$$\tan \theta = \frac{d\Phi(x)}{dx} = \Phi'(x) \qquad [6.48b]$$

Equation [6.47] can be rewritten in the form of a differential equation,

$$\frac{R + \Phi(x)}{\sqrt{1 + \Phi'^2(x)}} = np \qquad [6.49]$$

where p is a system constant

$$p = b\left(\frac{S}{\gamma} + 1\right) \qquad [6.50]$$

The solution of Equation [6.49] is the function $\Phi(x)$ that represents the equilibrium profile of the liquid mass clinging onto the fiber bundle

$$\Phi(x) = np \cosh\left(\frac{x - x_o}{np}\right) - R \qquad [6.51a]$$

where x_o specifies the peak point of the macroscopic meniscus. We can set x_o = 0 so that

$$\Phi(x) = np \cosh\left(\frac{x}{np}\right) - R \quad 0 \leq x < \infty \qquad (3.51b)$$

where x is the height along the fiber bundle but measured from the top of the liquid profile as shown in Fig. 6.11. It is clear that, in order to maintain the solution of the equation meaningful, i.e. $\Phi(x) \geq 0$, first there has to be $p > 0$, which translates into

$$\frac{S}{\gamma} > -1 \quad \text{or } \gamma_{SO} > \gamma_{SL} \qquad [6.52]$$

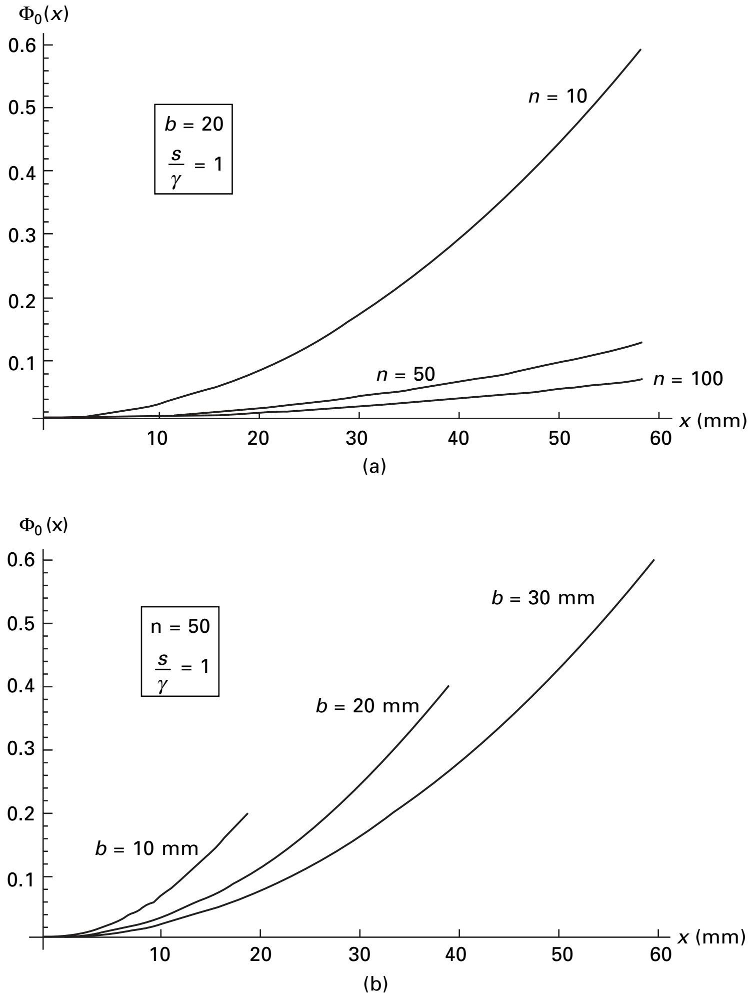

(a)

(b)

6.11 The liquid profile $\Phi(x)$ over a fiber bundle. From Lukas, D. and N. Pan (2003). 'Wetting of a fiber bundle in fibrous structures.' *Polymer Composites* 24(3): 314–322 with kind permission of the Society of Plastics Engineers. (a) $\Phi(x)$ distribution at different fiber number n; (b) $\Phi(x)$ distribution at different fiber radius b; (c) $\Phi(x)$ distribution at different spreading ratio S/γ.

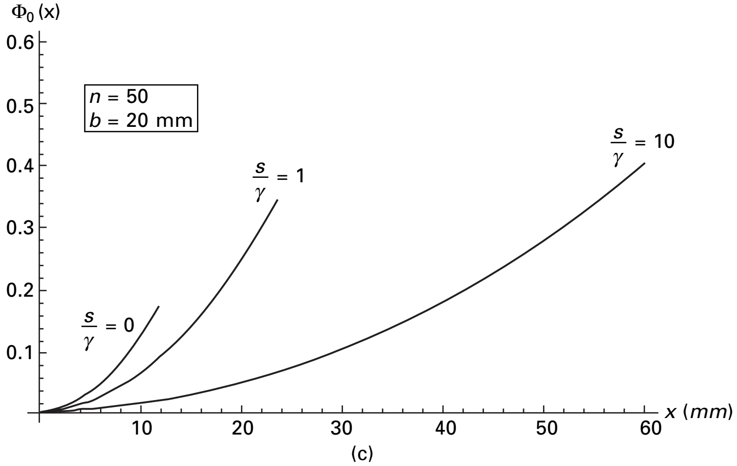

6.11 Continued

The physical implication of this inequity is obvious – a necessary condition for wetting a fiber bundle is that the surface tension of the fiber γ_{SO} has to be greater than the surface tension of the fiber/liquid, γ_{SL}.

Furthermore, from Equation [6.51b], we can see that there is a criterion for determining the equivalent fiber bundle radius R, since $\Phi(x) \geq 0$ so that

$$R \leq np \cosh\left(\frac{x}{np}\right) \qquad [6.53]$$

As cosh(x) achieves the minimum when $x = 0$, and cosh(0) = 1, we have the limit for R

$$R \leq np = nb\left(\frac{S}{\gamma} + 1\right) \qquad [6.54]$$

In the case $R > np$, the mathematical solution of $\Phi(x)$ no longer has physical meaning. Shown in Equation [6.54], the spacing between fibers in the bundle is limited by the spreading ratio S/γ. By using Equation [6.52], i.e. $S/\gamma > -1$, the minimum value of the bundle radius $R = R_{min} > 0$.

Furthermore, when $x = 0$, and cosh (0) = 1, then Equation [6.51b] gives $\Phi(0) = np - R$. It means that, according to Equation [6.54], beneath the liquid meniscus with the *hyperbolic cosine* shape, there exists a microscopic liquid film on the fiber bundle, whose thickness is

$$\Phi(0) = np - R > 0 \qquad [6.55]$$

This may indicate that, at the point where the liquid mass profile starts, i.e. $x = 0$, the liquid first coats the fiber bundle with a thin layer of thickness $np - R$, a phenomenon similar to what is reported in Brochard (Brochard,

1986) for the single-fiber wetting case. However, it is recommended that this conclusion be verified in view of the omission of the gravitational effects in the analysis.

Considering the upper limit for the bundle radius $R = np$ in Equation [6.55], the lower limit $\Phi_0(x)$ of the liquid profile $\Phi(x)$ in Equation [6.51b] can be expressed in terms of the Harkinson spreading parameter S and the liquid surface tension γ:

$$\Phi_o(x) = nb\left(\frac{S}{\gamma} + 1\right)\cosh\left(\frac{x}{nb\left(\frac{S}{\gamma} + 1\right)}\right) - nb\left(\frac{S}{\gamma} + 1\right) \quad 0 \le x \le \infty \tag{6.56}$$

That is, $\Phi_o(x)$ is a function of the height x, the spreading ratio S/γ reflecting the surface properties of liquid, the fiber, and the liquid/fiber interfacial property, as well as the fiber parameters nb, as plotted in Fig. 6.11 based on Equation [6.56] (which may be regarded as [6.51c] in the series).

In general, $\Phi_o(x)$ increases with x when other parameters are given. The effect of the number of fibers in a bundle is seen in Fig. 6.11(a) where a small bundle (small n value) will have a greater amplitude of $\Phi_o(x)$ at a given position x.

The fiber radius b has the similar influence on $\Phi_o(x)$, i.e. $\Phi_o(x)$ increasing with b for a given x, except that it also determines the maximum value, $\Phi_m(x)$ and the maximum height x_m as seen in Fig. 6.11(b); when b is smaller, the $\Phi_m(x)$ value as well as x_m will be accordingly smaller. Figure 6.11(c) shows that the same thing can be said about the effect of the spreading ratio S/γ; a smaller ratio S/γ results in a smaller $\Phi_m(x)$ and x_m.

Once again, the solution to Equation [6.51] has a shortcoming resulting from the exclusion of gravity in the analysis. The consequence is an asymptotical behavior of $\Phi(x)$ that does not converge to the flat horizontal surface of the liquid source perpendicular to the fiber bundle.

6.6.2 Lucas–Washburn theory

The first attempt to understand the capillary driven non-homogeneous flows for practical applications was made by Lucas (1918) and Washburn (1921). Good (1964) and Sorbie *et al.* (1995) have successively derived more generalized expressions of the theory. The theory aroused public excitement in England in 1999 about what is called dunking, or dipping a biscuit into a hot drink such as tea or coffee to enhance flavor release by up to ten times (Fisher, 1999).

Lucas–Washburn theory has been used in, and further developed for, the textile area by a few authors. Chatterjee (1985) dealt with these kinds of flow in dyeing. Pillai and Advani (1996) conducted an experimental study of the capillarity-driven flow of viscous liquids across a bank of aligned fibers. Hsieh (1995) has discussed wetting and capillary theories, and applications of these principles to the analysis of liquid wetting and transport in fibrous materials. Several techniques employing fluid flow to characterize the structure of fibrous materials were also presented in Hirt *et al.* (1987). Lukas and Soukupova (1999) carried out a data analysis to test the validity of the Lucas–Washburn approach for some fibrous materials and obtained a solution for the Lucas–Washburn equation including the gravity term.

Non-homogeneous flows have also been studied using stochastic simulation since the beginning of the 1990s. Manna, Herrmann and Landau (1992) presented a stochastic simulation that generates the shape of a two-dimensional liquid drop, subject to gravity, on a wall. The system was based on the so-called Ising model, with Kawasaki dynamics. They located a phase transition between a hanging and a sliding droplet. Then Lukkarinen (1995) studied the mechanisms of fluid droplet spreading on flat solids, and found that in the early stages the spreading is of nearly linear behavior with time, and the liquid precursor film spreading is dominated by the surface flow of the bulk droplet on the solid; whereas in the later stages, the dynamics of liquid spreading is governed by the square root of time. A similar study of fluid droplet spreading on a porous surface was also recently reported (Starov, *et al.* 2003). First attempts to simulate liquid wetting dynamics in fiber structures using the Ising Model have been done by Lukas *et al.* (Lukas, Glazyrina *et al.*, 1997; Lukas and Pan, 2003; Lukas *et al.*, 2004), also by Zhong *et al.* (Zhong, Ding *et al.*, 2001, 2001a, though the simulation was restricted to 2-D systems only.

For both scientific and practical purposes, the so-called wicking (or absorbency) rate is of great interest. EDANA and INDA recommended tests (EDANA, 1972; INDA, 1992) to determine the vertical speed at which the liquid is moving upward in a fabric, as a measure of the capillarity of the test material. The vertical rate of absorption is measured from the edges of the test specimen strips suspended in a given liquid source. The resultant report of the test contains a record of capillary rising heights after a time 10 s, 30 s, 60 s (and even 300 s if required). Gupta defined absorbency rate as the quantity that is characterized based on a modification of the Lucas–Washburn equation, and he then modified it to apply to a flat, thin, circular fabric on which fluid diffuses radially outward (Gupta, 1997).

Miller and Friedman (Miller *et al.*, 1991; Miller and Friedman, 1992) introduced a technique for monitoring absorption rates for materials under compression. Their Liquid/Air Displacement Analyser (LADA) measures the rate of absorption by recording changes of the liquid weight when liquid is sucked into a flat textile specimen connected to a liquid source.

A more scientific definition of the wicking rate is based on the Lucas–Washburn theory. This simple theory deals with the rate at which a liquid is drawn into a circular tube via capillary action. Such a capillary is a grossly simplified model of a pore in a real fibrous medium with a highly complex structure (Berg, 1989). The theory is actually a special form of the Hagen–Poiseuille law (Landau, 1988) for laminar viscous flows. According to this law, the volume dV of a Newtonian liquid with viscosity μ that wets through a tube of radius r, and length h during time dt is given by the relation

$$\frac{dV}{dt} = \frac{\pi r^4 (p_1 - p_2)}{8h\mu} \qquad [6.57]$$

where $p_1 - p_2$ is the pressure difference between the tube ends. The pressure difference here is generated by capillarity force and gravitation. The contact angle of the liquid against the tube wall is denoted as θ, and β is the angle between the tube axis and the vertical direction shown in Fig. 6.12. The capillary pressure p_1 has the value

$$p_1 = \frac{2\gamma \cos\theta}{r} \qquad [6.58]$$

while the hydrostatic pressure p_2 is

$$p_2 = h\zeta g \cos\beta \qquad [6.59]$$

where γ denotes the liquid surface tension, ζ is the liquid density, g is gravitational acceleration and h, in this case, is the distance traveled by the liquid, measured from the reservoir along the tube axis. This distance obviously is the function of time, $h = h(t)$, for a given system. When we substitute the

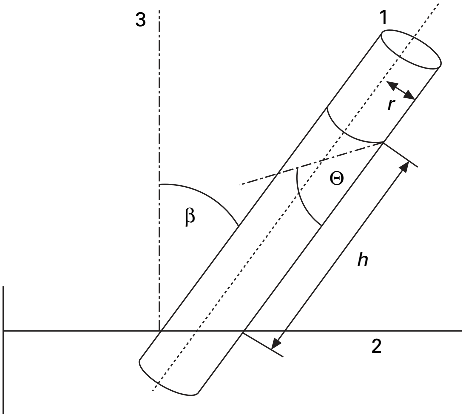

6.12 A single fiber in a liquid pool; From Lukas, D. and N. Pan (2003). 'Wetting of a fiber bundle in fibrous structures.' *Polymer Composites* 24(3): 314–322 with kind permission of the Society of Plastics Engineers.

quantities p_1, p_2, and $h(t)$ into Equation 6.57, expressing the liquid volume in the capillary V as $\pi r^2 h$, we obtain the Lucas–Washburn equation

$$\frac{dh}{dt} = \frac{r\gamma\cos\theta}{4\mu h} - \frac{r^2\zeta g\cos\beta}{8\mu} \qquad [6.60]$$

For a given system as shown in Fig. 6.13(a), parameters such as r, γ, θ, μ, ζ, g, and β remain constant. We can then reduce the Lucas–Washburn Equation [6.60] by introducing two constants

$$K' = \frac{r\gamma\cos\theta}{4\mu}, \quad \text{and} \quad L' = \frac{r\zeta g\cos\beta}{8\mu} \qquad [6.61]$$

into a simplified version

$$\frac{dh}{dt} = \frac{K'}{h} - L' \qquad [6.62]$$

The above relation is a non-linear ordinary differential equation that is solvable only after ignoring the parameter L'; this has a physical interpretation, when either the liquid penetration is horizontal ($\beta = 90°$), or r is small, or the rising liquid height h is low so that $\frac{K'}{h} >> L'$ or $L' \to 0$, the effects of the gravitation field are negligible and the acceleration g vanishes. The Lucas–Washburn Equation [6.62] could thus be solved with ease

$$h = \sqrt{2K't}, \qquad [6.62]$$

6.6.3 Radial spreading of liquid on a fibrous material

Now we turn our attention back to Gupta's (1997) approach to wicking rate where a fluid from a point source in the centre of a substrate is spreading

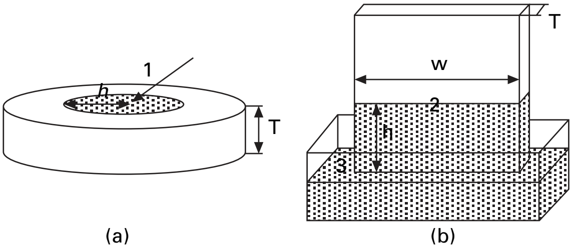

6.13 Two liquid spreading routes in fibrous materials. (a) liquid spreading in radial directions; (b) liquid ascending vertically. Adapted from Lukas, D. Soukupova, V., Pan, N. and Parikh, D. V. (2004). 'Computer simulation of 3-D liquid transport in fibrous materials.' *Simulation-Transactions of The Society For Modeling and Simulation International* 80(11): 547–557.

radially outward, instead of the ascending liquid front in a fibrous substrate partially dipped into a liquid, as illustrated in Fig. 6.13(a) and (b), respectively.

It is useful now to transfer the Lucas–Washburn equation into a modified version by replacing the distance h with liquid mass uptake m. Such a transition is described in detail in Ford (1933) and Hsieh (1995). This manipulation does not influence the fundamental shape of Equation [6.63], because the relationship between h and m is linear for a circular tube of fixed cross-section. Furthermore, for the radial spreading, the liquid mass $m_R = \pi h^2 T \zeta V_L$ and for the ascending liquid front $m_A = whT\zeta V_L$, denoting T as the thickness of the substrate, and V_L as the liquid volume fraction inside the substrate of width w.

For the radial liquid spreading in a flat textile specimen, as in Fig. 6.13(b), we can then write, using Equation [6.63]

$$Q = \frac{m_R}{t} = 2\pi K' T \zeta V_L \qquad [6.64]$$

where Q is the liquid wicking (absorbency) rate used by Gupta (1997), which is independent of time during the spreading process. Equation [6.64] can be used to predict a drop radial spreading as shown in Fig. 6.14.

Let us now substitute liquid mass uptake m_A into the original Lucas–Wasbhurn Equation [6.62], with the result as

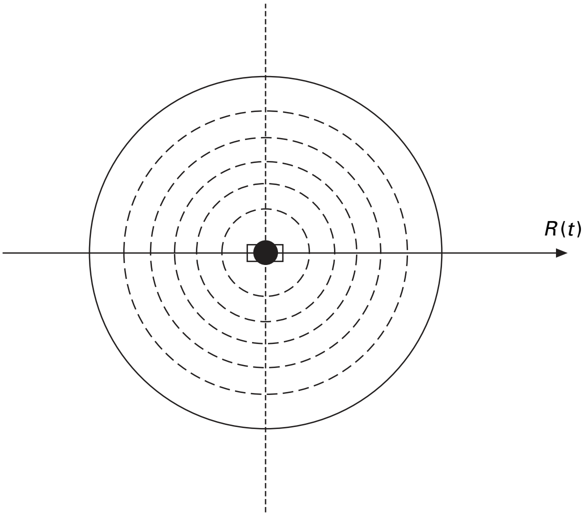

6.14 Radial spreading of a liquid drop. From Brochard-Wyart, F., 'Droplets: Capillarity and Wetting', in *Soft Matter Physics*, M. Daoud, C.E. Williams, Editors. 1999, Springer: New York. pp. 1–45. With kind permission of Springer Science and Business Media.

$$\frac{dm_A}{dt} = \frac{K}{m_A} - L \qquad [6.65]$$

The new constants K and L are

$$K = (wT\zeta V_L)^2 K', \quad L = wT\zeta V_L L' \qquad [6.66]$$

It is obvious that the constant K in the modified Lucas–Washburn Equation Equation [6.65] is proportional to the wicking (absorbency) rate Q which is defined in Equation [6.64], and from Equations [6.64] and [6.66] it follows that

$$Q = \frac{2\pi}{w^2 T\zeta V_L} K \qquad [6.67]$$

Hence, the parameter K can be used as a measure of the spreading wicking rate Q in the experiments when a fabric is hung vertically into a liquid. The values of K and L can be derived from the slope and intercept of the dm_A/dt versus $1/m_A$.

On the other hand, Equations [6.62] and [6.65] can be solved in terms of the functions $t(h)$ or $t(m_A)$ without dropping the gravity term g, as shown by Lukas and Soukupova (1999). For the liquid mass uptake Lucas–Washburn Equation 6.65, one obtains for the ascending liquid front the relationship

$$t(m_A) = -\frac{m_A}{K} - \frac{K}{L^2} \ln\left(1 - \frac{L}{K} m_A\right) \qquad [6.68]$$

Conversely, however, we are unable to acquire the inverse solution $m_A(t)$ using the common functions.

The Lucas–Washburn approach presents an approximate but effective tool to investigate the wicking and wetting behaviour of textiles despite the complicated, non-circular, non-uniform, and non-parallel structure of their pore spaces. It has been shown that Equations [6.62] and [6.65] hold for a variety of fibrous media, including paper and textile materials [(Berg, 1989; Everet *et al.*, 1978) and 3-D pads (Miller and Jansen, 1982). Nevertheless, this theory is unable to deal with issues such as the influence of structure, e.g. fiber orientation and deformation, on wetting and wicking behavior of fibrous media.

6.6.4 Capillary rise in a fibrous material

Wetting a fiber assembly is very different from wetting a single fiber, for the specific surface areas in the two cases are very different. Instead of a single dimension of fiber radius r, we have to deal with a medium of complex surface structural geometry made of fibers and irregular pores.

For a medium with regular pore diameter d_p, the specific surface area A_s (m^2/kg) is defined as the total surface area per kg of the medium, and can be approximately calculated as

$$A_s \cong \frac{1}{\rho_s d_p} \qquad [6.69]$$

where ρ_s is the solid density of the medium without any pores. For a pore diameter $d_p = 10\ \mu\text{m}$ and $\rho_s = 1\ \text{g/cm}^3$, A_s is in the order of 100 m^2/kg. This value will be only 6 m^2/kg if no pores exist.

If we know the volume fraction of the fibers V_f, then density of the fibrous material is $\rho_s V_f$ and the total specific surface area is

$$A_f = A_s \rho_s V_f \cong \frac{V_f}{d_p} \qquad [6.70]$$

Now consider a column made of this medium, with cross-sectional area S and thus a wet volume Sh. When the height increases from h to $h + dh$, there is a corresponding change in capillary energy

$$dE_{cap} = A_f S dh\ (\gamma_{SL} - \gamma_{Sa}) \qquad [6.71]$$

and in liquid volume (assuming that all the pores are accessible by the liquid of density ρ_l)

$$dM = \rho_l (1 - V_f) S dh \qquad [6.72]$$

Associated with dM is a change in gravitational energy dE_g

$$dE_g = ghdM \qquad [6.73]$$

At equilibrium, the total energy change vanishes so that $dE_{cap} + dE_g = 0$, so that the new height

$$h = \frac{A_f (\gamma_{Sa} - \gamma_{SL})}{\rho_l (1 - V_f) g} \cong \frac{V_f}{d_p} \frac{(\gamma_{Sa} - \gamma_{SL})}{\rho_l (1 - V_f) g} = \frac{V_f}{d_p} \frac{\gamma \cos \theta}{\rho_l (1 - V_f) g} \qquad [6.74]$$

Although this result is completely analogous to Jurin's law, it is expressed in explicit macroscopic parameters of the fibrous materials. When pore diameter $d_p = 10\ \mu\text{m}$, $V_f = 0.5$ and water is the liquid, this results in $h = 10$ cm!

6.7 Understanding wetting and liquid spreading

Leger and Joanny (1992), de Gennes (1985) and Joanny (1986) have each written a comprehensive and excellent review on the liquid spreading phenomena. Some of the relatively new developments and discoveries in these reviews are summarized below.

6.7.1 The long-range force effects and disjoining pressure

In a situation of partial wetting, the liquid does not spread completely and shows a finite contact angle on a solid surface. Partial wetting behavior on perfect solid surfaces is well described by classical capillarity. Heterogeneities of the solid surface lead to contact angle hysteresis. Experimentally, it is very easy to tell the difference between partial wetting and complete wetting. In the latter case, there exists a microscopic liquid film underneath the water droplet covering the fiber, so that the contact angle $\theta = 0$ (as mentioned in Fig. 6.7) (Brochard–Wyart 1999).

In a complete wetting situation, the liquid forms a film on a solid surface with a thickness in the mesoscopic range. The direct long-range interaction between liquid and solid described by the so-called disjoining pressure governs the physics of these films. Films of mesoscopic thickness also appear in the spreading kinetics of liquids. These precursor films form ahead of macroscopic advancing liquid fronts. The spreading kinetics is extremely slow. In fact, it is only recently that it has been fully recognized that an essential aspect of the physics of thin films, i.e. long range force effects, has to be added to classical capillarity (Leger and Joanny, 1992). When a liquid spreads on a solid or on another immiscible liquid, thin liquid zones always appear close to the triple line. There, as soon as the thickness becomes smaller than the range of molecular interactions, the interfacial tensions are not sufficient to describe the free energy of the system: a new energy term has to be included, which takes into account the interactions between the two interfaces (solid–liquid and liquid–gas for a liquid spreading on a solid). This new free energy contribution has a pressure counterpart which is the disjoining pressure introduced by Derjaguin (1955) to describe the physics of thin liquid films. It may dominate the spreading behavior, especially in situations of total wetting in the late stages of spreading where thin films are likely to appear.

A recent paper by Rafai *et al.* (2005) has pointed out that wetting transition proceeds in two schemes: the first-order process and the critical process, depending on the thermal fluctuations, i.e. the competition between the short-range interactions and the long-range van der Waals interactions. The sign of the system's Hamaker constant determines the outcome of the competition. First-order implies a discontinuity in the first derivative of the surface free energy. This discontinuity then suggests a jump in the liquid layer thickness. Thus, at a first-order wetting transition, a discontinuous change in film thickness occurs, such as in the case of Rayleigh's instability. However, the critical wetting is a continuous transition between a thin and a thick adsorbed film at bulk two-phase coexistence.

6.7.2 Experimental investigation of the liquid wetting and spreading processes

The macroscopic scales are the easiest to investigate and have been most widely studied for a long time, either by observation through an optical microscope or by contact angle measurements. With the development of computer image analysis, this can now be performed in an automated way (Cheng, 1989), either for an advancing or a receding liquid front. A less classical method, based on the use of the whole drop as a convex mirror reflecting a parallel beam of light into a cone of aperture angle 2θ has been proposed by Allain *et al.* (1985), as it allows one to test simultaneously the whole periphery of the drop. Sizes and thicknesses can be deduced from direct observations through a microscope. If monochromatic light is used, equal thickness fringes are quite a convenient way of investigating drop profiles, with a vertical resolution of $A/2n$ (A is the wavelength of the radiation used and n the index of refraction of the liquid), the first black fringes being located at a thickness of $A/4n$, i.e. typically 800 Å for visible light (Tanner, 1976). In order to investigate thinner parts of the drop, typical thin film methods have to be used. As a liquid is present, methods requiring high vacuum are inadequate.

Teletzke, Davis *et al.* (1988) have settled on a description of spreading, including the long-range force contributions, which has stimulated a strong activity in the field, both theoretically and experimentally. Decisive progress has thus recently been achieved in the understanding of spreading and wetting phenomena.

This progress has only been possible because of the parallel development of very refined experimental techniques that allow the detailed investigation of the properties of thin liquid films (Cazabat, 1990). As a spreading drop may develop characteristic features at various thicknesses, ranging from microscopic (a few Å) to macroscopic (larger than 0.1 mm), complementary techniques have to be used in order to completely probe the spreading behavior.

6.7.3 The scale effects

One of the most interesting features is the variety of length scales involved in these problems: macroscopic scales for liquid thicknesses larger than a few thousand angstroms, mesoscopic scales for liquid thicknesses between 10 and 1000 Å, and even microscopic scales at the molecular level (de Gennes *et al.*, 2003).

At the macroscopic level the liquid is characterized by thermodynamic quantities and the spreading kinetics have been described as a hydrodynamic process. For simple liquids on ideal solid surfaces, the agreement between theory and experiment seems rather good both for static and dynamic properties. This is particularly true for Tanner's (1976) law, giving the variation of the dynamic contact angle with the advancing velocity that has been extensively verified experimentally. The extension of this law to more complex situations where the spreading is driven by other than the capillary forces, or to situations where the spreading is unstable, also gives good quantitative descriptions of the experimental results.

On the other hand, the viscous effects predominate over inertial effects when length scale becomes sufficiently small. Therefore, the dissipative mechanism in destabilizing a liquid cylinder becomes dominant and has to be considered (Schultz and Davis, 1982; Eggers, 1997). Another major additional difficulty comes from the fact that the thickness may vary rapidly with distance from the center of the drop, especially at mesoscopic scales. High spatial resolution is then required and the number of available techniques is not very large. Ellipsocontrast, i.e. observation under a microscope in reflected polarized light, has proven to be very useful to probe thicknesses in the range 100 Å and up, with a spatial resolution of 1 nm (Ausserre *et al.*, 1986); it is not however, up to now, fully quantitative. Ellipsometry (Azzam, 1977) appears to be the technique of choice, and tricks have been developed to increase the spatial resolution (Leger, Erman *et al.*, 1988; Heslot, Cazabat *et al.*, 1989). One has to notice, however, that it only gives access to the product *ne* (*n* is the index of refraction of the liquid, *e* its thickness). X-ray reflectivity has proven to be a unique tool to study spreading processes (Daillant *et al.*, 1988, 1990). The spatial resolution is poorer than in ellipsometry, as grazing incidence is used, and the dimensions of the illuminated area of the sample cannot be decreased below 100 nm × 1 or 2 mm. It is, however, a unique tool, because it gives access independently to three important characteristics of the liquid film: its thickness, its density and its roughness. It is thus valuable for microscopic scales and for studying the late stages of spreading. Many other techniques have been used to visualize the presence of thin liquid films, such as dust particle motion, vapor blowing patterns (Hardy, 1919) and the use of fluorescent or absorbing dyes, but they can hardly lead to quantitative profiles determination.

6.7.4 Heterogeneity

As in all surface phenomena, heterogeneities of the solid surface play an important role which is only partially understood. There are several models for contact angle hysteresis but very few quantitative experiments on this matter. In the case of partial wetting, the spreading kinetics of a liquid on a heterogeneous surface have been studied only in very artificial geometries and the spreading law (relation between the contact angle and the advancing velocity) on a strongly heterogeneous surface is not known either experimentally or theoretically (Joanny, 1986).

In a case of complete wetting, the dynamic contact angle only depends very weakly on the nature of the solid surface and heterogeneities play a less important role. At the mesoscopic level, the properties of thin liquid films are described by continuum theories that ignore the molecular nature of the liquid and by macroscopic hydrodynamics; the long-range character of the molecular interactions is then taken into account through the disjoining pressure.

For liquids for which the interactions are well known, the calculated static properties of the film are in very good agreement with the experimental measurements: this agreement is extremely good for superfluid helium but it is also satisfactory for van der Waals liquids such as silicone oils. The most spectacular recent progress in this field is the important development of surface scattering techniques such as X-ray reflection ellipsometry, which now allows measurements of thicknesses with a precision of the order of 1 Å or less; one should note, however, that the lateral resolution of these techniques is in the micron range and that the measured thicknesses are averaged over this size, thus eliminating heterogeneities of the film at small sizes.

For many liquids, however, and in particular for water, the disjoining pressure is only poorly known and this is a strong limitation of the theory. Recent studies start to consider cases where the disjoining pressure is non-monotonic. A qualitatively different spreading behavior is observed that is not entirely understood. These very refined techniques have also been applied to the study of precursor films that form ahead of spreading drops. Detailed determinations of the precursor film profile have been made experimentally; they are in qualitative agreement with the semi-microscopic theory but no quantitative agreement has been obtained, the reason for that being unclear.

For liquids spreading on high energy surfaces, the continuum description of the liquid breaks down in the last stages of the spreading where the beautiful experiments of Heslot *et al.* (1998, a, b) have shown that the liquid shows well-defined layers of molecular thickness. Some phenomenological theories have been proposed to describe this layered spreading but a systematic description of these experiments is far from being available. This looks like a very promising subject for future studies.

6.7.5 For liquids other than water

Other extensions of the hydrodynamic theory than the one discussed here have been made; for instance, to the spreading on a liquid substrate or to the case where the external phase is not a vapor, or systems of immiscible viscous liquids (Pumir, 1984; Joanny and Andelman, 1987). For more complex liquids such as polymeric liquids or surfactant solutions, our understanding of the spreading dynamic is poorer and further theoretical work is certainly needed to understand in more detail the role of surface tension gradients and the spreading hydrodynamics of polymer melts.

Finally, most of the theoretical studies of liquids spreading describe the spreading as a purely hydrodynamic process and use classical hydrodynamics down to liquid thicknesses of a few molecular diameters. In certain cases this works surprisingly well (as is known from helium physics) but should certainly be questioned for more complex liquids such as polymeric liquids or liquid crystals. Even for simple liquids, the spreading may involve non-hydrodynamic processes such as the evaporation and re-condensation of the liquid (which we have avoided, focusing on non-volatile liquids). This has received very little theoretical attention but experimentally, volatile liquids often show an instability when they spread (Williams, 1977).

We would like to finish this chapter using a paragraph by Herminghaus (2005) in his preface for a recent special edition of *J. Phys.: Condens. Matter* entirely devoted to the topic – 'By the mid-nineties, the physics of wetting had made its way into the canon of physical science topics in its full breadth. The number of fruitful aspects addressed by that time is far too widespread to be covered here with any ambition to completeness. The number of researchers turning to this field was continuously growing, and many problems had already been successfully resolved, and many questions answered. However, quite a number of fundamental problems remained, which obstinately resisted solution.'

6.8 References

Allain, C., Ausserre, D. and Rondelez, F. (1985). 'A new method for contact angle measurement of sessile drops' *J. Colloid Interface Sci.* **107**: 5.

Ausserre, D., Picard, A. M. and Leger, L. (1986). Existence and role of the precursor film in the spreading of polymer liquids' *Phys. Rev. Lett.* **57**: 2671–2674.

Azzam, R. M. and Bashara, A. (1977). *Ellipsometry and Polarized Light*. Amsterdam, North-Holland.

Bacri, J. C., Frenois, C. *et al.* (1988). 'Magnetic Drop-sheath Wetting Transition of a Ferrofluid on a Wire.' *Revue De Physique Appliquee* **23**(6): 1017–1022.

Bacri, L. and F. Brochard-Wyart (2000). 'Droplet suction on porous media.' *European Physical Journal E* **3**(1): 87–97.

Batch, G. L., Chen, Y. T. *et al.* (1996). 'Capillary impregnation of aligned fibrous beds: Experiments and model.' *Journal of Reinforced Plastics and Composites* **15**(10): 1027–1051.

Bauer, C., Bieker, T. *et al.* (2000). 'Wetting-induced effective interaction potential between spherical particles.' *Physical Review E* **62**(4): 5324–5338.

Baumbach, V., Dreyer, M. *et al.* (2001). 'Coating by capillary transport through porous media.' *Zeitschrift Fur Angewandte Mathematik Und Mechanik* **81**: S517–S518.

Berg, J. C. (1989). The Use of Single-fibre Wetting Measurements in the Assessment of Absorbency. *Nonwovens Advanced. Tutorial.* F. T. Allin and L. V. Tyrone (eds), Atlanta, TAPPI Press: 313.

Bieker, T. and Dietrich S. (1998). 'Wetting of curved surfaces' *Physica A* **252**(1–2), 85–137.

Brochard-Wyart, F. (1999). Droplets: Capillarity and Wetting. *Soft Matter Physics*. Daoud, M. and Williams C.E. (eds) New York, Springer: 1–45.

Brochard, F. (1986). 'Spreading of Liquid-drops on Thin Cylinders – the Manchon–Droplet Transition.' *Journal of Chemical Physics* **84**(8): 4664–4672.

Brochard-Wyart, F. and Dimeglio, J. M. (1987). 'Spreading of Liquid-drops on Fibers.' *Annali Di Chimica* **77**(3–4): 275–283.

Carroll, B. J. (1976). 'Accurate Measurement of Contact Angle, Phase Contact Areas, Drop Volume, and Laplace Excess Pressure in Drop-on-Fiber Systems.' *Journal of Colloid and Interface Science* **57**(3): 488–495.

Carroll, B. J. (1984). 'The Equilibrium of Liquid-drops on Smooth and Rough Circular Cylinders.' *Journal of Colloid and Interface Science* **97**(1): 195–200.

Carroll, B. J. (1992). 'Direct Measurement of the Contact Angle on Plates and on Thin Fibers – Some Theoretical Aspects.' *Journal of Adhesion Science and Technology* **6**(9): 983–994.

Cazabat, A. M. (1990). 'Experimental Aspects of Wetting' *Liquids at Interfaces*. J. Charvolin. Amsterdam, North-Holland, 371.

Cazabat, A. M., Gerdes, S. *et al.* (1997). 'Dynamics of wetting: From theory to experiment.' *Interface Science* **5**(2–3): 129–139.

Chatterjee, P. K. (1985). *Absorbency*. New York, Elsevier.

Cheng, P., Li, D., Boruvka, L., Rotenberg, Y. and Neuman, A.W. (1989). 'Colloids and Surfaces.' **43**: 151.

Daillant, J., Benattar, J. J. and Leger, L. (1990). *Phys. Rev. Lett.*, **A 41**: 1963.

Daillant, J., Bennattar, J. J, Bosio, L. and Leger, L. (1988). *Europhys. Lett.* **6**: 431.

de Gennes, P. G. (1985). 'Wetting: Statics and dynamics.' *Rev Mod Physics* **57**: 827–863.

de Gennes, P. G., Brochard-Wyart, F. and Quere, D. (2003). *Capillarity and Wetting Phenomena: Drops, Bubbles, Pearls, Waves*. New York, Springer.

Derjaguin, B. V. (1955). 'The definition and magnitude of disjoining pressure and its role in the statics and dynamics of thin fluid films.' *Kolloid Zhurnal* **17**: 204.

Derjaguin, B. V. and Levi S. M. (1943). *Film Coating Theory*. London, The Focal Press.

EDANA (1972). Recommended Test: Absorption. **10**.

Eggers, J. (1997). 'Nonlinear dynamics and breakup of free-surface flows.' *Reviews Of Modern Physics* **69**(3): 865–929.

Everet, D. H., Haynes, J. M. and Miller, R. J. (1978). 'Kinetics of capillary imbibition by fibrous materials. In *Fibre-water interactions in papermaking*, edited by the Fundamental Research Committee. London: Clowes.'

Fisher, L. (1999). Physics takes the biscuit, *Nature*, V. 397, 11 Feb., p. 469.

Ford, L. R. (1933). *Differential Equations*. New York: McGraw-Hill.

Good, R. J. (1964). *Contact Angle, Wettability, and Adhesion*, Washington DC, ACS, p. 74.

Grigorev, A. I. and Shiraeva S. O. (1990). 'Mechanism of electrostatic polydispersion of liquid.' *J. Phys. D: Appl. Phys.* **23**: 1361–1370.

Gupta, B. S. (1997). *Some Recent Studies of Absorbency in Fibrous Nonwovens*. XXV. International Nonwovens Colloquium, Brno, Czech.

Hardy, H. (1919). *Phil. Mag*. **38**: 49.

Herminghaus, S. (2005). 'Wetting: Introductory note.' *Journal of Physics: Condensed Matter* **17**(9): S261.

Heslot, F., Cazabat, A. M. *et al.* (1989). 'Diffusion-controlled Wetting Films.' *Journal of Physics – Condensed Matter* **1**(33): 5793–5798.

Heslot, F., Cazabat, A. M. *et al.* (1989). 'Dynamics of Wetting of Tiny Drops – Ellipsometric Study of the Late Stages of Spreading.' *Phys. Rev. Lett.* **62**: 1286.

Heslot, F., Fraysse, N. and Cazabat, A. M. (1989b). 'Molecular layering in the spreading of wetting liquid drops.' *Nature* **338**: 640.

Hirt, D. G., Adams, K. L., Hommer, R. K. and Rebenfeld, L. (1987). 'In-plane radial fluid flow characterization of fibrous materials.' *J. Thermal Insulation* **10**: 153.

Hsieh, Y. L. (1995). 'Liquid Transport in Fibrous Assemblies.' *Textile Res. J.* **65**: 299–307.

INDA (1992). Standard Test: Absorption. **10**.

Joanny, J. F. (1986). 'Dynamics of Wetting – Interface Profile of a Spreading Liquid.' *Journal De Mecanique Theorique et Appliquee*: 249–271.

Joanny, J. F. and Andelman, D. (1987). 'Steady-state Motion of a Liquid – Solid Contact Line.' *J. Coll. Int. Sci.* **119**: 451.

Keey, R. B. (1995). Drying of Fibrous Materials. *Handbook of Industrial Drying*. A. S. Mujumdar (ed). New York, Marcel Dekker, Inc. **2**: 825.

Kissa, E. (1996). 'Wetting and wicking.' *Textile Research Journal* **66**(10): 660–668.

Landau, L. D. and Lifshitz, E. M. (1988). *Theoretical Physics: Hydrodynamics*. Moscow, Nauka.

Leger, L., Erman, M. *et al.* (1988). 'Spreading of Non Volatile Liquids on Smooth Solid Surfaces – Role of Long-range Forces.' *Revue De Physique Appliquee* **23**(6): 1047–1054.

Leger, L. and Joanny J. F. (1992). 'Liquid Spreading.' *Rep. Pro. Phys.* **431**.

Lucas, R. (1918). 'Ueber das Zeitgesetz des kapillaren Aufstiegs von Flussigkeiten.' *Kolloid - Z.* **23**: 15.

Lukas, D., Soukupova, V., Pan, N. and Parikh, D. V. (2004). 'Computer simulation of 3-D liquid transport in fibrous materials.' *Simulation – Transactions of The Society For Modeling and Simulation International* **80**(11): 547–557.

Lukas, D. and Soukupova, V. (1999). *Recent Studies of Fibrous Materials' Wetting Dynamics*. INDEX 99 Congress, Geneva.

Lukas, D., Glazyrina, E. *et al.* (1997). 'Computer simulation of liquid wetting dynamics in fiber structures using the Ising model.' *Journal of the Textile Institute* **88**(2): 149–161.

Lukas, D. and Pan N. (2003). 'Wetting of a fiber bundle in fibrous structures.' *Polymer Composites* **24**(3): 314–322.

Lukkarinen, A. (1995). 'Mechanisms of fluid spreading: Ising model simulations.' *Phys. Rev. E.* **51**: 2199.

Manna, S. S., Herrmann, H. J. and Landau, D. P. (1992). 'A stochastic method to determine the shape of a drop on a wall.' *J Stat. Phys.* **66**: 1155.

McHale, G., Kab, N. A. *et al.* (1997). 'Wetting of a high-energy fiber surface.' *Journal of Colloid and Interface Science* **186**(2): 453–461.

McHale, G. and Newton, M. I. (2002). 'Global geometry and the equilibrium shapes of liquid drops on fibers.' *Colloids and Surfaces a-Physicochemical and Engineering Aspects* **206**(1–3): 79–86.

McHale, G., Rowan, S. M. *et al.* (1999). 'Estimation of contact angles on fibers.' *Journal of Adhesion Science and Technology* **13**(12): 1457–1469.

Meister, B. J. and Scheele, G. F. (1967). 'Generalized Solution of the Tomotika Stability Analysis for a Cylindrical Jet.' *AIChE J.* **13**: 682.

Miller, B. and Friedman, H. L. (1992). 'Adsorption rates for materials under compression.' *Tappi Journal*: 161.

Miller, B., Friedman, H. L. and Amundson, R. J. (1991). 'In-plane Flow of Liquids into Fibrous Networks.' *International Nonwovens Res.* **3**: 16.

Miller, B. and Jansen, S. H. (1982). 'Wicking of liquid in nonwoven fiber assemblies: Advances in nonwoven technology. In *10th Technical Symposium*, New York, pp. 216–26.

Neimark, A. V. (1999). 'Thermodynamic equilibrium and stability of liquid films and droplets on fibers.' *Journal of Adhesion Science and Technology* **13**(10): 1137–1154.

Perwuelz, A., Mondon, P. *et al.* (2000). 'Experimental study of capillary flow in yarns.' *Textile Research Journal* **70**(4): 333–339.

Pillai, K. M. and Advani, S. G. (1996). 'Wicking across a fiber-bank.' *J. Colloid Interface Sci*, **183**: 100.

Plateau, J. (1869). *Phil. Mag.* **38**: 445.

Princen, H. M. (1969). 'Capillary Phenomena in Assemblies of Parallel Cylinders. I. Capillary Rise between Two Cylinders.' *J. Coll. Interface Sci.* **30**: 69–75.

Princen, H. M. (1992). 'Capillary pressure behavior in pores with curved triangular cross-section: effect of wettability and pore size distribution.' *Colloids and Surfaces* **65**: 221–230.

Princen, H. M., Aronson, M. P. *et al.* (1980). 'Highly Concentrated Emulsions. II. Real Systems. The Effect of Film Thickness and Contact Angle on the Volume Fraction in Creamed Emulsions.' *J. Colloid Interface Sci.* **75**: 246–270.

Pumir, A. and Pomeau, Y. (1984). *C. R Acad. Sci.* **299**: 909.

Quere, D. (1999). 'Fluid coating on a fiber.' *Annual Review of Fluid Mechanics* **31**: 347–384.

Quere, D., Dimeglio, J. M. *et al.* (1988). 'Wetting of Fibers – Theory and Experiments.' *Revue De Physique Appliquee* **23**(6): 1023–1030.

Rafai, S., Bonn, D. and Meunier, J. (2005). 'Long-range critical wetting: Experimental phase diagram.' *Physica A.* **358**: 197.

Rayleigh, L. (1878). 'On the Instability of Jets.' *Proc. London Math Soc., Vol. 10, No. 4, 1878.* **10**.

Roe, R. J. (1957). 'Wetting of fine wires and films by a liquid film.' *Journal of Colloid and Interface Science* **50**: 70–79.

Schultz, W. W. and Davis S. H. (1982). 'One-Dimensional Liquid Fibers.' *Journal of Rheology* **26**(4): 331–345.

Seemann, R., Herminghaus, S. *et al.* (2005). 'Dynamics and structure formation in thin polymer melt films.' *Journal of Physics – Condensed Matter* **17**(9): S267–S290.

Sekimoto, K., Oguma, R. and Kawasaki, K. (1987). *Ann. Phys., NY* **176**: 379.

Skelton, J. (1976). 'Influence of Fiber Material and Wetting Medium on Capillary Forces in Wet Fibrous Assemblies.' *Textile Research Journal* **46**(5): 324–329.

Sorbie, K. S., Wu, Y. Z. *et al.* (1995) 'The extended Washburn equation and its application to the oil/water pore doublet problem; *J. Colloid and Interface Sci.*, **174**(2), 289–301.

Starov, V. M., Zhdannov, S. A., Kosvinstev, S. R., Sobolev, V. D. and Velarde, M. G. (2003). 'Effect of interfacial phenomena on dewetting in dropwise condensation.' *Advan. in Colloid and Interface Sci.* **104**: 123.

Tanner, L. H. (1976). *J. Phys.* **E9**: 967.

Teletzke, G. F., Davis, H. T. *et al.* (1988). 'Wetting Hydrodynamics.' *Revue De Physique Appliquee* **23**(6): 989–1007.

Tomotikav, S. (1935). 'On the instability of a cylindrical thread of a viscous liquid surrounded by another viscous fluid.' *Proc. Roy. Soc. London*, **A 150**: 322–337.

Washburn, E. W. (1921). 'The Dynamics of Capillary Flow.' *Phys. Rev.* **17**: 273–283.

Williams, R. B. (1977). *Nature* **156**: 266.

Young, T. (1805). 'An essay on the cohesion of liquids.' *Philos. Trans. R. Soc. London* **95**: 65.

Zhong, W., Ding, X. *et al.* (2001). 'Modeling and analyzing liquid wetting in fibrous assemblies.' *Textile Research Journal* **71**(9): 762–766.

Zhong, W., Ding, X. *et al.* (2001a). 'Statistical modeling of liquid wetting in fibrous assemblies.' *Acta Physico-Chimica Sinica* **17**(8): 682–686.